

Resonant Converter Topologies for Constant-Current Power Supplies and Their Applications

By

Mangesh Balkrishna Borage

Raja Ramanna Centre for Advanced Technology, Indore

A thesis submitted to the

Board of Studies in Engineering Sciences

In partial fulfillment of requirements

for the Degree of

DOCTOR OF PHILOSOPHY

of

HOMI BHABHA NATIONAL INSTITUTE

Guide

Dr. K. V. Nagesh

Co-Guide

Dr. M. S. Bhatia

Technical Advisor

Mr. Sunil Tiwari



September, 2011

Homi Bhabha National Institute

Recommendations of the Viva Voce Board

As members of the Viva Voce board, we certify that we have read the dissertation prepared by Mangesh Balakrishna Borage entitled RESONANT CONVERTER TOPOLOGIES FOR CONSTANT-CURRENT POWER SUPPLIES AND THEIR APPLICATIONS and recommend that it may be accepted as fulfilling the dissertation requirement for the Degree of Doctor of Philosophy.

Chairman:

Mannohan Singh
Prof. M. S. BHATIA

Date:

18-08-2011

Convener:

Mannohan Singh
Prof. M. S. BHATIA

Date:

18-08-2011

Member 1:

Badodkar
(Dr. D. N. BADODKAR)

Date:

18.08.2011.

Member 2:

CSPTIA

Date:

18-08-2011

Examiner:

Vinodgawad

Date: 18-8-2011

Final approval and acceptance of this dissertation is contingent upon the candidate's submission of the final copies of the dissertation to HBNI.

I hereby certify that I have read this dissertation prepared under my direction and recommend that it may be accepted as fulfilling the dissertation requirement.

Date: 18-8-2011

Place: Mumbai

Guide:

K.V. Nagella

DECLARATION

I hereby declare that the investigation presented in this thesis has been carried out by me. The work is original and has not been submitted earlier as a whole or in part for a degree/diploma at this or any other institution or university.

Mangesh Balkrishna Borage

*Dedicated to my mother
Late Prof. Mrs. Madhavi Balkrishna Borage
and her loving memories...*

ACKNOWLEDGEMENT

I express my sincere gratitude to my Guide Dr. K. V. Nagesh, Co-Guide Dr. M. S. Bhatia and Technology Advisor Mr. S. R. Tiwari. Their persistent encouragement, perpetual motivation, everlasting patience and valuable technical input have benefited me to an extent, which is beyond expression. Their contributions are beyond the purview of the acknowledgement.

I am thankful to Mr. A. C, Thakurta, Head, PSIAD, RRCAT, Indore for his support and encouragement. I take this opportunity to thank Mr. S. Kotaiah, Ex Head, PSD, and Project Manager, Indus-2 for motivation and support during the early phase of my Ph. D. work. I sincerely thank Dr. P. D. Gupta, Director, RRCAT for constant encouragement.

I am grateful to Dr. D. N. Bododkar and Dr. A. P. Tiwari for their advice and monitoring the yearly progress of the research work. I thank Dr. S. B. Roy, Dean-Academic, RRCAT for the words of support and advice. I also thank Dr. Avijit Chowdhury and Shri S. C. Bapna, BARC Training School, RRCAT for their help. Thank you, Dr. Biswaranjan Dikshit, BARC, for sharing your experience and the help. I am blessed with many loving friends in BARC - they all, as usual, have been very supportive.

My father, Dr. Balkrishna Maruti Borage, has always been a constant source of inspiration. His advice, words and presence plays a great role in my life, carrier, and now, the Ph. D. work. I miss my mother, Late Prof. Mrs. Madhavi Balkrishna Borage, who congratulated me for the last time on the

acceptance of research proposal in HBNI, just a week before she left all of us forever.

Thank you, Madhura, my wife, for being very supportive, giving me all freedom to work and sparing me from some of the responsibilities by managing them so well! I thank my son, Manthan, and daughter, Maithili, for keeping my interests alive. I realize, I haven't been able to enjoy some of the precious days of their childhood with them.

While our professions are different, our academic discussions are always lively. Thank you, Manisha, my younger sister and Mayur, my younger brother.

I would like to acknowledge the support and company of my colleagues in PSIAD, RRCAT in enriching my life. Special thanks to Vinod Somkuwar, Trepan Singh, Manohar Koli, Alok Singh, Harish Khatwani and Prashant Pareek for brilliant support during different stages of the research work.

Mangesh Balkrishna Borage

Contents

Abstract	vi
List of Abbreviations	viii
List of Symbols	x
List of Figures	xv
List of Tables	xxv
List of Publications	xxvii
1. Resonant Converters and Constant-Current Power Supplies	1
1.1 Switch-Mode Power Conversion and Soft-Switching	1
1.2 Resonant Converters: History and Present Status	3
1.2.1 RC Topologies	4
1.2.1.1 Two-element RC Topologies	5
1.2.1.2 Three-element RC Topologies	7
1.2.1.3 Higher-Order RC Topologies	9
1.2.2 Modes of Operation	11
1.2.3 Methods of Control	13
1.2.3.1 Variable Frequency Control	13
1.2.3.2 Phase Control	13
1.2.3.3 Clamped Mode Control	13
1.2.3.4 Asymmetrical Pulse Width Modulation Control	14
1.2.3.5 Asymmetrical Voltage Cancellation Control	14
1.2.3.6 Integral Cycle Control	14

1.2.3.7 Self-Sustained Oscillating Control	15
1.2.4 Methods of Analysis	15
1.2.4.1 State-space Approach	15
1.2.4.2 State-plane Approach	16
1.2.4.3 AC Analysis with Fundamental Frequency Approximation	16
1.2.4.4 Fourier-Series Method, or, Frequency Domain Approach	16
1.2.4.5 Discrete Time Domain Modeling	17
1.2.4.6 Small-signal Analysis	17
1.2.5 Integrated Magnetic and Reactive Components	18
1.2.6 Applications	19
1.2.6.1 Ballasts for Fluorescent Lamps	19
1.2.6.2 Power Factor Correction	19
1.2.6.3 Capacitor Charging	20
1.2.6.4 Induction Heating	20
1.2.6.5 Welding	21
1.2.6.6 Inductive Power Transfer	21
1.2.6.7 High Voltage Power Supply	22
1.3 Constant-Current Power Supplies	22
1.3.1 Applications	23
1.3.1.1 Electric arc welding	23
1.3.1.2 Laser Diode Drivers	24
1.3.1.3 Magnet Power Supplies	24
1.3.1.4 Illumination Systems	25
1.3.1.5 Battery Charging	25
1.3.1.6 Capacitor Charging	26
1.3.1.7 Electrochemical Processes	26
1.3.2 Conventional Techniques	26
1.4 Application of RCs to CC Power Supplies	27
1.5 Conclusion and Motivation	29
1.6 Organization of the Thesis	31

2. Resonant Immittance Converter Topologies	34
2.1 Immittance Converter	34
2.2 Resonant Immittance Converter	38
2.3 Identification of RINs	40
2.3.1 One-, Two- and Three-Branch Topological Structures	41
2.3.2 Four-Branch Topological Structures	46
2.3.2.1 Topology N_7	47
2.3.2.2 Topology N_8	48
2.3.2.3 Topology N_9	48
2.3.2.4 Topology N_{10}	49
2.4 Design Conditions	52
2.5 General Features	53
2.6 Conclusion	55
3. Analysis, Design and Topological Extensions of Type-II RICs	56
3.1 Topology T_1 : LCL-T RC	57
3.1.1 Analysis	58
3.1.2 Design	61
3.1.3 Experimental Results	63
3.1.4 Merits and Limitations	66
3.2 Topology LA_2 : The LC-LC RC	66
3.2.1 Analysis	67
3.2.2 Design	71
3.3 Topology T_3	72
3.3.1 Analysis	73
3.3.2 Design	76
3.3.3 Experimental Results	77
3.4 A Higher Order T-Type RIC Topology	80
3.4.1 Analysis	82
3.4.2 Design	86
3.4.3 Experimental Results	88
3.5 Topological Extensions	93

3.5.1 Type-II RIC With Inherent CCCV Characteristics	93
3.5.1.1 Experimental Results	97
3.5.2 Multi-phase Type-II RIC	100
3.5.2.1 Source- and Load-Side Harmonics	100
3.5.2.2 Phase-staggered Operation	102
3.5.2.3 Simulation Results	105
3.6 Conclusion	105
4. Asymmetrical Pulse Width Modulation Control	108
4.1 APWM Controlled LCL-T RC	109
4.2 State-Space Model and Modes of Operation	111
4.2.1 Mode-I	113
4.2.2 Mode-II	114
4.2.3 Mode-III	114
4.2.4 Mode-IV	115
4.2.5 Discussion	116
4.3 Mode Boundaries	117
4.4 Converter Design	120
4.5 Experimental Results	122
4.6 Conclusion	125
5. Equivalent Circuit Modeling and Analysis	126
5.1 Approximate Equivalent Circuit Model for Type-II RINs	127
5.2 Construction of Equivalent Circuit Model	129
5.3 Simulation and Experimental Results	133
5.4 Conclusion	139
6. Application Examples	140
6.1 HV DC Power Supply	140
6.1.1 Suitable Type-II RIC Topologies	141
6.1.2 Effect of C_w on LCL-T RC	142
6.1.3 Design of Topology LA ₂ as a HV Power Supply	146

6.1.4 Experimental Results	148
6.2 Capacitor Charging Power Supply	151
6.2.1 Design of LCL-T RC with Clamp Diodes as a CCPS	153
6.2.2 Experimental Results	154
6.3 Ultracapacitor Charger	156
6.3.1 Accounting Diode Drops in Design	157
6.3.2 Effect of L_{lk}	159
6.3.3 Experimental Results	161
6.4 Pulsed Current Sources	163
6.4.1 Configurations of Type-II RICs as Pulsed Current Sources	165
6.5 Conclusion	169
7. Conclusions	170
7.1 Accomplishments	171
7.2 Suggestions for Future Research	175
Appendix I	176
References	179

Abstract

Resonant converters have been an active area of research in power electronics field due to variety of topologies, diverse, peculiar and useful characteristics, and, wide applicability for voltage regulator modules, fluorescent lamps ballasts, power factor correction, capacitor charging, induction heating, welding, inductive power transfer, high-voltage power supply etc., due to soft switching, high frequency operation, high efficiency, and small size. While the majority of the previous work on resonant converters has been directed towards developing methods of analysis and control techniques for the mentioned applications, very little has been done to explore their suitability for application as a constant-current power supply, which is either inherently required or can be advantageously applied in electric arc welding, laser diode drivers, magnet power supplies, capacitor charging, illumination systems, battery charging, electrochemical processes etc.

Impedance converter topologies are suitable for transforming a voltage source to a current source and are deemed to be a promising alternative for developing topologies suitable for constant-current power supplies. This dissertation is dedicated to present an orderly search procedure for identification of a family of lumped-element impedance converter topologies suitable for power converter circuits, termed here as the resonant impedance converter topologies (RICs). In all 24 RIC topologies are identified with three and four reactive elements, of which 15 are suitable for application as a constant-current power supply.

Analysis and design procedure is exemplified with selected topologies. Fundamental frequency ac analysis is performed to gain insight into the steady-state

characteristics, derive closed-form expressions for converter gain and the ratings of various components. A methodology to design the converter by minimizing the kVA/kW rating of resonant network is presented. Experimental results on prototype converters demonstrate the converter performance and current source behaviour. Two topological extensions, namely RICs with inherent constant-current constant-voltage characteristics and multiphase RICs, are proposed featuring inherent over-load protection and improvement in converter dynamics, respectively, which are important and useful in many practical applications.

Feasibility of asymmetrical pulse width modulation control is analyzed with state-space model that identifies four distinct operating modes. The mode-boundaries are obtained and plotted on the $D-Q$ plane showing a region for the converter design wherein all the switches operate under zero-voltage-switching. An equivalent circuit model is proposed and a small-signal model is subsequently derived. These models greatly simplify and speed-up the transient and small-signal analysis. It has been shown that the open-loop transient and small-signal ac behaviour of resonant immittance converters is governed by only the filter and the converter along with the resonant immittance network does not contribute to the dynamics.

Applicability of resonant immittance converters in some of the application areas such as high-voltage dc power supply, capacitor charging power supply and a constant-current charger for ultracapacitor is demonstrated with application-specific design issues and prototype implementation. Application of multiphase topologies with various source-switch configurations as pulsed current sources is suggested and discussed.

List of Abbreviations

APWM	Asymmetrical pulse-width-modulation
BJT	Bipolar junction transistor
CC	Constant-current
CCCV	Constant-current constant-voltage
CCPS	Capacitor charging power supply
CM	Clamped-mode
CS-PRC	Current source parallel resonant converter
CV	Constant-voltage
CVCC	Constant-voltage, constant-current
EDM	Electrical discharge machining
EMI	Electromagnetic interference
FC	Finite current
FV	Finite voltage
GMAW	Gas metal arc welding
GTAW	Gas tungsten arc welding
HID	High intensity discharge
HV	High voltage
IC	Immittance converter
IGBT	Insulated-gate bipolar transistor
IMC	Integrated magnetic component
INI	Current source – resonant network – current sink

INV	Current source – resonant network – voltage sink
LED	Light emitting diode
LISN	Line impedance stabilization network
MOSFET	Metal oxide semiconductor field effect transistor
NC	Non-conducting
NR	Non-resonant
PAC	Plasma arc cutting
PCB	Printed circuit board
PRC	Parallel resonant converter
PRI	Parallel resonant inverter
PSPWM	Phase-shift pulse width modulation
PWM	Pulse width modulation
RC	Resonant converter
RHS	Right hand side
RIC	Resonant immittance converter
RIN	Resonant immittance network
RN	Resonant network
SAW	Submerged arc welding
SMAW	Shielded metal arc welding
SPRC	Series-parallel resonant converter
SRC	Series resonant converter
SRI	Series resonant inverter
VNI	Voltage source – resonant network – current sink
VNV	Voltage source – resonant network – voltage sink
ZC	Zero current
ZCS	Zero-current-switching
ZV	Zero voltage
ZVS	Zero-voltage-switching
ZV-ZCS	Zero-voltage, zero-current switching

List of Symbols

A	Transmission parameter (reverse voltage gain) of a two-port network
A_1, A_2	General coefficients defined for expression (3.71)
B	Transmission parameter (transfer impedance) of a two-port network
B_1, B_2	General coefficients defined for expressions (3.63) and (3.71)
C	Transmission parameter (transfer admittance) of a two-port network
C_A, C_B	Split dc-link capacitors in half-bridge converter
C_f	Output filter capacitor
C_i	Capacitor of a RN ($i = 1, 2, 3$)
C_o	Load capacitance in charging applications
C_w, C_w'	Equivalent lumped transformer winding capacitance referred on primary side and secondary side, respectively.
C_x	Capacitance per unit length of a distributed constant line
C_2'	Resonant capacitor reflected on the transformer secondary side
D	Transmission parameter (reverse current gain) of a two-port network. Also, duty ratio of a PWM waveform
D_{max}	Maximum value of duty ratio
D_A, D_B	Diodes in a half-bridge converter
$D_{c1} - D_{c4}$	Clamp diodes in CC-CV RIC circuits

$D_{r1} - D_{r4}$	Output rectifier diodes
$D_1 - D_4$	Diodes in a full-bridge converter
f_s	Switching frequency
G_1	Small-signal line-to-output current transfer function
G_2	Small-signal line-to-output voltage transfer function
H	Current gain
h	Order of harmonic in a non-sinusoidal periodic waveform
H'	Current gain of Topology LA ₂ modified due to tolerance in C_w
i_{C_i}	Instantaneous current in capacitor C_i ($i = 1, 2, 3$)
I_{C_i}	Rms value of i_{C_i}
I_{C_iN}	Normalized value of I_{C_i}
i_{C_w}	Instantaneous current in capacitor C_w
i_d	Instantaneous current in input dc source
$\langle i_d \rangle_{T_s}$	Average value of i_d over one period T_s
\hat{i}_d	Small-signal perturbation in i_d
i_{in}	Instantaneous input current of a RN
i_{L_i}	Instantaneous current in inductor L_i ($i = 1, 2, 3$)
I_{L_i}	Rms value of i_{L_i}
I_{L_iN}	Normalized value of I_{L_i}
i_{L_p}	Instantaneous current in inductor L_p
i_{L_s}	Instantaneous current in inductor L_s
i_{L_t}	Instantaneous current in inductor L_t
$I_{L_t, pk}$	Amplitude of i_{L_t} or i_{pri}
I_m	Amplitude of rectified output current of one module
i_o	Instantaneous output current
I_o	Average output current
i_{pri}	Instantaneous current in transformer primary winding
i_r	Instantaneous rectified output current

$\langle i_r \rangle_{T_s}$	Average value of i_r over one period T_s
\hat{i}_r	Small-signal perturbation in i_r
i_t	Instantaneous value of total rectified output current in multiphase RICs
i_1	Instantaneous current at the input port
i_2	Instantaneous current at the output port
I_1	Rms value of i_1
I_2	Rms value of i_2
kVA/kW	The kilo-volt-ampere per kilo-watt rating of RN
$(kVA/kW)_{opt}$	Optimum value of kVA/kW
L_a	Auxiliary inductor
L_i	Inductor of a RN ($i = 1, 2, 3$)
L_{lk}	Transformer leakage inductance referred to primary side
L_m	Transformer magnetizing inductance
L_p	Leakage inductance of transformer's primary winding
L_s	Leakage inductance of transformer's secondary winding
L_t	Total value of resonant inductor including L_{lk}
M	Voltage gain
m	Number of parallel-connected modules in multiphase RICs
n	Ratio of turns in secondary winding to number of turns in primary winding
n_3	Ratio of number of turns in tertiary winding to number of turns in primary winding
p	Number of cycle of operation
Q	Quality factor of a RN
Q_{FL}	Value of Q corresponding to full-load operation
Q_{opt}	Optimum value of Q
R_{ac}	Equivalent ac resistance
R_{eff}	Effective value of load resistance
R_L	Load resistance
$R_{L,max}, R_{L,min}$	Maximum and minimum values of R_L

s	Laplace operator
S_A, S_B	Switches in a half-bridge converter
$S_1 - S_4$	Switches in a full-bridge converter
T_c	Time required to charge a capacitor
t_i	Time instance ($i = 1, 2, 3, \dots$)
T_s	Time period of one switching cycle
V_{aux}	Auxiliary dc voltage source
v_{C_i}	Instantaneous voltage across capacitor C_i ($i = 1, 2, 3$)
V_{C_i}	Rms value of v_{C_i}
V_{C_iN}	Normalized value of V_{C_i}
v_d	Instantaneous value of input dc source
V_d	Average value of v_d
$\langle v_d \rangle_{T_s}$	Average value of v_d over one period T_s
\hat{v}_d	Small-signal perturbation in v_d
V_{dc}	On-state drop across clamp diode
V_{dmax}, V_{dmin}	Maximum and minimum value of V_d
V_{dr}	On-state drop across rectifier diode
v_{in}	Instantaneous voltage across the input port of a RN
$V_{in,rms}$	Rms value of the fundamental component of v_{in}
V_{in1}	Amplitude of fundamental component of v_{in}
v_{L_i}	Instantaneous voltage across inductor L_i ($i = 1, 2, 3$)
V_{L_i}	Rms value of v_{L_i}
V_{L_iN}	Normalized value of V_{L_i}
v_{pri}	Instantaneous voltage across transformer primary
V_{pri}	Amplitude of v_{pri}
$V_{pri, FL}$	Amplitude of v_{pri} corresponding to full-load operation
v_o	Instantaneous output voltage
$\langle v_o \rangle_{T_s}$	Average value of v_o over one period T_s
\hat{v}_o	Small-signal perturbation in v_o

V_o	Average output voltage
$V_{o,max}$	Maximum value of V_o
v_1	Instantaneous voltage across the input port
v_2	Instantaneous voltage across the output port
V_1	Rms value of v_1
V_2	Rms value of v_2
x	Length of distributed constant line
X_i	Generic reactance ($i = 1, 2, 3, 4$) in topological structure of electrical network
Z_{in}	Small-signal input impedance
Z_n	Characteristic impedance
Z_1	Input impedance of a two-port network
Z_2	Load impedance connected at the output port of a two-port network
α	Ratio of inductor (L_3/L_1). Also, non-conduction angle (in radian) of the rectifier diodes
β	Ratio of capacitors (C_3/C_1)
γ	Ratio of inductor (L_2/L_1)
θ	Phase angle in phase-staggered operation of multiphase RICs
λ	Wavelength
ρ	A parameter in transmission matrix of Type-II RICs
σ	Tolerance in value of C_w
φ	Phase angle between inverter output voltage and current
ψ	Ratio of capacitors (C_2/C_1) and (C_w/C_1)
ψ_{crit}	Critical value of ψ
ψ_{opt}	Optimum value of ψ
ω	Angular switching frequency
ω_n	Normalized switching frequency
ω_{ni}	Normalized switching frequency when a network behaves as RIN
ω_o	Angular resonant frequency

List of Figures

Fig. 1.1	Output characteristics of a common-emitter transistor	2
Fig. 1.2	(a) Block diagram of a dc-dc RC. (b)Simplified block diagram of a dc-dc RC.	3
Fig. 1.3	Two-element RNs. (a) SRC, (b) PRC, (c) CS-PRC, and, (d) CS-SRC.	6
Fig. 1.4	Three-element VNV RNs. Topologies shown in (b), (e), (h) and (i) have been studied in the past.	8
Fig. 1.5	Three-element VNI RNs. (a) PRC with input inductor, (b) LLC-type PRC, (c) LCC or series-parallel RC, and, (d) hybrid RC.	9
Fig. 1.6	Higher-order RNs reported in the literature.	10
Fig. 1.7	Circuit diagram of full-bridge converter [(a)] and waveforms of v_{in} and i_{in} in the discontinuous conduction mode [(b)], continuous conduction mode with leading power factor [(c)] and continuous conduction mode with lagging power factor [(d)].	12
Fig. 2.1	Block diagram of an IC.	35
Fig. 2.2	Loss free distributed constant line.	36
Fig. 2.3	Some application examples of distributed constant line type IC converters. (a) A MOSFET bridge exciting the sending end. The circuit configuration at the receiving end for (b) HID lamp ballast, (c) induction heating, and, (d) corona and plasma discharge application.	37

Fig. 2.4	Some lumped-element IC networks.	38
Fig. 2.5	Block diagram of a dc-dc RIC.	39
Fig. 2.6	Topological structures of electrical networks composed of maximum up to three branches.	41
Fig. 2.7	Composition of generic reactance X_i .	41
Fig. 2.8	Three- and Four-element RINs synthesized from topological structures N_5 and N_6 .	45
Fig. 2.9	Topological structures of electric networks composed of four branches.	46
Fig. 2.10	Equivalent T-networks of (a) N_7 , (b) N_8 and (c) N_9 .	46
Fig. 2.11	Four-element RINs synthesized from topological structures N_7 , N_8 and N_9 .	51
Fig. 2.12	Illustrations of transformer parasitic components being absorbed in various RINs. (a) Topology T_1 , (b) Topology T_4 , (c) Topology LA_2 and (d) Topology T_7 .	54
Fig. 3.1	Circuit diagram of (a) half-bridge and (b) full-bridge LCL-T RC.	57
Fig. 3.2	Plots of (a) H and (b) ϕ in LCL-T RC as a function of ω_n for different values of Q and $\gamma = 1$.	61
Fig. 3.3	kVA/kW rating of LCL-T RC as a function of Q for $\gamma=1$ and $\omega_n = 1$.	62
Fig. 3.4	Open loop output characteristics of prototype LCL-T RC.	64
Fig. 3.5	Voltage and current waveforms at the output of inverter bridge. (a) $R_L=0.53 \Omega$ and (b) $R_L=0.1 \Omega$. Scale: 20 V/div (voltage), 5 A/div (current) and 2.5 μs /div.	65
Fig. 3.6	Efficiency of prototype converter as a function of output power. Plot-(a): $R_L = 0.53 \Omega$ and V_d is varied from 5 V to 50 V. Plot-(b): $V_d = 50$ V and R_L is varied.	65
Fig. 3.7	Circuit diagram of half-bridge LC-LC RC.	67
Fig. 3.8	Plots of (a) H and (b) ϕ in LC-LC RC as a function of ω_n for different values of Q and for $\psi=0.2$, $\gamma=0.8$.	69

Fig. 3.9	kVA/kW rating of LC-LC RC as a function of Q for different values of ψ under the conditions $\omega_n = 1$ and $\gamma + \psi = 1$ (a) without considering the rating of C_2 and (b) considering the rating of C_2 .	72
Fig. 3.10	Circuit diagram of half-bridge T_3 RIC.	73
Fig. 3.11	Plots of (a) H , (b) I_{LIN} and (c) ϕ as a function of ω_n .	75
Fig. 3.12	kVA/kW rating of T_3 RIC as a function of Q .	76
Fig. 3.13	Photograph of the experimental prototype of T_3 RIC.	78
Fig. 3.14	(a) Experimental waveforms of voltage across switch S_B [trace (1)] and i_{L2} [trace (2)] at full-load (upper pair, 100 V/div, 5 A/div) and at no-load (lower pair, 100 V/div, 2 A/div). X-scale: 2.5 μs /div. (b) Experimental waveforms of voltage across switch S_B [trace (1)] and current through it [trace (2)] at full-load (upper pair, 100 V/div, 2 A/div) and at no-load (lower pair, 100 V/div, 1 A/div). X-scale: 2.5 μs /div.	79
Fig. 3.15	Open-loop output characteristic and plots of I_{L2} as well as efficiency of prototype T_3 RIC.	79
Fig. 3.16	Circuit diagram of proposed half-bridge LCLCL-T RC with (a) discrete reactive components and (b) IMC.	81
Fig. 3.17	Plots of (a) H and (b) ϕ in LCLCL-T RC as a function of ω_n for different values of Q and for $\alpha = \psi = \gamma = 1$.	84
Fig. 3.18	kVA/kW rating of LCLCL-T RC as a function of Q for different values of α and γ and respective $\psi = \psi_{crit}$ showing the existence of Q_{opt} .	87
Fig. 3.19	Photograph of the experimental prototype of LCLCL-T RC.	89
Fig. 3.20	Experimental waveforms of voltage across switch S_B [trace (1), 50 V/div], i_{Lp} [trace (2), 5 A/div], i_{Ls} [trace (3), 1 A/div] and i_o [trace (4), 1 A/div]. (a) At full-load. (b) At 5 % of full-load. X-scale: 2.5 μs /div.	90
Fig. 3.21	Experimental waveforms of voltage across switch S_B [trace (1)] and current through it [trace (2)]. Upper pair of	90

	waveforms: full-load condition, 50 V/div and 5 A/div, respectively. Lower pair of waveforms: At 10 % of the full-load, 50 V/div and 2 A/div, respectively. X-scale: 2.5 μ s/div..	
Fig. 3.22	Experimental output characteristic of LCLCL-T RC.	91
Fig. 3.23	Experimental waveforms of v_o [trace (1), 100 V/div], rectified output current [trace (2), 1 A/div] and i_o [trace (3), 1 A/div] under transient condition with step change in R_L from 140 Ω to 230 Ω at instant t_1 and vice versa at instant t_2 . X-scale: 25 ms/div.	92
Fig. 3.24	Measured (open circles) and predicted (dashed curve) rms value of i_{Lp} . Experimental efficiency is shown by solid circles.	92
Fig. 3.25	Half-bridge type-II RIC.	94
Fig. 3.26	Idealized waveforms at the input and output port of the RIN.	94
Fig. 3.27	Proposed topological extension of a half-bridge Type-II RIC with clamp diode for in built CCCV characteristics.	95
Fig. 3.28	Half-bridge Type-II RIC with tertiary winding and clamp diodes.	96
Fig. 3.29	(a) Topological variant of a half-bridge Type-II RIC allowing variable CV-limit. The CV-limit is changed by changing the value of V_{aux} . (b) Possible practical realization of V_{aux} using a class-B chopper.	96
Fig. 3.30	Prototype half-bridge LCL-T RC with clamp diodes.	97
Fig. 3.31	Circuit waveforms of prototype LCL-T RC with clamp diodes for operation with (a) $R_L=200 \Omega$, (b) $R_L=500 \Omega$ and (c) $R_L=1000 \Omega$. Legends: (1) v_{in} , 50 V/div. (2) v_{pri} , 50 V/div. (3) i_L , 10 A/div. (4) $(i_{Dc1}-i_{Dc2})$, 10 A/div. X-scale: 2.5 μ s/div.	98
Fig. 3.32	Experimental characteristics (a) I_o and V_o as a function of change in R_L . Legends: $-\square-$: I_o , $-\blacksquare-$: V_o . (b) I_o - V_o plot with R_L as the running parameter. Solid curve with marker shows the experimentally measured characteristics and the dashed curve shows the characteristics of an ideal CCCV power supply.	99

Fig. 3.33	Output power and efficiency of experimental converter as a function of R_L . Legends: \square - : Efficiency , \blacksquare -: Output power (W)	99
Fig. 3.34	Generic waveform for the rectified output current, i_r , and the current drawn from the input dc source, i_d .	100
Fig. 3.35	Experimental waveform (1 A/div, 2.5 μ s/div) and frequency spectrum (10 db/div, 125 Hz/div) of (a) i_r and (b) i_d in Topology T ₃ .	101
Fig. 3.36	Computed and measured dominant harmonics of (a) i_r and (b) i_d in Topology T ₃ .	101
Fig. 3.37	Conducted EMI along with CISPR 11 limit lines: (a) complete spectrum and (b) spectrum details between 100 kHz and 1 MHz.	101
Fig. 3.38	Parallel operation of Type-II RICs.	103
Fig. 3.39	Ripple reduction in the output current of (a) two paralleled Type-II RICs operating with $\theta=90^\circ$ and (b) three paralleled Type-II RICs operating with $\theta=120^\circ$	104
Fig. 3.40	Peak-peak ripple in the rectified output current normalized to its average value as a function of θ in multiphase Type-II RICs.	104
Fig. 3.41	Simulation results of topology T ₃ . (a) Waveforms of rectified output currents of the three modules and the total current, (b) their spectrum (dashed curve for output current of individual module and continuous curve for total current) and (c) waveform of the current at the output of MOSFET bridge.	106
Fig. 4.1	Circuit diagrams of (a) Half-bridge and (b) full-bridge LCL-T RC.	110
Fig. 4.2	Idealized waveforms of gate pulses for the switches and v_{in} with APWM control. The switches mentioned in the bracket correspond to the full-bridge converter.	111
Fig. 4.3	Equivalent circuit diagram of LCL-T RC.	112

Fig. 4.4	Steady-state waveforms of v_{in} and i_{L1} in Mode-I operation.	113
Fig. 4.5	Steady-state waveforms of v_{in} and i_{L1} in Mode-II operation.	114
Fig. 4.6	Steady-state waveforms of v_{in} and i_{L1} in Mode-III operation.	115
Fig. 4.7	Steady-state waveforms of v_{in} and i_{L1} in Mode-IV operation.	116
Fig. 4.8	Waveforms of v_{in} and i_{L1} in steady-state as the converter makes transition from one mode into another. Boundary between (a) Mode-I and Mode-IV, (b) Mode-II and Mode-IV, (c) Mode-III and Mode-IV and (d) Mode-I and Mode-III.	118
Fig. 4.9	D - Q plane of APWM controlled LCL-T RC showing the regions of different modes of operation.	119
Fig. 4.10	Variation of ϕ as a function of Q for operation at $D=0.5$ in APWM controlled LCL-T RC.	119
Fig. 4.11	Regions of ZVS operation of all the switches in LCL-T RC with APWM (solid line) and CM control (broken line).	120
Fig. 4.12	Experimental waveforms of v_{in} [trace (1), 20 V/div] and i_{L1} [trace (2), 0.5 A/div in (a), (c) and 1 A/div in (b), (d)] in APWM controlled LCL-T RC (a) Mode-I ($D=0.5$, $Q=1.2$), (b) Mode-II ($D=0.5$, $Q=0.3$), (c) Mode-III ($D=0.2$, $Q=1.2$) and (d) Mode-IV ($D=0.4$, $Q=0.6$). X-scale: 2.5 μ s/div.	123
Fig. 4.13	Experimental waveforms of v_{in} [trace (1), 100 V/div] and i_{L1} [trace (2), 5 A/div] at $Q=1.2$. (a) Mode-I ($D=0.5$) and (b) Mode-III ($D=0.2$). X-scale: 2.5 μ s/div.	124
Fig. 4.14	Open-loop control characteristics of prototype APWM controlled LCL-T RC.	124
Fig. 4.15	Experimental efficiency of APWM controlled LCL-T RC.	125
Fig. 5.1	Small-signal input voltage-to-output current transfer function for topology T ₁ , LA ₂ and T ₃ obtained from envelop-simulation method. Component values used for simulation are given in table 5.1.	128
Fig. 5.2	Equivalent circuit representation of Type-II RIN.	128
Fig. 5.3	Block diagram of a voltage-source Type-II RIC.	129

Fig. 5.4	Idealized circuit operating waveforms at the input and output port of the shaded portion of the block diagram.	130
Fig. 5.5	Equivalent circuit model of (a) shaded portion of the block diagram of Fig. 5.2 and (b) Type-II RIC.	131
Fig. 5.6	Small-signal ac equivalent circuit model of (a) shaded portion of the block diagram of Fig. 5.2 and (b) Type-II RIC.	132
Fig. 5.7	Response of Topology T ₃ to step change in input dc voltage. (a) Predicted average response from the equivalent circuit model. Top trace: $\langle v_d \rangle_{T_s}$, dotted trace: $\langle i_r \rangle_{T_s}$ and continuous trace: $\langle i_o \rangle_{T_s}$. (b) Results of cycle-by-cycle simulation. (c) Experimental results. In (b) and (c), the waveform at the top shows $v_d(t)$, the envelope shows $i_r(t)$ and the trace at the bottom shows $i_o(t)$.	134
Fig. 5.8	Response of Topology T ₃ to step change in R_L . (a) Predicted average response from the equivalent circuit model. Top trace: $\langle v_o \rangle_{T_s}$, dotted trace: $\langle i_r \rangle_{T_s}$ and continuous trace: $\langle i_o \rangle_{T_s}$. (b) Results of cycle-by-cycle simulation. (c) Experimental results. In (b) and (c), the waveform at the top shows $v_o(t)$, the envelope shows $i_r(t)$ and the trace at the bottom shows $i_o(t)$.	135
Fig. 5.9	Response of Topology T ₃ to sinusoidal perturbations in dc voltage. (a ₁)-(a ₃): 10 Hz, (b ₁)-(b ₃): 100 Hz and (c ₁)-(c ₃): 1000 Hz.. Parts (a ₁), (b ₁) and (c ₁) show the predicted average response from the equivalent circuit model [Top trace: $\langle v_d \rangle_{T_s}$, dotted trace: $\langle i_r \rangle_{T_s}$ and continuous trace: $\langle i_o \rangle_{T_s}$]. Parts (a ₂), (b ₂) and (c ₂) show the results of cycle-by-cycle simulation. Parts (a ₃), (b ₃) and (c ₃) show the experimental results. In (b ₂)-(b ₃) and (c ₂)-(c ₃), the waveform at the top shows $v_d(t)$, the envelope shows $i_r(t)$ and the trace at the bottom shows $i_o(t)$.	136 137
Fig. 5.10	Simulated response of Topology T ₃ to sinusoidal perturbations	138

	in dc voltage at (a) 10 kHz and (b) 50 kHz. Waveform from top to bottom: $v_d(t)$, $i_r(t)$ and $i_o(t)$.	
Fig. 5.10	Theoretical and experimental line-to-output small-signal transfer function of Topology T ₃ .	139
Fig. 6.1	Circuit diagram of half-bridge LCL-T RC. Transformer L_{lk} and C_w are shown explicitly inside the shaded area.	142
Fig. 6.2	(a) Equivalent circuit diagram of the output stage of LCL-T RC and (b) its waveforms for analysis of the effect of C_w .	143
Fig. 6.3	Effect of C_w on the current gain of LCL-T RC. (a) Variation of H as a function of Q . (b) Variation of H as a function of ψ at $Q=Q_{opt}$. Markers show the data points obtained from simulation.	145
Fig. 6.4	Plot of ratio (H'/H) as a function of $(\psi\sigma/Q)$ showing the effect of manufacturing tolerances in C_w on the current gain of LC-LC RC at $\omega_n = 1$.	147
Fig. 6.5	Photograph of the experimental prototype HV power supply.	148
Fig. 6.6	Output characteristic of open-loop LCL-T RC (—■—) and LC-LC RC (—●—) with C_w .	149
Fig. 6.7	Waveforms of transformer primary voltage (Ref A, 50V/div) and secondary current (Ref B, 100 mA/div) in LCL-T RC at $R_L=20$ k Ω . X-scale: 2.5 μ s/div.	149
Fig. 6.8	Waveforms of transformer primary voltage (Ref A, 50V/div) and secondary current (Ref B, 100 mA/div) in LCL-T RC at $R_L=5$ k Ω . X-scale: 2.5 μ s/div.	150
Fig. 6.9	Waveforms of bridge output voltage [trace (1), 50 V/div] and current [trace (2), 2 A/div] in LC-LC RC with (a) $R_L=20$ k Ω , and, (b) $R_L=1$ k Ω . X-scale: 2.5 μ s/div.	151
Fig. 6.10	Experimental efficiency of LCL-T RC (—■—) and LC-LC RC (—●—).	151
Fig. 6.11	Typical charge – discharge cycle of a CCPS	152
Fig. 6.12	Circuit diagram of LCL-T half-bridge RC with clamp diodes	154

	as a CCPS.	
Fig. 6.13	Circuit waveforms of experimental prototype CCPS during charging and refresh mode of the charging cycle. Legends: (1) Output voltage, V_o , 500 V/div. (2) Current in resonant inductor L , i_{L1} , 10 A/div. (3) Transformer primary current, 10 A/div. (4) Clamp diode current, i_{Dc1} - i_{Dc2} , 10 A/div. X-scale: 250 μ s/div.	155
Fig. 6.14	Magnified waveforms of V_o and i_{L1} at the commencement of (a) charging mode (details around $t=t_1$ of Fig. 6.11) and (b) discharge cycle (details around $t=t_3$ of Fig. 6.11). Legends: (1) V_o , 100 V/div. (2) i_{L1} , 2 A/div. X-scale: 100 μ s/div	155
Fig. 6.15	Circuit diagram of Type-II RIC with clamp diodes used as a CC charger for ultracapacitor.	158
Fig. 6.16	Circuit diagram of CC charger for ultracapacitor showing L_{lk} explicitly.	159
Fig. 6.17	Simulated waveforms: (1) primary current, (2) v_{pri} when L_{lk} is insignificant and (3) v_{pri} when L_{lk} is 0.3 times the value of resonant inductor.	160
Fig. 6.18	Simulated waveforms of v_{pri} (upper plot), the current in D_{C1} (middle plot) and the voltage across output capacitor (lower plot) when (a) L_{lk} is insignificant and (b) L_{lk} is 0.3 times the value of resonant inductor.	160
Fig. 6.19	Photographs showing the charger for ultracapacitor.	161
Fig. 6.20	Experimental waveforms of capacitor voltage (upper trace, 5 V/div) and charging current (lower trace, 5 A/div) with (a) clamp diodes and (b) without clamp diodes showing the effect of pre-mature clamping. X-scale: 10 sec/div.	162
Fig. 6.21	Charging cycle of ultracapacitor showing capacitor voltage [(1), 5 V/div] and charging current [(2), 5 A/div] when two chargers are operating in parallel. (3) and (4) respectively show these waveforms with one charger. X-scale: 10 sec/div.	163

Fig. 6.22	Profile of pulse current required for (a) GMAW, and, (b) GTAW.	164
Fig. 6.23	Advanced pulse charging cycle for batteries. The discharge pulse is present in only in burp-charging method.	165
Fig. 6.24	Realization of pulsed current source by modulating the source voltage.	166
Fig. 6.25	(a) Configuration of pulsed current source using a m -phase RIC and switch. (b) Timing waveforms.	166
Fig. 6.26	(a) Configuration of pulsed current source using two m -phase RICs and a switch to generate current pulse with offset. (b) Timing waveforms.	167
Fig. 6.27	(a) Configuration of pulsed current source using two m -phase RICs and two switches to generate bipolar current pulses. (b) Timing waveforms.	168
Fig. A1.1	Equivalent circuit diagram of LC-LC RC for ac analysis.	176

List of Tables

Table 1.1	Number of RC topologies.	5
Table 1.2	Summary of characteristics parameters of a CV and CC power supply.	23
Table 2.1	Transmission parameters of various topological structures of electrical networks shown in Fig. 2.6.	42
Table 2.2	Synthesis of RINs resulting from topological structure N_5 .	43
Table 2.3	Synthesis of RINs resulting from topological structure N_6 .	44
Table 2.4	Condition for immittance conversion characteristics of N_7 , N_8 and N_9 .	47
Table 2.5	Synthesis of RINs resulting from topological structure N_7 .	49
Table 2.6	Synthesis of RINs resulting from topological structure N_8 .	50
Table 2.7	Synthesis of RINs resulting from topological structure N_9 .	50
Table 2.8	Synthesis of RINs resulting from topological structure N_{10} .	51
Table 2.9	Operating point and design condition of RINs.	53
Table 3.1	Specifications, component values and ratings of reactive components in prototype LCL-T RC.	64
Table 3.2	The kVA/kW rating, Q_{opt} , $(kVA/kW)_{opt}$ and ψ_{opt} in LC-LC RC.	71
Table 3.3	Specifications, component values and ratings of reactive components in prototype T_3 RIC.	78
Table 3.4	Coefficients A_1 and A_2 in the general form (3.71) of the expressions for various normalized currents and voltages.	85

Table 3.5	Specifications and component values in prototype LCLCL-T RC.	89
Table 4.1	Switching conditions for the switches and diodes in half-bridge LCL-T RC in various operation modes with APWM control.	117
Table 4.2	Specifications and design parameters of the prototype APWM controlled LCL-T RC. The respective values actually used in the prototypes are given in the brackets.	122
Table 5.1	Component values used for obtaining voltage-to-output current transfer function for T_1 , LA_2 and T_3 using envelop-simulation method.	128
Table 6.1	Specifications and design parameters of the converter used for simulation studies to compare the analytical and simulation results as shown in Fig. 6.3.	145

List of Publications

Papers published/accepted for publication in refereed Journals

- [1] Mangesh Borage, K. V. Nagesh, M. S. Bhatia, Sunil Tiwari, “Design of LCL-T resonant converter including the effect of transformer winding capacitance,” IEEE Transactions on Industrial Electronics, Vol. 56, no. 5, pp. 1420-1427, May 2009.
- [2] Mangesh Borage, K. V. Nagesh, M. S. Bhatia, Sunil Tiwari, “Characteristics and design of an asymmetrical duty-cycle-controlled LCL-T resonant converter,” IEEE Transactions on Power Electronics, Vol. 24, no. 10, pp. 2268-2275, October 2009.
- [3] Mangesh Borage, K. V. Nagesh, M. S. Bhatia and Sunil Tiwari, “Analysis and design of higher-order T-type resonant convertor as a constant current power supply”, IET Transactions on Power Electronics, Vol. 4, no. 1, pp. 72-80, January 2011.
- [4] Mangesh Borage, K. V. Nagesh, M. S. Bhatia and Sunil Tiwari, “Resonant immittance converter topologies”, IEEE Transactions on Industrial Electronics, vol. 58, no. 3, pp. 971-978, March 2011.

Chapter 1

Resonant Converters and Constant-Current Power Supplies

1.1 Switch-Mode Power Conversion and Soft-Switching

As opposed to linear power supplies, in switch-mode power supplies, the transformation of dc voltage from one level to another is accomplished by using dc-to-dc switch-mode power converters, in which power semiconductor devices are operated as a switch. In linear regulators, the regulation device - for instance, a transistor - is operated in active region (see Fig. 1.1). This mode of operation requires high voltage drop across its terminals, thereby resulting in high power dissipation. In the switch-mode operation, the transistor is operated saturation (switch on) and cut-off (switch off) regions. High voltage and current therefore do not co-exist in the device, except during switching transitions, the latter being a small fraction of a switching period. Therefore, the switch-mode operation results in lower power dissipation. Further, due to high-frequency operation, the size of isolation transformer and passive components in the filter are drastically reduced. Increased speeds, higher voltage and current rating and a relatively low cost of these devices are the other factors that have contributed to the emergence of switching power supplies. However, these benefits of switching power supplies come at the cost of higher complexity, more switching losses, higher switching stresses and electromagnetic interference (EMI).

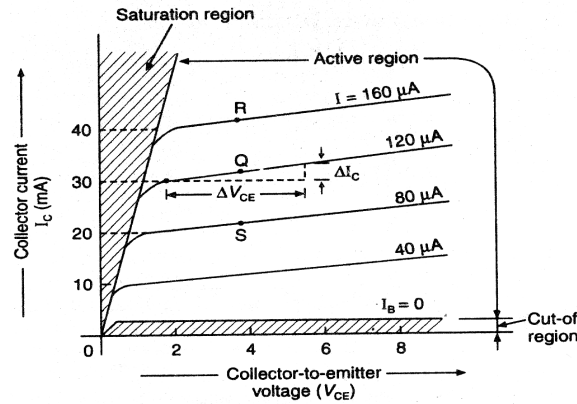


Fig. 1.1: Output characteristics of a common-emitter transistor.

These problems are exacerbated with increasing switching frequency. Therefore, although the power devices are capable of being operated at higher frequency, these problems pose a practical upper limit on the switching frequency.

Further miniaturization of power converter circuits is possible if they operate at still higher switching frequency, and to do this, a way to reduce or eliminate the switching losses and stresses must be conceived. Passive turn-on and turn-off snubbers are used to control the rate of rise of voltage and current, clamp overshoots during switching transitions, to reduce switching losses and to reduce EMI. However, snubbers only transfer the losses from switch to the snubber resistor, and therefore do not result in overall reduction in the losses [1]. Improvement in the efficiency is possible with loss-less or energy recovery snubbers, in which the energy stored in the snubber capacitor or inductor is transferred to the source or load, instead of being dissipated. [2].

If the switch is made to change its state (from off to on and vice versa) at an instant when either voltage across it or current through it is zero, then aforementioned shortcomings are minimized. Such switching action is termed as the soft switching. In zero-voltage-switching (ZVS), the switch changes its state when the voltage across it is zero, whereas in zero-current-switching (ZCS), the switch changes its state when current through it is zero. The ZVS or ZCS, collectively termed as soft switching, can be achieved by different ways, which are broadly classified as follows:

- 1) Adding passive auxiliary reactive components (e.g. quasi-resonant converters [3])

- 2) Adding active auxiliary circuit (e.g. resonant transition converters [4])
- 3) Modifying the switching strategy (e.g. full-bridge ZVS converter [5] and zero-voltage, zero-current-switching (ZV-ZCS) converter [6])
- 4) Changing the converter topology (e.g. resonant converters [7] – [210])

Merits and limitations of various soft switching methods are reviewed by M. Jovanovic [7], [8].

1.2 Resonant Converters: History and Present Status

Figure 1.2(a) shows the block diagram of a dc-dc resonant converter (RC). The input can either be a dc voltage source or a dc current source. An inverter (full-bridge, half-bridge or push-pull) excites the resonant network (RN) with high frequency square-wave waveform. A transformer at the output of RN is used to step-up or down the voltage according to the requirement and provides galvanic isolation. Rectifier and filter is used to get the dc output. The nature of the filter, inductive or capacitive, decides the nature of load to be current sink or voltage sink, respectively. Simplified block diagram of a RC is shown in Fig. 1.2(b), in which the dc source and square-wave inverter are shown as the voltage or current source to the RN whereas transformer, rectifier, filter and load resistance are shown as voltage or current load. Therefore, based on the type of source, type of load and the RN, it is possible to group RCs as follows [9]:

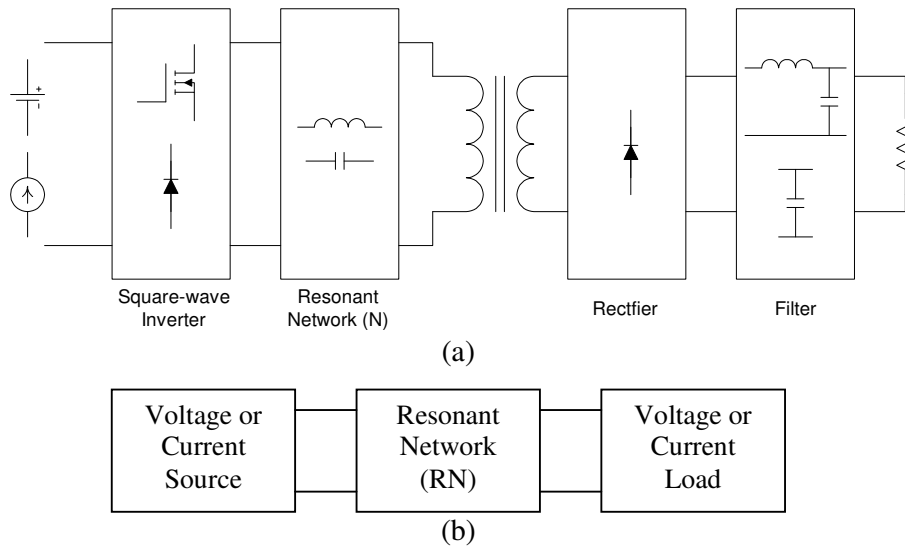


Fig. 1.2: (a) Block diagram of a dc-dc RC. (b) Simplified block diagram

1. Voltage source-RN-voltage sink, or VNV topologies,
2. Voltage source-RN-current sink, or VNI topologies,
3. Current source-RN-voltage sink, or INV topologies,
4. Current source-RN-current sink, or INI topologies.

The RN has two or more reactive components. Not all network combinations of reactive components are useful for RCs. The RCs are defined [9] as the ones in which,

- The power transfer from input to output is primarily via the fundamental component of switching frequency. The harmonics of source and load contribute little to the power transfer. What this implies is that the RN acts either as a low pass or a band pass filter, isolating the input and output at harmonics of switching frequency.
- The waveforms of the voltage or current response of RN to the excitation of source and load is piecewise sinusoidal.

This definition decides which topologies are resonant. It is not implied that the topologies that do not meet this criteria are not usable. They are only not classified as RCs. Further, for practical usability of RCs, some restrictions are placed [9] on the input and output impedances of a RN for different types of sources and loads. They are as follows:

- For voltage source or loads, impedance seen by the source or load must be high at the harmonics of switching frequency.
- For current sources or loads, impedance seen by the source or load must be low at the harmonics of switching frequency.
- Only those networks, for which the transfer function is either low pass or band pass type, are considered as resonant.

1.2.1 RC Topologies

A RC has a RN with minimum two reactive energy storage components. Two-element RCs are the simplest configurations. However, significant work has been reported in the literature on three-, four- and higher-element RCs. An orderly search procedure for systematic investigation of RC topologies with two, three and four energy storage elements is given in [9], [10]. Table 1.1 summarizes the number of

topologies, which are classified as RCs and grouped as VNV, VNI, INV and INI. Note that I. Batarseh [10] uses slightly different restrictions in classifying the RCs than defined by R. Severns [9]. Also, only those four-element RC topologies have been explored in [10] which have 2 inductors and 2 capacitors. The other combinations such as 3 inductors – 1 capacitor or 1 inductor – 3 capacitors are not considered. Also, the complete classification into all four groups is also not reported. The topologies of INV and INI group are also not reported.

Detailed analysis of some of the RC topologies has been reported in the literature. A review of the characteristic features of these topologies is presented in the following sub-sections. Various types of RCs are formed by using different RNs and suitable sources and loads in the block diagram of Fig. 1.1. Therefore, in the subsequent discussion, only RNs are shown instead of complete circuit diagram for each converter.

1.2.1.1 Two-element RC Topologies

Two-element RNs, shown in Fig. 1.3, are the simplest of various possible configurations. Figure 1.3(a) shows the RN of series resonant converter (SRC). It is one of the oldest RC topology [11] – [15] where it was primarily used for commutation of thyristors in bridge inverters. Modeling and analysis of SRC is described in [16] – [22]. A complete steady state analysis of SRC for all operating modes has been reported by A. Witulski, [23] which is then applied for its design with minimum component stress [24]. The advantages of SRC are: simple topology, inherent dc blocking of isolation transformer, high part-load efficiency, and possibility to integrate leakage inductance of transformer as the resonant inductor. The major limitations of SRC are: lack of no-load regulation, large frequency variation for output control and high output ripple current. It is not inherently short-

Table 1.1: Number of RC topologies.

Resonant Converters	Number of topologies				
	VNV	VNI	INV	INI	Total
Two-element	1	1	1	1	4
Three-element	9	4	4	9	26
Four-element	17	44	-	-	61

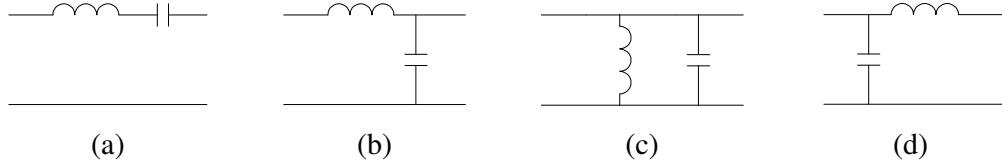


Fig. 1.3: Two-element RNs. (a) SRC, (b) PRC, (c) CS-PRC, and, (d) CS-SRC.

circuit proof. However, overload protection can be achieved by clamping the resonant capacitor voltage to the supply voltage [25], [26] using diodes. It is primarily suitable for high-output-voltage and low-output-current applications.

The RN of a parallel resonant converter (PRC) is shown in Fig. 1.3(b) [27] – [30]. A complete steady state analysis of PRC for all operating modes has been reported by S. Johnson, et. al. [31]. Analysis of PRC for operation above the resonant frequency, which is only possible with forced commutated switches, has been reported by A. Bhat, et. al. [32]. An effect of the leakage and magnetizing inductance of transformer on the operation of PRC is analyzed [33] and it is suggested that by placing the resonant capacitor on the secondary side of the transformer [34], or on the tertiary winding [35], the transformer leakage inductance can be used advantageously as the part of RN. A comparison among conventional PRC, the PRC with secondary side resonance and the PRC with tertiary side resonance are reported by M. Swamy, et. al. [36]. PRC offers load independent output current, which makes it a candidate topology for application as a constant-current power supply [37]. The advantages of PRC are: simple topology, inherently short-circuit proof, capability of no-load regulation, low output ripple current and gainful utilization of transformer parasitic components as a part of RN. The major limitations of PRC are: lack of inherent dc blocking of isolation transformer and poor part-load efficiency. It is primarily suitable for low-output-voltage and high-output-current applications.

A current-source parallel resonant converter (CS-PRC) [38] – [40], and current-source series resonant converter (CS-SRC) [41], [42], whose RNs are shown in Fig. 1.3(c) and Fig. 2(d), respectively, are the two input-current-fed two-element RC topologies. Current-fed topologies, in general, have been less popular since a large inductance is needed at the input to realize input current source. However, a current-fed converter offers following advantages: non-pulsating input current, less

input filter requirement, simplified driving requirement for low-side switches in push-pull [43] configuration and inherent immunity to shoot-through failures. Due to this, they have been used for applications such as induction heating [44], ozone generation [45] and lamp ballasts [46]. Detailed analysis using fundamental frequency approximation is reported by M. Kazimierczuk, et. al. [47]. While ZVS operation is achieved in the steady-state, it is not guaranteed during start-up conditions. A solution to this problem using forced dc current is proposed recently by A. P. Hu, et. al. [48].

1.2.1.2 Three-element RC Topologies

Three-element VNV RNs are shown in Fig. 1.4. Only four topologies out of nine VNV networks have been further analyzed in the past. The RN of Fig. 1.4(b) is termed as the LLC-type SRC [49], [50]. This network was developed as an attempt to overcome the inability in SRC to achieve no-load regulation by placing an inductor in parallel with the resonating capacitor. This modifies control characteristics in such a way that the output voltage can be varied from zero to maximum under any loading condition with moderate sweep of switching frequency.

SRC was modified with an additional inductor in parallel with the output port resulting in one of the most popular and useful topology, shown in Fig. 1.4(e), which was known as LCL-type SRC or modified SRC [51] – [53]. With the said modifications, control characteristics are altered in two ways: (i) it offers load independent output voltage when operated at resonant frequency and (ii) no-load regulation is possible. The analysis and operation of the topology with fixed-frequency pulse width modulation (PWM) control is reported by A. K. S. Bhat [54] and it is shown that the converter can operate over the entire range without losing ZVS of the switches. Recently, there has been renewed interest in this topology (which is also termed as the LLC RC) for application as voltage regulator modules, front-end converter [55], [56] and power factor correction [57]. Series and shunt inductor along with the transformer can be integrated in a single magnetic component [58] – [59]. The converter is, however, not inherently short-circuit proof and various over-current protection schemes are discussed in [60].

A T-type RN of Fig. 1.4(h) shows interesting properties and has been extensively studied in the past. It exhibits load independent output voltage suitable for

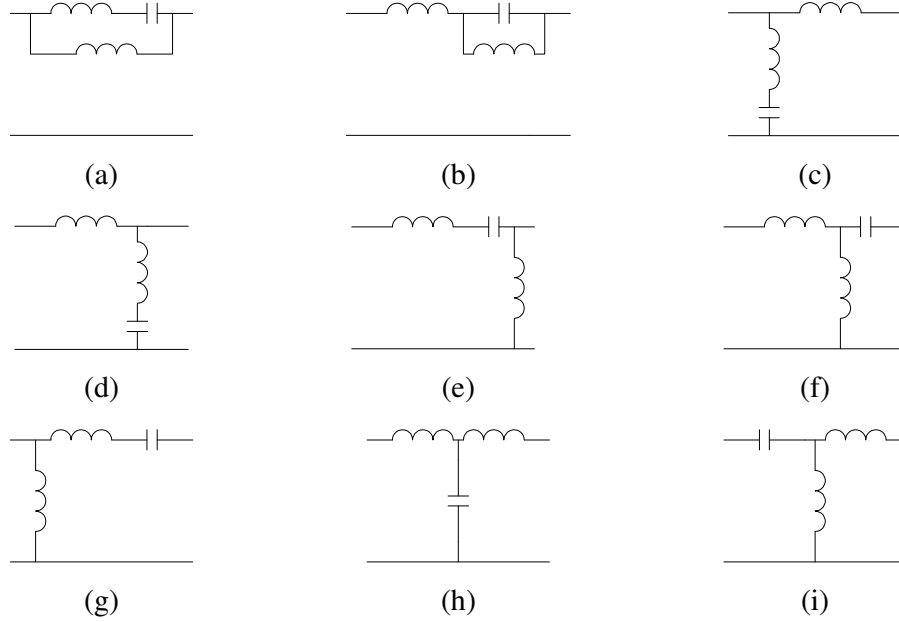


Fig. 1.4: Three-element VNV RNs. Topologies shown in (b), (e), (h) and (i) have been studied in the past.

voltage regulator modules [61]. The high ratio of load current to source current when operated at resonant frequency makes it attractive for induction heating [62] and inductive power transfer [63]. Also, the topology offers load independent output current when operated at resonant frequency which renders it useful as a current source [64], [65] with power factor correction [66]. Addition of clamp diodes adds inherent constant-voltage property to the converter [67], which is useful for capacitor charging applications [68].

The CLL RC of Fig. 1.4(i) is also a modified form of SRC. The topology offers load independent output voltage and no-load regulation making it a potential candidate for voltage regulator type of applications [69], [70]. The topology is also amenable for full integration of magnetic components. The application of topology for single-phase power factor correction has been reported by C. Chakraborty, et. al. [71].

Three-element VNI RNs are shown in Fig. 1.5, out of which three topologies have been analyzed in the past. Topology of Fig. 1.5(b) has been termed as the LLC-type PRC [72], [73]. Since, the leakage and magnetizing inductance as well as the winding capacitance of transformer are absorbed in the RN, it is deemed to be

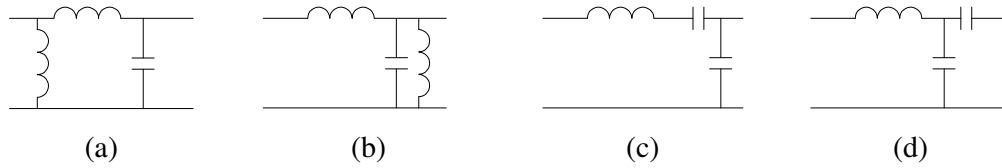


Fig. 1.5: Three-element VNI RNs. (a) PRC with input inductor, (b) LLC-type PRC, (c) LCC or series-parallel RC, and, (d) hybrid RC.

advantageous in high-voltage power supplies.

Series-parallel resonant converter (SPRC) or LCC RC, shown in Fig 1.5(c), has been the topic of extensive investigation [74] – [81]. Although the LCC RC normally a VNI topology, it is also reported with capacitive output filter [82], [83]. It can be viewed as a combination of SRC and PRC, thereby taking their advantages and eliminating most of their drawbacks. It has been advantageously applied also to lighting ballast applications [84]; power factor correction [85]; arc welding [86]; capacitor charging [87]; high frequency ac power distribution [88] etc. SPRC offers load independent output voltage as well as load independent output current [89], rendering it suitable for both types of applications. Three-phase SPRC [90], [91] is attractive for high power applications because of increased output ripple frequency and easier filtering. The clamped-mode [92] and phase controlled SPRC [93] is reported for fixed-frequency operation.

The RN of Fig. 1.5(d) has been termed as the hybrid RC [94] and it combines desirable properties of SRC and PRC. It operates into short-circuit, provides commutating current under all conditions, offers load independent output voltage and current - the latter property has made this topology useful for ballast applications [95] and corona discharge process [96]. Hybrid RC is also reported to be useful in single-phase ac-dc converter with power factor correction [97], [98].

1.2.1.3 Higher-Order RC Topologies

The number of discrete components, size, cost and analytical complexity of an RC increases with increasing order of RN. However, higher-order RC topologies have been explored and studied in the past mainly because of their ability to absorb circuit parasitic components and peculiar characteristics. RNs of these circuits are

summarized in Fig. 1.6. The 4th order LCLC RC of Fig. 1.6(a) can be viewed as a combination of LCL RC and LCC RC. It can also be viewed as a combination of LLC-type PRC and LCC RC. Therefore, it is claimed to have the merits of all these topologies. Leakage and magnetizing inductance of transformer along with its winding capacitance is absorbed in the RN. Therefore, it is deemed suitable for high-voltage application by P. Jain et. al. [99]. Analysis and design methodology of this topology is reported in [100] – [104]. Issues involved in its application as lamp ballast is described by R. Liu, et. al. [105]. It is also found suitable for compensation of leakage and magnetizing inductance of loosely coupled transformer [106].

The topology of Fig. 1.6(b) is a double tuned network with two series LC arms [107]. By properly selecting the resonant frequencies of two series arms, full-range control of output voltage under any loading condition can be achieved with moderate sweep of resonant frequency. The topologies of Fig. 1.6(c) and (d) were developed to compensate a loosely coupled transformer, characterized by large leakage inductance and small magnetizing inductance, in transcutaneous energy transmission system for medical application using a series capacitor [108]. When used in conventional dc-dc converter, all magnetic components can be integrated [109].

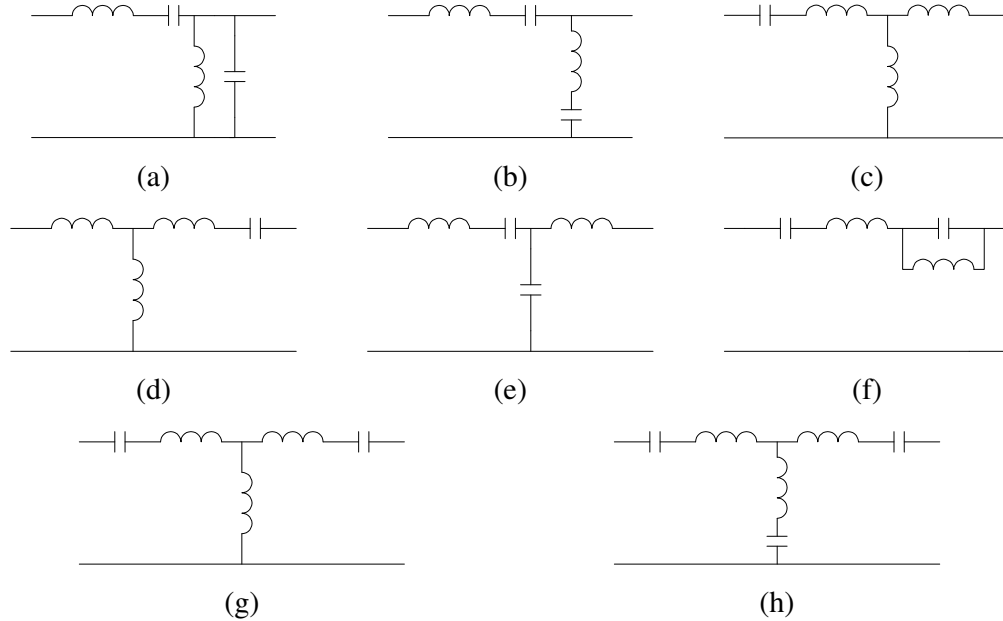


Fig. 1.6: Higher-order RNs reported in the literature.

The RN of Fig. 1.6(e) is LCC RC with transformer leakage inductance [110]. Since transformer leakage inductance can be used as the part of resonant inductor in basic LCC RC by placing the parallel capacitor on the secondary side, this topology does not hold any advantage over LCC RC.

Series-loaded series-parallel 4th order RN of Fig. 1.6(f) is used for high power factor single-phase ac-dc interface with high-frequency isolation [111] since it offers voltage boosting property. Three-phase version of this higher order RN is described by M. A. Choudhary, et. al. [112] for high-power application.

As a modification over the topology of Fig. 1.6(b) and Fig. 1.6(c), the five-element RN of Fig. 1.6(g) was suggested to compensate large-air-gap transformer in transcutaneous energy transmission system for medical application [113] by placing the compensating capacitors in series with both the windings. This topology results in more complete compensation with less reactive power loading on the source, less circulating current and better efficiency.

Six-element T-type RN of Fig. 1.6(h) exhibits an interesting property: the circuit remains in resonance (in-phase input voltage and current) with minimum reactive current loading and ZCS operation over a wide frequency range while the output power can be continuously varied [114]. This property is exploited by H. Pollock, et. al. for developing a power supply for electric arc welding [115].

1.2.2 Modes of Operation

A RC, in general, can be operated in three basic modes of operation. The modes of operation are decided based on the ratio of switching frequency to the resonant frequency, which decides if the input current, i_{in} , of the RN flows continuously or discontinuously. Further, if i_{in} is continuous it needs to be seen whether the current lags or leads the applied voltage, v_{in} [116]-[118]. The modes of operation are described referring to the circuit diagram and waveforms of Fig. 1.7.

1. *Discontinuous conduction mode [Fig. 1.7(b)]*: This mode of operation occurs when switching frequency is less than the half of the resonant frequency. Switches turn off naturally at zero current and zero voltage but turn on with zero current only. Diodes, however, turn on and turn off at zero current. Due to discontinuous operation, the ratio of peak current to rms current is large resulting in higher

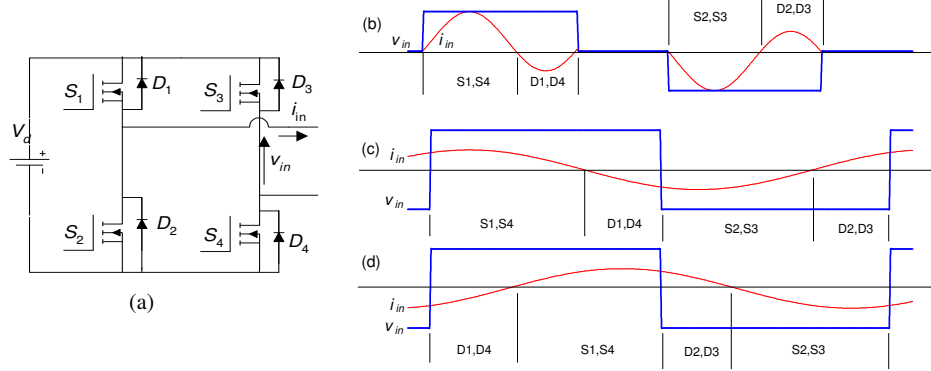


Fig. 1.7: Circuit diagram of full-bridge converter [(a)] and waveforms of v_{in} and i_{in} in the discontinuous conduction mode [(b)], continuous conduction mode with leading power factor [(c)] and continuous conduction mode with lagging power factor [(d)].

conduction loss. Since frequency needs to be decreased to reduce the output voltage, bigger filter is required to meet ripple specification at the low output. Therefore, it is not the preferred mode of operation.

2. *Continuous conduction mode with leading power factor [Fig. 1.7(c)]:* If RN presents capacitive input impedance, input current leads the applied voltage. Switches get turned off at zero current. When a switch is turned on the anti-parallel diode of the other switch in the same leg is conducting. Therefore, fast anti-parallel diodes and lossy (or complicated energy recovery) turn-on snubbers are required. Body-drain diode of metal oxide field effect transistor (MOSFET) cannot be used. Additionally, switches carry diode reverse-recovery current and the discharge current of switch output capacitance at turn-on, causing more losses. Therefore, it is also not the preferred mode of operation.
3. *Continuous conduction mode with lagging power factor [Fig. 1.7(d)]:* If RN presents inductive input impedance, input current lags the applied voltage. Anti-parallel diode of each switch conducts prior to the conduction of the switch resulting in ZVS turn-on. Turn-on snubbers are eliminated. Slower anti-parallel diodes and loss-less capacitor turn-off snubber can be used. Snubber capacitors can be placed directly across the switches to reduce the turn-off dissipation. Body-drain diode and output capacitance of power MOSFET can therefore be used

reducing the component count. Therefore, this is the most preferred mode of operation.

1.2.3 Methods of Control

1.2.3.1 Variable Frequency Control

Since the gain of a RN is a function of excitation frequency, the output voltage of a RC can be controlled by varying the operating frequency. However, it is difficult to optimize the design of magnetic components and filters for variable frequency operation. Operation away from the resonant frequency causes reactive power loading on the inverter switches, thereby reducing the conversion efficiency [119]. It is unsuitable for applications with frequency locking requirements.

1.2.3.2 Phase Control

In this scheme, two RCs are fed by a common dc input voltage and their outputs are vectorially added to produce common ac output. The RCs are operated at constant frequency but their gating signals are phase shifted to control the power transfer. Synthesis of phase controlled RCs is reported by M. Kazimierczuk [120] and detailed analysis of various phase-controlled topologies, namely SRC, PRC, LCC RC, CLL RC, are described in greater details in [93], [121] – [123]. However, for this method two RNs are needed and they are unequally loaded. High circulating current at light load and unbalanced currents in some converters can cause commutation failures.

1.2.3.3 Clamped Mode Control

The clamped mode (CM) operation is possible with full-bridge RC circuit and was developed as the functional equivalent of phase controlled RCs with the advantages of single RN and no current or voltage imbalance. In this method, output voltage is controlled by phase-shift pulse width modulation (PSPWM). Different operating modes are possible with this control depending on the topology, operating duty cycle, and circuit Q . Operating modes can be broadly grouped into natural commutation mode and forced commutation mode. In the latter mode of operation, ZVS of all switches is obtained. Loss of ZVS in the other operating mode is a serious

limitation of this control method. The CM control, complete steady state analysis, investigation of different operating modes and mode boundaries has been extensively reported for SRC [119], [124] – [127]; PRC [128], [129]; LCC RC [131]; LCL-type SRC [53], [54], [56] and for 4th order LCLC RC [99], [102], [104], [132]. The mode boundaries for ZVS and non-ZVS operation in SRC and PRC and their design are discussed by S. Gonzales, et. al. [133]. A comparison between frequency control, CM control and combined variable frequency – CM control is described in [134], [135].

1.2.3.4 Asymmetrical Pulse Width Modulation Control

In this type of control, the gate pulses to the two switches of bridge legs have complementary duty cycles. Therefore, the bridge output voltage has dc component, which needs to be blocked before applying to the RN. In this context, RNs with band-pass characteristics, such as SRC, LCL-type SRC and LCLC RC [136] – [139], are advantageous. While this control method leads to asymmetric operation of the high-side and the low-side switches and leads to unequal voltages across the leg capacitors, it has been popularly applied to power converters (resonant as well as non-resonant) due to simpler implementation and soft-switching over the wide range of operation.

1.2.3.5 Asymmetrical Voltage Cancellation Control

This control method [140], [141] is reported recently as a generalization of conventional CM and asymmetrical pulse width modulation control techniques, which is applicable for full-bridge RCs. Since the bridge output voltage has dc component, RNs with band-pass characteristics are advantageous. The proposed control technique is reported to achieve better efficiency performance while considering ZVS operation, output power and load variations.

1.2.3.6 Integral Cycle Control

To control the output voltage while maintaining near resonance operation, the integral cycle control was proposed [70], [142] – [146]. In this scheme, discrete number of half cycles (pulses) are properly selected repeatedly by feedback algorithm to control the output voltage. The output voltage is controlled by the duty ratio of powering mode and free-resonant mode. RCs using this method are also called the

quantum RCs. However output levels are quantized, increasing the output ripple. With non-periodic integral cycle control, [143], [145], in which the control period is no longer fixed and is allowed to change at any valid control instant, these limitations are minimized. To reduce the quantization effect, modified quantum and phase sequence is proposed [144] with optimum quantum sequence [146]. The quantized control technique, termed as the pulse density modulation [96], [147] has been used for industrial applications such as induction heating, ozone generation and corona discharge.

1.2.3.7 Self-Sustained Oscillating Control

The phase angle between the bridge output voltage and current can be controlled for ZVS operation by generating the bridge output voltage and by sensing the phase of the current. The switching frequency is no longer externally imposed as in the conventional variable frequency control and the converter is said to be operating in so called self-sustained oscillating mode [55], [148], [149]. As a result, the ZVS can be ensured over a wide range of operation. Since the current needs to be sensed, the controller is complex. For parallel operation of RCs, the phase of bridge output voltage must also be controlled. For such applications pulse-phase modulation is proposed recently [150] in which the phase of output voltage is controlled by controlling the phase angle of pulses.

1.2.4 Methods of Analysis

Analysis and design of RCs is more difficult compared to PWM converters due to nonlinear loading, more number of reactive energy storage components and different operating modes. Various techniques have been developed for analysis of steady-state and transient operation.

1.2.4.1 State-space Approach

In the state-space method, first order differential equations are formulated describing various state variables of the converter, which are then analytically or numerically solved to identify circuit modes during a switching cycle along with the boundary conditions associated with the transitions between the modes. Although this

method is very accurate, it is relatively more complex, cumbersome and difficult to apply, especially for higher-order converters. Therefore, it is reported to be applied for mainly second and third order RCs [28], [31] – [36], [129], [137], [72], [76], [82], [94], [151] except for [104], wherein it is applied for fourth order LCLC RC.

1.2.4.2 State-plane Approach

A simplified technique is to use the state-plane diagrams, where state variables are graphed on a two-dimensional plane graph. Once the state-plane diagrams are obtained, geometrical properties of state-trajectory can be used to derive control characteristics and time-domain steady-state solutions. The basic principle behind the state-plane approach is described by R. Oruganti, et. al. [152]. Applicability of this method of analysis is demonstrated for various topologies [49], [73], [126], [128], [153] – [155]. For higher order RCs, suitable transformation is derived in order to decouple the state variables.

1.2.4.3 AC Analysis with Fundamental Frequency Approximation

In this method of analysis, only fundamental component of square-wave excitation is used and all other harmonics are neglected. At the output port of the RN, the rectifier and filter is replaced by an equivalent ac-side resistance [117]. With these approximations, classical ac analysis is applied to determine simple closed-form expressions for converter gain and component stresses. This method is simple, easy to understand, gives fundamental insight into the characteristics and is fairly accurate. Therefore it is popularly applied by the researchers for steady-state analysis and design [52], [61], [64], [65], [67], [68], [71], [75], [77], [85], [88], [93], [95], [107], [109], [117], [156] – [160].

1.2.4.4 Fourier-Series Method or Frequency Domain Approach

This method is the generalization of fundamental frequency approach in which all dominant harmonics of source and load are taken into account and classical ac analysis techniques are used to analyze the converter using superposition principle for the solution of each harmonic. This method therefore gives more accurate results but is more intricate than the fundamental frequency approximation method. Applicability

of this method in analysis and design of RCs is reported in [20], [29], [53], [90], [132], [136], [138], [139], [161] – [163].

1.2.4.5 Discrete Time Domain Modeling

Dynamic response of a converter during the transients is quite significant and must be considered while formulating the converter design procedure. The transient response also determines the choice of appropriate component ratings because it is mostly during the transients that the converter components have to bear maximum stress. Since the exact nature of transient is unpredictable and the dynamic response of the converter is quite complex, exact transient analysis is intricate. Discrete time domain model [17], [51], [54], [78], [164], greatly simplifies this problem by modeling for a major design constraint, such as peak current or voltage stress of the components.

1.2.4.6 Small-signal Analysis

Small-signal analysis is necessary to derive various transfer functions and design of the feedback controller. A small signal model based on the discrete time domain analysis is reported in [165] – [167], in which steady-state operating point is obtained and the model is linearized around it for small-signal variations. Approximate small-signal analysis of RCs under high- Q conditions [168] shows that the dominant behaviour of these transfer functions is determined by the output low-pass filter modified by the internal impedance of the converter. The high-frequency behaviour is given by a second-order response whose cut-off frequency is at the difference between the resonant and switching frequency.

A general analytical approach for equivalent circuit modeling of RCs is reported by A. Witulski, et. al. [169]. The circuit models are shown to completely characterize the terminal behaviour of the converters and give the transfer function of the interest. In small signal analysis based on the state-plane approach [170], the transfer functions are obtained by introducing perturbations on the state variables, switching frequency and input voltage.

A simplified methodology for developing average models of RCs based on ac analysis with fundamental frequency approximation and concept of time dependent

equivalent ac resistance is reported by S. Ben-Yaakov, et. al. [79]. Once obtained, the model can be run on circuit simulators to obtain steady-state, large-signal transient and small-signal behaviour.

1.2.5 Integrated Magnetic and Reactive Components

Reactive elements in the RN act as a constraint over achievable miniaturization with RCs. Therefore, integration of reactive components as well as the transformer has been the subject of research over the last few years. Integrated components save space. Moreover, flux ripple cancellation can be achieved which is beneficial in reducing the core loss. With these benefits, high power density can be achieved. Integration of passive components has evolved with two distinct types of integrated components, namely, wound integrated components and planar integrated components.

In wound integrated components, two copper foils insulated from each other by a thin dielectric layer are wound in air to get integrated series and parallel LC resonating structures [171], or around the ferrite pot-core limb [172] to get a wound resonating structure integrated with transformer, named the L-C-T structure. By adjusting the air-gap in the core pieces of a transformer, the leakage and magnetizing inductance of the transformer can be suitably adjusted to match a particular application [109].

Planar version of integrated generic reactive component suitable for SRC, PRC, LCC RC and LCL RC is reported in [173]-[175]. It uses planar windings separated by ferroelectric ceramic dielectric material. Integrated planar L-C-T module that combines inductors, capacitor, and transformer for LCL RC is reported in [58], [59]. A comprehensive loss model for planar integrated passive module is reported by J. T. Strydom, et. al. [176], which takes account of non-sinusoidal core excitation, skin and proximity effect loss. The material, technological limits, construction constraints and thermal issues in an integrated magnetic/passive module are discussed in [177], [178]. Successful application of integrated resonant module for high-frequency, high-power converter application [179] shows that integrated passive and

magnetic components can successfully replace discrete components and help in achieving higher power density.

1.2.6 Applications

The majority of the efforts towards the analysis, design and optimization of the RCs have been directed towards their application for dc-dc power conversion. However, RCs have also been applied to many other demanding applications utilizing peculiar characteristics exhibited by RCs. Some of these application areas are reviewed in this section.

1.2.6.1 Ballasts for Fluorescent Lamps

Conventional 50 Hz magnetic ballast suffers from lamp flicker, shorter lamp life, audible noise, poor power factor, bigger size and larger weight. Operating the lamp at high frequency eliminates light flicker and audible noise, improves lamp life and efficiency (lumens/watt), retains high power factor and makes the ballast lightweight and compact. Various RCs, since they can inherently perform the ballast's functions, are ideally suited for this application. Suitability of PRC [105], [180], [181]; LCC RC [84], [182]; hybrid RC [95], and CS-PRC [43] for this application has been widely explored. A comparison among various topologies and their characteristics is reported in [183], [184]. Another advantage of resonant electronic ballast is that the output power can be controlled easily to incorporate dimming feature [185] using either variable input voltage or variable switching frequency.

1.2.6.2 Power Factor Correction

Diode rectifiers are used to synthesize dc voltage from ac utility. These rectifiers pollute the utility with harmonic currents, which have undesirable effects on the power system. Several harmonic limit specifications, recommendations, guidelines and standards have been introduced for prevention of harmonic pollution. RCs have been successfully applied for power factor correction since the high power factor inherently results even without the active control of input line current. This is due to the pulsating dc link voltage and the capability of some of the RCs to boost the voltage during valleys of the input ac wave. With active control, near unity power

factor can easily be achieved. Voltage source topologies like PRC [186]; LCC RC [85], [97], CLL RC [71]; LCL-T RC [66]; hybrid RC [97], [98]; SRC [187] are reported suitable for power factor correction applications. Current source RCs are also deemed suitable for this application [46] due to non-pulsating input current.

1.2.6.3 Capacitor Charging

Various industrial applications require pulsed energy transfer. The required energy is provided to the pulsed loads by rapidly discharging a pre-charged capacitor. A special type of power supply required for charging of the capacitor is commonly termed as capacitor charging power supply (CCPS). The charge cycle of a CCPS consists of charge and refresh modes during which CCPS operates in constant-current and constant-voltage modes respectively. SRC has been extensively used for CCPS applications [188]-[191]. However, SRC does not inherently behave as a constant-current source (except for operation in discontinuous mode with switching frequency below half the resonant frequency) and complex control methods such as dead-time control, variable frequency control and constant on-time variable frequency control are required for controlling the charging current. PRC has the advantage of high voltage gain that helps in reducing transformer turns ratio and absorbs transformer parasitic elements [192]. On a similar argument, application of LCC RC for CCPS has been reported in [87]. By virtue of its current source property [68], LCL-T RC is potentially applicable as CCPS [193]. Besides, issues like conversion efficiency, EMI, precision of charged voltage, harmonic pollution in utility ac mains, power density etc. are also important for this demanding applications.

1.2.6.4 Induction Heating

With the exception of low power applications wherein single-switch quasi-resonant converters are used, full-bridge or half-bridge resonant inverters are most commonly used as the power supplies for induction heating. Two most commonly used resonant inverter topologies are: voltage-source series resonant inverter (SRI) [127], [134], [194] – [197], in which the compensating capacitor is placed in series with the coil, and, current-source parallel resonant inverter (PRI) [44], [198], [199], in which the compensating capacitor is placed in parallel with the coil. A detailed

comparison of merits and limitations of SRI and PRI is reported by F. Dawson, et. al. [200]. The LCL-T RC [62] has emerged as a promising topology for induction heating, due to the fact that source current is Q times smaller than the coil current. Therefore, secondary winding of matching transformer is not required to carry full coil current, simplifying its design. Resonating capacitor can be placed near to the work coil thereby minimizing the loop of high-frequency high-current feeders.

1.2.6.5 Welding

Modern electronic welders are required to feature portability, robustness, safety, reliability, flexibility of operation, good power factor, fast response, wide current setting and fault tolerance. Application of RCs has also been reported for this application. Various aspects of LCC RC such as design and control for desired current variation, over-voltage limitation, avoiding leading power factor mode, etc., are discussed by H. Pollock [86]. Characteristics of a sixth order RC for welding application are studied in [115] with a control method for power factor correction and output power control. A high-voltage low-current supply is required in some applications for arc-striking, where SRC can be advantageously applied [201], [202].

1.2.6.6 Inductive Power Transfer

Inductive power transfer systems, in general, are designed to transmit power efficiently from stationary source to moving load used in contact-less power transmission for professional tools, contact-less battery charging over large gap for electric vehicles, compact electronic equipments, mobile phones and to transmit electrical energy to circulatory assist devices for cardiac patients transcutaneously, i.e. through the intact skin. Loosely coupled transformer used for power transfer is characterized by large leakage and small magnetizing inductance. These reactive components can be used as a part of RN, by using compensating capacitors [108]. Various compensation schemes are compared and it is concluded that both the primary and secondary side leakage inductance need to be compensated for better performance [204], [205]. Resulting five-element LC-LC-L T-type RN is studied in further details by J. Joung, et. al. [113]. Suitability of LCL-T RC for such application is investigated in [63], [203] and its power transfer capability is examined in [130].

1.2.6.7 High Voltage Power Supply

Large step-up ratio and inter-winding insulation in the transformer of high-voltage power supplies exacerbates the leakage inductance and winding capacitance. Since these parasitic components can easily be accommodated in a RN, RCs are popularly applied for these applications. The performance comparison of SRC, PRC and LCC RC including the effect of these parasitic components is elaborated by S. D. Johnson, et. al. [206] and it is concluded that PRC is the most suitable candidate. The application of fourth order LCLC RC [99] also includes the magnetizing inductance of the transformer in the RN. High voltage power supply for medical applications like x-ray generator is popularly developed using PRC [207] and also using SRC with voltage multiplier [208]. High voltage ac power supply for corona discharge process required for rendering affinity of polyethylene film to ink or glue using transformer leakage inductance and electrode capacitors results in SRC [96]. Electrical discharge machining (EDM) is an electro-thermal process that needs pulsating high voltage dc power supply. Such a power supply using LCC RC has been reported in [89]. Suitability of current-fed PRC has been demonstrated in [45]. High power electrostatic precipitators are widely used for industrial emission control requiring 20-50 kV output voltage. Phase controlled LCC RC for this application has been reported in [209]. High voltage power supply for corona surface treatment using LCC RC is described in [147]. Use of third order RN for mega-hertz range high-voltage ac power supply for low temperature plasma generation is reported in [210].

1.3 Constant-Current Power Supplies

A regulated power supply provides electrical energy which is precisely controlled. Power supplies can be of constant-voltage (CV), constant-current (CC), and constant-voltage, constant-current (CVCC) type. A CV supply provides a constant output voltage independent of output current and therefore has zero output impedance. A CC supply gives a constant output current independent of the output voltage, and therefore has infinite output impedance. Additionally, output voltage (current) of a CV (CC) power supply can be set to any desired value over a specified range. A CVCC supply is more versatile as it can be used to operate either as a CV or

Table 1.2: Summary of characteristics parameters of a CV and CC power supply.

Parameter	CV Power Supply	CC Power Supply
Output	Constant voltage (adjustable)	Constant current (adjustable)
Compliance parameter	Output current	Output voltage
Output Impedance	Low (ideally zero)	High (Ideally infinite)
Stability	Subject to capacitive load	Subject to inductive load
Ripple, stability, transient response	Measured with respect to steady state output voltage	Measured with respect to steady state output current

a CC supply. Properties of a CV and CC power supply are complementary to each other and those of a CVCC power supply are combination of both. Table 1.2 summarizes key performance parameters of CV and CC power supplies.

1.3.1 Applications

With the recent developments in the field of power electronics, devices, circuits and techniques, it is now possible to develop variety of power supplies which can satisfy the demands of different applications. CC sources are either inherently required or can be advantageously applied in domestic, industrial, laboratory and scientific utilities. Some of these application areas of a CC power supply are briefly reviewed in following sub sections.

1.3.1.1 Electric Arc Welding

Many types of power sources are required to meet unique electrical requirements of various arc welding processes. The power source is required to provide high welding current, typically 30 to 1500 A. The output of power source can be ac, dc or both. It may be CV, CC or CVCC. Additionally, it may also provide a pulsing output.

A CC power supply is preferred for gas tungsten arc welding (GTAW), shielded metal arc welding (SMAW), plasma arc cutting (PAC), plasma arc welding (PAW), stud welding and submerged arc welding (SAW). In SMAW, a small change in arc length can cause a large change in arc current; therefore CC power supplies are preferred for uniform metal transfer and reduction of metal spatter [211]. CC type

power supplies are used for GTAW as the arc current controls the weld penetration [212]-[213]. GTAW power sources typically have drooping or nearly true CC static output characteristics. While former characteristic is suitable for manual welding, the latter is desired for machine and automatic welding to provide accuracy and repeatability [213].

1.3.1.2 Laser Diode Drivers

Electrically, a semiconductor laser diode behaves as an ordinary diode but with a turn-on knee voltage greater than 1 V and with much smaller series resistance. When the laser diode is biased with a sufficient current, lasing occurs and its optical output increases in proportion to the biasing current [214]. These devices are coupled together to form stacks and arrays with high power and brightness, which are then used to pump a solid state media that makes a diode-pumped solid state laser. Laser diodes tolerate a very little current over-stress. It is, therefore, preferred that the power supply itself behaves as a CC source.

Conventionally, laser diode drivers are developed using a MOSFET operating in linear region [215]. To provide pulsating output current, required energy is stored in additional energy storage capacitors. In the event of catastrophic failure of controlling MOSFET, a crow-bar circuit is activated to prevent the stored energy of capacitors from flowing to the laser diodes. Linear power supplies have typical conversion efficiency of 50% and are bulky. The problems are magnified at high current levels. Instead, a laser diode driver using buck converter with hysteretic current mode control is proposed [216]. However, due to finite bandwidth of control loop, the converter ceases to perform as a current source in transient conditions and additional inductor is required at the output. Although the approach is more efficient, the energy storage requirement is shifted from output capacitor to output inductor.

1.3.1.3 Magnet Power Supplies

Electromagnets are required in many industrial and scientific installations. One of the largest installations of electromagnets is particle accelerators. In a particle accelerator, a large number of electromagnets are used to guide, bend, focus and steer the beam of charged particles. The power supplies are output current controlled,

magnetic field being directly proportional to the current. Various types of CC magnet power supplies are required, such as dc or slow varying, ramping and bipolar power supplies. The requirements of a magnet power supply are quite different from conventional dc power supplies [217], [218]. These power supplies feed a highly inductive load. The variation in the load resistance are due to tolerances in magnet resistance, cable drops and change in operating temperature. Also the converter should have wide conversion range for wide variation in output current. The output current stability specification is very stringent and is typically in the range of 0.001 to 0.05 per cent.

1.3.1.4 Illumination Systems

Application of a CC instead of a CV power supply for illumination and lighting of large installations is preferred mainly for better efficiency, uniform illumination and to avoid surge current at turn-on. The lights of runways and airfield of domestic as well military airports are supplied from series circuits served by CC regulators. Commercially available CC regulators are based on the thyristorized ac voltage controllers [219], [220]. Light emitting diodes (LED) have been increasingly applied to various illumination requirements. LEDs are basically current driven devices. The conventional method of using a voltage source and a series ballast resistor has several drawbacks. A preferred method of regulating LED current is to drive them with a CC power supply which eliminates the forward current mismatch and translates into uniform brightness. Integrated circuits are available for low-power LED CC drivers [221].

1.3.1.5 Battery Charging

Several methods are practiced for charging of rechargeable batteries [222] – [224]. They are: CV charging, CC charging, taper current charging, trickle current charging, automatic charging, high-rate or boost charging and diagnostic charging. In CC charging, battery is charged at a preset rate of constant current. In taper current charging method as the voltage increases, the current decreases or tapers off to a minimum. Boost chargers provide high charging current (40 to 250 A) for quick recharging or boosting a battery or assist in starting a vehicle. Trickle chargers are

basically manual small current chargers used to maintain a battery at its full state of charge over a long period of time. Diagnostic chargers additionally include circuitry to detect a good or a bad battery. Essentially, all charging methods need a CC power supply to pump required current into a discharged battery.

1.3.1.6 Capacitor Charging

Peculiarities and demanding features of this application are briefed in section 1.2.6.3. To limit initial charging current, when the load capacitor is uncharged, as well as to control the charging interval a CC power supply is preferred.

1.3.1.7 Electrochemical Processes

Several electro-chemical processes, such as electrolysis, electrophoresis, electroplating, electro-deposition, anodizing and printed circuit board (PCB) fabrication need to use CC power supplies [225]. They are of both types: continuous or pulsed. While the former is the most common and used in variety of electro-chemical processes the latter is particularly used in pulse-electroplating. Pulse plating improves the deposit properties (porosity, ductility, hardness, electrical conductivity, roughness, etc.). It is used for deposition of alloys, the composites and structures of which are not obtainable with dc plating. By periodic inversion of polarity of current pulse, plating thickness distribution can be improved. CC power supplies for chemical processes are conventionally made using line frequency transformer and controlled SCR rectifier mainly due to simplicity. Transistor series-pass stage is used to make the CC source. High frequency switching power converters are also applied now-a-days. A detailed comparison of different techniques is given in [226].

1.3.2 Conventional Techniques

Aforementioned review of some of the applications of CC power supplies reveals a few techniques conventionally followed to realize a CC source.

A passive way to keep the load current nearly constant for a short period of time is to place a large inductance in series with the load (e.g welding power sources and laser diode drivers). An obvious drawback of this method is large size, weight and cost of the series inductor.

Any power converter can be forced to behave as a CC power supply by incorporating an additional feedback loop to control and limit the load current (e.g. the power supplies used for electromagnets, illumination etc.). The steady state and transient characteristics of such forced current source depend on the performance of feedback control loop. The practical control loop bandwidths are finite and supply loses current source property under transient conditions.

A bipolar junction transistor (BJT) operating in active region or a MOSFET operating in saturation region behaves as a CC source (e.g. magnet power supplies, laser diode drivers etc.). In this operating region, collector current of BJT is proportional to its base current and the drain current of a MOSFET is proportional to the gate-to-source voltage. The output characteristics of BJT are steeper than that of MOSFET in the respective operating modes. Control of drain current of a MOSFET is simpler than the control of the collector current of a BJT, the former being a voltage controlled device and latter needs another current source for base biasing. Unlike BJT, MOSFET is not susceptible to failure due to secondary breakdown. Therefore MOSFET can make a better CC source. However, for high output current when the individual devices need to be paralleled, MOSFET needs a larger series equalizing resistor than BJT for stable operation. Nevertheless, large power dissipation across the regulating transistor is a serious limitation of this technique using both the devices, which worsens the conversion efficiency particularly under part-load conditions or for low voltage – high current applications.

1.4 Application of RCs to CC Power Supplies

Suitability of RCs for application as a CC power supply has been explored in the past. It is well known that SRC operating in discontinuous conduction mode with switching frequency less than one half of the resonant frequency behaves as a CC source. High ratio of peak current to rms current, which is the characteristic of discontinuous operation, and associated increase in the conduction loss has been major limitation of this technique. Further, a large output filter capacitor is required due to lower switching frequency of operation. Nevertheless, SRC behaving as a CC

source was popularly used for capacitor charging applications as mentioned earlier in the section 1.2.6.3.

Operation of PRC as CC power supply is reported in [37]. It is shown that the PRC operating at the resonant frequency exhibits load independent output current rendering it suitable for a CC power supply. Similarly LCC RC and hybrid RC also give constant output current at the resonant frequency. The current-source property of LCC RC has been explored in the past for EDM [89]. The hybrid RC has been applied lamp ballast [95] application. However, the inverter output current in these topologies tend to be highly reactive under output short-circuit condition, thereby reducing the conversion efficiency under part-load conditions.

When operated at the resonant frequency, the LCL-T RC behaves like a current source [64]. That is, under these conditions the output current is constant irrespective of load variations. If two inductors of the RN are equal, inverter output voltage and current are always in phase. Further, inverter output current reduces proportionally under part-load condition. This maximizes full-load and part-load converter efficiency due to lower conduction losses. A detailed analysis and design of LCL-T RC as a CC power supply has been reported recently in [65].

LCL-T RC, in fact, is one of the, so called, immittance converter (IC) circuits. An IC, a term derived from the combination of impedance and admittance, is a two-port network, in which input impedance is proportional to the load admittance connected across the output terminals. This property is very useful in transforming a voltage source into a current source and vice versa [227]. It is well known that a quarter-wave distributed constant line exhibits immittance conversion characteristics. This property has been explored in the past for lamp ballast [228], induction heating [229], corona and plasma discharge application [230]-[232] operating in megahertz-range.

While the length of distributed constant line is manageable for operation in megahertz-range, it becomes prohibitively long for power converters operating in kilohertz-range. Therefore, some lumped-element IC topologies, based on transmission line approximation emulated using discrete inductors and capacitor, have been studied and reported [227]. Immittance conversion characteristics of LCL-T RC topology is also found useful in various applications such as radio frequency inductive

discharges [233], inverter for photovoltaic systems [234] and non-contact energy transmission system [235]. Another IC topology, a CLC- π network, is found suitable in high-voltage dc transmission link [236]. Characteristics of a five-element IC topology, that uses the fundamental and third harmonic of the source excitation for power transfer, are studied in [237].

1.5 Conclusion and Motivation

RCs have been a potential candidate in many power electronics applications due to soft switching, high frequency operation, high efficiency and small size. It has been an active area of research in power electronics field due to variety of topologies, diverse, peculiar and useful characteristics and wide applicability. A large number of RC topologies have been explored and studied mainly due to the following reasons:

1. Second-order RCs have inherent limitation.
2. Higher-order RCs offer steeper fall of the gain with frequency, thereby exhibiting better controllability against wide line and load variation with smaller frequency variation.
3. A properly designed higher-order RC can have overall smaller rating of RN and achieve better efficiency.
4. Parasitic components of practical circuit elements force a second-order topology to behave as a higher-order RC. Depending on the topology, these parasitic components can be gainfully utilized as a part of the RN.
5. Diversity in the available topologies gives a designer a freedom to choose the most suitable topology for a given application.
6. A more insight is gained by studying the characteristics of new family of RCs.

Researchers' interest in RC topologies is also due some peculiar characteristics that may not exhibited by the other class of power converters:

1. Some RCs exhibit load independent output voltage (e.g. LCL RC). This is a useful characteristic for regulation where load is expected to vary over a wide range.
2. High voltage gain of some RCs (e.g. PRC) is advantageous in the design of high voltage power supplies. This voltage boosting property is also useful in the application of RCs for power factor correction and electronic lamp ballasts.

3. High current gain or current amplification of resonant transformation circuits (e.g. LCL-T RC) simplifies the design of an induction heating inverter.
4. Some RCs are shown to behave as immittance converters that are useful in transforming a voltage source into a current source and vice versa.

A variety of techniques have been developed for analysis and design of RCs. State-space analysis gives accurate results but is complex. State-plane analysis, suitable mainly for second-order RCs and third-order RCs with suitable transformation, is a graphical analysis method. AC analysis with fundamental frequency approximation and the Fourier series analysis methods are simpler tools that give fairly accurate results. These methods, particularly the former, have therefore gained popularity among the researchers.

RCs are fundamentally controlled by varying the switching frequency. To alleviate the drawbacks associated with variable frequency operations, various fixed frequency PWM control methods, such as CM control, asymmetrical pulse width modulation control and asymmetrical voltage cancellation control, have been proposed. The merits of fixed frequency operation, however, are gained at the cost of possibility of hard-switching operation of the converter switches under certain operating condition. The range of soft-switching operation under different PWM control methods depend varies from topology to topology and therefore it is difficult to compare these topologies, in general. Quantized control methods suffer from discrete output levels and high output ripple.

Integration of reactive and magnetic component has also been an area of active research for RCs, mainly to reduce the number of discrete components and to achieve high power density. Extensive work toward the conception, analysis, design and feasibility of integrated components in high-power applications has been reported.

A CC power supply is either inherently required or can be advantageously applied in a variety of application areas. Conventional techniques for realizing a CC power supply are limited and have certain demerits. Suitability of RCs for application as a CC power supply has been explored in the past. Discontinuous-mode SRC is unattractive for higher conduction loss and bigger output filter. Poor part-load efficiency of PRC, LCC and hybrid RC due to high circulating current has been a serious limitation.

ICs, due to immittance conversion characteristics, are suitable for transforming a CV source to CC source and is deemed to be a promising alternative for developing topologies suitable for CC power supplies. The distributed constant line type ICs are not suitable for power electronics applications because the length of distributed constant line becomes prohibitively long for power converters operating in kilohertz-range. Therefore a few lumped-element IC topologies, based on transmission line approximation emulated using discrete inductors and capacitor, have been studied and reported. However, all of the published lumped-element IC topologies are not suitable for power electronics applications, wherein the exciting voltage is commonly square-wave which is conveniently obtained by operating power semiconductor switches at high frequency. The efforts to identify, study, characterize and apply the lumped-element IC topologies have been largely intuitive in nature and systematic investigation to identify and explore a family of IC topologies has not been carried out so far. Moreover, published work mainly emphasizes on the peculiarities in the applications of a couple of IC topologies. The published IC topologies also have certain limitations such as lack of inherent dc blocking for isolation transformer and inability to absorb circuit parasitic element. For instance, LCL-T does not provide inherent dc blocking and transformer winding capacitance is not absorbed in the RN.

Therefore, the motivating objective of this thesis is to present an orderly search procedure for identification of a family of lumped-element IC topologies suitable for power converter circuits, termed here as the Resonant Immittance Converter (RIC) topologies, perform detailed analysis, design optimization, investigate control issues and experimentally demonstrate the suitability of a new family of RIC topologies for application as a CC power supply.

1.6 Organization of the Thesis

This thesis presents an effort towards investigating RIC topologies, their analysis, characteristics and control issues, rendering them suitable for CC power supplies. The work presented in this thesis is organized as follows:

Chapter 2 introduces to IC topology and its two types, namely, distributed constant line type and lumped element type ICs. Not all IC topologies are useful for

power conversion applications. Therefore, the concept of RIC topologies is introduced and defined. A family of RIC topologies is identified by investigating transmission parameters of various topological structures of electrical networks. Design conditions in terms of the relationship among the values of various reactive elements and operating point is derived for each of the RIC topologies. A few general observations are made with respect to practical aspects in their application. RICs are classified as Type-I (suitable for CC to CV conversion) and Type-II (suitable for CV to CC conversion).

While it is difficult to address the detailed analysis and design all RIC topologies in this thesis, analysis of a few Type-II RIC topologies is performed in Chapter 3 using ac analysis with fundamental frequency approximation. Closed form expressions for converter gain, component stresses and the condition for converter design optimized for minimum size of RN are reported. Experimental results on laboratory prototype converters are presented to confirm the analytical findings and demonstrate the performance and current-source property of Type-II RIC topologies. Chapter 3 also describes two topological extensions that are useful in practical applications. In the first extension, an addition of clamp diodes in Type-II RIC circuits attributes inherent CV characteristics to the converter in addition to the CC behaviour. Since Type-II RIC is an inherent current source, multiple modules can directly be connected in parallel. The second topological extension, namely, multiphase RICs, describes the phase-staggered operation of paralleled modules resulting in reduced filter size and improved open-loop dynamic response.

For practical application as a CC power supply, it should be possible to regulate the output current against input voltage variations. Since Type-II RICs behave as a current-source only when it is operated at a certain frequency, the method using variation of switching frequency can not be applied to control the output. Therefore, fixed-frequency control methods need to be used. Application of asymmetrical pulse width modulation control for Type-II RIC topologies is examined in Chapter 4 and is exemplified using LCL-T RC. Four operating modes are identified having different circuit waveforms representing different device conduction sequence, thereby creating different conditions during the device switching. The mode boundaries for all the four modes of operation are derived and plotted on, what is

termed, the D - Q plane. A prototype 500 W, 100 kHz converter is designed and built to experimentally confirm the operating modes, control characteristics and the converter performance.

Use of equivalent circuits is a physical and intuitive approach which allows the well-known techniques of circuit analysis to be employed. Averaging has been one of the most important tools for power converter design and analysis since it adequately describes the functional relationships between sources, outputs and control parameters. Average model is useful in determining both static regulation and transient response and can predict large-scale changes in voltages and currents as the source, load or control input undergoes a change. An equivalent circuit model of Type-II RICs is derived in Chapter 5 that predicts the averaged response of the terminal voltages and currents under the large-signal variation in the operating conditions. A small-signal model is subsequently derived by applying perturbation and linearization to the average model. These models are validated by comparing obtained transient and small-signal results with cycle-by-cycle simulation and experimental results.

The property of Type-II RICs that it converts a voltage source into a current source is very useful in variety of applications wherein a CC source is either inherently required or can be advantageously applied. Applicability of Type-II RIC topologies in some of these application areas such as high-voltage dc power supply, CCPS and a CC charger for ultracapacitor is demonstrated with application-specific design issues and prototype implementation in Chapter 6. Application areas of multiphase RICs with source-switch configurations as pulsed current sources for laser diode drivers, welding, battery charging and electrochemical processes are also suggested and discussed.

Chapter 7 provides the conclusions of this dissertation and suggests directions for future research.

Chapter 2

Resonant Immittance Converter Topologies

The review presented in Chapter 1 suggests that immittance conversion characteristic is suitable for transforming a CV source to CC source and is deemed to be a promising alternative for developing topologies suitable for CC power supplies. Few lumped-element immittance converter topologies, based on transmission line approximation emulated using discrete inductors and capacitor, have been studied and reported in the past. Not all immittance converter topologies are useful for power conversion applications. Therefore, the concept of resonant immittance converter is introduced in this chapter. A family of resonant immittance converter topologies is identified by investigating transmission parameters of various topological structures of electrical networks. Design conditions in terms of the relationship among the values of various reactive elements and operating point is derived. Few general observations are made with respect to practical aspects in their application.

2.1 Immittance Converter

An immittance converter (IC) is a term derived from the combination of impedance and admittance. It is a two-port network, as shown in Fig. 2.1, in which input impedance is proportional to the load admittance connected across the output terminals.

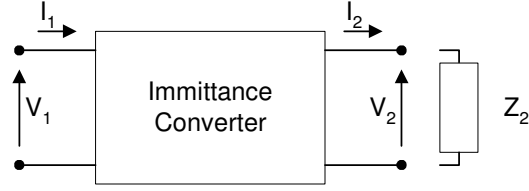


Fig. 2.1: Block diagram of an IC.

Voltages and currents at the input and output ports of an IC (represented by V_1 , I_1 , V_2 and I_2 , respectively) are related as given by the following expression [227]:

$$\begin{bmatrix} V_1 \\ I_1 \end{bmatrix} = \begin{bmatrix} 0 & \mp jZ_n \\ \pm j\frac{1}{Z_n} & 0 \end{bmatrix} \cdot \begin{bmatrix} V_2 \\ -I_2 \end{bmatrix} \quad (2.1)$$

where, Z_n is the characteristic impedance of the circuit. Input impedance, Z_1 , can then be derived as,

$$Z_1 \equiv \frac{V_1}{I_1} = Z_n^2 \frac{I_2}{V_2} = \frac{Z_n^2}{Z_2} \quad (2.2)$$

where $Z_2 \equiv (V_2/I_2)$ is a load impedance connected at the output port of the network. Equation (2.2) shows that the input impedance is proportional to the load admittance connected across the output terminals. In other words, admittance at the output port is converted to the impedance at the input port. This conversion characteristic is called as immittance conversion characteristic.

From (2.1), we also get the following relationship between the input-output voltages and currents:

$$I_2 = \frac{V_1}{\pm jZ_n} \quad (2.3)$$

$$V_2 = \mp jZ_n I_1 \quad (2.4)$$

Thus, output current of an IC is proportional to input voltage and output voltage is proportional to input current. This characteristic feature of an IC enables the conversion of a CV source to CC source and vice versa.

For a loss-free distributed constant line of length x shown in Fig. 2.2, voltages and currents at the sending and receiving ends (V_1 , I_1 , V_2 and I_2 , respectively) are expressed by the following relationship:

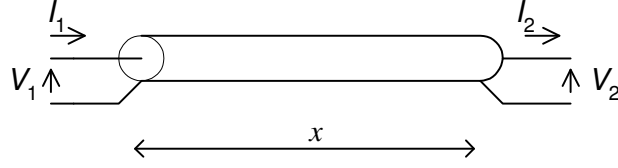


Fig. 2.2: Loss free distributed constant line.

$$\begin{bmatrix} V_1 \\ I_1 \end{bmatrix} = \begin{bmatrix} \cos\left(\frac{2\pi x}{\lambda}\right) & -jZ_n \sin\left(\frac{2\pi x}{\lambda}\right) \\ j\frac{1}{Z_n} \sin\left(\frac{2\pi x}{\lambda}\right) & -\cos\left(\frac{2\pi x}{\lambda}\right) \end{bmatrix} \cdot \begin{bmatrix} V_2 \\ -I_2 \end{bmatrix} \quad (2.5)$$

where Z_n is the characteristic impedance of distributed constant line and λ is the propagation wavelength. When $x = \lambda/4, 3\lambda/4, 5\lambda/4, \dots$, then,

$$\left. \frac{2\pi x}{\lambda} \right|_{x=\lambda/4, 3\lambda/4, 5\lambda/4, \dots} = \frac{\pi}{2}, \frac{3\pi}{2}, \frac{5\pi}{2}, \dots \quad (2.6)$$

Substituting (2.6) into (2.5), the following relationship is obtained:

$$\begin{bmatrix} V_1 \\ I_1 \end{bmatrix} = \begin{bmatrix} 0 & -jZ_n \\ j\frac{1}{Z_n} & 0 \end{bmatrix} \cdot \begin{bmatrix} V_2 \\ -I_2 \end{bmatrix} \quad (2.7)$$

Equation (2.7) is the characteristic equation of an IC. Thus, on a distributed constant line of length $x = \lambda/4, 3\lambda/4, 5\lambda/4, \dots$ the admittance at the receiving end is converted into impedance at the sending end.

The immittance conversion characteristic of a quarter-wave distributed constant line has been used for various applications. The sending end is excited with square-wave ac voltage using MOSFET bridge, as illustrated in Fig. 2.3(a). The circuit configuration at the receiving end is different for different applications such as high intensity discharge (HID) lamp ballast [228] [Fig. 2.3(b)], induction heating [229] [Fig. 2.3(c)], corona and plasma discharge application [230]-[232] [Fig. 2.3(d)] etc. operating in megahertz-range.

Propagation wavelength can be expressed in terms of operating frequency f_s , capacitance of transmission line per unit length, C_x , and Z_n as,

$$\lambda = \frac{1}{f_s Z_n C_x} \quad (2.8)$$

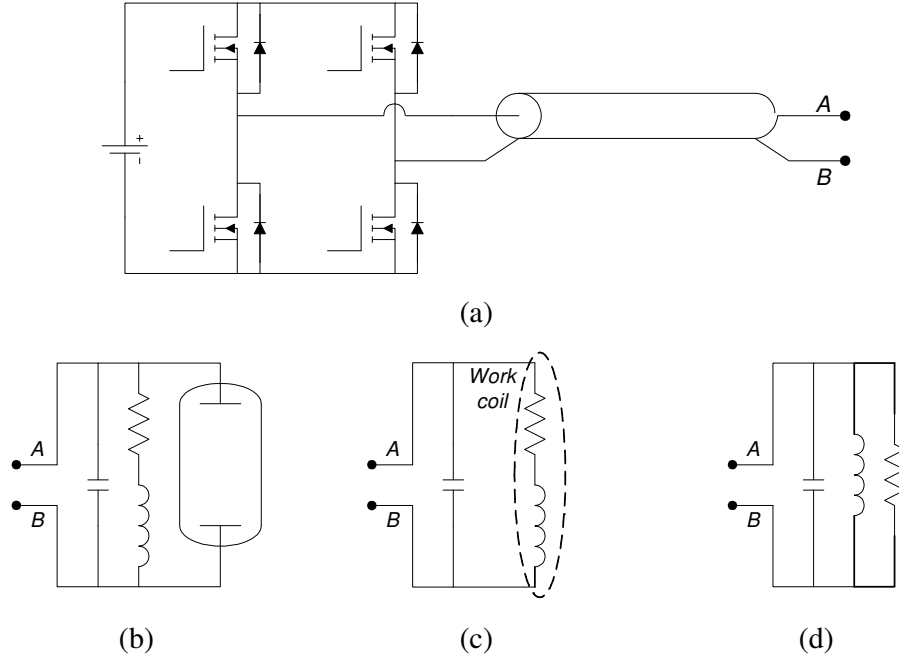


Fig. 2.3: Some application examples of distributed constant line type IC converters. (a) A MOSFET bridge exciting the sending end. The circuit configuration at the receiving end for (b) HID lamp ballast, (c) induction heating, and, (d) corona and plasma discharge application.

If $Z_n = 50 \, \Omega$ and $C_x = 100 \, \text{pF/m}$, then $\lambda = 20 \, \text{m}$ for $f_s = 10 \, \text{MHz}$ and $\lambda = 2000 \, \text{m}$ for $f_s = 100 \, \text{kHz}$. Therefore, while the length of distributed constant line is manageable for operation in megahertz-range, it becomes prohibitively long for power converters operating in kilohertz-range. Therefore lumped-element IC topologies based on the transmission line approximation emulated using discrete inductors and capacitors have been proposed. Lumped-element type ICs are more compact. These IC networks are shown in Fig. 2.4. The IC networks shown in Fig. 2.4 (a) – (e) were proposed in [227]. However, only two of them, those shown in Fig. 2.4(a) and (b), have low pass characteristics and therefore are suitable for power electronics circuits. In lumped-element type ICs, only the fundamental frequency component of input excitation can be converted according to immittance conversion characteristics. Therefore a higher order lumped-element network, shown in Fig. 2.4(f) was proposed [237] to convert the fundamental and the third harmonic of input excitation according to immittance

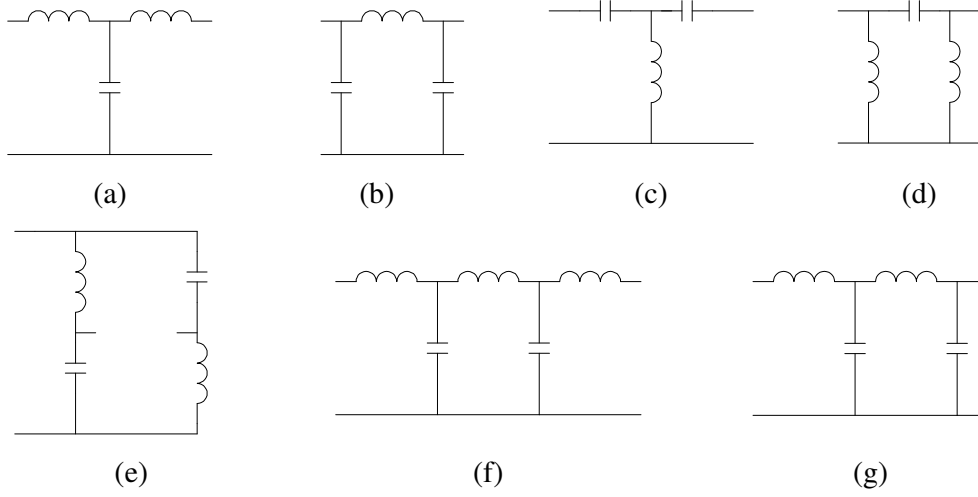


Fig. 2.4: Some lumped-element IC networks.

conversion characteristics. A fourth order IC network, shown in Fig. 2.4(g) was proposed [238] as a combination of topologies shown in Fig. 2.4(a) and (b).

2.2 Resonant Immittance Converter

ICs are deemed to be a promising alternative for developing topologies suitable for CC power supplies, mainly for the following reasons:

1. An IC is a natural current source. Output current is proportional to the input voltage and independent of load variation when operated at a particular frequency. Therefore, output current regulation will be small against wide load variation for constant input voltage, even without the feedback control of the output current. Coarsely regulated output current is sufficient for many industrial applications and elimination of feedback control circuit serves to enhance ruggedness of the power converter.
2. Input impedance of an IC is proportional to the output admittance. With resistive load at the output port, input impedance of an IC is also resistive. This means, input current of an IC is always in phase with input voltage and reduces proportionally with load. Thus, an IC does not draw reactive power from the source, which is typically a bridge of semiconductor switches, minimizing conduction loss and maximizing the efficiency of the source itself. In-phase

source voltage and current also results in zero-current-switching, reducing the switching loss.

As discussed in the previous section, the distributed constant line type ICs are not suitable for power electronics applications because the length of distributed constant line becomes prohibitively long for power converters operating in kilohertz-range. Only a few IC topologies proposed in the past, intuitively as the lumped-element approximation of distributed constant line, are found suitable. The published work mainly emphasizes on the peculiarities in the applications of a couple of IC topologies. These IC topologies have certain limitations such as lack of inherent dc blocking for transformer (used for matching the load parameters with available source, isolation and converter optimization) and inability to absorb circuit parasitic element. The efforts to identify, study, characterize and apply the lumped-element IC topologies have been largely discrete in nature and systematic investigation to identify and explore a family of IC topologies has not been carried out so far.

It is, therefore, important to identify and explore a family of electrical networks composed of lumped reactive elements (inductors and capacitors) with following characteristic features:

1. It should exhibit immittance conversion characteristics,
2. It should have either low-pass or band-pass frequency response, and,
3. It need not necessarily be the lumped-element approximation of a distributed constant line.

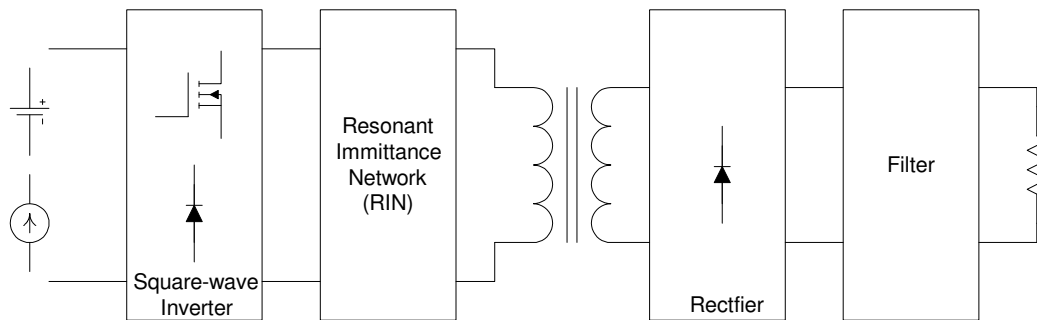


Fig. 2.5: Block diagram of a dc-dc RIC.

An electrical network that satisfies these characteristic requirements is termed as resonant immittance network (RIN). When a RIN is used in place of ordinary RN in a RC, the resulting power converter topology is termed as the resonant immittance converter (RIC). A dc-dc RIC can thus be represented with block diagram of Fig. 2.5. If rectifier and filter blocks of Fig. 2.5 are removed, a dc-ac RIC is formed.

By specifically defining a class of circuits as RIC topologies it is not implied that the other electrical networks that are non-resonant, resonant and non-resonant-immittance converters, are not usable. They are only not classified as RIC.

2.3 Identification of RINs

The voltage and current at the input port of a two-port network is related to the voltage and current at the output port using transmission, or, $ABCD$ parameters as,

$$\begin{bmatrix} V_1 \\ I_1 \end{bmatrix} = \begin{bmatrix} A & B \\ C & D \end{bmatrix} \cdot \begin{bmatrix} V_2 \\ -I_2 \end{bmatrix} \quad (2.9)$$

wherein,

$$A = \left. \frac{V_1}{V_2} \right|_{I_2=0}, \quad B = \left. \frac{V_1}{-I_2} \right|_{V_2=0}, \quad C = \left. \frac{I_1}{V_2} \right|_{I_2=0} \quad \text{and} \quad D = \left. \frac{I_1}{-I_2} \right|_{V_2=0} \quad (2.10)$$

Comparing (2.9) with (2.1), for a two-port network to be an IC, its reverse voltage gain (A) and the reverse current gain (D) must be zero. Also, its transfer admittance (C) and transfer impedance (B) must be reciprocal of each other. That is, the conditions for a network to be an IC can be written as:

$$A = D = 0 \quad \text{and} \quad BC = 1 \quad (2.11)$$

Therefore, transmission parameters of various topological structures of electrical networks can be examined to identify those which can exhibit the immittance conversion characteristics. Subsequently, RINs can be identified by placing reactive elements (inductors and capacitors) in these topological structures simultaneously checking for the low-pass or band-pass characteristics of the resulting network, consistent with the definition of a RC.

The search is restricted to the maximum of four reactive elements since more reactive elements increase size, weight, cost of the converter and complicates the circuit analysis and design.

2.3.1 One-, Two- and Three-Branch Topological Structures

Various topological structures of electrical networks composed of maximum up to three branches are shown in Fig. 2.6. Each branch has a generic reactance X_i ($i=1, 2, 3$), which can be composed of one or more reactive elements, illustrated in Fig. 2.7. The transmission parameters for topologies of Fig. 2.6 are derived and are summarized in Table 2.1.

Applying the condition of (2.11), it is concluded that only two topological structures, N_5 and N_6 (commonly called the T-network and the π -network, respectively), can exhibit immittance conversion characteristics if,

$$X_1 = X_2 = -X_3 \quad (2.12)$$

The condition expressed by (2.12) can be interpreted as follows:

- Magnitudes of all branch reactances should be equal.
- Reactances X_1 and X_2 should be similar (both inductive or both capacitive).
- If X_1 and X_2 are inductive (capacitive), X_3 should be capacitive (inductive).

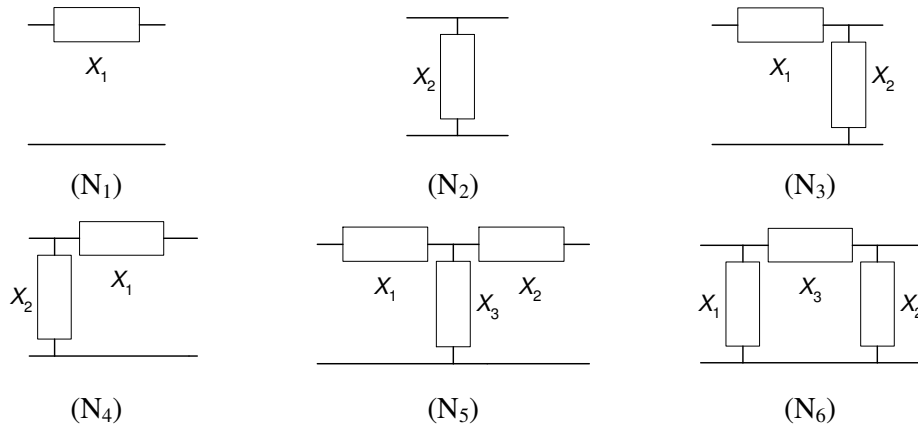


Fig. 2.6: Topological structures of electrical networks composed of maximum up to three branches.

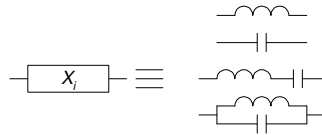


Fig. 2.7: Composition of generic reactance X_i .

Table 2.1: Transmission parameters of various topological structures of electrical networks shown in Fig. 2.6.

Topological Structure	A	B	C	D
N_1	1	$-X_1$	0	-1
N_2	1	0	$\left(\frac{1}{X_1}\right)$	-1
N_3	$\left(1 + \frac{X_1}{X_2}\right)$	$-X_1$	$\left(\frac{1}{X_2}\right)$	-1
N_4	1	$-X_1$	$\left(\frac{1}{X_2}\right)$	$-\left(1 + \frac{X_1}{X_2}\right)$
N_5	$\left(1 + \frac{X_1}{X_3}\right)$	$-\left(\frac{X_1X_2 + X_1X_3 + X_2X_3}{X_3}\right)$	$\left(\frac{1}{X_3}\right)$	$-\left(1 + \frac{X_2}{X_3}\right)$
N_6	$\left(1 + \frac{X_3}{X_2}\right)$	$-X_3$	$\left(\frac{X_1 + X_2 + X_3}{X_1X_2}\right)$	$-\left(1 + \frac{X_3}{X_1}\right)$

Next, reactive elements (inductors and capacitors) are placed for each X_i in topologies N_5 and N_6 satisfying the condition expressed in (2.12). The resulting network configurations are summarized in Table 2.2 for network N_5 and in Table 2.3 for network N_6 . To restrict the maximum number of reactive elements in a network to four, one of the branch reactance is constrained to be composed of maximum two reactive elements while the other two branch reactances are constrained to be composed of single reactive element. This constraint can be relaxed further to explore higher order RINs topologies, if desired. In all, 9 T-type RINs (identified by T_1 to T_9) and 7 π -type RINs (identified by P_1 to P_7) with maximum of four reactive elements are obtained. They are summarized in Fig. 2.8. Tables 2.2 and 2.3 also show the non-resonant (NR) networks exhibiting immittance conversion characteristics.

To the best of researcher's knowledge, only two out of 16 RINs shown in Fig. 2.8, namely, LCL-T (topology T_1) and CLC- π (topology P_1), have appeared in the literature as mentioned in section 2.1. The rest of the networks are newly identified RINs and, unlike previously published topologies, these are not lumped circuit equivalents of distributed constant line.

Topological structures N_1 through N_4 can not exhibit immittance conversion characteristics. Thus a large number of second and higher order RINs explored in [9], [10] and belonging to these topological structures are systematically eliminated from being an RIC topology.

Table 2.2: Synthesis of RINs resulting from topological structure N_5 .



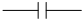
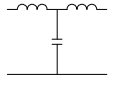
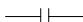
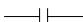

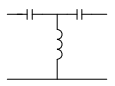

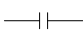

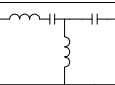


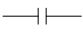
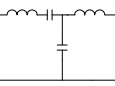


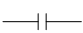
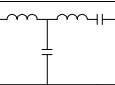
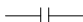


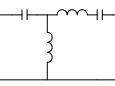



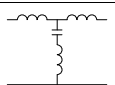



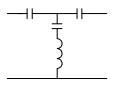

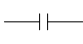

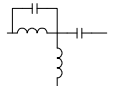


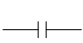
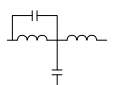


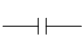
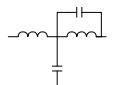



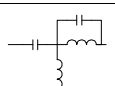



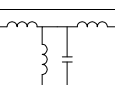



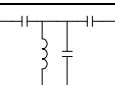


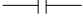
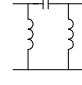
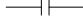
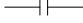

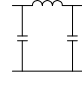

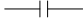

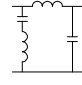


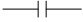
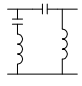



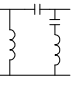
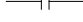
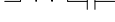
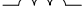
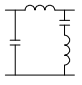

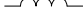
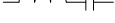
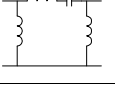
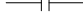
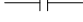
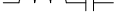


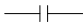

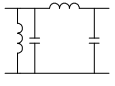



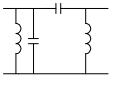



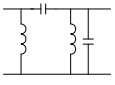



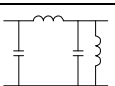



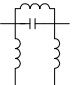



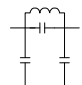
X_1	X_2	X_3	Network	Topology Identifier
				T_1
				NR
				T_4
				T_3
				T_2
				T_5
				T_8
				NR
				NR
				T_6
				T_7
				NR
				T_9
				NR

Table 2.3: Synthesis of RINs resulting from topological structure N_6 .

X_1	X_2	X_3	Network	Topology Identifier
				NR
				P_1
				P_2
				NR
				NR
				P_3
				P_7
				P_6
				P_4
				NR
				NR
				P_5
				NR
				NR

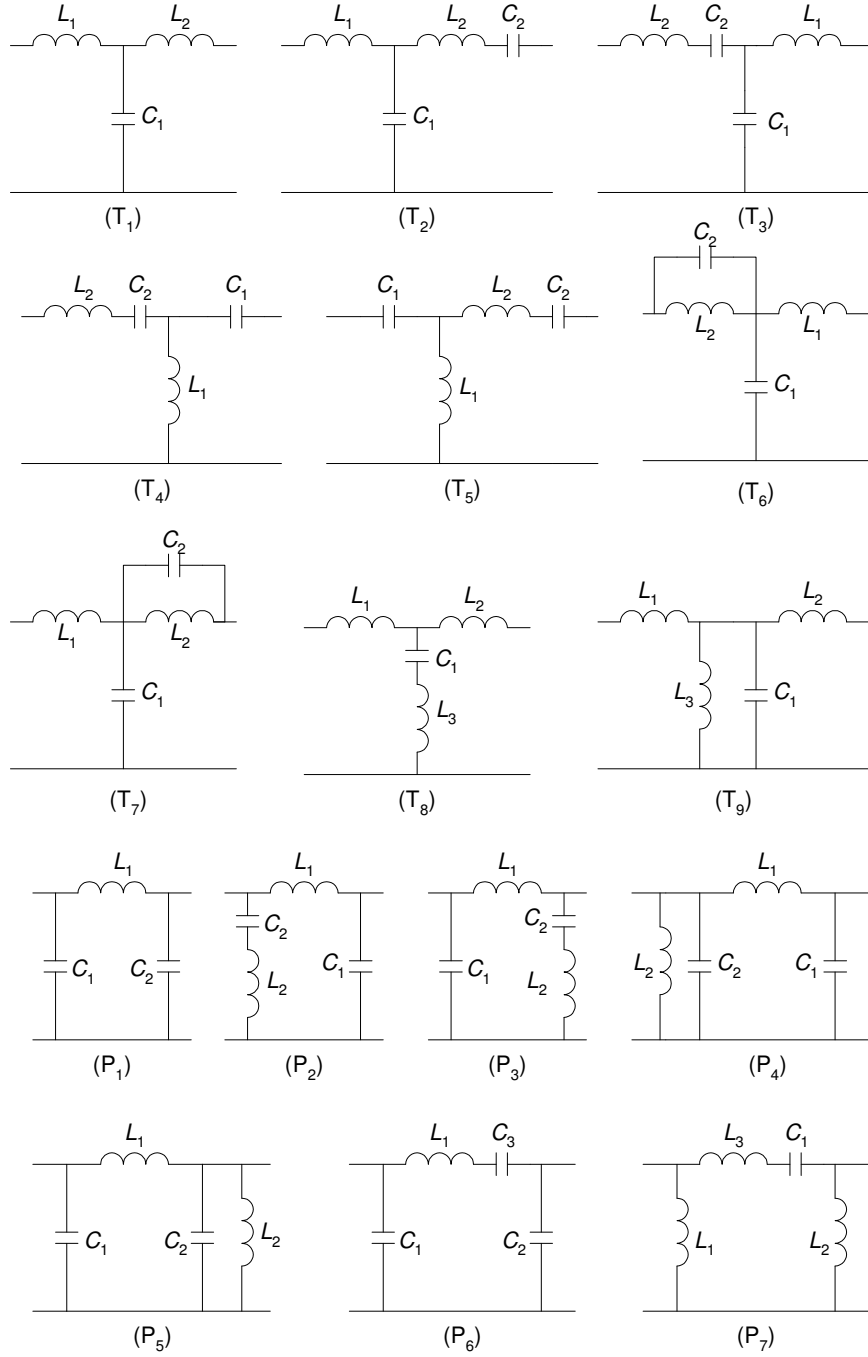


Fig. 2.8: Three- and Four-element RINs synthesized from topological structures N₅ and N₆.

2.3.2 Four-Branch Topological Structures

Four-branch topological structures are shown in Fig. 2.9. These topologies have been commonly termed as the ladder network (N_7 and N_8), the bridged-T network (N_9) and the lattice network (N_{10}). As before, X_i ($i=1, 2, 3, 4$) represents the generic reactance, which can be a single reactive element to restrict the maximum number of reactive elements in a network to four.

To derive immittance conversion characteristics of N_7 , N_8 and N_9 , these topologies are first converted to equivalent T-networks, as shown in Fig. 2.10 (a), (b) and (c), respectively, by applying star-delta transformation. Expressions for X_A , X_B and X_C in these equivalent T-networks can readily be derived. Analogous to (2.12),

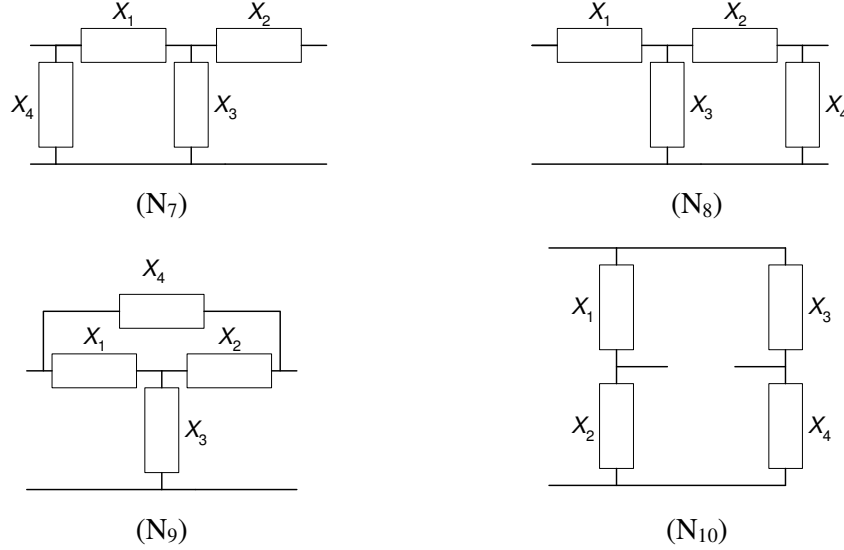


Fig. 2.9: Topological structures of electric networks composed of four branches.

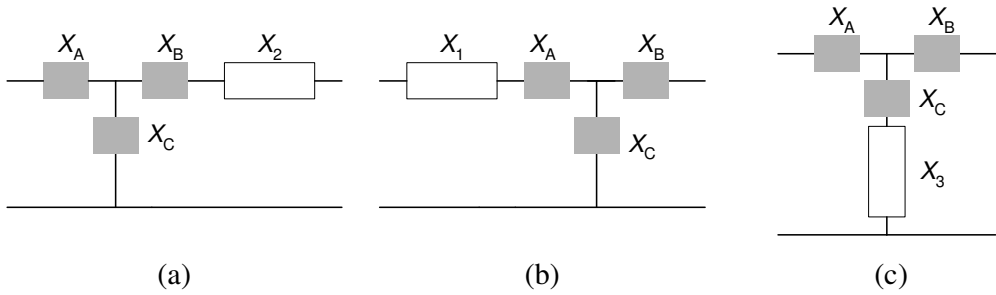


Fig. 2.10: Equivalent T-networks of (a) N_7 , (b) N_8 and (c) N_9 .

the condition for immittance conversion characteristics of topologies N_7 , N_8 and N_9 can be written and further simplified in terms of branch reactances X_1 to X_4 , as summarized in Table 2.4.

Deriving transmission parameters of N_9 and applying the condition of (2.11), it can be shown that this topology can exhibit immittance conversion characteristics if the following condition is satisfied:

$$X_1 = X_4 = -X_2 = -X_3 \quad (2.19)$$

2.3.2.1 Topology N_7

Topology N_7 can behave as an IC if the conditions expressed in (2.13) and (2.14) are satisfied. These conditions can be interpreted as follows:

- The magnitude of branch reactances X_1 and X_3 should be equal. If X_1 is inductive (capacitive), X_3 should be capacitive (inductive).
- While the magnitude of branch reactances X_4 and X_3 is related by (2.14), their nature (inductive or capacitive) is decided as follows:
 - If X_1 and X_2 are similar reactance, the denominator on the right hand side (RHS) of (2.14) can be a positive or a negative real number. Therefore, X_3 and X_4 can either be similar or dissimilar reactances.

Table 2.4: Condition for immittance conversion characteristics of N_7 , N_8 and N_9 .

Topological Structure	Condition for Immittance Conversion Characteristics	Equation Number
N_7	$X_1 = -X_3$	(2.13)
	$X_4 = \frac{X_3}{1 - \frac{X_2}{X_1}}$	(2.14)
	$X_2 = -X_3$	(2.15)
N_8	$X_4 = \frac{X_3}{1 - \frac{X_1}{X_2}}$	(2.16)
	$X_1 = X_2$	(2.17)
N_9	$X_4 = -X_3 \left(\frac{2 + \frac{X_1}{X_3}}{1 + \frac{X_1}{X_3}} \right)$	(2.18)

- If X_1 and X_2 are dissimilar reactances, the denominator on the RHS of (2.14) is a positive real number. Therefore X_3 and X_4 should be similar reactances.

Substituting reactive elements in place of X_i in topology N_7 , satisfying the condition given by (2.13) and (2.14), six networks are formed as shown in Table 2.5, out of which four are classified as RIN and two are NR ICs.

2.3.2.2 Topology N_8

Topology N_8 can behave as an IC if the conditions expressed in (2.15) and (2.16) are satisfied. These conditions can be interpreted as follows:

- The magnitude of branch reactances X_2 and X_3 should be equal. If X_2 is inductive (capacitive), X_3 should be capacitive (inductive).
- While the magnitude of branch reactances X_4 and X_3 is related by (2.16), their nature (inductive or capacitive) is decided as follows:
 - If X_1 and X_2 are similar reactance, the denominator on RHS of (2.16) can be a positive or a negative real number. Therefore, X_3 and X_4 can either be similar or dissimilar reactances.
 - If X_1 and X_2 are dissimilar reactance, the denominator on the RHS of (2.16) is a positive real number. Therefore, X_3 and X_4 should be similar.

Substituting reactive elements in place of X_i in topology N_8 , satisfying the condition given by (2.15) and (2.16), six networks are formed as shown in Table 2.6, out of which four are classified as RIN and two are NR ICs.

2.3.2.3 Topology N_9

Topology N_9 can behave as an IC if the conditions expressed in (2.17) and (2.18) are satisfied. These conditions can be interpreted as follows:

- The branch reactances X_1 and X_2 should be equal and similar.
- While the magnitude of branch reactances X_4 and X_3 is related by (2.18), their nature (inductive or capacitive) is decided as follows:
 - If X_1 and X_3 are similar reactance, the term inside the bracket on the RHS of (2.18) is a positive real number. Therefore, X_3 and X_4 should be dissimilar reactances.

- If X_1 and X_3 are dissimilar reactance, the term inside the bracket on RHS of (2.18) can be positive or negative real number. Therefore, X_3 and X_4 can either be dissimilar or similar reactances.

Substituting reactive elements in place of X_i in topology N_9 , satisfying the condition given by (2.17) and (2.18), six networks are formed as shown in Table 2.7, out of which only one is classified as RIN and the rest are NR ICs.

2.3.2.4 Topology N_{10}

Topology N_{10} can behave as an IC if the condition expressed in (2.19) is satisfied. This condition can be interpreted as follows:

- The magnitude of all branch reactances should be equal.
- Branch reactances X_1 and X_2 should be similar.
- Branch reactances X_3 and X_4 should be similar.
- If X_1, X_2 are inductive (capacitive), X_3, X_4 should be capacitive (inductive).

Substituting reactive elements in place of X_i in topology N_{10} satisfying the condition given by (2.19), two networks are formed as shown in Table 2.8 and both are NR ICs.

Table 2.5: Synthesis of RINs resulting from topological structure N_7 .



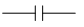

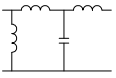




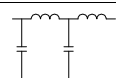


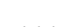

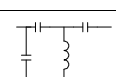




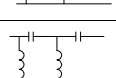
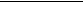
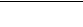
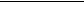
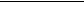
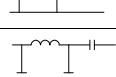
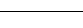
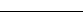
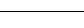
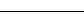
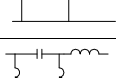
X_1	X_2	X_3	X_4	Network	Topology Identifier
					LA ₃
					LA ₁
					NR
					NR
					LA ₅
					LA ₇

Table 2.6: Synthesis of RINs resulting from topological structure N_8 .



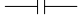

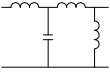


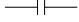
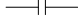
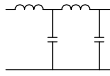
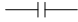
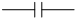

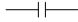
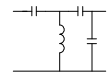
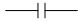
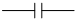


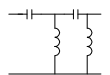

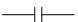


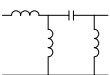



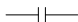
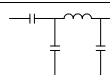
X_1	X_2	X_3	X_4	Network	Topology Identifier
					LA ₄
					LA ₂
					NR
					NR
					LA ₈
					LA ₆

 Table 2.7: Synthesis of RINs resulting from topological structure N_9 .




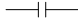
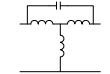




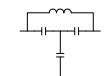



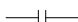
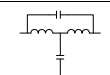




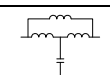




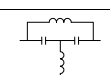




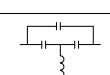




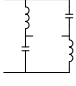
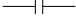


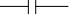
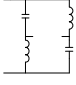
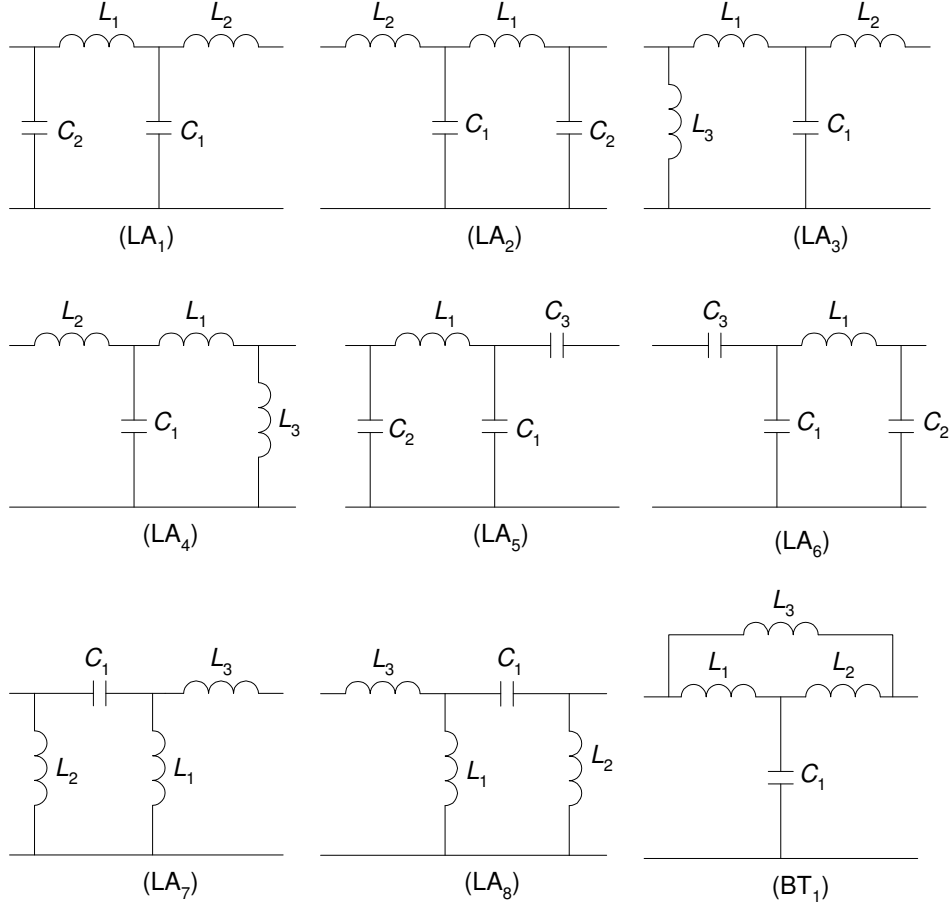
X_1	X_2	X_3	X_4	Network	Topology Identifier
					NR
					NR
					NR
					BT ₁
					NR
					NR

Table 2.8: Synthesis of RINs resulting from topological structure N_{10} .

X_1	X_2	X_3	X_4	Network	Topology Identifier
					NR
					NR


 Fig. 2.11: Four-element RINs synthesized from topological structures N_7 , N_8 and N_9 .

To summarize, in all 8 ladder type RINs (identified by LA_1 to LA_8) and 1 bridged-T type RIN (identified by BT_1) with four reactive elements are obtained. They are summarized in Fig. 2.11. However, the bridged-T type network (BT_1) is topologically equivalent to network T_8 in Fig. 2.8 after star-delta transformation. Therefore BT_1 is not considered as an independent RIN.

To the best of researcher's knowledge, only one out of 9 RINs, shown in Fig. 2.11 (topology LA₂) has appeared in the literature as mentioned in section 2.1. The rest of the networks are newly identified RINs and, unlike previously published topologies, these are not lumped circuit equivalents of distributed constant line.

2.4 Design Conditions

The RINs of Fig. 2.8 and Fig. 2.11 exhibit immittance conversion characteristics only if various reactances obey certain conditions, which are satisfied only at a particular frequency of operation and when the values of reactive elements are suitably chosen. The circuits have different characteristics at other frequencies. To derive this operating point and the design condition the following terms are defined:

$$\text{Angular resonant frequency: } \omega_o = \frac{1}{\sqrt{L_1 C_1}} \quad (2.20)$$

$$\text{Normalized switching frequency: } \omega_n = \frac{\omega}{\omega_o} \quad (2.21)$$

ω being the angular operating or switching frequency.

$$\text{Ratio of inductances: } \gamma = \frac{L_2}{L_1} \text{ and } \alpha = \frac{L_3}{L_1} \quad (2.22)$$

$$\text{Ratio of capacitances: } \psi = \frac{C_2}{C_1} \text{ and } \beta = \frac{C_3}{C_1} \quad (2.23)$$

Inductors L_1 , L_2 and L_3 as well as capacitors C_1 , C_2 and C_3 are marked in Fig. 2.8 and Fig. 2.11.

The operating point and the design condition can be obtained by substituting actual branch reactances of various RINs in the respective condition for immittance conversion characteristics given by (2.12) to (2.18). Table 2.9 summarizes the derived design conditions in terms of operating point $\omega_n = \omega_{ni}$ (the normalized switching frequency where a RIN exhibits immittance conversion characteristics) and relationship among the values of reactive elements (in terms of α , β , γ and ψ).

Table 2.9: Operating point and design condition of RINs

RIN	Operating Point $\omega_n = \omega_{ni}$	Design Condition	Equation Number
T ₁	1	$\gamma = 1$	(2.24)
T ₂ , T ₃	1	$\gamma = \frac{1+\psi}{\psi}$	(2.25)
T ₄ , T ₅	1	$\gamma = \frac{1-\psi}{\psi}$	(2.26)
T ₆ , T ₇	1	$\gamma = \frac{1}{1+\psi}$	(2.27)
T ₈	$\frac{1}{\sqrt{\alpha+1}}$	$\gamma = 1$	(2.28)
T ₉	$\sqrt{\frac{\alpha+1}{\alpha}}$	$\gamma = 1$	(2.29)
P ₁	1	$\psi = 1$	(2.30)
P ₂ , P ₃	1	$\psi = \frac{1}{\gamma+1}$	(2.31)
P ₄ , P ₅	1	$\psi = \frac{1+\gamma}{\gamma}$	(2.32)
P ₆	$\sqrt{\frac{\beta+1}{\beta}}$	$\psi = 1$	(2.33)
P ₇	$\frac{1}{\sqrt{1+\alpha}}$	$\gamma = 1$	(2.30)
LA ₁ , LA ₂	1	$\psi + \gamma = 1$	(2.34)
LA ₃ , LA ₄	1	$\alpha = \frac{1}{\gamma-1}$	(2.35)
LA ₅ , LA ₆	1	$\beta = \frac{1}{\psi-1}$	(2.36)
LA ₇ , LA ₈	1	$\gamma = \frac{1}{\alpha+1}$	(2.37)

2.5 General Features

It may not be obvious to identify, in the first look, practically useful ones out of 24 RINs explored in the previous sections (see Fig. 2.8 and Fig. 2.11) unless they are analyzed further. However, a few general observations can be made with respect to practical aspects in their application.

A capacitor of RIN directly appears across the input port of 9 topologies, namely, T₆, P₁, P₃-P₆, LA₁, LA₅ and LA₆. A square-wave voltage source can not be connected at the input port of these topologies. Instead, they can be excited with a square-wave current source. Therefore, topologies T₆, P₁, P₃-P₆, LA₁, LA₅ and LA₆ are suitable for conversion of current source into a voltage source. They are termed Type-I RIC topologies.

The rest 15 RINs, namely, T_1 - T_5 , T_7 - T_9 , P_2 , P_7 , LA_2 - LA_4 , LA_7 and LA_8 can be excited with a square-wave voltage source and are suitable for conversion of a voltage source into a current source. They are termed Type-II RIC topologies.

An important advantage of RC circuits is their ability to absorb circuit parasitic elements as the part of the RN. While parasitic components are associated with all practical components, those associated with the high-frequency isolation transformer affect the most. In low-voltage high-current applications, leakage inductance is important. In high-voltage power supplies, transformer is associated with significant leakage inductance as well as winding capacitance. Loosely coupled transformer used for inductive power transfer is characterized by large leakage and small magnetizing inductance.

It is observed that the transformer leakage inductance (L_{lk}) can be advantageously used as the part of all RINs when the transformer is either connected directly across the output port, e.g. in topology T_1 as shown in Fig. 2.12(a), or inserted in between the RN and shifting some of the components on the secondary side, e. g. in topology T_4 with C_1 placed on the secondary side as shown in Fig. 2.12(b). In the latter illustration, it is also possible to use transformer magnetizing inductance (L_m)

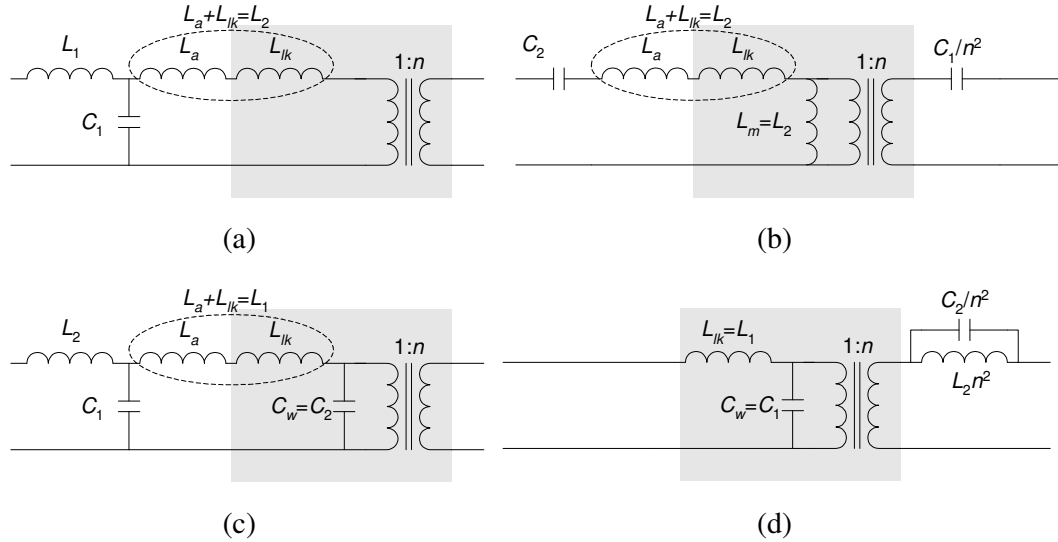


Fig. 2.12: Illustrations of transformer parasitic components being absorbed in various RINs. (a) Topology T_1 , (b) Topology T_4 , (c) Topology LA_2 , and (d) Topology T_7 .

as inductor L_2 of the RIN. Topologies T_4 , T_5 , T_9 , P_5 , P_7 , LA_4 , LA_7 and LA_8 advantageously integrate L_m and L_{lk} into RIN.

Some of the RINs (T_2 - T_4 , T_7 , T_9 , P_1 , P_2 , P_4 - P_6 , LA_1 - LA_6) absorb L_{lk} and transformer winding capacitance (C_w) when the transformer is at the output port, e.g. in topology LA_2 as shown in Fig. 2.12(c), or inserted in the RN, e.g. in topology T_7 with L_2 , C_2 placed on the secondary side as shown in Fig. 2.12(d).

It is advantageous if a resonant capacitor also does the dc blocking to prevent saturation of isolation transformer. Else, additional bulky dc blocking capacitor may be required. Some of the RIC topologies (T_2 - T_5 , P_6 , P_7 , LA_5 - LA_8) offer inherent dc blocking of isolation transformer.

2.6 Conclusion

A family of lumped-element RIC topologies is identified by investigating transmission parameters of various topological structures of electrical networks. In all 24 RINs have been identified with three and four reactive elements. Unlike previously published topologies, newly identified RINs are not lumped circuit equivalents of distributed constant line. The operating point and design condition, under which these topologies exhibit immittance conversion characteristics, is derived. Suitability of these topologies in terms of absorbing parasitic components and providing inherent dc blocking to the transformer is examined. While 9 circuits (Type-I RICs) are useful for applications demanding current-to-voltage conversion, 15 circuits (Type-II RICs) are suitable for application as a CC power supply.

Chapter 3

Analysis, Design and Topological Extensions of Type-II RICs

In all 24 RIC topologies are explored in Chapter 2, out of which 15 Type-II RICs are suitable for application as CC power supplies. Analysis and design procedure of Type-II RICs as a CC power supply is exemplified in this chapter with selected topologies. Fundamental frequency ac analysis is performed to gain insight into the steady-state characteristics. Closed-form expressions for converter gain as well as ratings of various components are derived. A condition for optimized converter design is determined. Experimental results on prototype converters are presented to demonstrate the converter performance and CC behaviour. An illustrative higher-order RIC topology featuring feasibility of integrated magnetic component is also analyzed and validated with experimental results.

The chapter also describes two topological extensions. In the first extension, an addition of clamp diodes in Type-II RIC circuits attributes inherent CV characteristics to the converter in addition to the CC behaviour. The second topological extension, namely, multiphase Type-II RICs, describes the phase-staggered operation of paralleled modules resulting in reduced filtering requirement and improved open-loop dynamic response.

3.1 Topology T₁: LCL-T RC

Topology T₁ or LCL-T RC is the simplest Type-II RIC topology with three reactive elements. Apart from its application as a CC power supply [65], the topology is also reported for application as voltage regulator module [61], induction heating [62], inductive power transfer [63] and power factor correction [66].

The circuit diagram of half-bridge LCL-T RC is shown in Fig. 3.1(a). The RIN is composed of inductors L_1 , L_2 and capacitor C_2 . The half-bridge converter (composed of MOSFET switches S_A , S_B , their body-drain diodes D_A , D_B , respectively and capacitors C_A , C_B) drives the input port of the RIN with high-frequency square-wave voltage waveform, v_{in} . The circuit diagram of full-bridge LCL-T RC is shown in Fig. 3.1(b) wherein MOSFET switches $S_1 - S_4$ and their body-drain diodes $D_1 - D_4$, respectively, constitute the full-bridge square-wave inverter. At the output port of the RIN an isolation transformer of turns ratio $1:n$ matches the required output voltage, V_o , and current, I_o , to the input dc voltage ($2V_d$ in the half-bridge and V_d in the full-

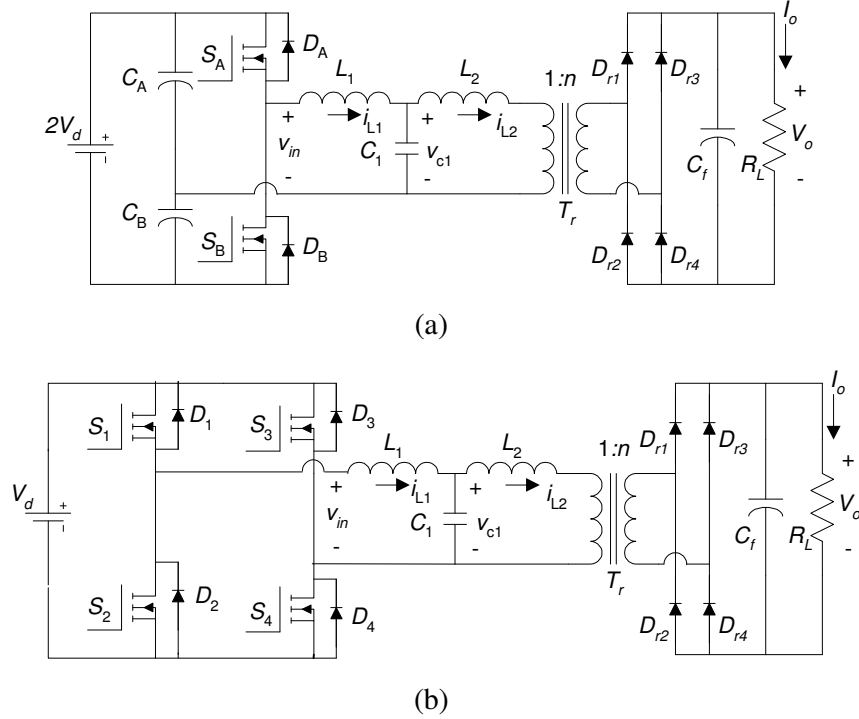


Fig. 3.1: Circuit diagram of (a) half-bridge and (b) full-bridge LCL-T RC.

bridge circuit). A diode rectifier (D_{r1} through D_{r4}) and filter capacitor (C_f) convert high-frequency ac to output dc.

3.1.1 Analysis

Fundamental frequency ac analysis method is used, in which the output rectifier and filter are replaced by an equivalent ac resistance and the square-wave input voltage source is replaced by its fundamental sinusoidal equivalent. The power transfer from input to output is assumed to be only via the fundamental component and the contribution of all harmonics is neglected. With these approximations, classical ac analysis is applied to determine closed-form expressions for converter gain and component stresses. An equivalent ac resistance (R_{ac}) for rectifier with capacitive filter and rms value of the fundamental component of square-wave input voltage to the RIN ($V_{in,rms}$) are given by,

$$R_{ac} = \frac{8}{\pi^2} \frac{R_L}{n^2} \quad \text{and} \quad V_{in,rms} = \frac{2\sqrt{2}}{\pi} V_d \quad (3.1)$$

The resonant frequency and the normalized switching frequency are defined as,

$$\omega_o = \frac{1}{\sqrt{L_1 C_1}} \quad \text{and} \quad \omega_n = \frac{\omega}{\omega_o} \quad (3.2)$$

The characteristic impedance (Z_n) and Q of the RIN are defined as,

$$Z_n = \sqrt{\frac{L_1}{C_1}} \quad \text{and} \quad Q = \frac{n^2 \omega_o L_1}{R_L} = \frac{n^2 Z_n}{R_L} \quad (3.3)$$

The ratio of inductors is defined in (2.22) as,

$$\gamma = \frac{L_2}{L_1} \quad (3.4)$$

The voltage gain (M) and current gain (H) of the converter are defined as,

$$M = \frac{V_o/n}{V_d} \quad \text{and} \quad H = \frac{nI_o}{V_d/Z_n} \quad (3.5)$$

The voltage and current gain of LCL-T RC is derived as,

$$M = \frac{1}{(1 - \omega_n^2) + j \frac{\pi^2}{8} Q [(1 + \gamma)\omega_n - \gamma\omega_n^3]} \quad (3.6)$$

$$H = \frac{1}{\frac{1}{Q}(1 - \omega_n^2) + j\frac{\pi^2}{8}[(1 + \gamma)\omega_n - \gamma\omega_n^3]} \quad (3.7)$$

It can be noticed from (3.7) that the load current is independent of load if the converter is operated at $\omega_n = 1$. Under this condition,

$$H|_{\omega_n=1} = \frac{8}{\pi^2} \quad (3.8)$$

Next, the expressions for normalized rms current through inductor L_1 (I_{L_1N}), inductor L_2 (I_{L_2N}), capacitor C_1 (I_{C_1N}) and normalized rms voltages across these components (V_{L_1N} , V_{L_2N} , V_{C_1N} , respectively) are derived taking the base voltage and base current as V_d and (V_d/Z_n) , respectively. They are summarized as follows:

$$I_{L_1N} = \frac{I_{L_1,rms}}{V_d/Z_n} = \frac{\pi}{2\sqrt{2}} \frac{Q(1 - \gamma\omega_n^2) + j\frac{8}{\pi^2}\omega_n}{(1 - \omega_n^2) + j\frac{\pi^2}{8}Q[(1 + \gamma)\omega_n - \gamma\omega_n^3]} \quad (3.9)$$

$$I_{L_2N} = \frac{I_{L_2,rms}}{V_d/Z_n} = \frac{\pi}{2\sqrt{2}} \frac{Q}{(1 - \omega_n^2) + j\frac{\pi^2}{8}Q[(1 + \gamma)\omega_n - \gamma\omega_n^3]} \quad (3.10)$$

$$I_{C_1N} = \frac{I_{C_1,rms}}{V_d/Z_n} = \frac{\pi}{2\sqrt{2}} \frac{-Q\gamma\omega_n^2 + j\frac{8}{\pi^2}\omega_n}{(1 - \omega_n^2) + j\frac{\pi^2}{8}Q[(1 + \gamma)\omega_n - \gamma\omega_n^3]} \quad (3.11)$$

$$V_{L_1N} = \frac{V_{L_1,rms}}{V_d} = \frac{2\sqrt{2}}{\pi} \frac{-\omega_n^2 + j\frac{\pi^2}{8}Q(\omega_n - \gamma\omega_n^3)}{(1 - \omega_n^2) + j\frac{\pi^2}{8}Q[(1 + \gamma)\omega_n - \gamma\omega_n^3]} \quad (3.12)$$

$$V_{L_2N} = \frac{V_{L_2,rms}}{V_d} = \frac{2\sqrt{2}}{\pi} \frac{j\frac{\pi^2}{8}Q\gamma\omega_n}{(1 - \omega_n^2) + j\frac{\pi^2}{8}Q[(1 + \gamma)\omega_n - \gamma\omega_n^3]} \quad (3.13)$$

$$V_{C_1N} = \frac{V_{C_1,rms}}{V_d} = \frac{2\sqrt{2}}{\pi} \frac{1 + j\frac{\pi^2}{8}Q\gamma\omega_n}{(1 - \omega_n^2) + j\frac{\pi^2}{8}Q[(1 + \gamma)\omega_n - \gamma\omega_n^3]} \quad (3.14)$$

For operation at $\omega_n = 1$, (3.9) can be simplified as,

$$I_{L_1N}|_{\omega_n=1} = \frac{\pi}{2\sqrt{2}} \frac{Q(1-\gamma) + j\frac{8}{\pi^2}}{j\frac{\pi^2}{8}Q} \quad (3.15)$$

Therefore, the phase angle between v_{in} and i_{L1} can be derived as,

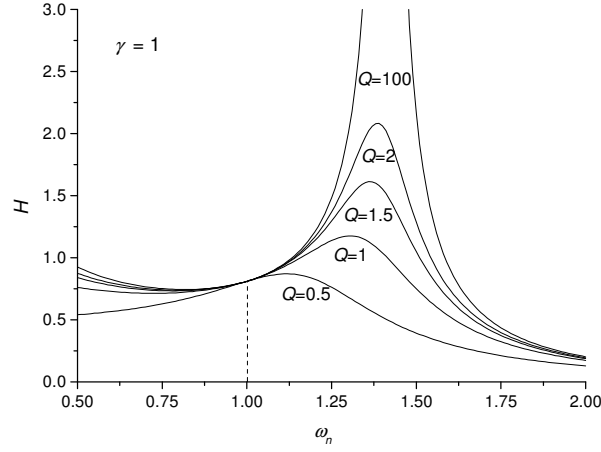
$$\phi|_{\omega_n=1} = \tan^{-1} \left(\frac{Q(\gamma-1)}{\frac{8}{\pi^2}} \right) \quad (3.16)$$

If the converter designed with $\gamma = 1$ is operating at $\omega_n = 1$ then $\phi = 0$ for all values of Q . Thus the converter exhibits constant output current and in-phase source voltage and current simultaneously at all loading conditions. In other words, the converter behaves as a RIC. The conditions $\omega_n = 1$ and $\gamma = 1$, derived as (2.24) in the previous chapter, are therefore verified with an independent analysis.

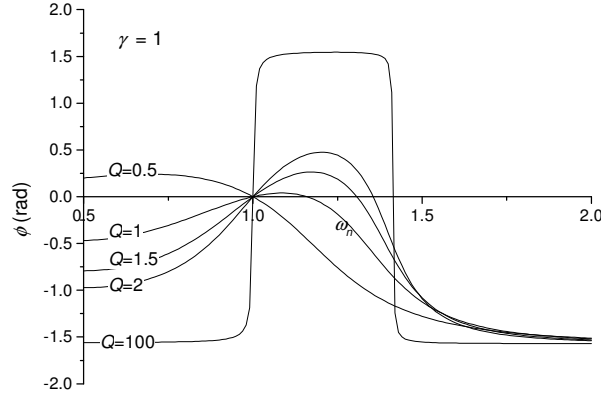
The plots of H are illustrated in Fig. 3.2(a) for different values of Q and $\gamma = 1$. A plot for $Q=100$ corresponding to nearly load-short-circuit condition is also included to demonstrate current-source behaviour of the converter. The plots of Fig. 3.2(b) show the variation of ϕ as a function of ω_n for different values of Q and for $\gamma = 1$. H is seen to be load independent at $\omega_n=1$ for all values of Q . It can also be noted that $\phi = 0$ at $\omega_n = 1$ for all values of Q . Advantages of a RC operating in lagging power-factor mode are very well known. Equation (3.16) suggests that LCL-T RC can operate in lagging power-factor mode if $\gamma < 1$. Thus the required phase lag can be realized by keeping γ slightly less than unity. Never-the-less, theoretically preferred operating parameters can be decided as $\omega_n = 1$ and $\gamma = 1$ and the magnitude of above-derived expressions can be written in simplified form as under. The resulting error for design with $\gamma \neq 1$ will not be significant as long as γ is close to unity.

$$|I_{L_1N}|_{\omega_n=\gamma=1} = |V_{L_1N}|_{\omega_n=\gamma=1} = \frac{16\sqrt{2}}{\pi^3} \frac{1}{Q} \quad (3.17)$$

$$|I_{L_2N}|_{\omega_n=\gamma=1} = |V_{L_2N}|_{\omega_n=\gamma=1} = \frac{2\sqrt{2}}{\pi} \quad (3.18)$$



(a)



(b)

Fig. 3.2: Plots of (a) H and (b) ϕ in LCL-T RC as a function of ω_n for different values of Q and $\gamma = 1$.

$$\left| I_{C_1 N} \right|_{\omega_n = \gamma = 1} = \left| V_{C_1 N} \right|_{\omega_n = \gamma = 1} = \frac{2\sqrt{2}}{\pi} \frac{\sqrt{\left(\frac{8}{\pi^2} \right)^2 + Q^2}}{Q} \quad (3.19)$$

3.1.2 Design

For the design of LCL-T RC, the values of reactive elements in the RIN and their voltage and current ratings need to be determined. $\omega_n = 1$ and $\gamma = 1$ are the necessary conditions for the operation of the converter as a current-source. If a

general design rule is formulated to decide the values of Q , then values of the reactive elements and their ratings can be calculated using the expressions derived in the previous section. Examining equations (3.17) to (3.19), it is noticed that Q has a profound effect on the ratings of reactive components, which increases the overall size of RIN. Therefore, the converter can be optimized for minimum size of RIN taking (kVA/kW) rating as an index for its physical size. The (kVA/kW) rating can be calculated from,

$$\left. \frac{kVA}{kW} \right|_{\omega_n=\gamma=1} = \left. \frac{V_{C_1N} \cdot I_{C_1N} + V_{L_1N} \cdot I_{L_1N} + V_{L_2N} \cdot I_{L_2N}}{H^2/Q} \right|_{\omega_n=\gamma=1} \quad (3.20)$$

Substituting equations (3.17) to (3.19) in (3.20) and simplifying,

$$\left. \frac{kVA}{kW} \right|_{\omega_n=\gamma=1} = \frac{\pi^2}{4} Q + \frac{16}{\pi^2} \frac{1}{Q} \quad (3.21)$$

Figure 3.3 shows the plots of (3.21) as a function of Q . The plots show the existence of a particular value of Q where (kVA/kW) is minimum. This is termed as the optimum value of Q , Q_{opt} , and corresponding value of (kVA/kW) is termed as $(kVA/kW)_{opt}$. The expressions for Q_{opt} and $(kVA/kW)_{opt}$ are derived from (3.21) as,

$$Q_{opt} \Big|_{\omega_n=\gamma=1} = \frac{8}{\pi^2} \quad (3.22)$$

$$\left(\frac{kVA}{kW} \right)_{opt} \Big|_{\omega_n=\gamma=1} = 4 \quad (3.23)$$

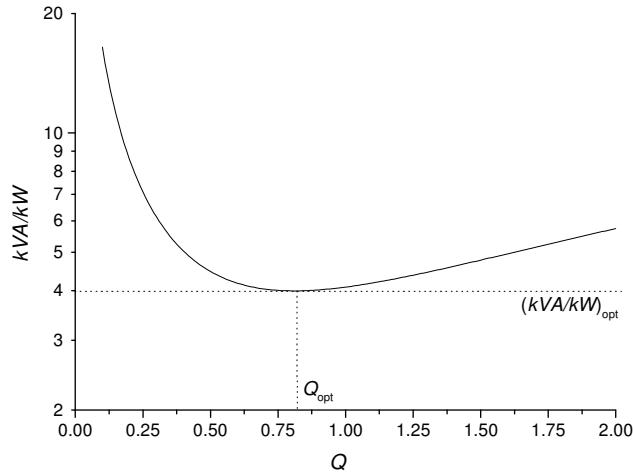


Fig. 3.3: kVA/kW rating of LCL-T RC as a function of Q for $\gamma=1$ and $\omega_n=1$.

Typical design inputs are: input dc voltage ($2V_d$ for half-bridge and V_d for full-bridge circuit), output current (I_o), maximum load resistance ($R_{L,\max}$) and switching frequency (f_s). Choosing full-load value of Q equal to Q_{opt} , the expression for n , L_1 , L_2 and C_1 are derived in terms of converter's terminal parameters as follows:

$$n = \frac{I_o R_{L,\max}}{V_d} \quad (3.24)$$

$$L_1 = L_2 = \frac{4}{\pi^3} \frac{V_d^2}{I_o^2 R_{L,\max} f_s} \quad (3.25)$$

$$C_1 = \frac{\pi}{16} \frac{I_o^2 R_{L,\max}}{V_d^2 f_s} \quad (3.26)$$

The voltage and current rating of various reactive elements can then be calculated using (3.17) through (3.19).

3.1.3 Experimental Results

A laboratory prototype has been designed and built to experimentally validate the current source property of LCL-T RC [65]. The converter has the following specifications: input dc supply voltage = 50 V, $I_o = 20$ A, $R_{L,\max} = 0.5 \Omega$, $f_s = 100$ kHz. Designing the converter with the full-load value of Q equal to Q_{opt} , the following values are calculated: $n=0.5$, $L_1=16.11 \mu\text{H}$, $L_2=16.11 \mu\text{H}$, $C_1=0.157 \mu\text{F}$. However, $0.157 \mu\text{F}$ is an odd value and could not be realized with available capacitors. Connecting three $0.047 \mu\text{F}$ capacitors in parallel, closest realizable value is $0.141 \mu\text{F}$. Accordingly, value of L_1 is scaled to $14.47 \mu\text{H}$ to retain equal Z_n . The resonant and switching frequency is consequently changed to 111.43 kHz. The input bridge inverter is realized with 200 V MOSFET switches (part number IRF640). A secondary center-tap transformer is used to reduce losses in the output rectifier stage. A common-cathode schottky module rated for 45 V and 40 A (part number MBR4045) is used for output rectification. A $20 \mu\text{F}$ capacitor forms the output filter in the prototype. The measured transformer leakage inductance reflected on primary side was $2.5 \mu\text{H}$. Hence, additional $11.5 \mu\text{H}$ inductance is added to make $L_2=14 \mu\text{H}$. L_1 is $14.5 \mu\text{H}$, resulting in γ slightly less than unity. Table 3.1 summarizes the specifications, designed component values, used components as well as calculated

Table 3.1: Specifications, component values and ratings of reactive components in prototype LCL-T RC

Parameter	Value	
<i>Specifications</i>		
I_o (A)	20	
$R_{L,max}$ (Ω)	0.5	
V_d (V)	50	
f_s (kHz)	100	
<i>Component values</i>		
	Designed	Used in prototype
L_1 (μ H)	16.11	14.47
L_2 (μ H)	16.11	14.00
C_1 (μ F)	0.157	0.141
n	0.2	0.2
f_s (kHz)	100	111.43
<i>Component ratings</i>		
	Calculated	Measured
I_{L_1} (A, rms)	4.45	5.02
I_{L_2} (A, rms)	4.45	4.43
I_{C_1} (A, rms)	6.30	6.88
V_{C_1} (V, rms)	63.72	69.90

and measured component ratings. The experimental prototype is operated in open-loop.

Figure 3.4 shows the open loop output characteristics of the prototype converter. The converter operates at 50 V dc input. The load was varied from short-

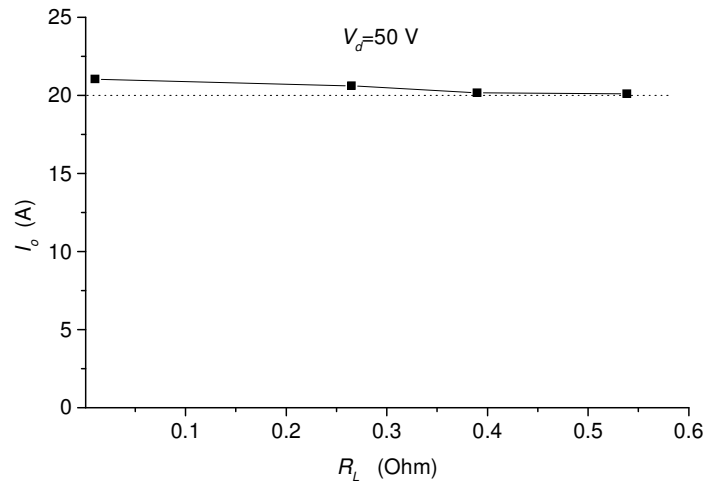


Fig. 3.4: Open loop output characteristics of prototype LCL-T RC.

circuit condition to full-load. The output current is seen to be approximately constant at 20 A. The slight droop in the characteristics is due to increase in conduction losses in the bridge inverter and RIN components. Voltage and current waveforms at the output of inverter bridge are shown in Fig. 3.5 (a) and (b) for $R_L=0.53 \Omega$ and 0.1Ω , respectively. Besides being in phase with the voltage, the inverter output current is seen to reduce with load as predicted in the analysis resulting in high part-load efficiency.

Figure 3.6 shows experimental converter efficiency as a function of output power. In plot (a), $R_L=0.53 \Omega$ and input dc voltage is varied from 5 V to 50 V. This

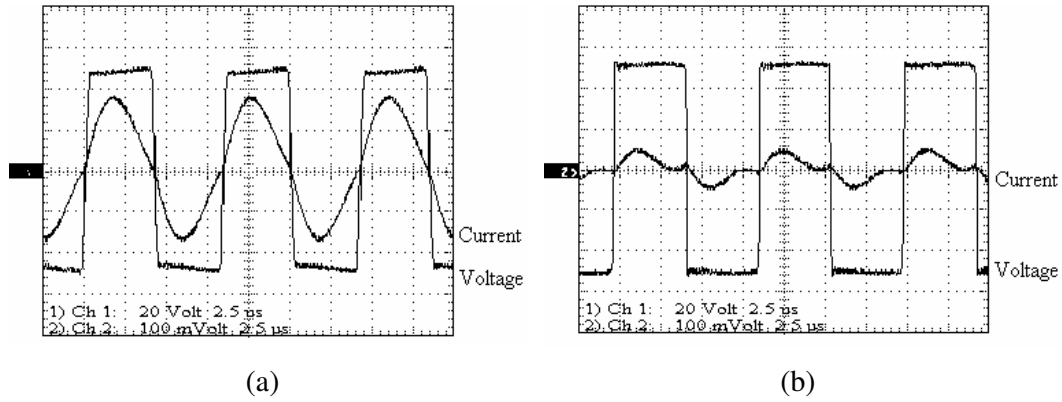


Fig. 3.5: Voltage and current waveforms at the output of inverter bridge. (a) $R_L=0.53 \Omega$ and (b) $R_L=0.1 \Omega$. Scale: 20 V/div (voltage), 5 A/div (current) and 2.5 μs/div.

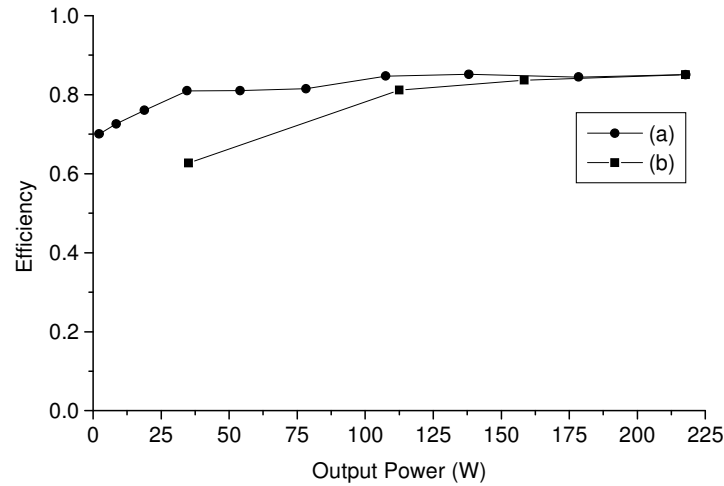


Fig. 3.6: Efficiency of prototype converter as a function of output power. Plot-(a): $R_L = 0.53 \Omega$ and V_d is varied from 5 V to 50 V. Plot-(b): $V_d = 50$ V and R_L is varied.

plot indicates high efficiency over entire conversion range. The maximum efficiency is 0.85 at 217 W output power which drops to 0.7 when the output power is reduced to 2.25 W. The highest efficiency is limited to 0.85 because secondary-side drops in the circuit become comparable with the low output voltage (10 V) of the experimental prototype. Plot (b) shows the efficiency of the experimental converter when operated at 50 V input and load resistance is varied to change the output power.

3.1.4 Merits and Limitations

Topology T_1 or LCL-T RC is the simplest RIC topology. Since the topology behaves as a CC source, the converter is inherently output short-circuit proof. This property, in general, is very useful for high voltage power supplies, wherein partial discharge and arcing can occur frequently. Further, the bridge output voltage and current are in phase. The current reduces proportionally with the load power thus maximizing full-load and part-load efficiency. The transformer leakage inductance is absorbed into the RIN.

On the other hand, the RIN of LCL-T RC does not inherently provide dc blocking for the isolation transformer and an additional bulky dc blocking capacitor may be required in practice. Further, the transformer winding capacitance, which can be significant in high-voltage transformer, is not gainfully utilized as the part of RIN and can significantly affect the converter characteristics.

3.2 Topology LA_2 : The LC-LC RC

The circuit diagram of half-bridge implementation of topology LA_2 , named the LC-LC RC, is shown in Fig. 3.7. The RIN is composed of inductors L_1 , L_2 and capacitors C_1 , C_2 . The half-bridge converter (composed of MOSFET switches S_A , S_B , their body-drain diodes D_A , D_B , respectively and capacitors C_A , C_B) drives input port of the RIN with high-frequency square-wave voltage waveform, v_{in} , of amplitude $\pm V_d$. At the output port of the RIN a transformer T_r of turns ratio $1:n$ matches the required output voltage, V_o , and current, I_o , to input dc voltage, $2V_d$. Diode rectifier (D_{r1} through D_{r4}) and filter capacitor (C_f) convert high-frequency ac to output dc.

LC-LC RC absorbs the transformer winding capacitance in the RIN in

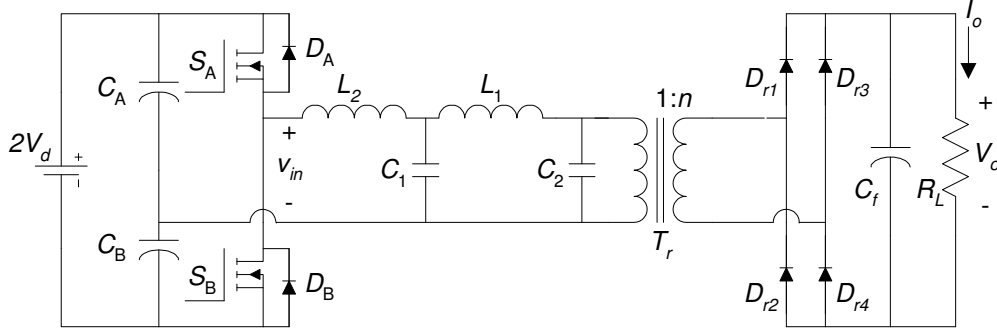


Fig. 3.7: Circuit diagram of half-bridge LC-LC RC.

addition to the transformer leakage inductance. This way, this fourth-order RIC topology overcomes one of the limitations of LCL-T RC.

3.2.1 Analysis

For the fundamental frequency ac analysis, the definition of R_{ac} , $V_{in,rms}$, ω_o , ω_n , Z_n and Q of the RIN is the same as given by (3.1) – (3.3). The values of inductors of the RIN are related by (3.4) and the ratio of capacitors in the RIN is additionally defined in (2.23) as:

$$\psi = \frac{C_2}{C_1} \quad (3.27)$$

The current gain of LC-LC RC is derived as

$$H = \frac{nI_o}{\frac{V_d}{Z_n}} = \frac{1}{\frac{1}{Q} [1 - (\gamma + \gamma\psi + \psi)\omega_n^2 + \gamma\psi\omega_n^4] + j\frac{\pi^2}{8} [(1 + \gamma)\omega_n - \gamma\omega_n^3]} \quad (3.28)$$

It can be observed that the output current is independent of load resistance (that is, Q) if the real term in the denominator is zero, that is,

$$1 - (\gamma + \gamma\psi + \psi)\omega_n^2 + \gamma\psi\omega_n^4 = 0 \quad (3.29)$$

In the following derivation of the expressions for normalized voltage and current ratings of different components, the base voltage and base current is taken as V_d and (V_d/Z_n) , respectively. The normalized rms current in inductor L_2 is derived as,

$$I_{L_2N} = \frac{I_{L_2,rms}}{V_d/Z_n} = \frac{\pi}{2\sqrt{2}} \frac{(1-\omega_n^2)Q + j\frac{8}{\pi^2}[(1+\psi)\omega_n - \psi\omega_n^3]}{[1-(\gamma+\gamma\psi+\psi)\omega_n^2 + \gamma\psi\omega_n^4] + j\frac{\pi^2}{8}Q[(1+\gamma)\omega_n - \gamma\omega_n^3]} \quad (3.30)$$

Applying the condition (3.29) in (3.30), an expression for phase angle (ϕ) between the v_{in} and i_{L2} as,

$$\phi = \tan^{-1} \left[\frac{-Q(1-\omega_n^2)}{\frac{8}{\pi^2}[(1+\psi)\omega_n - \psi\omega_n^3]} \right] \quad (3.31)$$

Therefore, if the condition of (3.29) is met and if $\omega_n=1$, then $\phi = 0$ for all values of Q . Substituting $\omega_n=1$ in (3.29),

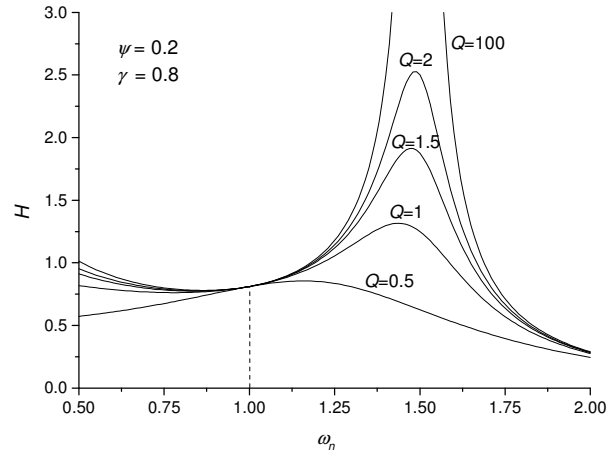
$$\gamma + \psi = 1 \quad (3.32)$$

Thus, LC-LC RC operating at $\omega_n=1$ and designed with the condition expressed in (3.32) exhibits constant output current and in-phase source voltage and current simultaneously at all loading conditions. In other words, LC-LC RC behaves as a RIC. The conditions $\omega_n = 1$ and $\gamma + \psi = 1$, derived as (2.34) in the previous chapter, are thus verified with an independent analysis.

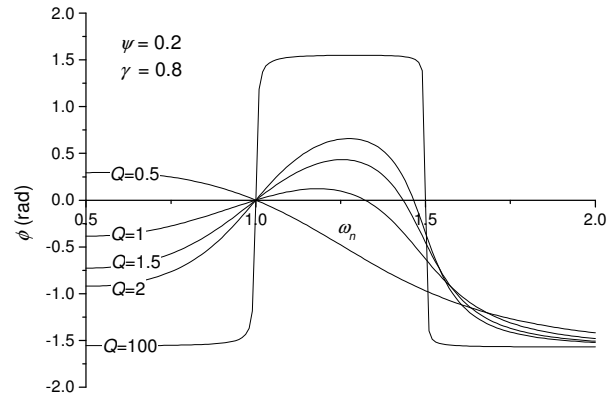
Plots of H are illustrated in Fig. 3.8(a) for different values of Q and for $\psi=0.2$, $\gamma=0.8$. A plot for $Q=100$ corresponding to nearly load-short-circuit condition is also included to demonstrate current-source behaviour of the converter. Plots of Fig. 3.8(b) show the variation of ϕ as a function of ω_n for different values of Q and for $\psi=0.2$, $\gamma=0.8$. H is seen to be load independent at $\omega_n=1$ for all values of Q . It can also be observed that $\phi = 0$ at $\omega_n=1$ for all values of Q .

The expressions for normalized rms current through inductor L_1 (I_{L_1N}), capacitor C_1 (I_{C_1N}), capacitor C_2 (I_{C_2N}) and the normalized rms voltage across inductor L_1 (V_{L_1N}), inductor L_2 (V_{L_2N}), capacitor C_1 (V_{C_1N}), capacitor C_2 (V_{C_2N}) are derived as follows:

$$I_{L_1N} = \frac{I_{L_1,rms}}{V_d/Z_n} = \frac{\pi}{2\sqrt{2}} \frac{Q + j\frac{8}{\pi^2}\psi\omega_n}{Den} \quad (3.33)$$



(a)



(b)

Fig. 3.8: Plots of (a) H and (b) ϕ in LC-LC RC as a function of ω_n for different values of Q and for $\psi=0.2, \gamma=0.8$.

$$I_{C_1N} = \frac{I_{C_1,rms}}{V_d/Z_n} = \frac{\pi}{2\sqrt{2}} \frac{-Q\omega_n^2 + j\frac{8}{\pi^2}(\omega_n - \psi\omega_n^3)}{Den} \quad (3.34)$$

$$I_{C_2N} = \frac{I_{C_2,rms}}{V_d/Z_n} = \frac{\pi}{2\sqrt{2}} \frac{j\frac{8}{\pi^2}\psi\omega_n}{Den} \quad (3.35)$$

$$V_{L_2N} = \frac{V_{L_2,rms}}{V_d} = \frac{2\sqrt{2}}{\pi} \frac{\gamma\psi\omega_n^4 - \gamma(1+\psi)\omega_n^2 + j\frac{\pi^2}{8}Q\gamma(\omega_n - \omega_n^3)}{Den} \quad (3.36)$$

$$V_{L_1N} = \frac{V_{L_1,rms}}{V_d} = \frac{2\sqrt{2}}{\pi} \frac{-\psi\omega_n^2 + j\frac{\pi^2}{8}Q\omega_n}{Den} \quad (3.37)$$

$$V_{C_1N} = \frac{V_{C_1,rms}}{V_d} = \frac{2\sqrt{2}}{\pi} \frac{1 - \psi\omega_n^2 + j\frac{\pi^2}{8}Q\omega_n}{Den} \quad (3.38)$$

$$V_{C_2N} = \frac{V_{C_2,rms}}{V_d} = \frac{2\sqrt{2}}{\pi} \frac{1}{Den} \quad (3.39)$$

wherein,

$$Den = \left[1 - (\gamma + \gamma\psi + \psi)\omega_n^2 + \gamma\psi\omega_n^4 \right] + j\frac{\pi^2}{8}Q[(1 + \gamma)\omega_n - \gamma\omega_n^3] \quad (3.40)$$

For operation of converter at $\omega_n=1$ and under the design condition expressed in (3.32), the magnitude of various currents and voltages given by the equations (3.30) and (3.33) to (3.39) can be simplified as,

$$|I_{L_2N}|_{\omega_n=1;(\gamma+\psi)=1} = \frac{16\sqrt{2}}{\pi^3} \frac{1}{Q} \quad (3.41)$$

$$|V_{L_2N}|_{\omega_n=1;(\gamma+\psi)=1} = \frac{16\sqrt{2}}{\pi^3} \frac{\gamma}{Q} \quad (3.42)$$

$$|I_{L_1N}|_{\omega_n=1;(\gamma+\psi)=1} = |V_{L_1N}|_{\omega_n=1;(\gamma+\psi)=1} = \frac{2\sqrt{2}}{\pi} \frac{\sqrt{Q^2 + \left(\frac{8}{\pi^2}\psi\right)^2}}{Q} \quad (3.43)$$

$$|I_{C_1N}|_{\omega_n=1;(\gamma+\psi)=1} = |V_{C_1N}|_{\omega_n=1;(\gamma+\psi)=1} = \frac{2\sqrt{2}}{\pi} \frac{\sqrt{Q^2 + \frac{8}{\pi^2}[(1-\psi)]^2}}{Q} \quad (3.44)$$

$$|I_{C_2N}|_{\omega_n=1;(\gamma+\psi)=1} = \frac{16\sqrt{2}}{\pi^3} \frac{\psi}{Q} \quad (3.45)$$

$$|V_{C_2N}|_{\omega_n=1;(\gamma+\psi)=1} = \frac{16\sqrt{2}}{\pi^3} \frac{1}{Q} \quad (3.46)$$

At no-load, $R_L = 0$ for a current-source power supply. Or in other words at no-load, $Q = \infty$. Note from (3.41) that under no-load condition inverter output current is zero. This shows that input current reduces proportionately from full-load to no-load and thus the converter maintains good part-load efficiency.

3.2.2 Design

If a general design rule is formulated to decide the values of ω_n , Q , γ and ψ then values of the reactive elements in LC-LC RC and their ratings can be calculated using the expressions derived in the previous section. $\omega_n = 1$ and $\gamma + \psi = 1$ are the necessary conditions for the operation of the converter as a current-source. Examining equations (3.41) through (3.46), it can easily be noticed that Q and ψ have a profound effect on the ratings and size of reactive components of the RIN, which can be optimized by minimizing (kVA/kW) rating of the RIN.

In application of LC-LC RC in high-voltage power supply C_2 can be a parasitic component of transformer. In such applications, therefore it is not considered as an external component to compute the (kVA/kW) rating. If LC-LC RC is intended to be used in applications where transformer winding capacitance is not significant, C_2 is a separate physical component and its rating needs to be accounted to compute the (kVA/kW) rating. Expressions for (kVA/kW), Q_{opt} , (kVA/kW) $_{opt}$ and the optimum value of ψ (ψ_{opt}) are derived in both the cases and summarized in Table 3.2. Figure 3.9 shows the plots of (kVA/kW) rating of as a function of Q for different values of ψ , in both the cases.

Table 3.2: The (kVA/kW) rating, optimum value of Q (Q_{opt}), the (kVA/kW) $_{opt}$ and the optimum value of ψ (ψ_{opt}) in LC-LC RC

	Without Considering the Rating of C_2	Considering the Rating of C_2
$\left. \frac{kVA}{kW} \right _{\omega_n=1; (\gamma+\psi)=1}$	$\frac{8}{\pi^2} \frac{1}{Q} \left[2 \left(1 - \frac{3}{2} \psi + \psi^2 \right) + \frac{\pi^4}{32} Q^2 \right]$	$\frac{8}{\pi^2} \frac{1}{Q} \left[2(1 - \psi + \psi^2) + \frac{\pi^4}{32} Q^2 \right]$
$Q_{opt} \big _{\omega_n=1; (\gamma+\psi)=1}$	$\frac{8}{\pi^2} \sqrt{1 - \frac{3}{2} \psi + \psi^2}$	$\frac{8}{\pi^2} \sqrt{1 - \psi + \psi^2}$
$\left(\frac{kVA}{kW} \right)_{opt} \big _{\omega_n=1; (\gamma+\psi)=1}$	$4 \sqrt{1 - \frac{3}{2} \psi + \psi^2}$	$4 \sqrt{1 - \psi + \psi^2}$
ψ_{opt}	0.75	0.50

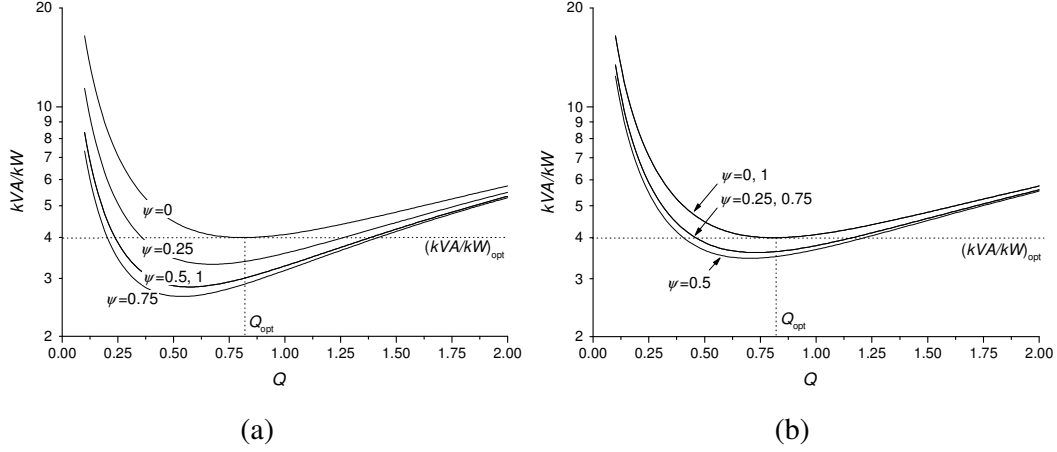
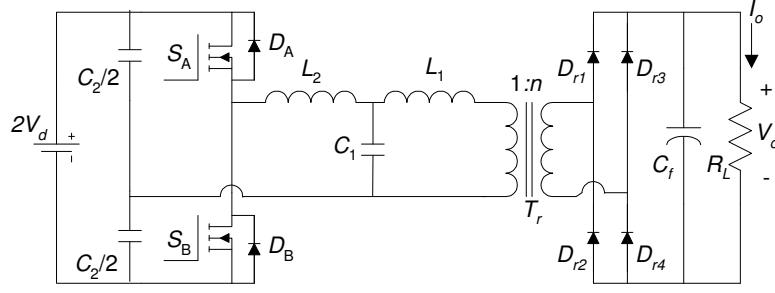


Fig. 3.9: kVA/kW rating of LC-LC RC as a function of Q for different values of ψ under the conditions $\omega_n = 1$ and $\gamma + \psi = 1$ (a) without considering the rating of C_2 and (b) considering the rating of C_2 .

Although an optimization method described above uniquely identifies ψ_{opt} and Q_{opt} , it would be practically difficult to ensure $\psi = \psi_{opt}$ by design, when C_2 is a parasitic component of transformer. This is because the prediction of C_2 is intricate and its actual value is subjected to significant variation due to tolerances in winding and spacing. Therefore issues in the design of LC-LC RC in the most practical case, the effect of manufacturing tolerance in C_2 , experimental results on a prototype converter and performance comparison of LC-LC RC with LCL-T RC when used in a high-voltage dc power supply are described in section 6.1 of Chapter 6.

3.3 Topology T₃

The circuit diagram of half-bridge T₃ RIC is shown in Fig. 3.10. The RIN is composed of inductors L_1 , L_2 and capacitors C_1 , C_2 . The resonant capacitor C_2 is equally split into two parts ($C_2/2$) and is re-located at the equivalent location in place of dc bus splitting capacitors of the half-bridge converter (C_A and C_B in Fig. 3.1 and Fig. 3.7), thereby reducing the number of capacitors in the circuit. Half-bridge converter is composed of MOSFETs S_A , S_B and their body-drain diodes D_A , D_B , respectively. At the output port of the RIN a transformer T_r of turns ratio $1:n$ matches the required output voltage, V_o , and current, I_o , to input dc voltage, $2V_d$. Diode


 Fig. 3.10: Circuit diagram of half-bridge T₃ RIC.

rectifier (D_{r1} through D_{r4}) and filter capacitor (C_f) convert high-frequency ac to output dc.

Resonant capacitor C_2 in T₃ RIC provides inherent dc blocking for the isolation transformer. This way, this fourth-order RIC topology overcomes one of the limitations of LCL-T RC.

3.3.1 Analysis

For the fundamental frequency ac analysis, the definition of R_{ac} , $V_{in,rms}$, ω_o , ω_n , Z_n and Q of the RIN is the same as given by (3.1) – (3.3). The values of inductors and capacitors of the RIN are related by (3.4) and (3.27), respectively.

As derived in Chapter 2 and given by (2.25), topology T₃ exhibits immittance conversion characteristics when operated at $\omega_n=1$ and if the values of reactive components satisfy the following condition:

$$\gamma = \frac{1+\psi}{\psi} \quad (3.47)$$

Under the condition of (3.47), the converter current gain is derived as,

$$H \Big|_{\gamma=\frac{1+\psi}{\psi}} = \frac{nI_o}{V_d/Z_n} = \frac{8}{\pi^2} \frac{j\psi\omega_n}{1 + (1+\psi)(\omega_n^4 - 2\omega_n^2) + j\frac{8}{\pi^2} \frac{(1+\psi)}{Q}(\omega_n - \omega_n^3)} \quad (3.48)$$

In the following derivation of the expressions for normalized voltage and current ratings of different components, the base voltage and base current is taken as V_d and (V_d/Z_n) , respectively. Expression for normalized rms current in inductor L_2 is derived as,

$$I_{L_2N} \Big|_{\gamma=\frac{1+\psi}{\psi}} = \frac{I_{L_2}}{V_d/Z_n} = \frac{2\sqrt{2}}{\pi} \frac{-\frac{8}{\pi^2} \frac{\psi}{Q} \omega_n^2 + j\psi(\omega_n - \omega_n^3)}{1 + (1+\psi)(\omega_n^4 - 2\omega_n^2) + j\frac{8}{\pi^2} \frac{(1+\psi)}{Q} (\omega_n - \omega_n^3)} \quad (3.49)$$

Figure 3.11 illustrates the plot of (3.48) and (3.49) for various values of Q and for $\psi=1$ and $\gamma=2$ demonstrating the immittance conversion characteristics of the converter. Figure 3.11(a) shows that H is independent of load (that is Q) at $\omega_n=1$. Plots of Fig. 3.11(b) show that the source current reduces progressively with reduction in R_L (that is, with increase in Q). Phase of (3.49), ϕ , as plotted in Fig. 3.11(c), is zero at $\omega_n=1$ for all values of Q . For the converter designed according to (3.47) and operating at $\omega_n=1$, (3.48) reduces to,

$$H \Big|_{\omega_n=1; \gamma=\frac{1+\psi}{\psi}} = \frac{8}{\pi^2} \quad (3.50)$$

Next, the expressions for normalized rms current through inductor L_I (I_{L_1N}), inductor L_2 (I_{L_2N}), capacitor C_1 (I_{C_1N}), capacitor C_2 (I_{C_2N}) and normalized rms voltages across these components (V_{L_1N} , V_{L_2N} , V_{C_1N} and V_{C_2N} , respectively) can be derived and further simplified under the condition of (3.47) and for operation at $\omega_n=1$. They are summarized as under:

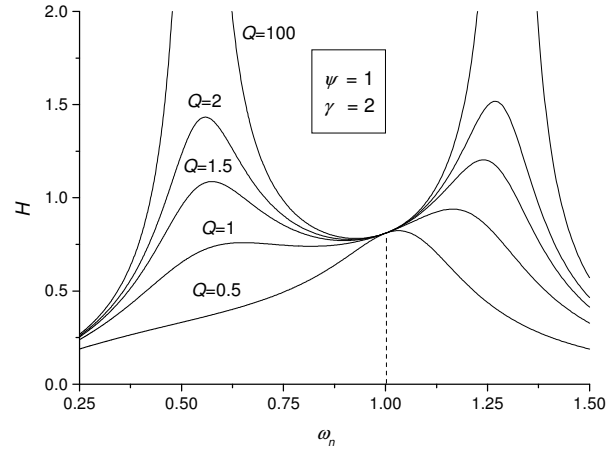
$$|I_{L_1N}|_{\omega_n=1; \gamma=\frac{1+\psi}{\psi}} = |V_{L_1N}|_{\omega_n=1; \gamma=\frac{1+\psi}{\psi}} = \frac{2\sqrt{2}}{\pi} \quad (3.51)$$

$$|I_{C_1N}|_{\omega_n=1; \gamma=\frac{1+\psi}{\psi}} = |V_{C_1N}|_{\omega_n=1; \gamma=\frac{1+\psi}{\psi}} = \frac{2\sqrt{2}}{\pi} \sqrt{1 + \left(\frac{8}{\pi^2} \frac{1}{Q} \right)^2} \quad (3.52)$$

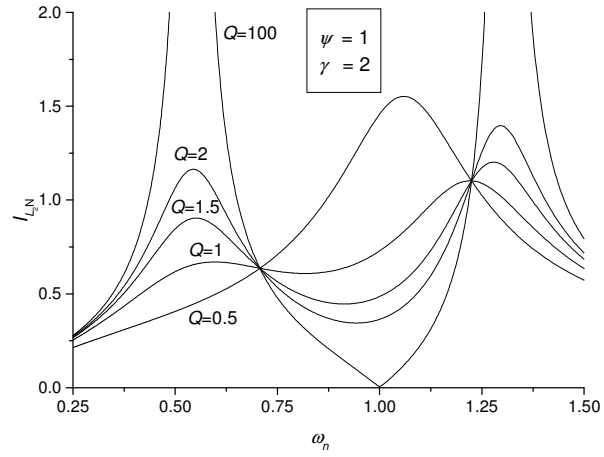
$$|I_{L_2N}|_{\omega_n=1; \gamma=\frac{1+\psi}{\psi}} = |I_{C_2N}|_{\omega_n=1; \gamma=\frac{1+\psi}{\psi}} = \frac{16\sqrt{2}}{\pi^3} \frac{1}{Q} \quad (3.53)$$

$$|V_{L_2N}|_{\omega_n=1; \gamma=\frac{1+\psi}{\psi}} = \frac{16\sqrt{2}}{\pi^3} \frac{1+\psi}{\psi Q} \quad (3.54)$$

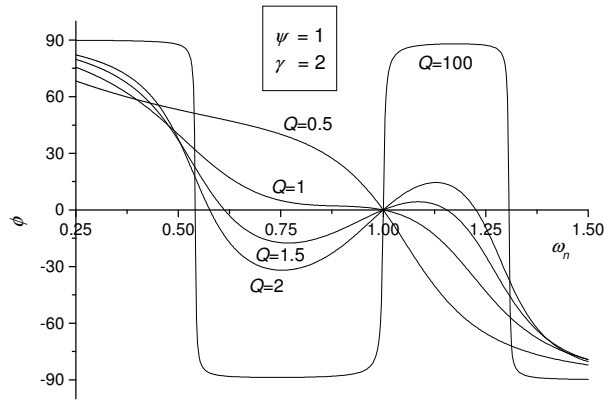
$$|V_{C_2N}|_{\omega_n=1; \gamma=\frac{1+\psi}{\psi}} = \frac{16\sqrt{2}}{\pi^3} \frac{1}{\psi Q} \quad (3.55)$$



(a)



(b)



(c)

 Fig. 3.11: Plots of (a) H , (b) I_{LIN} and (c) ϕ as a function of ω_n .

3.3.2 Design

If a general design rule is formulated to decide the values of ω_n , Q , γ and ψ then values of the reactive elements in T_3 RIN and their ratings can be calculated using the expressions derived in the previous section. $\omega_n = 1$ and $\gamma = (1 + \psi/\psi)$ are the necessary conditions for the operation of the converter as a current-source. Examining equations (3.51) through (3.57), it can easily be noticed that Q and ψ have a profound effect on the ratings and size of reactive components of the RIN and the size can be optimized by minimizing (kVA/kW) rating of the RIN, which is derived as,

$$\left. \frac{kVA}{kW} \right|_{\omega_n=1; \gamma=\frac{1+\psi}{\psi}} = \frac{\pi^2}{4} Q + \frac{16}{\pi^2} \left(\frac{1+\psi}{\psi} \right) \frac{1}{Q} \quad (3.56)$$

Figure 3.12 shows the plots of (3.56) as a function of Q . The plots show the existence of Q_{opt} . The expressions for Q_{opt} and $(kVA/kW)_{opt}$ are derived from (3.56) as,

$$Q_{opt} \Big|_{\omega_n=\gamma=1} = \frac{8}{\pi^2} \sqrt{\frac{1+\psi}{\psi}} \quad (3.57)$$

$$\left(\frac{kVA}{kW} \right)_{opt} \Big|_{\omega_n=\gamma=1} = 4 \sqrt{\frac{1+\psi}{\psi}} \quad (3.58)$$

The Q_{opt} and $(kVA/kW)_{opt}$ are thus function of ψ . Choice of ψ typically in the range of 1 – 2 is deemed to be suitable. A lower value of ψ will increase the value and size of L_2 and a higher value of ψ will increase the value and size of C_2 .

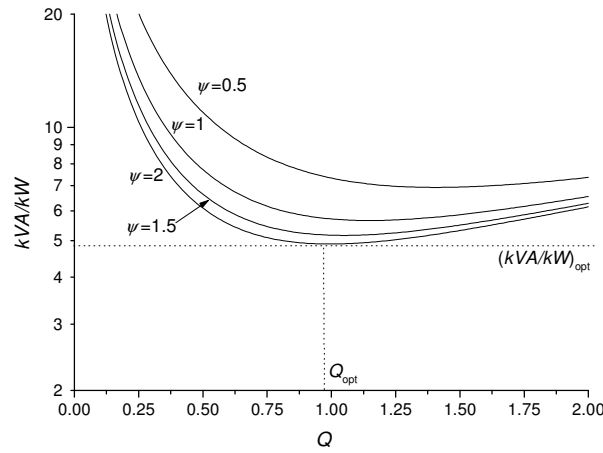


Fig. 3.12: kVA/kW rating of T_3 RIC as a function of Q .

For the design of LCL-T RC, typical design inputs are: input dc voltage ($2V_d$ for half-bridge and V_d for full-bridge circuit), output current (I_o), maximum load resistance ($R_{L,\max}$) corresponding to full-load condition and switching frequency (f_s). Choosing full-load value of Q equal to Q_{opt} , the expression for n , L_1 and C_1 are derived in terms of converter's terminal parameters as follows:

$$n = \frac{I_o R_{L,\max}}{V_d} \sqrt{\frac{1+\psi}{\psi}} \quad (3.59)$$

$$L_1 = \frac{4}{\pi^3} \frac{V_d^2}{I_o^2 R_{L,\max} f_s} \sqrt{\frac{1+\psi}{\psi}} \quad (3.60)$$

$$C_1 = \frac{\pi}{16} \frac{I_o^2 R_{L,\max}}{V_d^2 f_s} \sqrt{\frac{1+\psi}{\psi}} \quad (3.61)$$

With chosen values of ψ , the values of L_2 and C_2 can be calculated. Voltage and current rating of various reactive elements then can be calculated using (3.51) to (3.55).

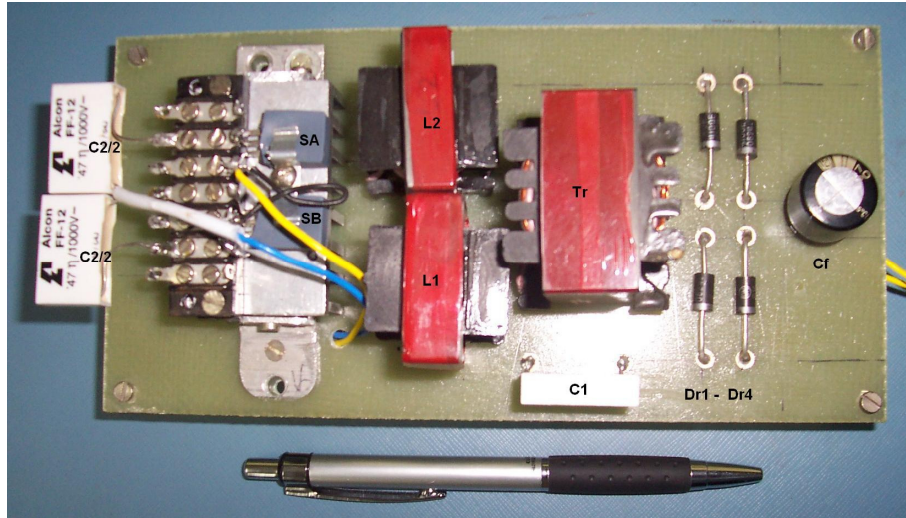
3.3.3 Experimental Results

A half-bridge prototype is designed and built to experimentally validate the current source property of topology T₃. The converter has the following specifications: input dc supply voltage ($2V_d$) = 220 V, I_o = 1 A, $R_{L,\max}$ = 250 Ω , f_s = 105 kHz. The converter is designed with $\psi=2$. The following design values are calculated: $Q_{opt}=0.99$, $n=2.784$, $L_1=48.55$ μ H, $L_2=72.83$ μ H, $C_1=47$ nF, $C_2=94$ nF. IRF 840 MOSFETs are used as the switches S_A , S_B and fast-recovery diodes MUR 4100 are used as D_{r1} through D_{r4} . A 47 μ F capacitor forms the output filter capacitor C_f . Table 3.3 summarizes the specifications, designed component values, used components as well as calculated and measured component ratings. Figure 3.13 shows the photograph of experimental prototype converter, which is operated in open-loop.

Experimental waveforms of voltage across switch S_B [trace (1)] and i_{L2} [trace (2)] at full-load (upper pair) and at no-load (lower pair) are shown in Fig. 3.14(a). Figure 3.14(b) shows the waveforms of voltage across switch S_B [trace (1)] and current through it [trace (2)] under full-load (upper pair) and no-load condition (lower

Table 3.3: Specifications, component values and ratings of reactive components in prototype T₃ RIC

Parameter	Value	
<i>Specifications</i>		
I_o (A)	1	
$R_{L,max}$ (Ω)	250	
V_d (V)	220	
f_s (kHz)	105	
<i>Component values</i>		
	Designed	Used in prototype
L_1 (μ H)	48.55	48.4
L_2 (μ H)	72.83	72.3
C_1 (nF)	47	47
C_2 (nF)	94	94
n	2.784	2.77 (9:25 turns)
f_s (kHz)	105	105
<i>Component ratings</i>		
	Calculated	Measured
I_{L_1} (A, rms)	3.08	3.06
I_{L_2} (A, rms)	2.49	2.98
I_{C_1} (A, rms)	3.96	4.25
V_{C_1} (V, rms)	127.71	136.2

Fig. 3.13: Photograph of the experimental prototype of T₃ RIC.

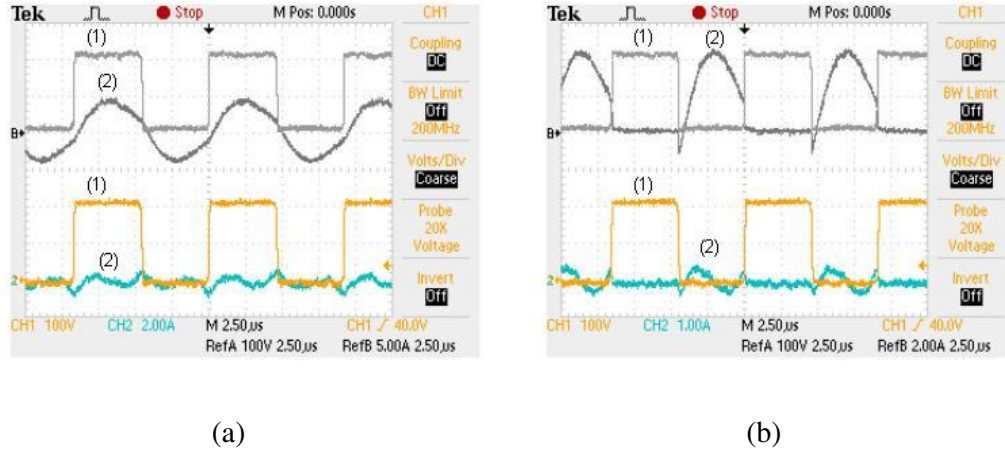


Fig. 3.14: (a) Experimental waveforms of voltage across switch S_B ([trace (1)] and i_{L2} [trace (2)] at full-load (upper pair, 100 V/div, 5 A/div) and at no-load (lower pair, 100 V/div, 2 A/div). X-scale: 2.5 μs/div. (b) Experimental waveforms of voltage across switch S_B ([trace (1)] and current through it [trace (2)] at full-load (upper pair, 100 V/div, 2 A/div) and at no-load (lower pair, 100 V/div, 1 A/div). X-scale: 2.5 μs/div.

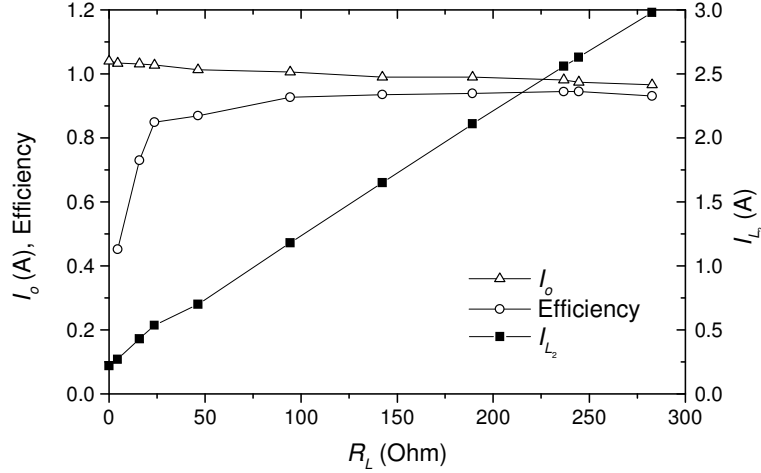


Fig. 3.15: Open-loop output characteristic and plots of I_{L2} as well as efficiency of prototype T_3 RIC.

pair). It can be noticed that the switching transitions are nearly lossless. Moreover, peak and rms switch current reduces with load, thereby reducing the conduction loss. Open-loop output characteristic, rms value of i_{L2} and efficiency of the experimental

prototype is obtained by varying the load resistance as shown in Fig. 3.15. Although output current is theoretically constant irrespective of variation in the load resistance, practically it droops slightly with load due to increase in conduction losses in the switches and RIN. The measured rms value of i_{L2} is also seen to reduce with load as predicted in the analysis, thereby resulting in high efficiency over a wide range of operation.

3.4 A Higher Order T-Type RIC Topology

RIC topologies with maximum of four reactive elements have been explored in Chapter 2 by suitably constraining the number of reactive elements in various branches of various topological structures that exhibit immittance conversion characteristics. As mentioned therein, the constraint on the number of reactive elements in a branch can be relaxed to further explore the RIC topologies with higher reactive elements. As an illustration, a fifth-order RIC topology derived from topological structure N_5 , named here as LCLCL-T RC, is analyzed further in this section. It provides inherent dc blocking for the transformer. Moreover, resonant inductors and transformer can be integrated in a single magnetic component, thereby reducing number of discrete magnetic components and overall size and weight of the converter.

The circuit diagram of proposed half-bridge LCLCL-T RC with discrete reactive components in the RIN is shown in Fig. 3.16(a). The LCLCL-T RIN is composed of two series inductors (L_1 , L_2) one shunt inductor (L_3) and two series capacitors (C_1 , C_2) arranged in the form of a T-network. The half-bridge converter is composed of MOSFET switches S_A , S_B , capacitors C_A , C_B and drives the input port of the RIN with high-frequency symmetrical square-wave voltage waveform, v_{in} , of amplitude $\pm V_d$. At the output port of RIN an isolation transformer T_r of turns ratio $1:n$ matches the required output voltage, V_o , and current, I_o , to available dc input, $2V_d$. A diode rectifier (D_{r1} through D_{r4}) and filter capacitor (C_f) convert high-frequency ac to output dc. Series capacitors of RIN provide inherent dc blocking for the isolation transformer.

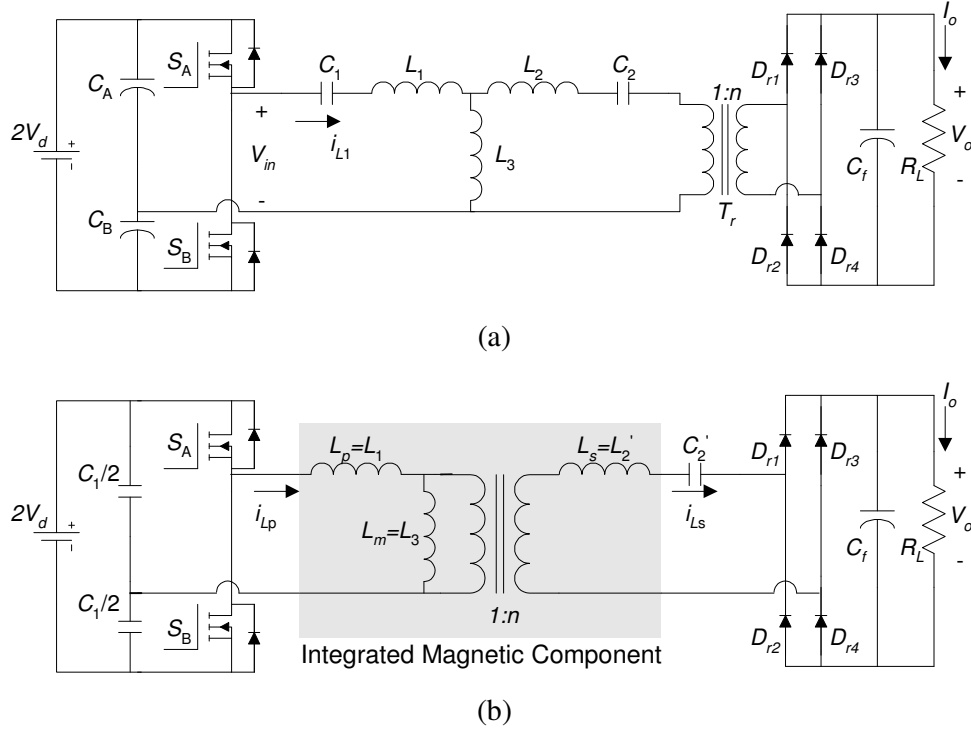


Fig. 3.16: Circuit diagram of proposed half-bridge LCLCL-T RC with (a) discrete reactive components and (b) IMC.

Discrete components in a RN increase size, weight and cost of a RC. Therefore, integration of passive components has been an area of research in the past. Techniques for integration of resonant inductor as the transformer leakage inductance, integration of resonant inductor and capacitor, integration of resonant inductor, capacitor and transformer are reported in the literature [171]-[178]. Proposed LCLCL-T RC is suitable for such integration. In the simplest case, three inductors (L_1 , L_2 and L_3) and transformer T_r can be integrated in a single magnetic component. Circuit diagram of LCLCL-T RC with integrated magnetic component (IMC) is shown in Fig. 3.16(b) wherein, primary leakage inductance (L_p) is used as the resonant inductor L_1 , secondary leakage inductance (L_s) is used as the resonant inductor L_2 reflected on the secondary side $L_2' (= n^2 L_2)$ and primary-side magnetizing inductance L_m is used as the resonant inductor L_3 . Usually, the leakage inductance of transformer is much smaller than the magnetizing inductance. However, it is possible to design a transformer with controlled leakage and magnetizing inductance. For instance, design

of such transformer using standard E-I cores is described in [109]. Resonant capacitor C_2 is placed in series with the secondary winding and is given by $C_2' = \left(\frac{C_2}{n^2}\right)$. Resonant capacitor C_1 is equally split into two parts ($C_1/2$) and is re-located at an equivalent location in place of capacitors C_A and C_B , thereby reducing the number of capacitors in the circuit.

3.4.1 Analysis

For the fundamental frequency ac analysis, the definition of R_{ac} , $V_{in,rms}$, ω_o , ω_n , Z_n and Q of the RIN is the same as given by (3.1) – (3.3). Various resonant inductors and capacitors are defined in (2.22) and (2.23) as,

$$L_2 = \gamma L_1, L_3 = \alpha L_1 \text{ and } C_2 = \psi C_1 \quad (3.62)$$

The current gain of LCLCL-T RC can be derived as,

$$H = \frac{nI_o}{V_d/Z_n} = \frac{8}{\pi^2} \left(\frac{-j\psi\alpha\omega_n^3}{B_1 + jB_2} \right) \quad (3.63)$$

wherein

$$B_1 = 1 - (1 + \gamma\psi + \alpha + \psi\alpha)\omega_n^2 + (\gamma\psi + \psi\alpha + \alpha\psi\gamma)\omega_n^4 \quad (3.64)$$

$$B_2 = \frac{8}{\pi^2} \frac{\psi}{Q} [\omega_n - (1 + \alpha)\omega_n^3] \quad (3.65)$$

It can be observed from (3.63) to (3.65) that the output current can be independent of load resistance (that is, Q) if $B_2=0$, that is, if the converter is operated at,

$$\omega_n = \omega_{ni} = \frac{1}{\sqrt{1 + \alpha}} \quad (3.66)$$

ω_{ni} being defined as the normalized switching frequency where H is independent of Q . In the following derivation of the expressions for normalized voltage and current ratings of different components, base voltage and base current is taken as V_d and V_d/Z_n , respectively. An expression for normalized rms current in inductor L_1 is derived as,

$$I_{L_1N} = \frac{I_{L_1,rms}}{V_d/Z_n} = \frac{2\sqrt{2}}{\pi} \frac{\left(-\frac{8}{\pi^2} \frac{\psi}{Q} \omega_n^2 \right) + j[\omega_n - \psi(\alpha + \gamma)\omega_n^3]}{B_1 + jB_2} \quad (3.67)$$

For operation of the converter at $\omega_n = \omega_{ni}$, an expression for phase angle (ϕ) between v_{in} and i_{L1} can be derived as,

$$\phi|_{\omega_n=\omega_{ni}} = \tan^{-1} \left[-\frac{\pi^2}{8} \frac{Q}{\psi} \frac{(1+\alpha) - \psi(\alpha+\gamma)}{(1+\alpha)\sqrt{1+\alpha}} \right] \quad (3.68)$$

It can be noticed from (3.68) that ϕ will always be equal to zero when operated at $\omega_n = \omega_{ni}$ and under all loading conditions if,

$$\psi = \psi_{crit} = \frac{1+\alpha}{\alpha+\gamma} \quad (3.69)$$

Although (3.69) gives the condition for zero phase angle that would result in lowest conduction loss for operation at $\omega_n = \omega_{ni}$, in practice the current is required to slightly lag the voltage so that the anti-parallel diode conducts prior to the switch giving zero-voltage turn-on. The other advantages of a RC operating in lagging power-factor mode are very well known. The required phase lag can be achieved by practically choosing ψ to be slightly less (typically 0.95 – 1 times) than the value given by (3.69).

For the operation of the converter at $\omega_n = \omega_{ni}$ and with $\psi = \psi_{crit}$, the current gain given by (3.63) simplifies as,

$$H|_{\omega_n=\omega_{ni}; \psi=\psi_{crit}} = \frac{8}{\pi^2} \frac{\sqrt{1+\alpha}}{\alpha} \quad (3.70)$$

The plots of H are illustrated in Fig. 3.17(a) for different values of Q and for $\alpha=\psi=\gamma=1$. A plot for $Q=100$ corresponding to nearly load-short-circuit condition is also included to demonstrate current-source behaviour of the converter. H is seen to be load independent at $\omega_n = \omega_{ni}$ for all values of Q . Plots of Fig. 3.17(b) show the variation of ϕ as a function of ω_n . It can be observed that $\phi=0$ at $\omega_n = \omega_{ni}$ for all values of Q .

Next, the expressions for normalized rms current through inductor L_1 (I_{L1N}), inductor L_2 (I_{L2N}), inductor L_3 (I_{L3N}), capacitor C_1 (I_{C1N}), capacitor C_2 (I_{C2N}) and normalized rms voltages across these components (V_{L1N} , V_{L2N} , V_{L3N} , V_{C1N} and V_{C2N} , respectively) are derived in the following general forms:

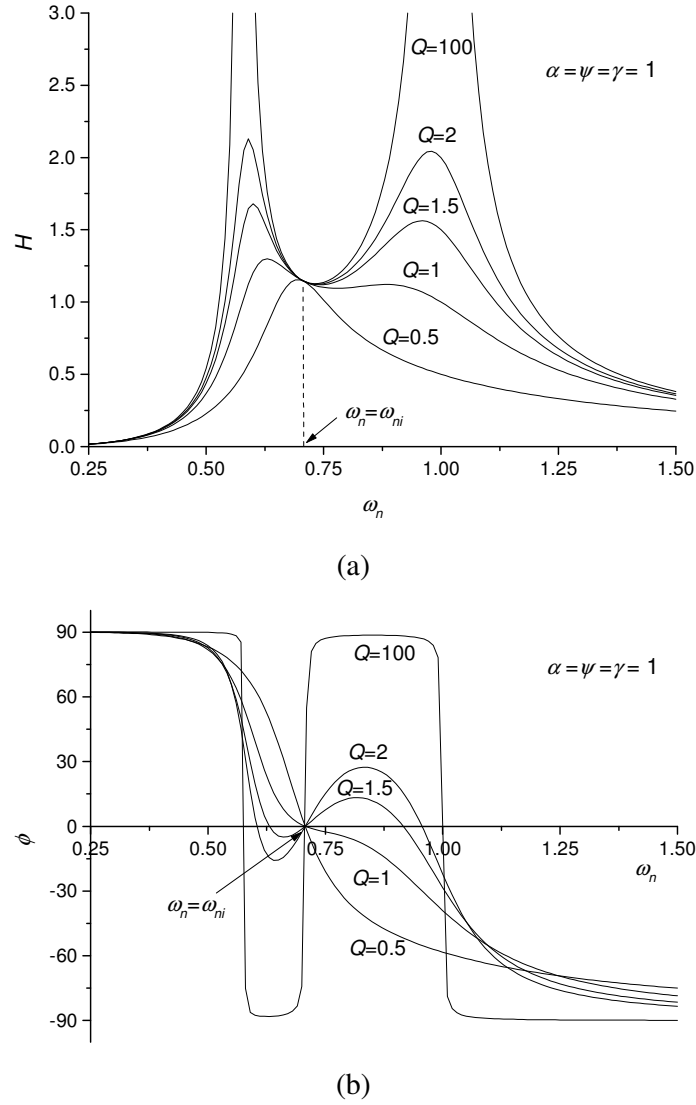


Fig. 3.17: Plots of (a) H and (b) ϕ in LCLCL-T RC as a function of ω_n for different values of Q and for $\alpha=\psi=\gamma=1$.

$$\begin{aligned}
 I_{xN} \left(\equiv \frac{I_{x,rms}}{\frac{V_d}{Z_n}} \right) &= \frac{2\sqrt{2}}{\pi} \frac{A_1 + jA_2}{B_1 + jB_2} \\
 V_{xN} \left(\equiv \frac{V_{x,rms}}{V_d} \right) &= \frac{2\sqrt{2}}{\pi} \frac{A_1 + jA_2}{B_1 + jB_2}
 \end{aligned} \tag{3.71}$$

wherein x is the respective component. Coefficients B_1 and B_2 are given in (3.64) and (3.65), respectively and coefficients A_1 and A_2 are listed in Table 3.4.

Table 3.4: Coefficients A_1 and A_2 in the general form (3.71) of the expressions for various normalized currents and voltages.

	A_1	A_2
$I_{L_1N} \equiv \frac{I_{L_1,rms}}{\frac{V_d}{Z_n}} \left(= I_{C_1N} \equiv \frac{I_{C_1,rms}}{\frac{V_d}{Z_n}} \right)$	$-\frac{8}{\pi^2} \frac{\psi}{Q} \omega_n^2$	$\omega_n - \psi(\alpha + \gamma)\omega_n^3$
$I_{L_2N} \equiv \frac{I_{L_2,rms}}{\frac{V_d}{Z_n}} \left(= I_{C_2N} \equiv \frac{I_{C_2,rms}}{\frac{V_d}{Z_n}} \right)$	0	$-\psi\alpha\omega_n^3$
$I_{L_3N} \equiv \frac{I_{L_3,rms}}{\frac{V_d}{Z_n}}$	$-\frac{8}{\pi^2} \frac{\psi}{Q} \omega_n^2$	$\omega_n - \psi\gamma\omega_n^3$
$V_{L_1N} \equiv \frac{V_{L_1,rms}}{V_d}$	$\psi(\alpha + \gamma)\omega_n^4 - \omega_n^2$	$-\frac{8}{\pi^2} \frac{\psi}{Q} \omega_n^3$
$V_{L_2N} \equiv \frac{V_{L_2,rms}}{V_d}$	$\alpha\psi\gamma\omega_n^4$	0
$V_{L_3N} \equiv \frac{V_{L_3,rms}}{V_d}$	$\alpha\psi\gamma\omega_n^4 - \alpha\omega_n^2$	$-\frac{8}{\pi^2} \frac{\psi\alpha}{Q} \omega_n^3$
$V_{C_1N} \equiv \frac{V_{C_1,rms}}{V_d}$	$1 - \psi(\alpha + \gamma)\omega_n^2$	$\frac{8}{\pi^2} \frac{\psi}{Q} \omega_n$
$V_{C_2N} \equiv \frac{V_{C_2,rms}}{V_d}$	$\alpha\omega_n^2$	0

For operation of the converter at $\omega_n = \omega_{ni}$ and with $\psi = \psi_{crit}$, expressions for the magnitude of various normalized currents and voltages [given by the general form of (3.71), wherein the coefficients are given in (3.64), (3.65) and Table 3.4)] are simplified as follows:

$$|I_{L_1N}|_{\omega_n=\omega_{ni};\psi=\psi_{crit}} = \frac{16\sqrt{2}}{\pi^3} \frac{1}{Q} \frac{1+\alpha}{\alpha^2} \quad (3.72)$$

$$|I_{L_2N}|_{\omega_n=\omega_{ni};\psi=\psi_{crit}} = \frac{2\sqrt{2}}{\pi} \frac{\sqrt{1+\alpha}}{\alpha} \quad (3.73)$$

$$|I_{L_3N}|_{\omega_n=\omega_{ni};\psi=\psi_{crit}} = \frac{2\sqrt{2}}{\pi} \frac{\sqrt{1+\alpha}}{\alpha} \sqrt{\left(\frac{8}{\pi^2} \frac{1}{Q} \frac{\sqrt{1+\alpha}}{\alpha}\right)^2 + 1} \quad (3.74)$$

$$|V_{L_1N}|_{\omega_n=\omega_{ni};\psi=\psi_{crit}} = \frac{16\sqrt{2}}{\pi^3} \frac{1}{Q} \frac{\sqrt{1+\alpha}}{\alpha^2} \quad (3.75)$$

$$|V_{L_2N}|_{\omega_n=\omega_{ni};\psi=\psi_{crit}} = \frac{2\sqrt{2}}{\pi} \frac{\gamma}{\alpha} \quad (3.76)$$

$$\left|V_{L_3N}\right|_{\omega_n=\omega_{ni};\psi=\psi_{crit}} = \frac{2\sqrt{2}}{\pi} \sqrt{\left(\frac{8}{\pi^2} \frac{1}{Q} \frac{\sqrt{1+\alpha}}{\alpha}\right)^2 + 1} \quad (3.77)$$

$$\left|V_{C_1N}\right|_{\omega_n=\omega_{ni};\psi=\psi_{crit}} = \frac{16\sqrt{2}}{\pi^3} \frac{1}{Q} \frac{(1+\alpha)\sqrt{1+\alpha}}{\alpha^2} \quad (3.78)$$

$$\left|V_{C_2N}\right|_{\omega_n=\omega_{ni};\psi=\psi_{crit}} = \frac{2\sqrt{2}}{\pi} \frac{\alpha+\gamma}{\alpha} \quad (3.79)$$

At no-load, R_L is zero for a current-source power supply. Or in other words at no-load, $Q = \infty$. Note from (3.72) that I_{L_1N} , being inversely proportional to Q , reduces from full-load to no-load. Therefore switch conduction losses also reduce proportionally with load and the converter maintains good part-load efficiency.

3.4.2 Design

$\omega_n = \omega_{ni}$ and $\psi = \psi_{crit}$ are the necessary conditions for converter's operation as a current-source. Examining equations (3.72) through (3.79), it can easily be noticed that Q , γ and α have the profound effect on the ratings of reactive components of the resonant network. Taking (kVA/kW) rating of resonant network as an index, the physical size of resonant network can be optimized. The (kVA/kW) rating is derived as,

$$\left.\frac{kVA}{kW}\right|_{\omega_n=\omega_{ni};\psi=\psi_{crit}} = \frac{8}{\pi^2} \left(\frac{2}{Q}\right) \frac{(1+\alpha)\sqrt{1+\alpha}}{\alpha^2} + \frac{\pi^2}{8} (2Q) \frac{\alpha+\gamma}{\sqrt{1+\alpha}} \quad (3.80)$$

The first term in (3.80) is independent of γ and the second term is linearly proportional to γ . Therefore, the overall (kVA/kW) rating of resonant network is proportional to γ . Figure 3.18 illustrates the plots of (3.80) as a function of Q for different values of α and γ . The plots show the existence of Q_{opt} , which can be derived from (3.80) as,

$$Q_{opt}\big|_{\omega_n=\omega_{ni};\psi=\psi_{crit}} = \frac{8}{\pi^2} \frac{1+\alpha}{\alpha\sqrt{\alpha+\gamma}} \quad (3.81)$$

The minimum value of (kVA/kW) rating is observed to be more for lower values of α and higher values of γ . This observation suggests that a higher α and lower γ should be preferred in the design. Theoretically, numerous combinations of α , γ and

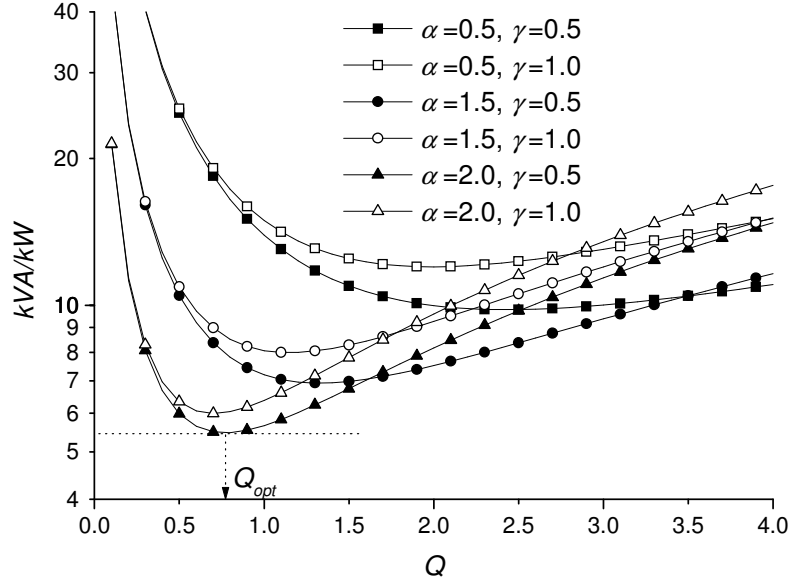


Fig. 3.18: kVA/kW rating of LCLCL-T RC as a function of Q for different values of α and γ and respective $\psi = \psi_{crit}$ showing the existence of Q_{opt} .

corresponding ψ are possible. In practice, the choice is limited by feasibility in realizing these design values due to practical limitations.

For the design of LCLCL-T RC, typical design inputs are: input dc voltage ($2V_d$), output current (I_o), maximum load resistance ($R_{L,max}$) corresponding to full-load condition and switching frequency (f_s). For the operation of the converter at $\omega_n = \omega_{ni}$ and with $\psi = \psi_{crit}$, the following design equations are derived:

$$n = \frac{I_o R_{L,max}}{V_d} \sqrt{\frac{1+\alpha}{\alpha+\gamma}} \quad (3.82)$$

$$L_1 = \frac{4}{\pi^3} \sqrt{\frac{\alpha+\gamma}{1+\alpha}} \frac{V_d^2}{I_o^2 R_{L,max} f_s \alpha} \quad (3.83)$$

$$C_1 = \frac{\pi}{16} \frac{I_o^2 R_{L,max} \alpha}{V_d^2 f_s \sqrt{(\alpha+\gamma)(1+\alpha)}} \quad (3.84)$$

With chosen values of α , γ and the condition $\psi = \psi_{crit}$, the value of L_2 , C_2 and L_3 can be calculated. Voltage and current rating of various reactive elements then can be calculated using (3.72) through (3.79).

3.4.3 Experimental Results

A prototype half-bridge LCLCL-T RC is designed and built to experimentally validate its current source property. The converter has the following specifications: input dc supply voltage ($2V_d$) = 100 V, $I_o = 1$ A, $R_{L,max}$ (full load) = 250 Ω , $f_s = 105$ kHz. The converter is designed with $\alpha = \gamma = 1$. Using equations (3.66), (3.69) and (3.81) - (3.84), the following designed values of various components are obtained: $\omega_n = \omega_i = 0.707$, $\psi = 1$, $Q_{opt} = 1.146$, $n = 5$, $L_1 = L_2 = L_3 = 12.28$ μ H, $C_1 = C_2 = 93.5$ nF. In the prototype, resonant inductors and transformer are integrated into a single magnetic component using an EE-type core wherein primary and secondary windings are placed on two side limbs and the central limb is used to provide the path for leakage flux. Values of leakage and magnetizing inductances ($L_p = L_1$, $L_s = L_2' (= n^2 L_2)$ and $L_m = L_3$, respectively) of this coupled magnetic structure can be designed and controlled by properly choosing the number of turns and air gaps on the side limbs and the central limb. Approximate design formulae are reported in [109]. However, these formulae do not account for the flux paths other than the intended core path. Therefore, the central limb air gap needs to be adjusted practically to achieve desired coefficient of coupling. Since the motive in the present work is only to illustrate feasibility of the use of IMC in the proposed converter, efforts are not put in to refine the expressions of [109]. In the present prototype, an IMC was realized using EE 42.21.20 core with 10 primary turns and 50 secondary turns placed on two side limbs. Air gap is 0.5 mm on side limbs and 2 mm on the central limb. Measured coefficient of coupling is 0.51 resulting in $L_p = L_1 = 11.45$ μ H, $L_s = L_2' (= n^2 L_2) = 299.5$ μ H and $L_m = L_3 = 12.07$ μ H. Two 47 nF capacitors constitute C_1 and four 15 nF capacitors are connected in series to closely realize the required value of resonant capacitor, $C_2' = (C_2/n^2) = 3.74$ nF, connected in series with the secondary winding [see Fig. 3.16(b)]. Since the actual values of resonant inductors differ slightly than the designed values, the switching frequency of the prototype was adjusted to 107 kHz. IRF 640 MOSFETs are used as the switches S_A , S_B and fast-recovery diodes MUR 4100 are used as D_{r1} through D_{r4} . A 47 μ F capacitor forms the output filter capacitor C_f . Table 3.5 summarizes the specifications, designed component values and used

components in the prototype. Figure 3.19 shows a photograph of the experimental prototype, which is operated in open-loop.

Experimental waveforms of voltage across switch S_B [trace (1)], i_{L_p} [trace (2)], i_{L_s} [trace (3)] and i_o [trace (4)] at full-load and at 5 % of the full-load are shown in Fig. 3.20(a) and (b), respectively. The waveform of i_{L_p} , besides being nearly in phase with the voltage across switch S_B , is also seen to reduce with load as predicted in the analysis. Similarly, i_{L_s} and i_o are observed to be nearly constant under the extreme loading conditions, thereby confirming the current-source behaviour of the converter.

Table 3.5: Specifications and component values in prototype LCLCL-T RC.

Parameter	Value	
<i>Specifications</i>		
I_o (A)	1	
$R_{L,max}$ (Ω)	250	
V_d (V)	100	
f_s (kHz)	105	
<i>Component values</i>		
	Designed	Used in prototype
L_1 (μ H)	12.28	11.45
L_2 (μ H)	12.28	L_2' =299.5
L_3 (μ H)	12.28	12.07
C_1 (nF)	93.5	94
C_2 (nF)	93.5	C_2' =3.75
n	2.784	5
f_s (kHz)	105	107

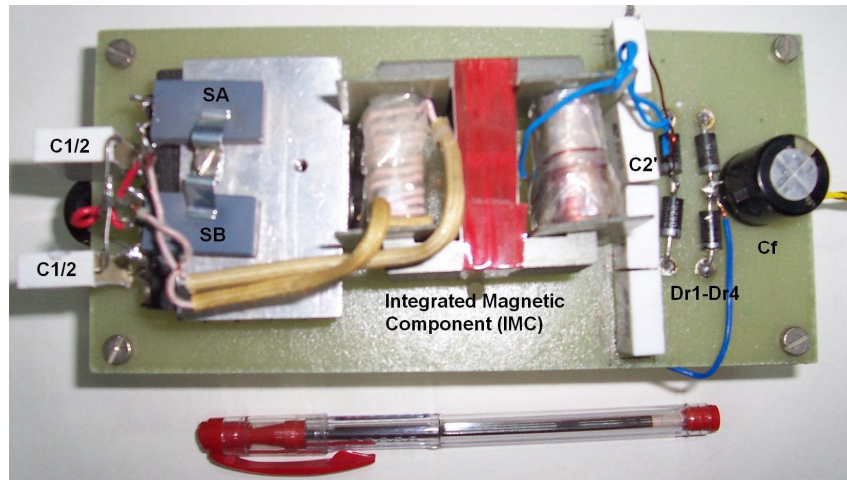


Fig. 3.19: Photograph of the experimental prototype of LCLCL-T RC.

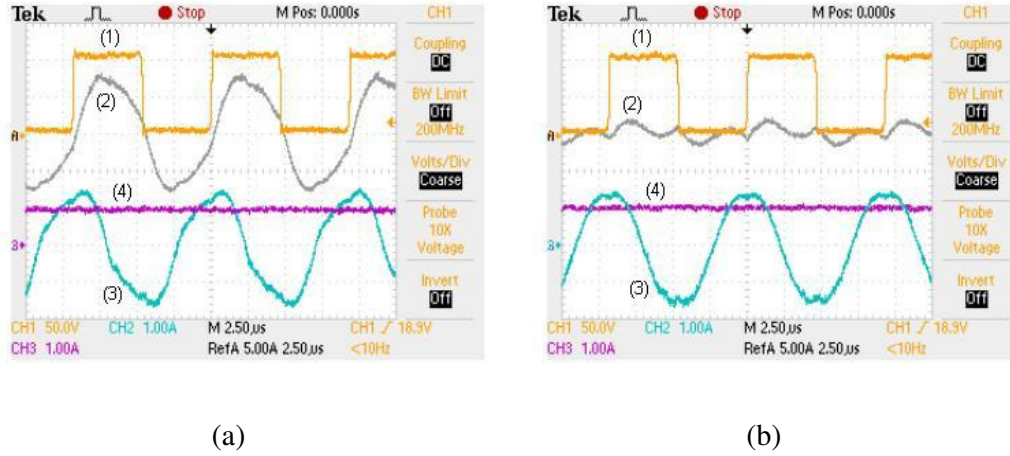


Fig. 3.20: Experimental waveforms of voltage across switch S_B [trace (1), 50 V/div], i_{Lp} [trace (2), 5 A/div], i_{Ls} [trace (3), 1 A/div] and i_o [trace (4), 1 A/div]. (a) At full-load. (b) At 5 % of full-load. X-scale: 2.5 μs/div.

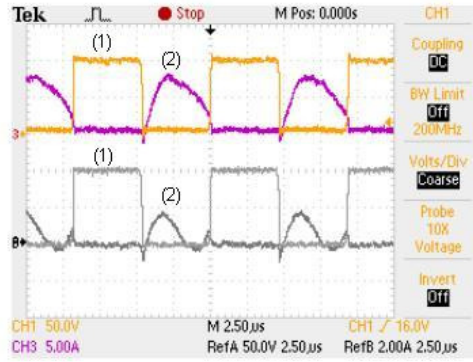


Fig. 3.21: Experimental waveforms of voltage across switch S_B [trace (1)] and current through it [trace (2)]. Upper pair of waveforms: full-load condition, 50 V/div and 5 A/div, respectively. Lower pair of waveforms: At 10 % of the full-load, 50 V/div and 2 A/div, respectively. X-scale: 2.5 μs/div..

Figure 3.21 shows the waveforms of voltage across switch S_B [trace (1)] and current through it [trace (2)] under full-load (upper pair of waveforms) and 10 % of the full-load condition (lower pair of waveforms). It can be noticed that the switching transitions are nearly lossless. Moreover, peak and rms switch current reduces with load, thereby reducing the conduction loss.

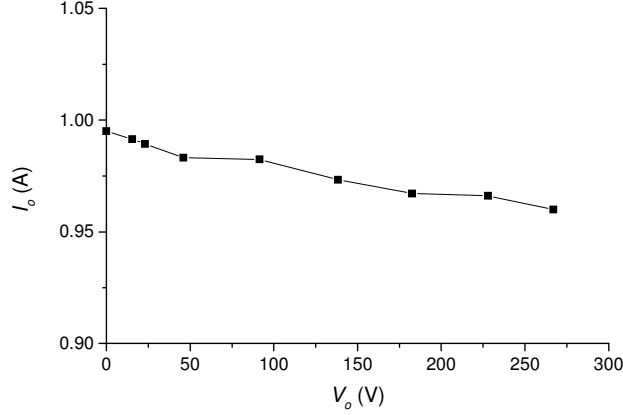


Fig. 3.22: Experimental output characteristic of LCLCL-T RC.

Open-loop steady-state output characteristic of the experimental prototype, obtained by varying R_L , is shown in Fig. 3.22. Although output current is theoretically constant irrespective of variation in the load resistance, practically it droops slightly with load due to increase in conduction losses in the switches and the components of RIN. Figure 3.23 shows the waveforms of V_o [trace (1)], rectified output current [trace (2)] and I_o [trace (3)] under transient condition with step change in R_L from $140\ \Omega$ to $230\ \Omega$ at instant t_1 and vice versa at instant t_2 . It is interesting to notice that the rectified output current of the converter is constant under the transient condition, demonstrating the CC behaviour. The waveform of I_o shows transient undershoot at instant t_1 and overshoot at instant t_2 due to additional current absorbed or delivered by C_f to maintain the charge balance with varying V_o due to changing R_L . However, being an inherent current source, the proposed converter lends itself for direct paralleling without any complex control for equal current sharing. If the paralleled modules are phase-shifted, the peak-peak ripple in the rectified output current is reduced and the ripple frequency is increased, as discussed further in section 3.5.2. This reduces the required value of C_f . With sufficient number of phase-shifted modules operating in parallel, it is possible to eliminate C_f . Thus it is possible to minimize the transient variation in output dc current. It can be noted that i_{Lp} (see Fig. 3.20) and switch current (see Fig. 3.21) reduces with load. Figure 3.24 shows the measured rms value of i_{Lp} (open circles). In close agreement with the theoretical

prediction (dashed curve), the current is observed to reduce with the load power, therefore a high converter efficiency (solid circles) is maintained over a wide range of output power variation. Full-load conversion efficiency of the prototype is measured to be 0.933. Out of total 18 W power loss in the prototype operating at 253 W, a major portion (9.22 W) is estimated to occur in the MOSFETs. Conduction loss in D_{r1} through D_{r4} is estimated to be 3 W. The rest of the losses (5.78 W) can be attributed largely to the core and winding loss in IMC.

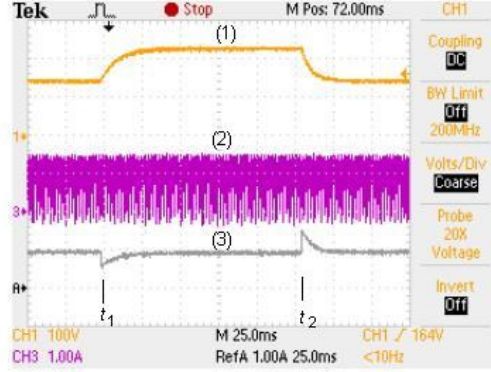


Fig. 3.23: Experimental waveforms of v_o [trace (1), 100 V/div], rectified output current [trace (2), 1 A/div] and i_o [trace (3), 1 A/div] under transient condition with step change in R_L from 140 Ω to 230 Ω at instant t_1 and vice versa at instant t_2 . X-scale: 25 ms/div.

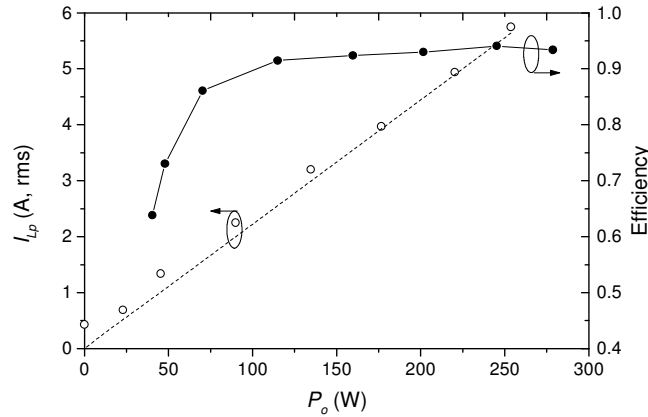


Fig. 3.24: Measured (open circles) and predicted (dashed curve) rms value of i_{Lp} . Experimental efficiency is shown by solid circles.

3.5 Topological Extensions

3.5.1 Type-II RIC With Inherent Constant-Current Constant-Voltage (CCCV) Characteristics

While the load current is required to be constant in a CC power supply when the power supply is loaded, in many applications the output voltage of the power supply also needs to be within specified (safe) limits when the output terminals are open circuited. For instances: (1) If the arc is extinguished during the welding process, the open circuit occurs across the power supply and under this condition, output terminal voltage should not exceed 113 V. (2) CC chargers are commonly used to charge the discharged batteries. A battery has natural voltage limit based on its chemistry. Once this limit is reached, further charging with constant current increases battery temperature and may damage the battery permanently. Therefore, the charging current should progressively reduce as the battery is charged. In these and other practical applications, therefore, it is also necessary to sense the output voltage and regulate it to the limiting value with a separate feedback control circuit.

In this section a topological extension of Type-II RIC circuits is described, with which the converter has built in CCCV characteristics. It is not necessary to sense the output current or voltage and the electronic circuit to implement the feedback control is eliminated. The inherent CCCV characteristics and elimination of feedback control make the proposed topology rugged and reliable.

Figure 3.25 shows the circuit diagram of a half-bridge dc-dc CC power supply wherein the RIN is represented by a two port network and can be any of 15 Type-II RIC circuits. Half-bridge converter drives the input port of RIN with high-frequency symmetrical square-wave voltage waveform, v_{in} , of amplitude $\pm V_d$. Since RIN has low pass or band pass characteristics, the current response to the square-wave excitation is nearly sinusoidal. Due to immittance conversion characteristics, v_{in} and i_1 are always in phase under all loading conditions. Assuming a large output filter capacitor and therefore ripple free output voltage, transformer primary voltage, v_{pri} , has a square-wave waveform of amplitude $(\pm V_o/n)$ and it is in phase with i_2 due to rectifier action. Further, the phase difference between v_{in} and v_{pri} as well as i_1 and i_2 will be 90° due to

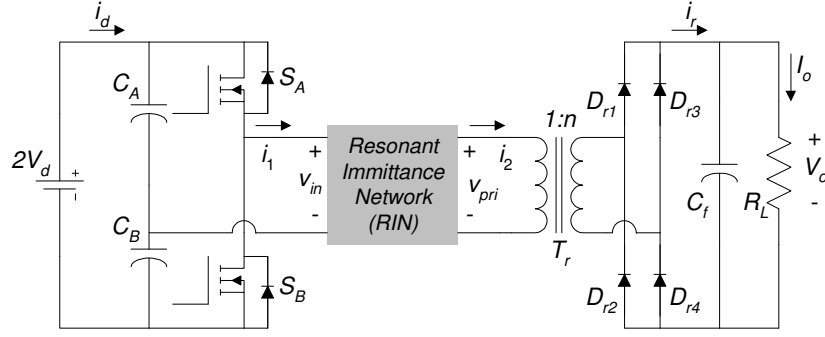


Fig. 3.25: Half-bridge Type-II RIC.

immittance conversion characteristics as shown in (2.3) and (2.4). Therefore, idealized voltage and current waveforms at the input and output port of RIN can be drawn as shown in Fig. 3.26. The amplitude (V_{pri}) of v_{pri} is given by,

$$V_{pri} = \frac{V_o}{n} = \frac{HV_d}{Q} \quad (3.85)$$

Under no-load condition, when R_L is zero, Q is infinity and V_{pri} is zero. As the load on the converter increases, V_{pri} increases proportionally and can be more than or less than V_d depending on the loading condition. With a proper choice of Q and n by design, the peak primary voltage at full-load condition, V_{pri_FL} , (corresponding to $R_L = R_{Lmax}$) can be made equal to V_d . With the proposed circuit modification, as shown in Fig. 3.27,

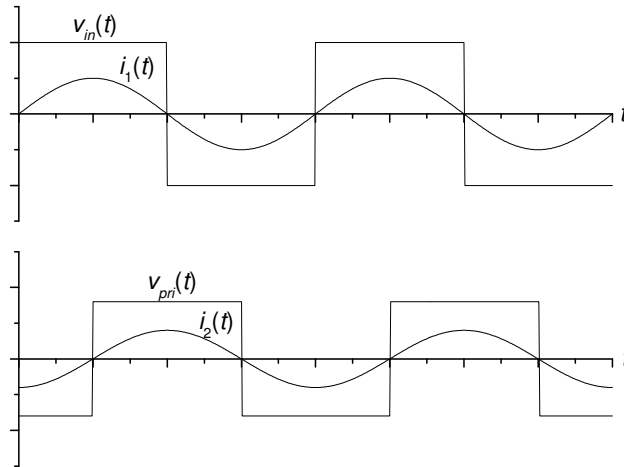


Fig. 3.26: Idealized waveforms at the input and output port of the RIN.

wherein two clamp diodes D_{c1} and D_{c2} are added from the transformer primary to the dc supply rails, v_{pri} will be clamped to V_d due to conduction of D_{c1} and D_{c2} . Indirectly, this action will make V_o constant irrespective of further increase in the load. This way the CV characteristic is inherently attributed to Type-II RIC with the addition of clamp diodes.

The half-bridge Type-II RIC with clamp diodes shown in Fig. 3.27 is the simplest proposed configuration of the circuit with in built CCCV characteristics. However, transformer primary voltage can only be clamped to the input dc supply voltage and therefore the CV limit of the converter is fixed. Although this is sufficient in most of the applications, it may be desired sometime to have flexible CV limit. Two topological variants are described next featuring flexible CV limit.

In the first alternative configuration, a third winding, with a turns ratio $1:n_3$ with respect to primary, is added to the transformer as shown in Fig. 3.28. Diodes D_{c1} through D_{c4} clamp the voltage across this third winding to V_d . Therefore, if diode drops are neglected, V_o gets clamped to $(n/n_3)V_d$ if the load resistance increases above the design value. Thus by varying the turns ratio of the third winding in design, it is possible to change the CV limit to any other value than the maximum output voltage.

Further if it is required in an application that it should be possible to vary the CV limit, the third winding of the transformer needs to be clamped by a variable auxiliary voltage source, V_{aux} , as illustrated by Fig. 3.29(a). In practice, V_{aux} can be realized by inserting a class-B chopper, for instance, as shown in Fig. 3.29(b) between the clamp rectifier formed by D_{c1} through D_{c4} and dc voltage source. The voltage at

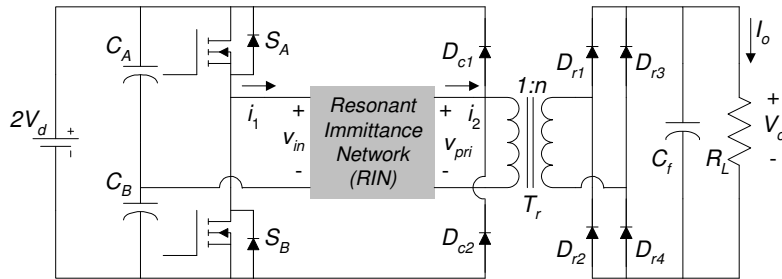


Fig. 3.27: Proposed topological extension of a half-bridge Type-II RIC with clamp diode for in built CCCV characteristics.

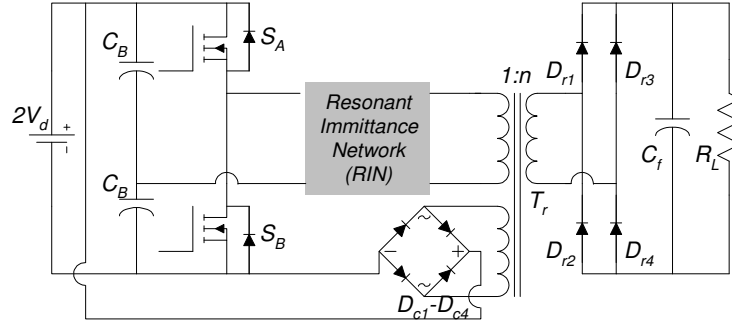


Fig. 3.28: Half-bridge Type-II RIC with tertiary winding and clamp diodes.

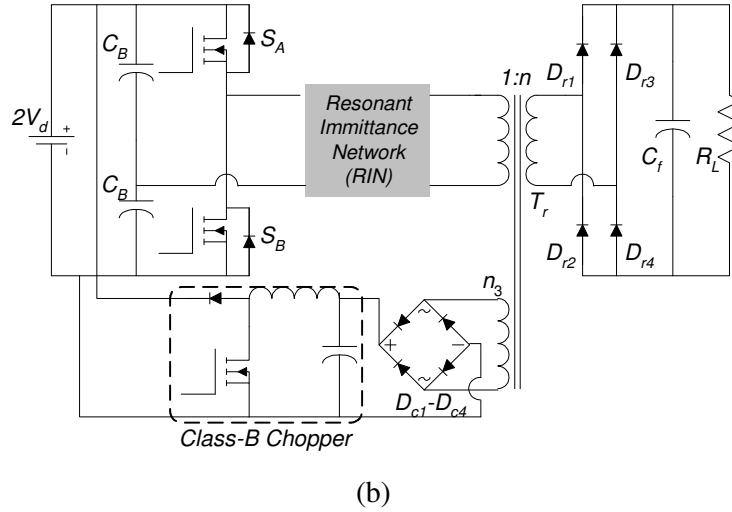
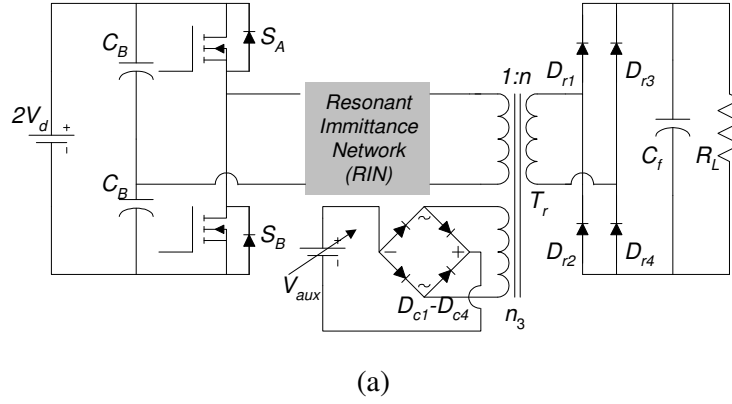


Fig. 3.29: (a) Topological variant of a half-bridge Type-II RIC allowing variable CV-limit. The CV-limit is changed by changing the value of V_{aux} . (b) Possible practical realization of V_{aux} using a class-B chopper.

the output terminals of the clamp rectifier can be sensed and regulated from zero to $2V_d$ by PWM control. Although this topological variation needs the voltage sensing and feedback control, it can still be an advantage in certain applications. For instance in a capacitor-charging power supply wherein the main output voltage V_o is in kilo volt range, the voltage-sensing and feedback control electronic circuit need not float on the high voltage. Instead, it will be referred to much lower primary-side dc voltage.

The topological variations of Type-II RIC CCCV converter shown in Fig. 3.28 and Fig. 3.29 also work as well for the full-bridge converter.

3.5.1.1 Experimental Results

The performance of the proposed Type-II RIC structure with CCCV characteristics has been verified with experimental studies on LCL-T RC [67]. The circuit diagram of laboratory prototype of a 1A, 500 W half-bridge LCL-T RC with clamp diodes is shown in Fig. 3.30. The experimental prototype is operating in open loop without any feedback control at 100 kHz. The principal circuit waveforms for operation with $R_L=200\ \Omega$, $500\ \Omega$ and $1000\ \Omega$ are shown in Fig. 3.31(a), (b) and (c), respectively. It can be seen from Fig. 3.31(a) and (b) that the clamp diodes do not conduct as long as the R_L is less than maximum designed value ($500\ \Omega$). As the R_L increases above the maximum designed value, the clamp diodes conduct effectively clamping the transformer primary voltage to supply voltage as shown in Fig. 3.31(c).

To obtain the open-loop I_o - V_o characteristics, R_L was varied in the range $10\ \Omega$ to $10\ \text{k}\Omega$. The experimental variation in V_o and I_o as a function of R_L is plotted in Fig.

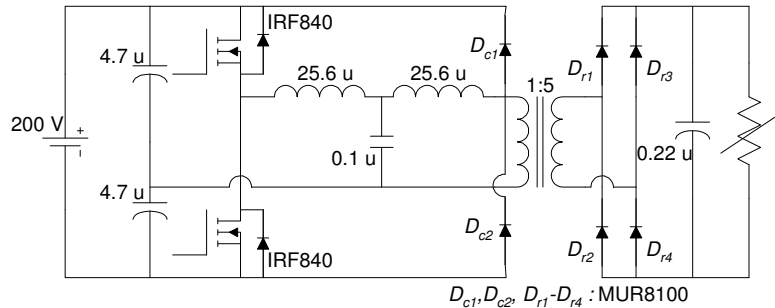


Fig. 3.30: Prototype half-bridge LCL-T RC with clamp diodes.

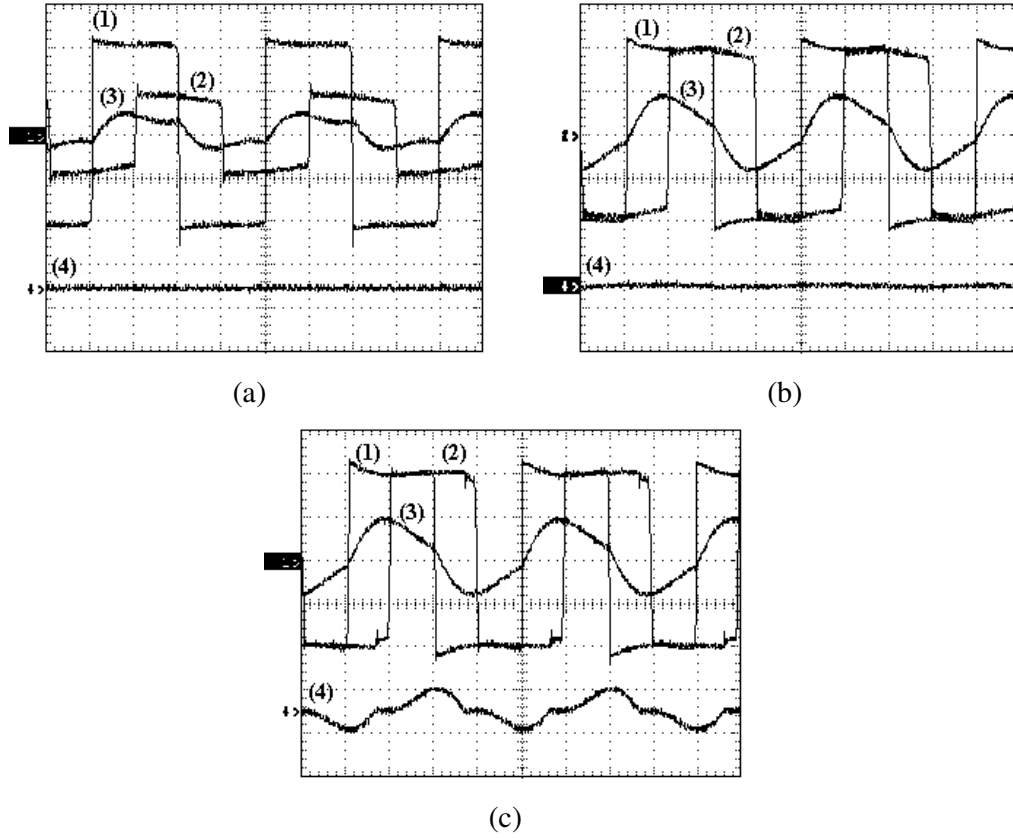


Fig. 3.31: Circuit waveforms of prototype LCL-T RC with clamp diodes for operation with (a) $R_L=200\ \Omega$, (b) $R_L=500\ \Omega$ and (c) $R_L=1000\ \Omega$. Legends: (1) v_{in} , 50 V/div. (2) v_{pri} , 50 V/div. (3) i_{L1} , 10 A/div. (4) $(i_{Dc1}-i_{Dc2})$, 10 A/div. X-scale: 2.5 μ s/div.

3.32 (a). The converter is seen to operate in CC mode if $R_L < 500\ \Omega$ and in CV mode if $R_L > 500\ \Omega$. The open-loop I_o - V_o characteristics of the prototype with R_L as a running parameter is shown in Fig. 3.32(b). The experimental characteristics (solid curve with markers) matches closely with ideal characteristics (dashed curve) of a CCCV power supply, demonstrating the inbuilt CCCV nature of the converter.

Figure 3.33 shows a plot of converter efficiency as a function of R_L . The figure also shows variation in output power. It can be observed that the output power of the converter initially increases with R_L in CC mode, reaches the maximum designed (full-load) value and thereafter reduces with further increase in R_L . Therefore, the output power of the converter is safely limited to maximum designed value over the entire operating range including two extremities – load short-circuit and load open-

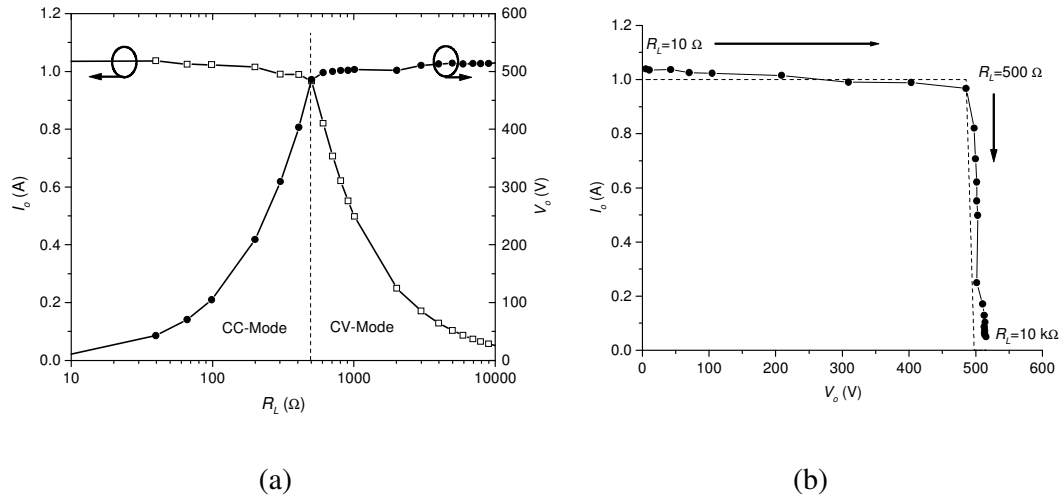


Fig. 3.32: Experimental characteristics (a) I_o and V_o as a function of change in R_L .
 Legends: $-\square-$: I_o , $-\blacksquare-$: V_o . (b) I_o - V_o plot with R_L as the running parameter. Solid curve with marker shows the experimentally measured characteristics and the dashed curve shows the characteristics of an ideal CC-CV power supply.

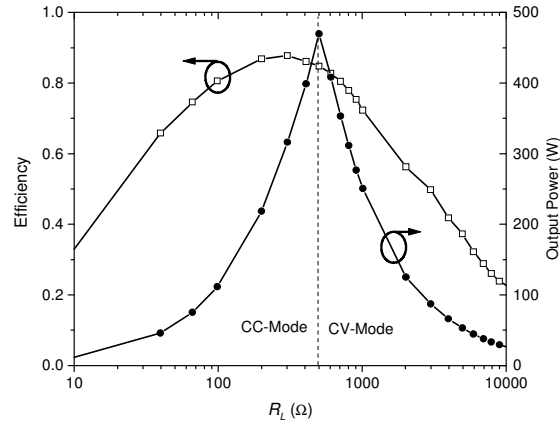


Fig. 3.33: Output power and efficiency of experimental converter as a function of R_L .
 Legends: $-\square-$: Efficiency , $-\blacksquare-$: Output power (W)

circuit. In CC mode, the maximum efficiency is 0.89 and it stays above 0.8 for operation down to 100 W output power (data point corresponding to $R_L=100$ Ω in Fig. 3.33). In CC mode, since the clamping diodes do not conduct, the efficiency of the proposed topological extension with clamp diodes and conventional Type-II RIC do not differ. In CV mode, efficiency is seen to be inferior as compared to that in CC

mode since the output power in CV mode decreases with increase in R_L and additional losses occur in clamp diodes.

3.5.2 Multiphase Type-II RIC

3.5.2.1 Source- and Load-Side Harmonics

The bridge inverter in a Type-II RIC operates at high frequency and produces a square-wave voltage waveforms at the input port of the RIN. Due to low-pass or band pass characteristics of RIN, the current at the input and output port is nearly sinusoidal, as shown in Fig. 3.26. Therefore, the waveform of rectified output current, i_r , as well as the current drawn from the input dc source, i_d , can be drawn as shown in Fig. 3.34. While the waveforms of i_r and i_d (see Fig. 3.15 for definition) are similar, their amplitude and phase could be different. Nevertheless, the generic waveform of Fig. 3.34 can be represented by Fourier series as,

$$i(t) = \frac{2I_m}{\pi} - \frac{4I_m}{\pi} \sum_{h=2,4,\dots} \frac{1}{(h+1)(h-1)} \cos(h\omega t) \quad (3.86)$$

Illustratively, Fig. 3.35 shows the experimental waveforms and their spectrum of i_r and i_d in Topology T_3 described in section 3.3. The waveforms of i_r and i_d are observed to be nearly sinusoidal, consistent with the fundamental frequency approximation. Figure 3.36 compares the amplitude of dominant harmonics computed from (3.86) with those measured experimentally.

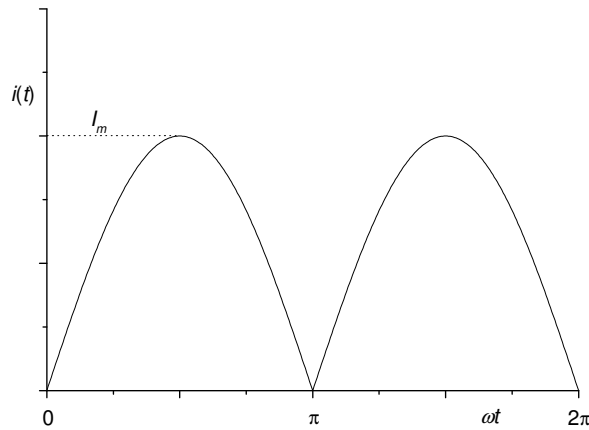


Fig. 3.34: Generic waveform for the rectified output current, i_r , and the current drawn from the input dc source, i_d .

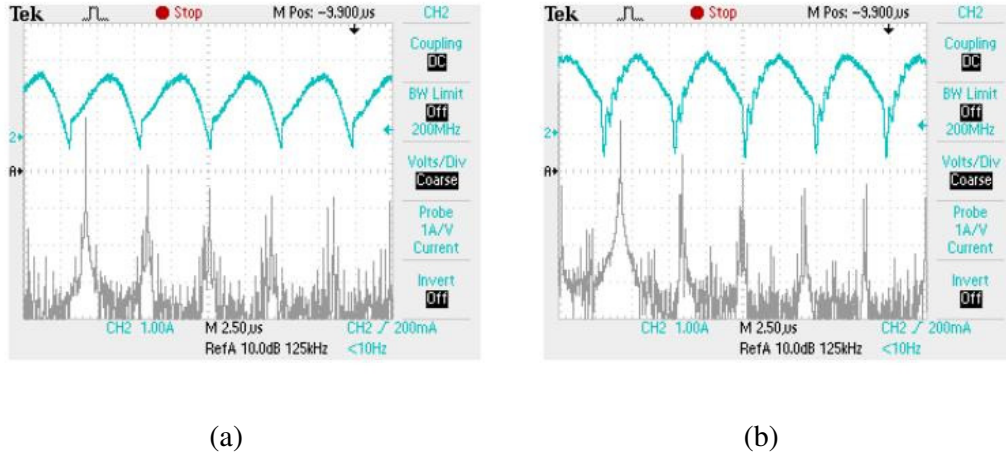


Fig. 3.35: Experimental waveform (1 A/div, 2.5 μ s/div) and frequency spectrum (10 db/div, 125 Hz/div) of (a) i_r and (b) i_d in Topology T_3 .

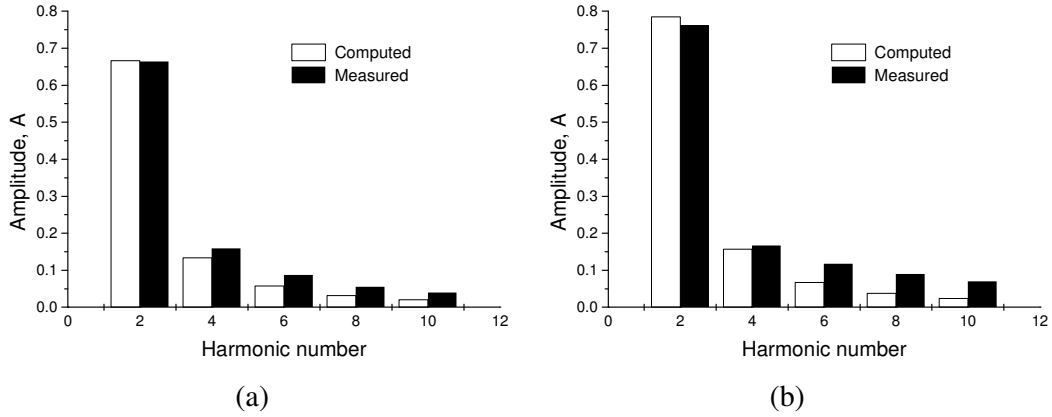


Fig. 3.36: Computed and measured dominant harmonics of (a) i_r and (b) i_d in Topology T_3 .

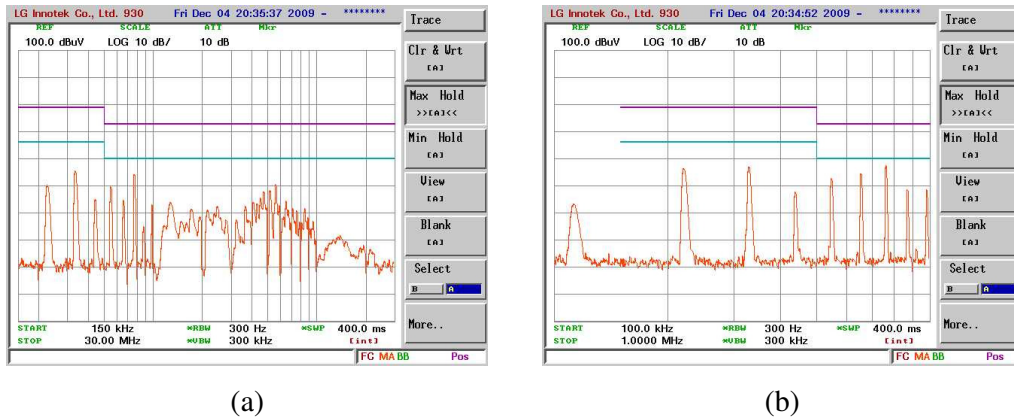


Fig. 3.37: Conducted EMI along with CISPR 11 limit lines: (a) complete spectrum and (b) spectrum details between 100 kHz and 1 MHz.

The conducted EMI over CISPR 11 specified band of 150 kHz to 30 MHz along with CISPR Group-1 Class-A quasi-peak and average limit lines, measured using line impedance stabilization network (LISN) and spectrum analyzer, is also shown in Fig. 3.37(a). Figure 3.37(b) shows the spectrum details over 100 kHz to 1 MHz. While the prototype converter is seen to comply with the limits, the harmonics at the multiples of switching frequency are clearly seen.

Dominant current harmonics at the input and output side of the dc-dc converter need to be filtered. While the size of the output filter is governed by specified ripple on the output dc voltage and current, the filter on the input side is decided by the requirement of compliance with conducted EMI norms. High source- and load-side harmonic currents demand a large filter on the respective side, which in turn has the following consequences:

1. A large-sized filter occupies a considerable portion of the total converter volume and thereby increases size, weight and cost.
2. The overall dynamic response of the converter is decided by the response of the filter. A large-sized filter results in the sluggish response. It is already observed in Fig. 3.23 that, while the rectified output current of LCLCL-T RC is constant with step load change, the dc output current deviates considerably from its steady-state value during this transient condition, the extent and duration of which is larger if the value of output filter capacitor is larger.
3. Output impedance of the input filter can interact with the input impedance of the converter, creating potential closed-loop instability.
4. Some sensitive and expensive loads (for instance, klystron and laser diodes) constrain the filter values due to limits on the maximum allowable stored energy in the converter for the safety of load under fault conditions (for instance, arcing in klystron).

Therefore, it is desired to minimize the source- and load-side harmonics to reduce the filtering requirements.

3.5.2.2 Phase-staggered Operation

A way to reduce the input and output filter size is to operate the converter at higher frequency, which, however, practically can not be increased beyond a certain

limit posed by limitations of devices, driver, capacitors, magnetic core materials, eddy current and proximity effect losses in the magnetic components etc.

Phase-staggered operation of power converters connected in series or parallel on the input and output side is a well established technique to reduce the ripple amplitude and to increase the ripple frequency, thereby drastically reducing the filtering requirement and size without increasing the switching frequency. Such an arrangement of low-power modules instead of a single high-power converter additionally provides modularity, standardization, redundancy and high reliability.

Most of the conventional PWM converters and RCs operating with their input and output ports connected in series or parallel are inherently unstable and equal load sharing is not guaranteed unless it is forced by implementing a feedback control. Since a Type-II RIC is inherently a current source, it lends itself for easy paralleling without any additional care for equal current sharing, as illustrated in Fig. 3.38.

For m identical modules operating in parallel at the same switching frequency but with constant phase shift θ , total rectified output current can be expressed by Fourier series as,

$$i_i(t) = \left(\frac{2I_m}{\pi} \right) m - \frac{4I_m}{\pi} \sum_{h=2,4,\dots} \frac{1}{(h+1)(h-1)} \sum_{x=0,1,2,\dots,(m-1)} [\cos n(\omega t - x\theta)] \quad (3.87)$$

The dc components of individual modules directly add independent of θ and the total dc current of the paralleled modules is m times the output current of one module.

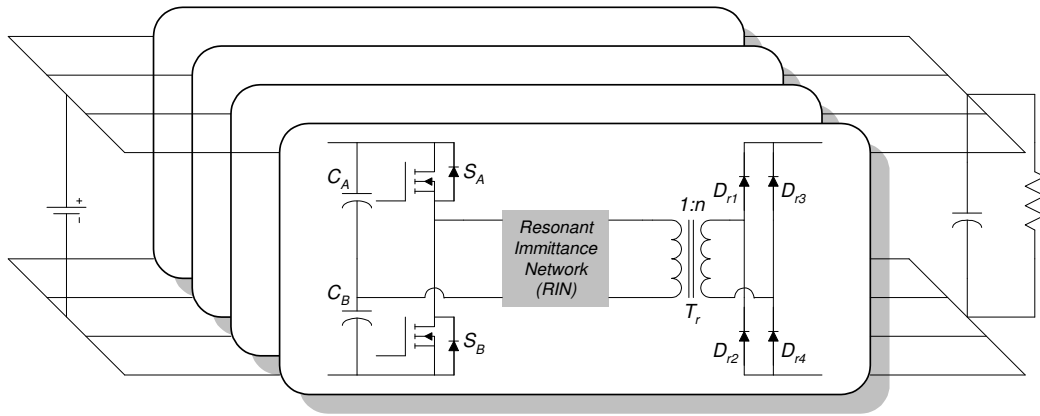


Fig. 3.38: Parallel operation of Type-II RICs.

However, harmonics can selectively get cancelled in the total current depending on θ . The required value of θ for cancellation of h^{th} harmonic component in i_t is given by:

$$\theta = \frac{2p\pi}{mh} \quad (3.88)$$

where,

$$p = 1, 3, 5, 7, 9, \dots \text{ if } m \text{ is even}$$

$$p = 1, 2, 3, 4, 5, \dots ; p \neq km; k = 1, 2, 3, \dots \text{ if } m \text{ is odd}$$

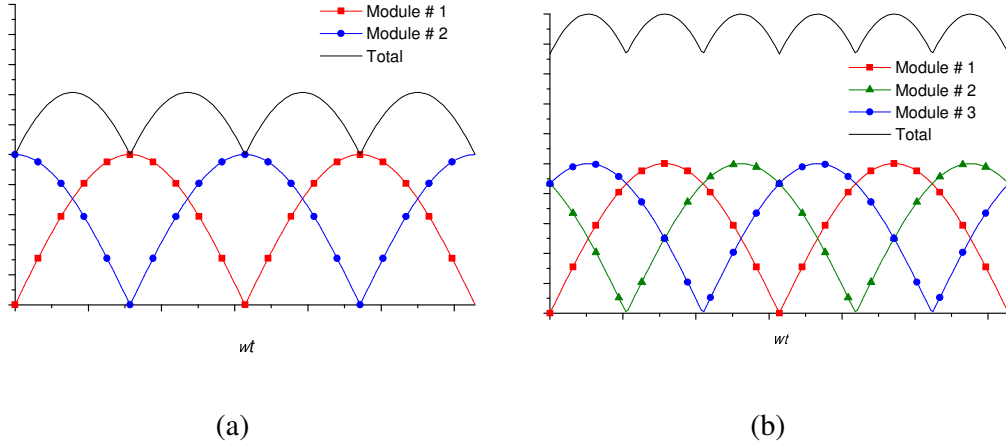


Fig. 3.39: Ripple reduction in the output current of (a) two paralleled Type-II RICs operating with $\theta=90^\circ$ and (b) three paralleled Type-II RICs operating with $\theta=120^\circ$.

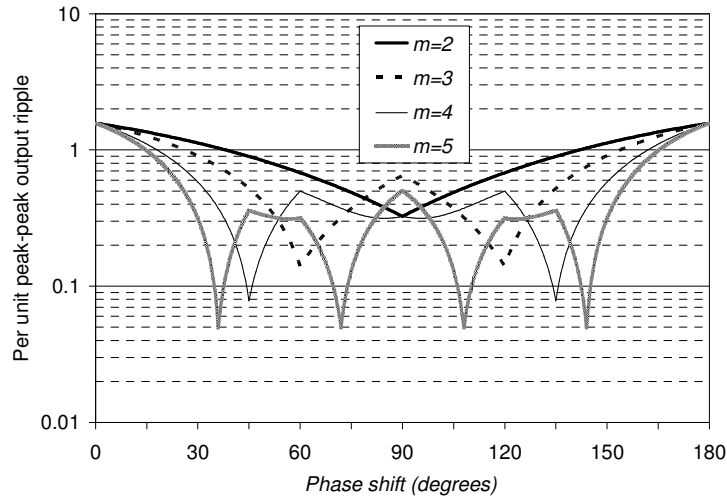


Fig. 3.40: Peak-peak ripple in the rectified output current normalized to its average value as a function of θ in multiphase Type-II RICs.

Fig. 3.39(a) illustrates ripple reduction in the output current of two Type-II RICs operating with $\theta=90^\circ$ optimized from (3.88) for 2nd harmonic elimination. Similarly, Fig. 3.39 (b) illustrates the ripple reduction in the output current of three Type-II RICs operating with $\theta=120^\circ$ optimized from (3.88) for 2nd and 4th harmonic elimination. The peak-peak ripple in the rectified output current normalized to its average value as a function of θ is shown in Fig. 3.40 for different values of m .

3.5.2.3 Simulation Results

In order to verify the stable and balanced operation of parallel connected Type-II RICs and reduction of harmonics with phase-staggered operation, the parallel operation of three Type-II RIC modules using topology T₃ (described in section 3.3 with parameters summarized in Table 3.3) operating with $\theta=120^\circ$ is simulated on OrCAD PSpice version 9.1.

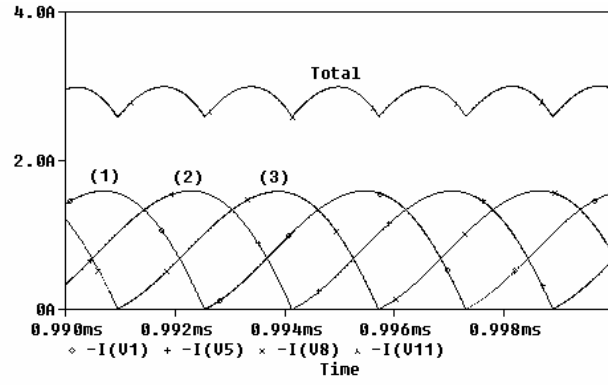
Figure 3.41(a) shows the waveforms of rectified output currents of three modules and the total current. Reasonable matching with the idealized waveforms of Fig. 3.39(b) can be observed.

Figure 3.41(b) shows the spectrum of rectified output current of one of the modules (dashed curve) and the total output current (continuous curve). The 2nd and 4th harmonics are seen to be eliminated in the total rectified output current since the first dominant harmonic is seen to be at 630 kHz, which is 6 times the switching frequency (105 kHz).

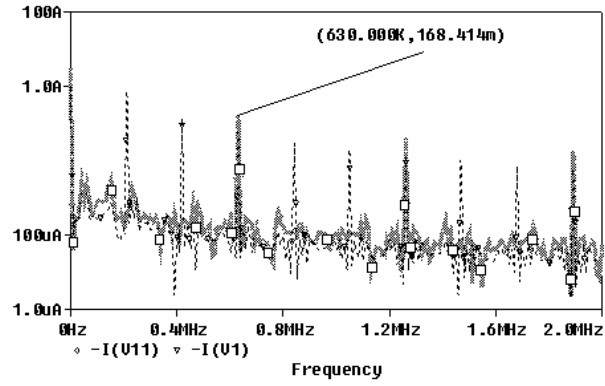
Figure 3.41(c) shows the current at the output of MOSFET bridge (that is, current in inductor L_2) in three modules, which is seen to be equal confirming the balanced operation of paralleled modules with equal current sharing.

3.6 Conclusion

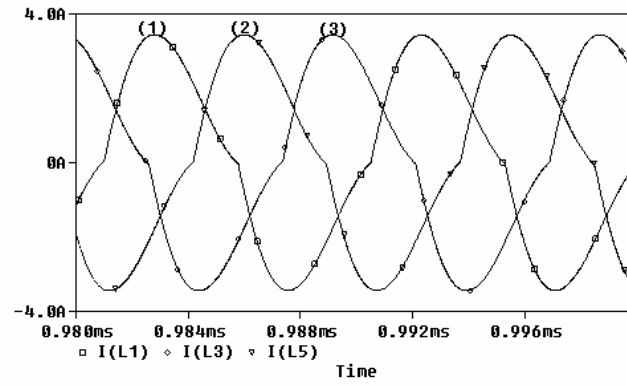
Fundamental frequency ac analysis of few Type-II RIC topologies presented in this chapter exemplified steady-state analysis and design procedure for their application as a CC power supplies. Closed form expressions for optimum design, component values and their ratings are derived for the converter design. Experimental results on the laboratory prototype converters demonstrated the immittance



(a)



(b)



(c)

Fig. 3.41: Simulation results of topology T_3 . (a) Waveforms of rectified output currents of the three modules and the total current, (b) their spectrum (dashed curve for output current of individual module and continuous curve for total current) and (c) waveform of the current at the output of MOSFET bridge.

conversion characteristics. The output current is nearly constant for fixed input voltage and the current at the input port of RIN is in phase with the voltage under all loading conditions.

Addition of clamp diodes in Type-II RIC circuits attributes inherent CV characteristics to the converter in addition to the CC behaviour, which is very useful in variety of practical applications.

Source- and load-side harmonics are significantly reduced with multiphase Type-II RICs operated with suitable phase-shift, closely approximating to a true dc-dc immittance converter.

Chapter 4

Asymmetrical Pulse Width Modulation Control

The output current of Type-II RICs is theoretically constant irrespective of changes in the load resistance, for constant input dc voltage. As examined experimentally in the previous chapter, the output current of practical circuits droops slightly with the output power, even with the constant input dc voltage, because of increasing drops in various circuit elements. Moreover, input dc voltage in most of the practical off-line applications itself is unregulated when it is conveniently obtained by rectifying the ac main voltage using diode rectifier and smoothened using passive filter. Therefore, for practical application of Type-II RIC as a current-source power supply, it is necessary to regulate the output current, particularly against the input voltage variations. Some applications also demand that it should be possible to set and regulate the output current from near-zero to the maximum rated value.

Since Type-II RICs behave as a current-source only when it is operated at a particular frequency, the method using variation of switching frequency can not be applied to control the output. The output current can be regulated and varied over a wide range by either varying the input dc voltage using another converter in the front-end or using fixed-frequency control methods. In the former case, two cascaded converters reduce overall conversion efficiency, increase complexity, component count and cost.

The CM or PSPWM control [119] – [132] and asymmetrical pulse-width-modulation (APWM) control [136] – [139] are the two common fixed-frequency PWM control strategies. The CM control can be applied only with the full-bridge converter whereas APWM control can be used with half-bridge as well as full-bridge converter. While APWM control leads to asymmetric operation of the high-side and the low-side switches and leads to unequal voltages across the leg capacitors, it has been popularly applied to power converters (resonant as well as non-resonant) due to simpler implementation and soft-switching. Moreover, half-bridge topology has a relatively simpler structure, less number of switches with associated driving circuits and has been a popular approach for low- and medium-power level applications. For these reasons, this chapter examines the possibility of using APWM control to Type-II RICs, exemplified using LCL-T RC.

4.1 APWM Controlled LCL-T RC

The circuit diagram of half-bridge LCL-T RC is shown in Fig. 4.1(a). The RN is composed of inductors L_1 , L_2 and capacitor C_1 . The half-bridge converter (composed of MOSFET switches S_A , S_B , their body-drain diodes D_A , D_B , respectively, and capacitors C_A , C_B) drives the input port of the RN with high-frequency square-wave voltage waveform. The circuit diagram of full-bridge LCL-T RC is shown in Fig. 4.1(b) wherein MOSFET switches $S_1 - S_4$ and their body-drain diodes $D_1 - D_4$, respectively, constitute the full-bridge square-wave inverter. At the output port of the RIN an isolation transformer matches the required output voltage, V_o , and current, I_o , to the input dc voltage ($2V_d$ in the half-bridge and V_d in the full-bridge circuit). A diode rectifier (D_{r1} through D_{r4}) and filter capacitor (C_f) convert high-frequency ac to output dc. In the half-bridge circuit, steady-state voltages across C_A and C_B adjust in such a way that there is no dc component in the input voltage to the RIN, v_{in} . A dc blocking capacitor C_{DC} is required in full-bridge circuit to block the dc component in voltage at the bridge output resulting from asymmetrical operation of the switches.

The current gain (H) and voltage gain (M) of LCL-T RC are derived, using fundamental frequency ac analysis, in Chapter 3 as given by (3.6) and (3.7)

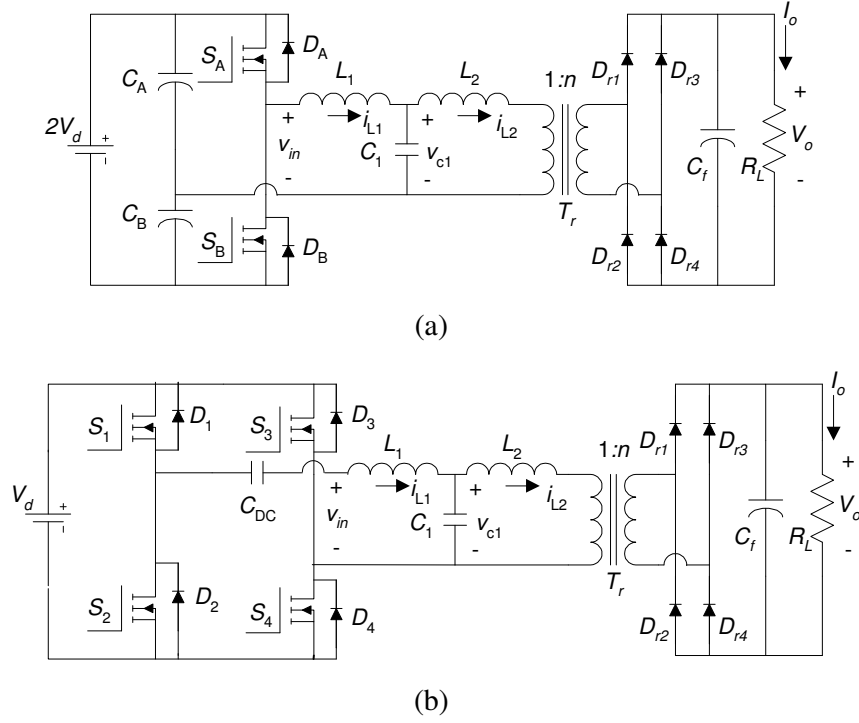


Fig. 4.1: Circuit diagrams of (a) half-bridge and (b) full-bridge LCL-T RC.

respectively and it is shown that the H is independent of load only if the converter is operated at $\omega_n = 1$, given by (3.8). Therefore, the method using variation of switching frequency to control the output can not be applied - or else current source behaviour will be lost. Besides, the plots of Fig. 3.2(a) show that H is relatively flat in the vicinity of the operating point $\omega_n = 1$. Thus, the variation of switching frequency will not provide wide conversion range and regulation against large input voltage variations. Therefore fixed-frequency control should be used. Additionally, if $\gamma = 1$, v_{in} and i_{L1} are in phase resulting in the lowest conduction loss in the switches. Therefore, for the subsequent analysis of LCL-T RC with APWM control, it is assumed that the converter operates at $\omega_n = 1$ and $\gamma = 1$.

Figure 4.2 shows switch gate pulses and the resulting waveform v_{in} with APWM control. The dead-gap between the complementary switches (S_A, S_B in half-bridge and S_1, S_2 and S_3, S_4 in full-bridge), required to discharge MOSFET output capacitance and to avoid shoot-through, is assumed to be very small and is neither

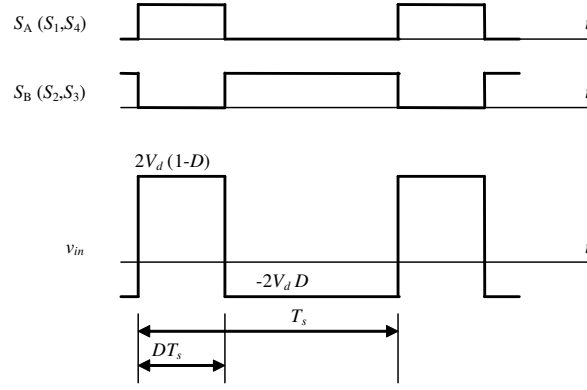


Fig. 4.2: Idealized waveforms of gate pulses for the switches and v_{in} with APWM control. The switches mentioned in the bracket correspond to the full-bridge converter.

explicitly shown in Fig. 4.2 nor considered in the analysis. Amplitude of the fundamental component of v_{in} can be derived as,

$$V_{in1} = \frac{4V_d}{\pi} \sin(\pi D) \quad (4.1)$$

where D is the duty-cycle defined in Fig. 4.2. Thus V_{in1} can be controlled from zero to its maximum value by changing D . Assuming that the power is transferred to the output only by the fundamental component of source excitation, H and M with APWM control can be approximated as,

$$H|_{\omega_n=1} = \frac{8}{\pi^2} \sin(\pi D) \quad (4.2)$$

$$M|_{\omega_n=1} = \frac{8}{\pi^2} \frac{1}{Q} \sin(\pi D) \quad (4.3)$$

4.2 State-Space Model and Modes of Operation

An equivalent circuit diagram of LCL-T RC is shown in Fig. 4.3 for the state-space analysis. The input bridge is represented by a square-wave voltage source v_{in} which can be expressed in the steady-state for the p^{th} cycle of operation as,

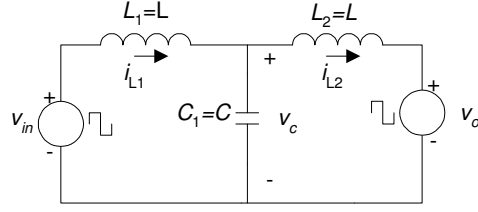


Fig. 4.3: Equivalent circuit diagram of LCL-T RC.

$$\begin{aligned} v_{in} &= 2V_d(1-D) \text{ for } pT_s < t < D(p+1)T_s \text{ and} \\ v_{in} &= -2V_d D \text{ for } D(p+1)T_s < t < (p+1)T_s \end{aligned} \quad (4.4)$$

wherein T_s is the time period of one cycle. Output filter capacitor, C_f , is assumed to be large enough so as to result in a very low ripple in the output voltage even with large values of Q . Under near no-load conditions where R_L tends to zero (that is, Q tends to infinity) this assumption breaks down as the ripple becomes significant. Since C_f in a practical power converter would be chosen to yield an acceptably low output voltage ripple down to typically 5 % of full-load condition (corresponding to a value of Q to be 20 times its full-load value) and since, as discussed subsequently, salient operating modes occur at lower values of Q , the aforementioned simplifying assumption is valid in the regions of interest. Therefore the transformer, rectifier and filter on the output side of the RN are represented in Fig. 4.3 by the square-wave voltage v_o which can be expressed as,

$$\begin{aligned} v_o &= \frac{V_o}{n} \text{ for } i_{L_2} > 0 \text{ and} \\ v_o &= -\frac{V_o}{n} \text{ for } i_{L_2} < 0 \end{aligned} \quad (4.5)$$

Choosing the inductor currents i_{L_1} , i_{L_2} and capacitor voltage v_c as the state variables, the state-space model is derived as,

$$\frac{d}{dt} \begin{bmatrix} v_c \\ i_{L_1} \\ i_{L_2} \end{bmatrix} = \begin{bmatrix} 0 & C^{-1} & -C^{-1} \\ -L^{-1} & 0 & 0 \\ L^{-1} & 0 & 0 \end{bmatrix} \times \begin{bmatrix} v_c \\ i_{L_1} \\ i_{L_2} \end{bmatrix} + \begin{bmatrix} 0 & 0 \\ L^{-1} & 0 \\ 0 & -L^{-1} \end{bmatrix} \times \begin{bmatrix} v_{in} \\ v_o \end{bmatrix} \quad (4.6)$$

The differential equations in (4.6) are numerically solved for the sources described by (4.4) and (4.5) to obtain steady-state waveforms of the state variables. It is observed

that the circuit can have four operating modes depending on the steady-state waveforms of v_{in} and i_{L1} , which, in turn, depend on D and Q . Each mode of operation is characterized by the different circuit waveforms representing different device conduction sequence, thereby creating different conditions during the device switching. The converter's operation in different modes is described for the half-bridge converter [Fig. 4.1(a)] in the following paragraphs. However, the conducting devices during various sub-intervals in full-bridge circuit [Fig. 4.1(b)] are also marked inside the respective figures for the completeness.

4.2.1 Mode-I

Steady-state waveforms of v_{in} and i_{L1} in these modes of operation are shown in Fig. 4.4. This mode of operation mainly occurs when $D \approx 0.5$. Before $t=t_0$, switch S_B was conducting. At $t=t_0$, S_B is turned off and gate pulse is applied to S_A . Since i_{L1} is negative at this instant, it flows through D_A . At $t=t_1$, D_A turns off naturally at zero current and i_{L1} now flows through S_A . Similarly in the next half cycle, S_A is turned off at $t=t_2$ and gate pulse is applied to S_B . Since i_{L1} is positive at this instant, flows through D_B . At $t=t_3$, D_B turns off naturally at zero current and i_{L1} flows through S_B . At $t=t_4$, S_B is turned off and S_A is turned on once again marking the beginning of the next cycle. Thus in this mode, the device conduction sequence is such that the

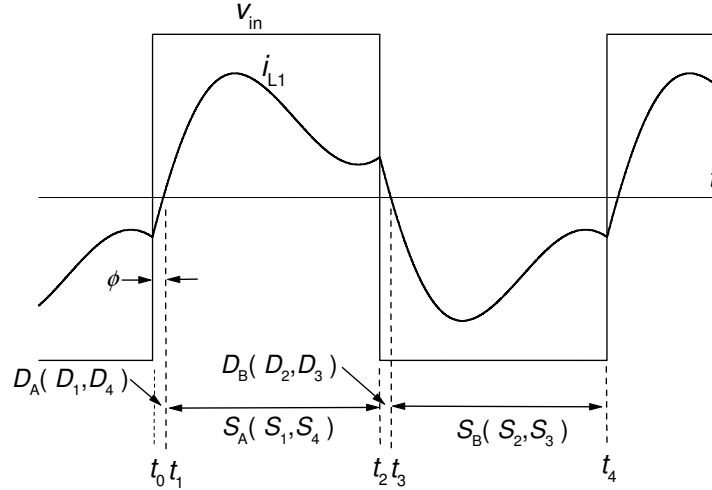


Fig. 4.4: Steady-state waveforms of v_{in} and i_{L1} in Mode-I operation.

anti-parallel diodes conduct prior to the switch conduction resulting in ZVS turn-on for both the switches.

4.2.2 Mode-II

Steady-state waveforms of v_{in} and i_{L1} in this mode of operation are shown in Fig. 4.5. This mode of operation can also occur when $D \approx 0.5$. Before $t=t_0$, diode D_B was conducting. At $t=t_0$ gate pulse is applied to S_A . Diode D_B turns off and i_{L1} flows through S_A . At $t=t_1$, i_{L1} reverses its direction and becomes negative. S_A turns off at zero current and i_{L1} is transferred to D_A until $t=t_2$ when gate pulse is applied to S_B . At this instant, diode D_A turns off and i_{L1} is carried by S_B . At $t=t_3$, S_B is turned off naturally with zero current as i_{L1} reverses its direction and starts flowing through D_B . At $t=t_4$, S_A is turned on once again marking the beginning of the next cycle. Thus in this mode, the device conduction sequence is such that the anti-parallel diodes conduct after the switch conduction resulting in ZCS turn-off for both the switches.

4.2.3 Mode-III

Steady-state waveforms of v_{in} and i_{L1} in this mode of operation are shown in Fig. 4.6. Similar to Mode-I, the device conduction sequence in this mode results in

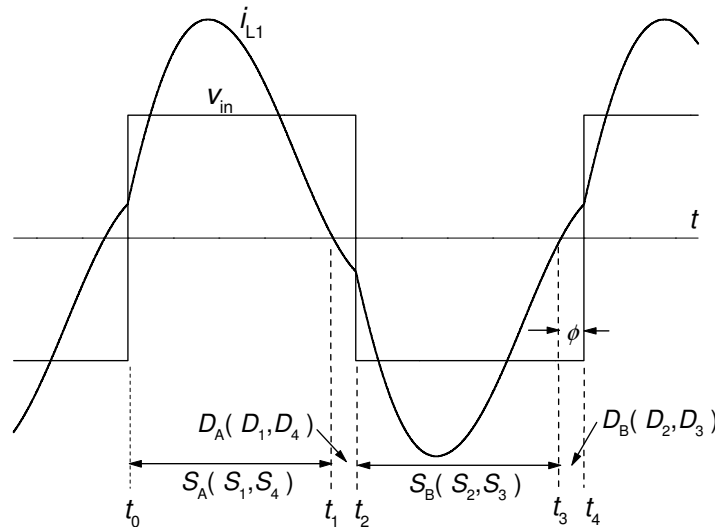
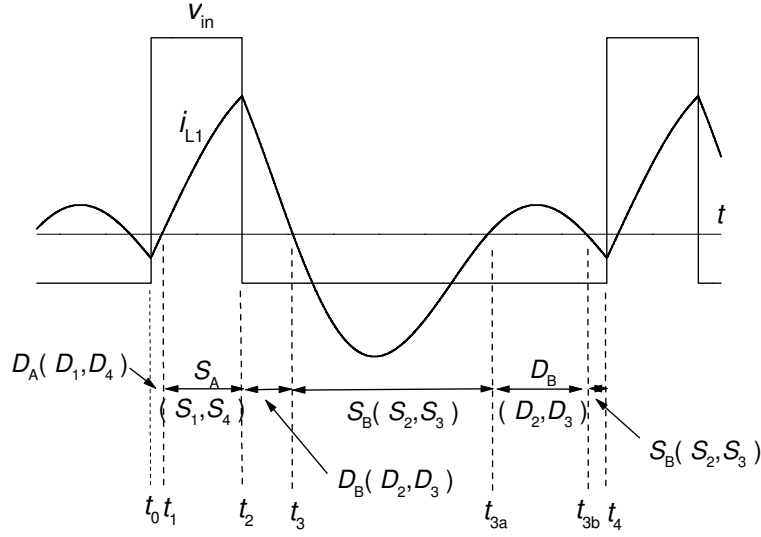


Fig. 4.5: Steady-state waveforms of v_{in} and i_{L1} in Mode-II operation.


 Fig. 4.6: Steady-state waveforms of v_{in} and i_{L1} in Mode-III operation.

ZVS turn-on of all the switches. The difference is that, i_{L1} oscillates across zero twice during the time interval between $t=t_2$ and $t=t_4$ causing S_B and D_B to conduct twice during this interval. At $t=t_2$, S_A is turned off and gate pulse is applied to S_B . Since i_{L1} is positive at this instant, it flows through D_B until $t=t_3$ when it reverses and starts flowing through S_B . Current i_{L1} reverses its direction at $t=t_{3a}$ causing D_B to conduct and once again at $t=t_{3b}$ causing S_B to conduct. The additional commutations of S_B and D_B in this mode of operation are ideally loss-less since they occur under zero current and zero voltage condition. At $t=t_4$, S_A is turned on once again marking the beginning of the next cycle.

4.2.4 Mode-IV

The steady-state waveforms of v_{in} and i_{L1} in this mode of operation are shown in Fig. 4.7. Before $t=t_0$, diode D_B was conducting. At $t=t_0$, switch S_A is turned on, which turns D_B off. The current i_{L1} flows through S_A until $t=t_2$ when it is turned off and gate pulse is applied to S_B . Since i_{L1} is positive at this instant, it flows through D_B . At $t=t_2$, D_B turns off naturally at zero current and i_{L1} now flows through S_B . At $t=t_{3a}$, i_{L1} reverses direction once again causing D_B to conduct until $t=t_4$ when S_A is turned on marking the beginning of the next cycle. As compared to Mode-II, in Mode-IV i_{L1} does not reverse its direction while gate pulse is applied to S_A . This causes D_B to

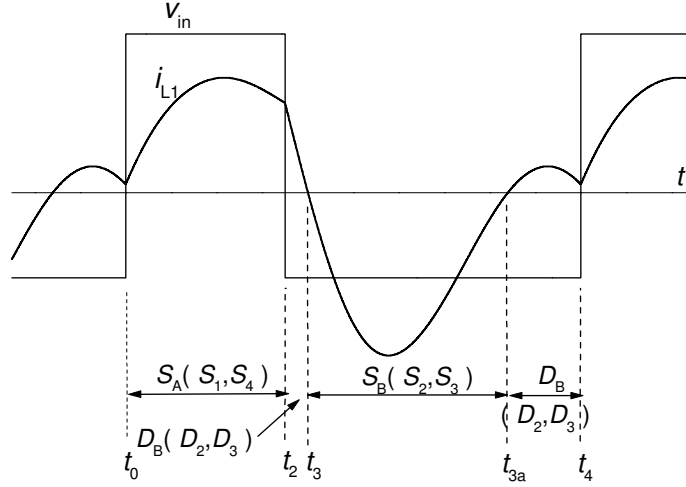


Fig. 4.7: Steady-state waveforms of v_{in} and i_{L1} in Mode-IV operation.

conduct twice during the time interval $t=t_2$ to $t=t_4$. Also, diode D_A never conducts in this mode. Observe that D_B conducts prior to the conduction of S_B , resulting in ZVS turn-on condition for S_B . However, S_A operates under hard-switching condition.

4.2.5 Discussion

The waveforms of v_{in} and i_{L1} in different operating modes shown in Fig. 4.4 to Fig. 4.7 along with the marked conducting devices during various sub-intervals enable the identification of conditions experienced by various switches and diodes during switching. This, in turn, enables the identification of desired operating modes, in which switches and diodes operate under the most favourable switching conditions. Table 4.1 summarizes the switching conditions for the switches and diodes in the four operating modes described above. In Mode-I and Mode-III, anti-parallel diode of each switch conducts prior to the conduction of the switch resulting in ZVS turn-on. Turn-on snubbers are eliminated. Slower anti-parallel diodes and loss-less capacitor turn-off snubber can be used. Body-drain diode and output capacitance of power MOSFET can therefore be used reducing component count. In Mode-II, all the switches are turned off at zero current. However, when a switch is turned on the anti-parallel diode of the other switch in the leg is conducting. Therefore, fast anti-parallel diodes and lossy (or complicated energy recovery) turn-on snubbers are required. Body-drain

Table 4.1: Switching conditions for the switches and diodes in half-bridge LCL-T RC in various operation modes with APWM control.

Mode	Switch S_A		Switch S_B		Diode D_A		Diode D_B	
	turn-on	turn-off	turn-on	turn-off	turn-on	turn-off	turn-on	turn-off
I	ZV, ZC	FV, FC [#]	ZV, ZC	FV, FC [#]	FV, FC [#]	ZV, ZC	FV, FC [#]	ZV, ZC
II	FV, FC	ZV, ZC	FV, FC	ZV, ZC	ZV, ZC	FV, FC	ZV, ZC	FV, FC
III	ZV, ZC	FV, FC [#]	ZV, ZC	FV, FC [#]	FV, FC [#]	ZV, ZC	FV, FC [#] (t_2 - t_3) ZV, ZC (t_{3a} - t_{3b})	ZV, ZC (t_2 - t_3) ZV, ZC (t_{3a} - t_{3b})
IV	FV, FC	FV, FC	ZV, ZC	ZV, ZC	NC	NC	FV, FC (t_2 - t_3) ZV, ZC (t_{3a} - t_4)	ZV, ZC (t_2 - t_3) FV, FC (t_{3a} - t_4)

ZV: zero-voltage, ZC: Zero-current, FV: Finite voltage, FC: Finite current, NC: No conduction

[#]: Loss-less capacitor turn-off snubber can be used to reduce rate of rise of voltage and switching loss during switch turn-off.

diode of MOSFET cannot be used. Additionally, the switches carry diode reverse-recovery current and the discharge current of MOSFET output capacitance at turn-on, causing more losses. In Mode-IV, switch S_B operates with favourable switching conditions since D_B conducts prior to its conduction. However, S_A operates with hard-switching condition.

4.3 Mode Boundaries

The above discussion suggests that Mode-I and Mode-III are the preferred modes of operation as ZVS of all the switches is achieved apart from the other mentioned advantages. It is therefore important to determine the boundaries between the transitions of converter's operation from one mode into another and define the operating regions. The waveforms of v_{in} and i_{L1} in the steady state as the converter makes transition from one mode into another are shown in Fig. 4.8.

Since the steady-state waveforms of v_{in} and i_{L1} depend on two parameters, D and Q , the regions of different modes of operation of the converter can be conveniently defined on, what is called here, the D - Q plane. Figure 4.9 shows the D - Q plane of APWM controlled LCL-T RC at $\omega_n = 1$ and $\gamma = 1$ explicitly showing the regions of converter's operation in various modes. The following important observations are made:

1. If the converter is designed in such a way that the value of Q at full-load condition is greater than 1.07, then the converter can operate only in Mode-I

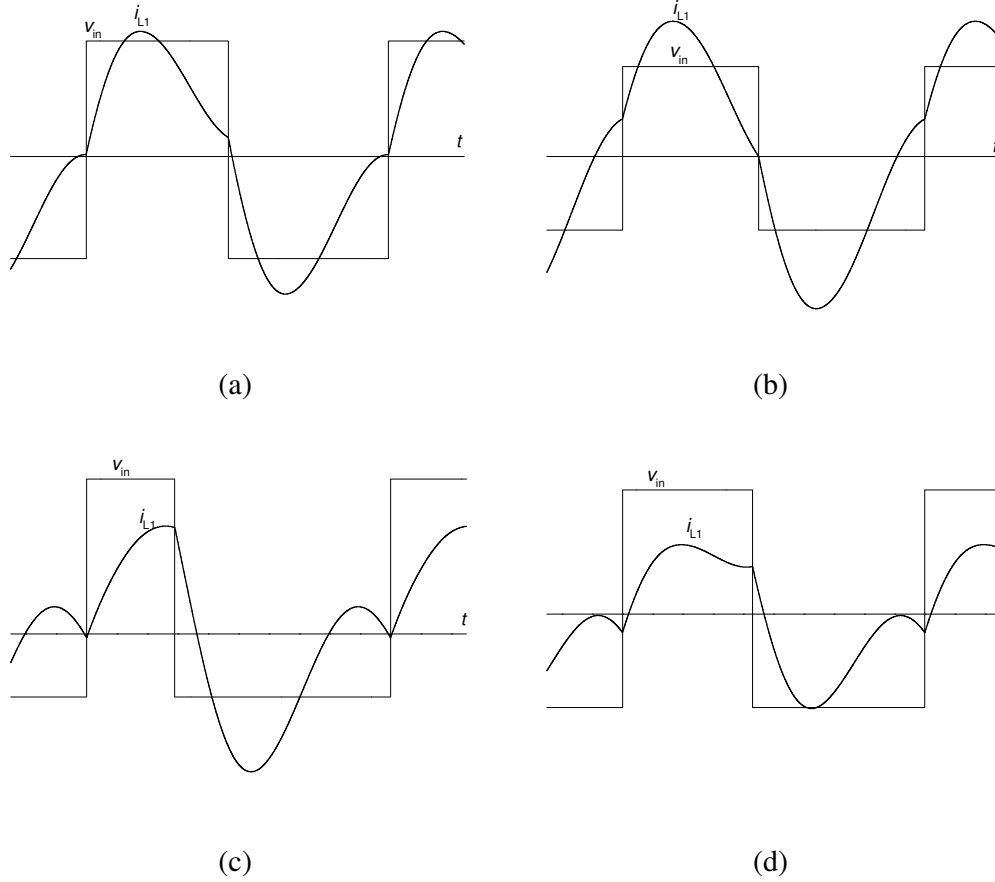


Fig. 4.8: Waveforms of v_{in} and i_{L1} in steady-state as the converter makes transition from one mode into another. Boundary between (a) Mode-I and Mode-IV, (b) Mode-II and Mode-IV, (c) Mode-III and Mode-IV and (d) Mode-I and Mode-III.

or Mode-III for all the values of D in the range 0 to 0.5 and down to the no-load operation.

2. Under the symmetrical input voltage waveform (that is, $D=0.5$), it is seen from the D - Q plane and the description of various operating modes, that i_{L1} lags v_{in} for $Q>0.81$ whereas i_{L1} leads v_{in} for $Q<0.81$. This behaviour is not predicted by the fundamental frequency ac analysis, which suggests that i_{L1} and v_{in} are always in phase. Figure 4.10 shows the variation of phase angle (ϕ) between i_{L1} and v_{in} for operation at $D=0.5$. A positive value of ϕ means i_{L1} is leading v_{in} , and vice versa.

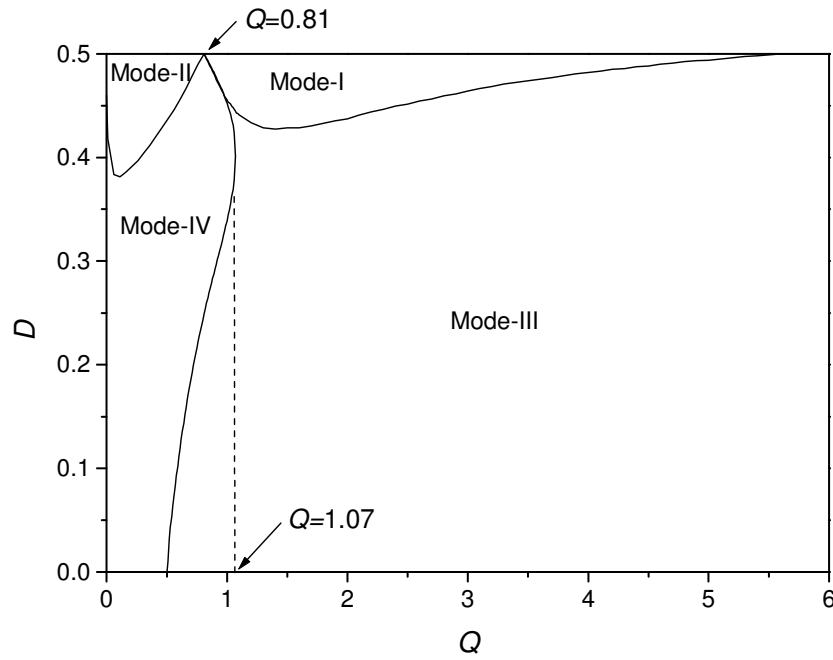


Fig. 4.9: D - Q plane of APWM controlled LCL-T RC showing the regions of different modes of operation.

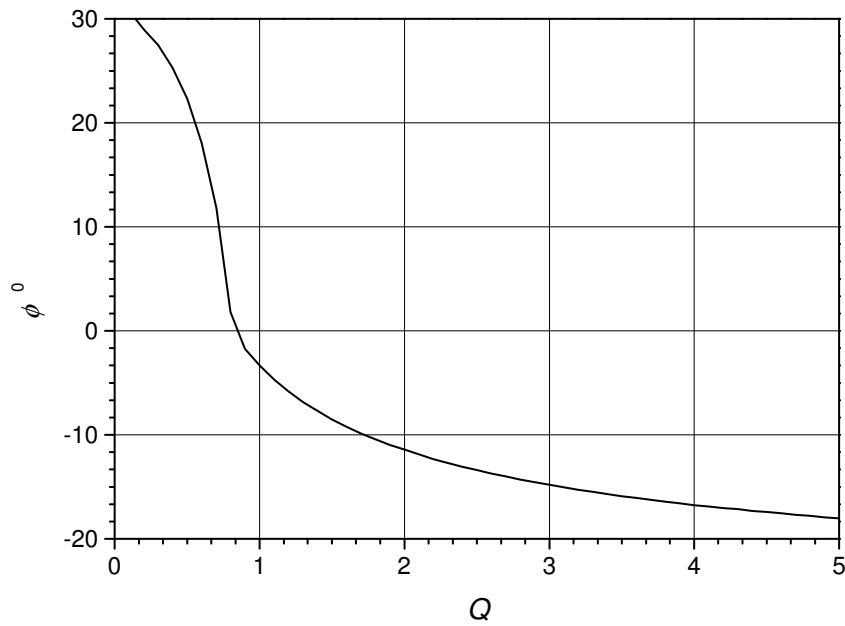


Fig. 4.10: Variation of ϕ as a function of Q for operation at $D=0.5$ in APWM controlled LCL-T RC.

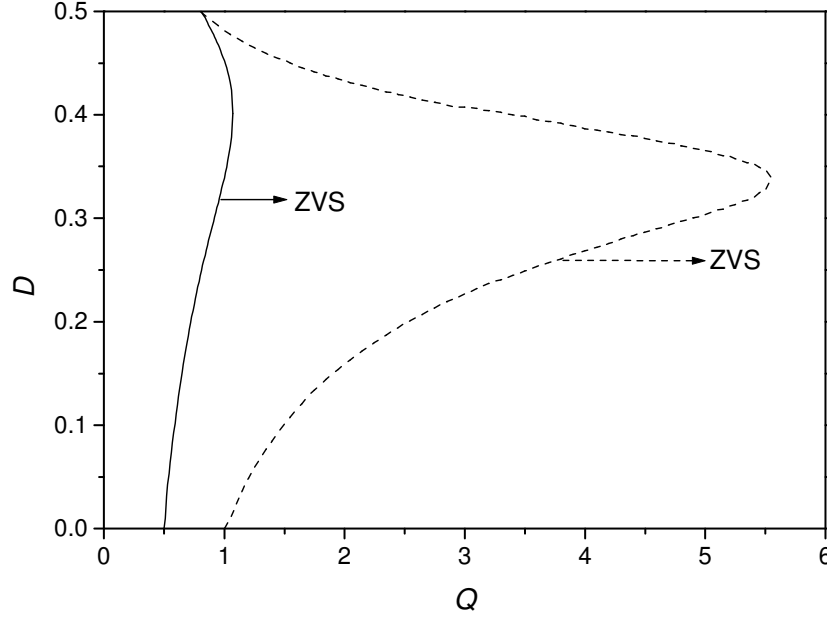


Fig. 4.11: Regions of ZVS operation of all the switches in LCL-T RC with APWM (solid line) and CM control (broken line).

CM control is another widely used fixed-frequency PWM control method. The state-space model described by (4.6) was also solved numerically under CM control to identify the region of ZVS operation of all the switches on the D - Q plane. Figure 4.11 compares the regions of ZVS operation of LCL-T RC with APWM and CM control. ZVS operation of all the switches is possible in the region to the right side of the boundary. APWM control is observed to allow ZVS operation in the entire range of D (0 to 0.5) over a wider range of Q than the CM control. Since CM control does not offer any advantage over APWM control in this regard, it is not studied and characterized any further.

4.4 Converter Design

For the design of LCL-T RC CC power supply the design specifications are: minimum and maximum value of input dc voltage ($V_{d,\min}$ and $V_{d,\max}$, respectively), maximum output current ($I_{o,\max}$), maximum load resistance ($R_{L,\max}$) corresponding to the full-load condition and switching frequency (f_s). The full-load Q (Q_{FL}) can be written as,

$$Q_{FL} = \frac{n^2 \omega_o L_1}{R_{L,\max}} = \frac{n^2 Z_n}{R_{L,\max}} \quad (4.7)$$

The expression for n , L_1 , L_2 and C_1 are derived in terms of converter's terminal parameters as follows:

$$n = \frac{\pi^2}{8} \frac{I_{o,\max} R_{L,\max} Q_{FL}}{V_{d,\min} \sin(\pi D_{\max})} \quad (4.8)$$

$$L_1 = L_2 = \frac{32}{\pi^5} \frac{V_{d,\min}^2 \sin^2(\pi D_{\max})}{I_{o,\max}^2 R_{L,\max} Q_{FL} f_s} \quad (4.9)$$

$$C = \frac{\pi^3}{128} \frac{I_{o,\max}^2 R_{L,\max} Q_{FL}}{V_{d,\min}^2 \sin^2(\pi D_{\max}) f_s} \quad (4.10)$$

The design of the converter is thus governed by the selection of Q_{FL} . The value of Q_{FL} is shown to have direct effect on the size of the reactive components, judged by the kVA/kW rating of the RIN (see Fig. 3.3). Additionally, the choice of Q_{FL} also governs the operation of converter in different modes with APWM control as described in the previous sections.

It can be observed from the D - Q plane of Fig. 4.9 that if the converter is designed in such a way that the value of Q_{FL} is greater than 1.07, then the converter can operate only in Mode-I or Mode-III for all the values of D in the range 0 to 0.5 and down to the no-load operation. In this way, the operation in Mode-II or Mode-IV can be avoided and ZVS operation of all the switches is ensured. However, this choice of Q_{FL} is different than the optimum value of $Q_{FL}=Q_{opt}=0.81$. The kVA/kW rating of the resonant tank first decreases as Q is increased, reaches minimum value at $Q=Q_{opt}$ and then again increases as Q is increased further (see Fig. 3.3). However, the increase in kVA/kW rating with increase in Q above $Q=Q_{opt}$ is not as steep as the fall in kVA/kW rating with increase in Q below $Q=Q_{opt}$. Therefore, increasing Q slightly from Q_{opt} does not result in large penalty in terms of size. Further, ϕ also does not increase significantly with increase in Q (see Fig. 4.10). Therefore for the same output power, i_{L1} also does not increase significantly. Thus the converter design with $Q_{FL} > 1.07$ does not significantly increase the size of the RIN and losses in semiconductors and it ensures ZVS operation of all the switches over the entire range of operation.

4.5 Experimental Results

A prototype half-bridge 500 W, 100 kHz converter is designed and built. The specifications and design values of the major components of the converter are summarized in Table 4.2. $Q_{FL}=1.2$ is chosen in order to have full-range ZVS operation of the switches. The Table also lists, inside the brackets, the values of the components actually used in the prototypes, which are adjusted to nearest available or realizable value. IRF 840 MOSFETs are used as the switches in the half-bridge converter. Fast-recovery diodes MUR 4100 are used for the output bridge rectifier. A 10 μ F capacitor forms the output filter in the prototype.

The experimental waveforms of v_{in} and i_{L1} demonstrating the different modes of operation are shown in Fig. 4.12. The converter was made to operate in these modes by using different combinations of D and Q , the latter being adjusted by changing the load resistance. Note that to demonstrate the converter's operation in Mode-II and Mode-IV, R_L was purposefully made higher (2000 Ω and 1000 Ω , respectively) than $R_{L,max}$ (500 Ω), thereby overloading the converter. Therefore, the waveforms of Fig. 4.12 are captured with reduced input dc voltage (50 V). The voltage waveforms in Fig. 4.12 can be observed to be cleaner in Mode-I and Mode-III

Table 4.2: Specifications and design parameters of the prototype APWM controlled LCL-T RC. The respective values actually used in the prototypes are given in the brackets.

Parameter	Value
<u>Design specifications</u>	
$2V_d$ (V)	300
$I_{o,max}$ (A)	1
$R_{L,max}$ (Ω)	500
D_{max}	0.5
f_s (kHz)	100
<u>Calculated component values</u>	
Q_{FL}	1.2
N_1/N_2	0.2025 (0.2)
C (nF)	64.72 (66)
L_1, L_2 (μ H)	39.18 (38.02)
f_s (kHz)	100

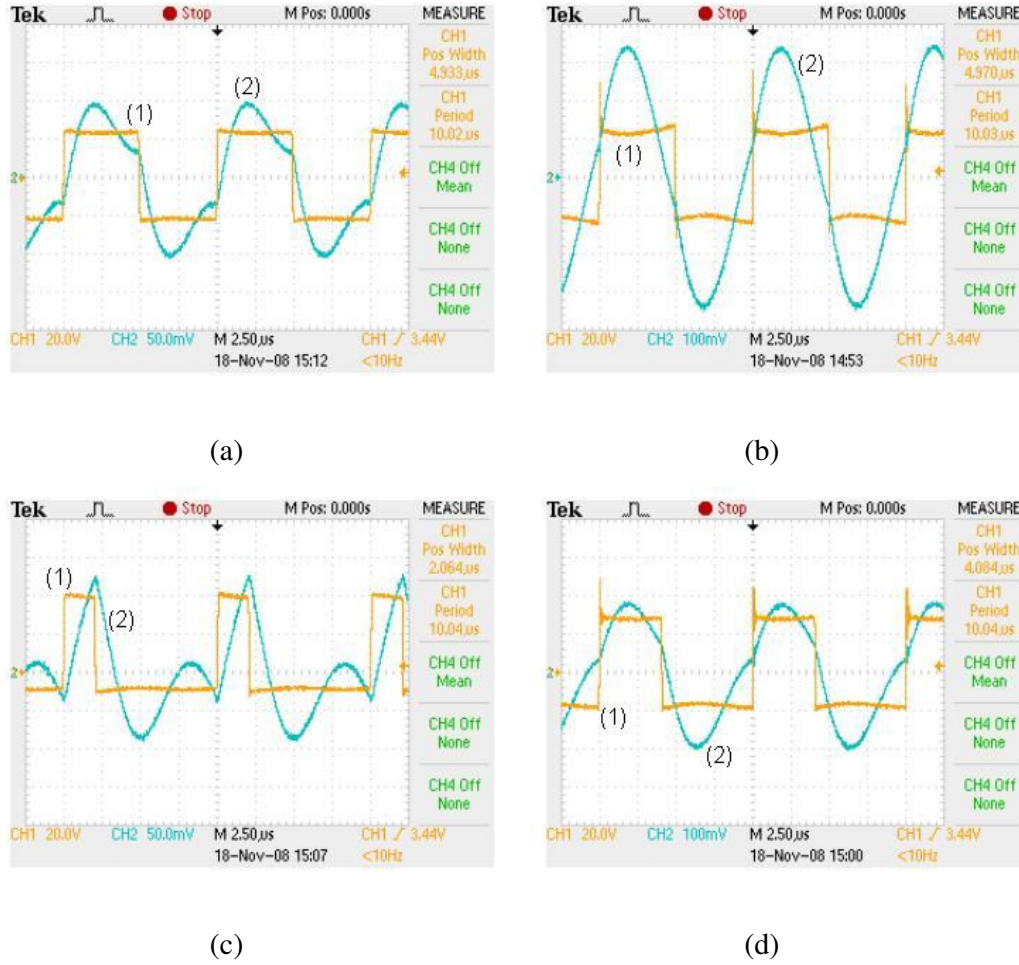


Fig. 4.12: Experimental waveforms of v_{in} [trace (1), 20 V/div] and i_{L1} [trace (2), 0.5 A/div in (a), (c) and 1 A/div in (b), (d)] in APWM controlled LCL-TRC (a) Mode-I (D=0.5, Q=1.2), (b) Mode-II (D=0.5, Q=0.3), (c) Mode-III (D=0.2, Q=1.2) and (d) Mode-IV (D=0.4, Q=0.6). X-scale: 2.5 μ s/div.

due to soft-switching. Figure 4.13 demonstrates converter's operation in the desired Mode-I and Mode-III at $Q=1.2$ with full input dc voltage (300 V).

Open-loop control characteristic of the experimental prototype at no-load ($R_L \sim 0 \Omega$) and full-load ($R_L=500 \Omega$) is obtained by measuring output current at different values of D . As shown in Fig. 4.14, the control characteristics is observed to closely match with the theoretical curve and the output current is seen to be nearly

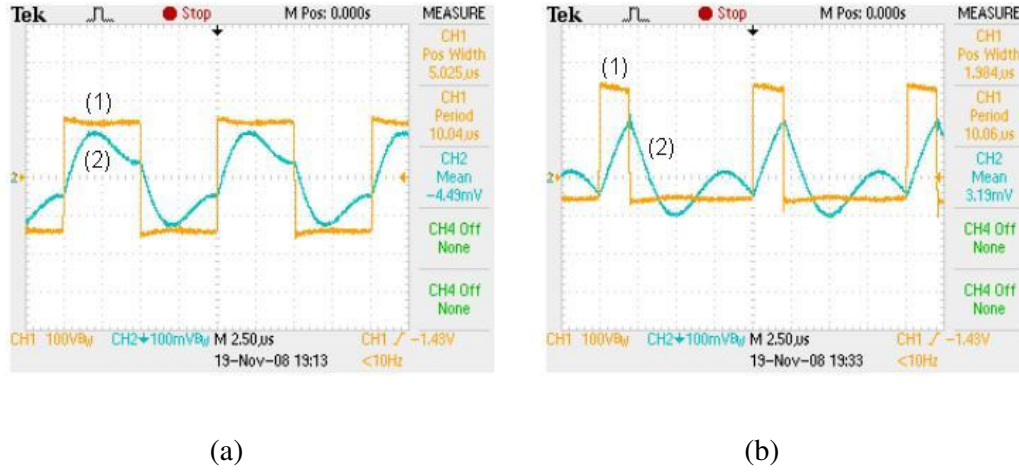


Fig. 4.13: Experimental waveforms of v_{in} [trace (1), 100 V/div] and i_{L1} [trace (2), 5 A/div] at $Q=1.2$. (a) Mode-I ($D=0.5$) and (b) Mode-III ($D=0.2$). X-scale: 2.5 μs/div.

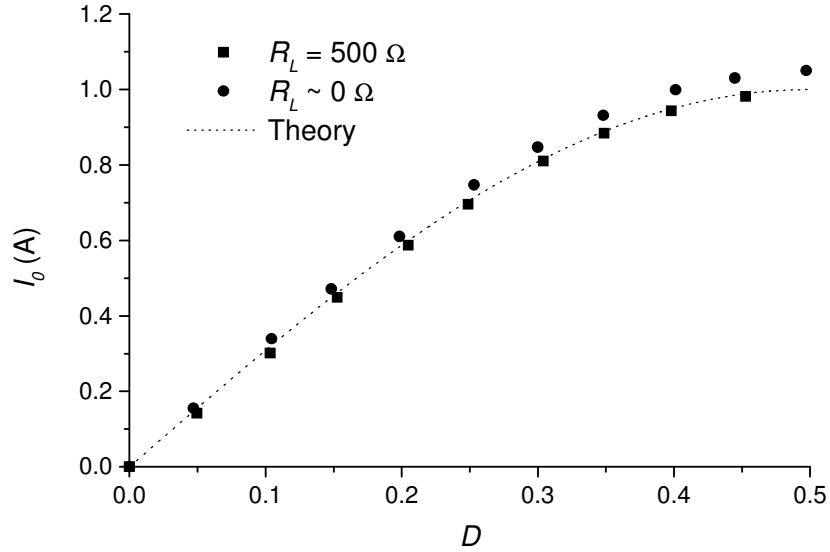


Fig. 4.14: Open-loop control characteristics of prototype APWM controlled LCL-T RC.

independent of load resistance (except for a small increase owing to the decrease in circuit drops from full-load to no-load) at all values of D .

The conversion efficiency of the prototype is measured by varying D to change the output power under different loading conditions at 300 V input dc voltage. Plots of experimental efficiency as a function of the output power are shown in Fig. 4.15. The full-load conversion efficiency of the prototype is measured to be 0.94 and

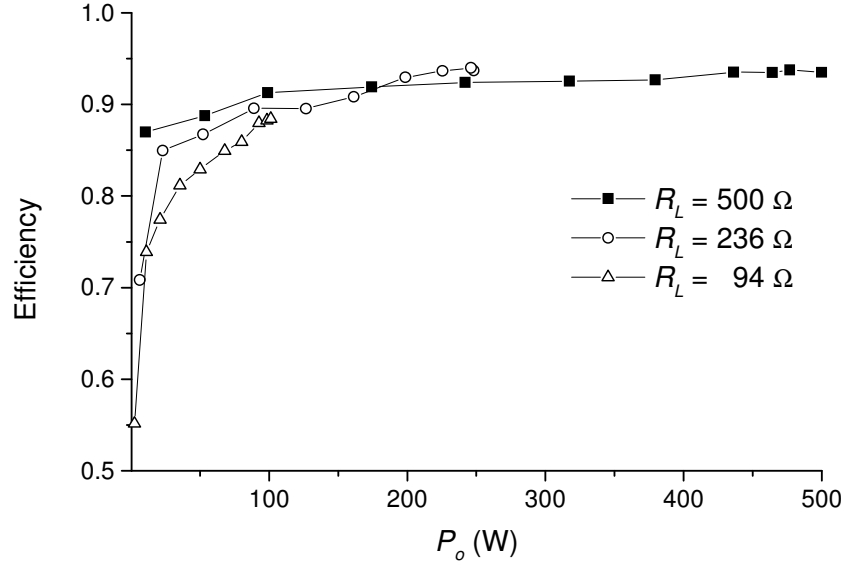


Fig. 4.15: Experimental efficiency of APWM controlled LCL-T RC.

it remains above 0.9 for 100 W – 500 W output power range at $Q=Q_{FL}$. Out of total 32 W power loss in the prototype operating at 500 W, a major portion (~20 W) is estimated to occur in the MOSFETs and diodes. The rest of the losses can be attributed largely to the core and winding loss in transformer and resonant inductor.

4.6 Conclusion

Fixed-frequency control methods need to be used with RICs since the topology behaves as a current-source only when operated at a particular frequency. Feasibility of APWM control to RICs is exemplified in this chapter with LCL-T RC. Four distinct operating modes are identified having different circuit waveforms representing different device conduction sequence, thereby creating different conditions during the device switching. The mode-boundaries are obtained and plotted on the D - Q plane. A region on the D - Q plane is identified for the converter design wherein all the switches operate with ZVS. It is observed that APWM control allows ZVS operation over a wider range than CM control. Experimental results on a prototype half-bridge 500 W, 100 kHz converter demonstrated the existence of various operating modes and the performance of APWM controlled LCL-T RC.

Chapter 5

Equivalent Circuit Modeling and Analysis

The use of equivalent circuits is a physical and intuitive approach which allows the well-known techniques of circuit analysis to be employed. Averaging has been one of the most important tools for power converter design and analysis since it adequately describes the functional relationships between sources, outputs and control parameters. Average behaviour gives information about dc or low-frequency action of the converter, ignoring ripple, commutation and other fast effects. Average model is useful in determining both static regulation and transient response and to track large-scale changes in voltages and currents as source, load or control input undergoes a change.

Fundamental frequency ac analysis of Type-II RICs presented in Chapter 2 describes the converter characteristic and component ratings in the steady-state. It does not predict the large-signal transient response and the small-signal behaviour of the converter. An approximate equivalent circuit model of Type-II RICs is derived in this chapter that predicts the averaged response of terminal voltages and currents under large-signal variation in the operating conditions. A small-signal model is subsequently derived by applying perturbation and linearization to the average model. These models are validated by comparing their transient and small-signal response with those obtained from cycle-by-cycle simulation and experiment.

5.1 Approximate Equivalent Circuit Model for Type-II RINs

The block diagram of a two-port IC is shown in Fig. 2.1. Recall that ICs exhibit immittance conversion characteristics given by (2.1) only at a particular frequency of operation and these circuits have different properties at other frequencies. For Type-II RINs, the operating frequency and the design conditions under which they exhibit immittance conversion characteristics are given in Table 2.9.

To study the small-signal behaviour of Type-II RINs, envelope simulation method using SPICE-compatible models developed in [238], [239] is used. Component values given in Table 5.1 are used to obtain input voltage-to-output current transfer functions from simulation. These values are in fact the designed component values of various prototype converters discussed in this thesis. Since small-signal behaviour of only RIN is being investigated, the transformer, rectifier, filter and load resistance connected at the output port of RIN are replaced by equivalent ac resistance (R_{ac}) whose typical value is also mentioned in Table 5.1.

Figure 5.1 shows the gain and phase response of input voltage-to-output current transfer functions in these circuits. It can clearly be seen from the plots of Fig. 5.1 that the low-frequency response of these converters is relatively flat and the state variables associated with these RINs affect the response only at the high frequencies in the vicinity of the switching frequency.

Overall response of a RIC depends on the response of RIN and its output filter. Output filter in a RIC has cut-off frequency much lower than the switching frequency. Therefore the filter response can be expected to dominate the overall low-frequency response of the whole converter. Dominant poles and response is practically important for the controller design. With this consideration and the fact that the Type-II RIN does not significantly contribute to the low-frequency response (evident from Fig. 5.1), the high-frequency behaviour of Type-II RIN can be neglected and the relationship between voltages and currents at its input and output ports of Type-II RIN can be represented by equivalent circuit using dependent sources as shown in Fig. 5.2.

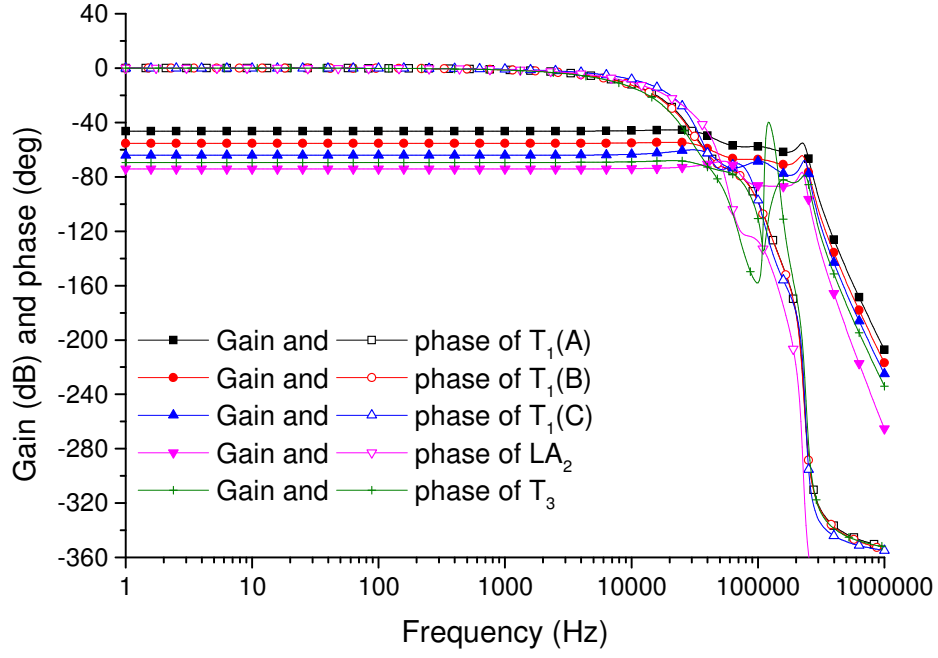


Fig. 5.1: Small-signal input voltage-to-output current transfer function for topology T_1 , LA_2 and T_3 obtained from envelop-simulation method. Component values used for simulation are given in Table 5.1.

Table 5.1: Component values used for obtaining voltage-to-output current transfer function for T_1 , LA_2 and T_3 using envelop-simulation method.

	T_1 (A)	T_1 (B)	T_1 (C)	LA_2	T_3
L_1 (μH)	16.11	25.6	39.18	77.7	48.4
L_2 (μH)	16.11	25.6	39.18	44.63	72.6
C_1 (μF)	0.151	0.1	0.065	0.047	0.047
C_2 (μF)	-	-	-	0.020	0.094
R_{ac} (Ω)	10.13	16.21	16.62	40.52	26.41
f_s (kHz)	100	100	100	83.28	105

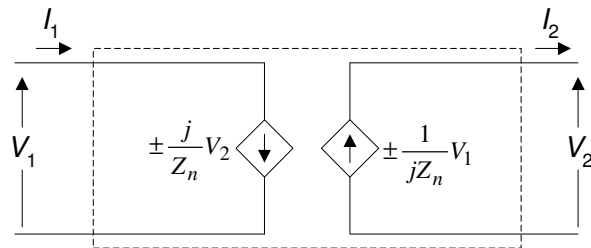


Fig. 5.2: Equivalent circuit representation of Type-II RIN.

5.2 Construction of Equivalent Circuit Model

Type-II RIN, constituted by reactive elements and having low-pass or band-pass characteristics is embedded in a switching power converter to form a RIC. Generic block diagram of a RIC is shown in Fig. 2.5. For a voltage-source or Type-II dc-dc RIC, the block diagram can be redrawn as shown in Fig. 5.2. The shaded portion shows the power converter circuit with a square-wave high-frequency inverter at the input side of Type-II RIN and a rectifier at the output side of the RIN.

While a Type-II RIN, can be represented by an equivalent circuit of Fig. 5.2, nonlinear elements of a RIC (inverter and rectifier at the input and output side, respectively) do not directly allow simpler equivalent circuit representation of complete RIC. If the shaded portion can be represented using an equivalent circuit describing the terminal relationship in terms of average values of v_d , i_d and v_o , i_r , the task of circuit analysis would greatly be simplified since the rest of the circuit elements are linear.

Idealized circuit operating waveforms at the input and output port of the shaded portion of the block diagram are shown in Fig. 5.4. While the waveforms at the input and output port of Type-II RIN are square-wave, the currents are drawn to be sinusoidal. This is consistent with the definition of a RC stating that the RN (Type-II RIN in this case of Type-II RICs) has low-pass or band-pass characteristics and power is transferred primarily via the fundamental components, whereas the harmonics contribute little to power transfer from input to output.

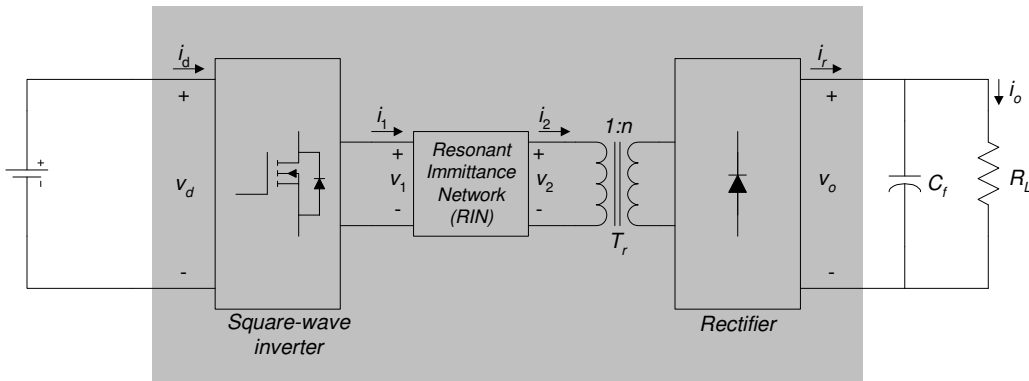


Fig. 5.3: Block diagram of a voltage-source Type-II RIC.

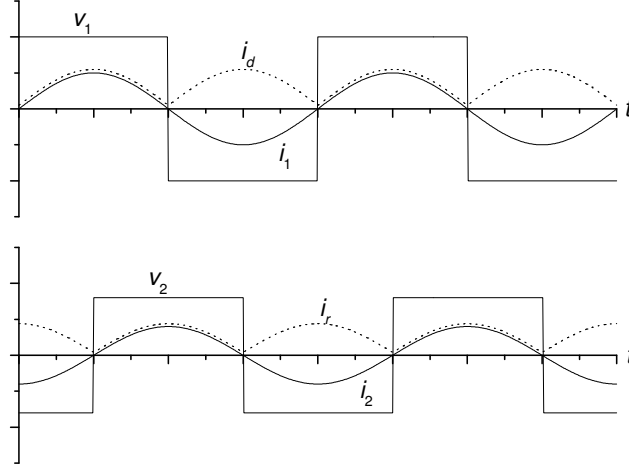


Fig. 5.4: Idealized circuit operating waveforms at the input and output port of the shaded portion of the block diagram.

The following relationships can readily be derived from the waveforms of Fig. 5.4. The average values of i_d and i_r are given by,

$$\langle i_d(t) \rangle_{T_s} = \frac{2\sqrt{2}I_1}{\pi} \quad (5.1)$$

$$\langle i_r(t) \rangle_{T_s} = \frac{2\sqrt{2}I_2}{n\pi} \quad (5.2)$$

wherein, $\langle x(t) \rangle_{T_s}$ denotes the average of $x(t)$ over an interval of one period T_s :

$$\langle x(t) \rangle_{T_s} = \frac{1}{T_s} \int_t^{t+T_s} x(\tau) d\tau \quad (5.3)$$

I_1 and I_2 are the rms values of i_1 and i_2 , respectively. Similarly, the rms values of the fundamental components of v_1 and v_2 (V_1 and V_2 , respectively) are given in terms of the dc input and output voltage (V_d and V_o , respectively) as,

$$V_1 = \frac{2\sqrt{2}\langle v_d(t) \rangle_{T_s}}{\pi} \quad (5.4)$$

$$V_2 = \frac{2\sqrt{2}\langle v_o(t) \rangle_{T_s}}{n\pi} \quad (5.5)$$

Substituting (5.1), (5.2), (5.4) and (5.5) in (2.1) and neglecting the phasor terms for dc quantities, we get:

$$\begin{bmatrix} \langle v_d(t) \rangle_{T_s} \\ \langle i_d(t) \rangle_{T_s} \end{bmatrix} = \begin{bmatrix} 0 & \rho \\ \rho^{-1} & 0 \end{bmatrix} \cdot \begin{bmatrix} \langle v_o(t) \rangle_{T_s} \\ \langle i_r(t) \rangle_{T_s} \end{bmatrix} \quad (5.6)$$

wherein,

$$\rho = \frac{\pi^2}{8} n Z_n \quad (5.7)$$

Thus the shaded portion of Fig. 5.2, whose terminal quantities are related as described by (5.6), can be represented by an equivalent circuit as shown in Fig. 5.5(a). Connecting source and load at the input and output terminals of the equivalent circuit, an equivalent circuit model of Type-II RIC can be constructed as shown in Fig. 5.5(b). This equivalent circuit model can be analyzed using the classical circuit theory to determine the steady-state characteristics as well as the transient response to track averaged large-scale changes in terminal voltages and currents as the source or load undergoes a change. Alternatively, the equivalent circuit can directly be simulated with various circuit simulation tools to directly obtain the averaged terminal response.

To construct a small signal ac model at a quiescent operating point it is assumed that the input voltage is equal to some given quiescent value V_d plus some superimposed small ac variation $\hat{v}_d(t)$. Therefore, we have,

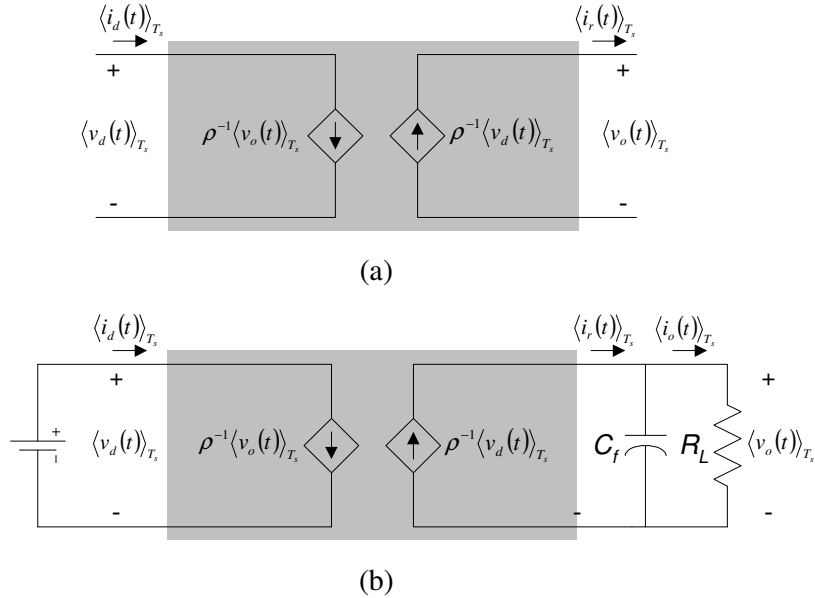


Fig. 5.5: Equivalent circuit model of (a) shaded portion of the block diagram of Fig. 5.2 and (b) Type-II RIC.

$$\langle v_d(t) \rangle_{T_s} = V_d + \hat{v}_d(t) \quad (5.8)$$

In response to this input, after the transients have subsided, averaged input current $\langle i_d(t) \rangle_{T_s}$, averaged rectified output current $\langle i_r(t) \rangle_{T_s}$ and averaged output voltage $\langle v_o(t) \rangle_{T_s}$ will be equal to corresponding quiescent values I_d , I_r and V_o , plus some superimposed small ac variations, $\hat{i}_d(t)$, $\hat{i}_r(t)$ and $\hat{v}_o(t)$, respectively. Therefore, we have,

$$\langle i_d(t) \rangle_{T_s} = I_d + \hat{i}_d(t), \langle i_r(t) \rangle_{T_s} = I_r + \hat{i}_r(t) \text{ and } \langle v_o(t) \rangle_{T_s} = V_o + \hat{v}_o(t) \quad (5.9)$$

Substituting (5.8) and (5.9) in (5.6) and simplifying, we get,

$$\begin{bmatrix} \hat{v}_d(t) \\ \hat{i}_d(t) \end{bmatrix} = \begin{bmatrix} 0 & \rho \\ \rho^{-1} & 0 \end{bmatrix} \cdot \begin{bmatrix} \hat{v}_o(t) \\ \hat{i}_r(t) \end{bmatrix} \quad (5.10)$$

This relationship in the small-signal quantities can be represented by an equivalent circuit shown in Fig. 5.6(a). Subsequently, small-signal ac equivalent circuit model of Type-II RIC can be constructed by connecting the remaining circuit element as shown in Fig. 5.6(b), which can easily be analyzed or simulated to derive line-to-output transfer functions and the input impedance to be:

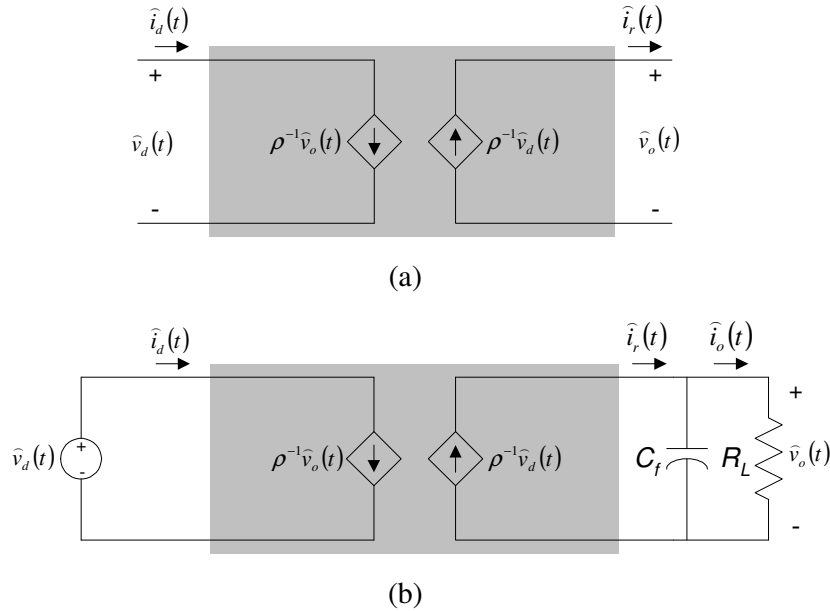


Fig. 5.6: Small-signal ac equivalent circuit model of (a) shaded portion of the block diagram of Fig. 5.2 and (b) Type-II RIC.

$$G_1(s) = \frac{\hat{i}_o(s)}{\hat{v}_d(s)} = \frac{1}{\rho} \frac{1}{1 + sR_L C_f} \quad (5.11)$$

$$G_2(s) = \frac{\hat{v}_o(s)}{\hat{v}_d(s)} = \frac{R_L}{\rho} \frac{1}{1 + sR_L C_f} \quad (5.12)$$

$$Z_{in}(s) = \frac{\hat{v}_d(s)}{\hat{i}_d(s)} = \frac{\rho^2}{R_L} (1 + sR_L C_f) \quad (5.13)$$

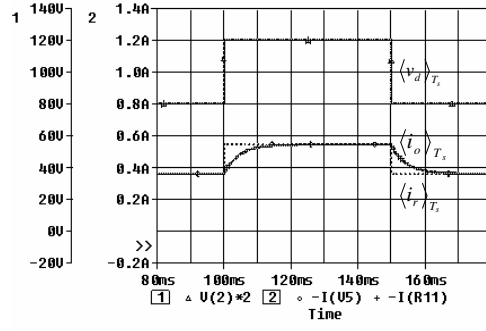
5.3 Simulation and Experimental Results

Equivalent circuit model of Type-II RICs of Fig. 5.5 and small-signal model of Fig. 5.6 greatly simplifies the prediction of averaged response of terminal voltages and currents under large-signal variation in operating conditions, derivation of small-signal transfer function and visualization of frequency response, either via simple analytical treatment or by using the model in circuit simulation tools.

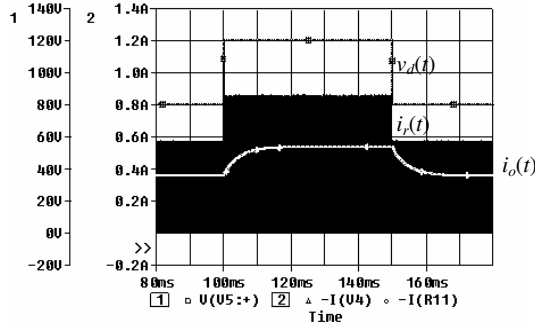
To validate, these models are implemented in OrCad PSpice 9.1 and results are compared with those obtained from cycle-by-cycle simulation as well as the experimental prototype of topology T_3 (described in section 3.3.3 and parameters listed in section 3.3). Filter capacitor C_f is 47 μ F. With $Z_n = 32.09$ ($L_1 = 48.4$ μ H and $C_1 = 47$ nF) and $n = 2.77$, ρ is calculated from (5.7) to be 109.66.

Figure 5.7 (page 134) shows the response of the converter operating with $R_L = 94$ Ω when input dc voltage ($2V_d$) undergoes a step change from 80 V to 120 V and vice versa. Similarly, Fig. 5.8 (page 135) shows the response of the converter with step change in R_L from 47 Ω to 94 Ω and vice versa. In Fig. 5.7 and Fig. 5.8, part (a) is obtained from the simulation of the equivalent circuit model, part (b) is obtained from the cycle-by-cycle simulation of the converter and part (c) shows the experimental results. The following observations are made from these results:

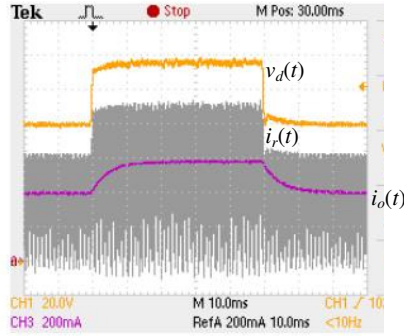
1. The results of equivalent circuit model are in excellent agreement with those obtained from the cycle-by-cycle simulation and experiment, thereby confirming the validity of proposed model.
2. In Fig. 5.7, the waveform of $i_r(t)$ (or, $\langle i_r \rangle_{T_s}$) almost instantaneously follows applied step variation in $v_d(t)$ (or, $\langle v_d \rangle_{T_s}$). However, the response of $i_o(t)$



(a)



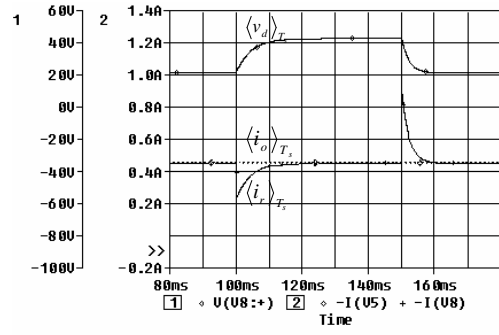
(b)



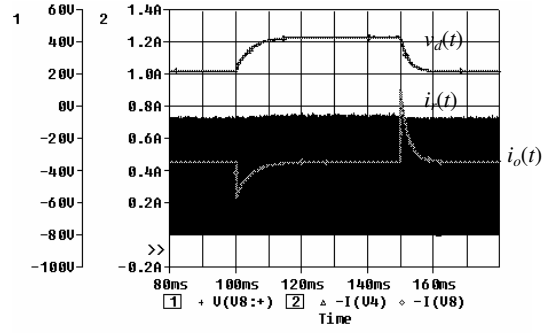
(c)

 Fig. 5.7: Response of Topology T_3 to step change in input dc voltage.

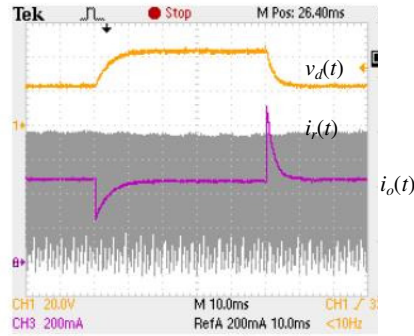
- (a) Predicted average response from the equivalent circuit model. Top trace: $\langle v_d \rangle_{T_s}$, dotted trace: $\langle i_r \rangle_{T_s}$ and continuous trace: $\langle i_o \rangle_{T_s}$. (b) Results of cycle-by-cycle simulation. (c) Experimental results. In (b) and (c), the waveform at the top shows $v_d(t)$, the envelope shows $i_r(t)$ and the trace at the bottom shows $i_o(t)$.



(a)



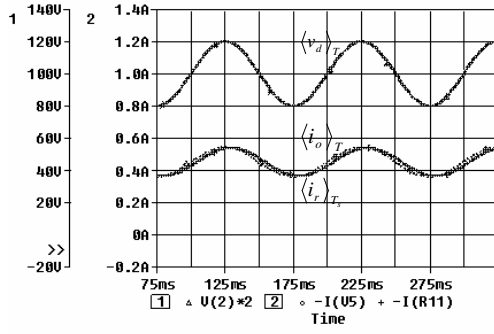
(b)



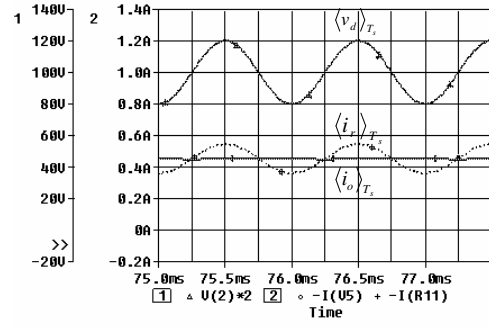
(c)

 Fig. 5.8: Response of Topology T_3 to step change in R_L .

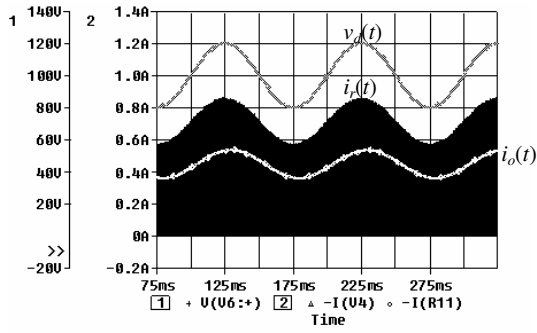
(a) Predicted average response from the equivalent circuit model. Top trace: $\langle v_o \rangle_{T_s}$, dotted trace: $\langle i_r \rangle_{T_s}$ and continuous trace: $\langle i_o \rangle_{T_s}$. (b) Results of cycle-by-cycle simulation. (c) Experimental results. In (b) and (c), the waveform at the top shows $v_o(t)$, the envelope shows $i_r(t)$ and the trace at the bottom shows $i_o(t)$.



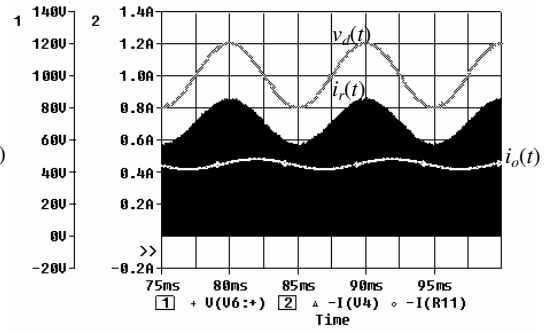
(a₁)



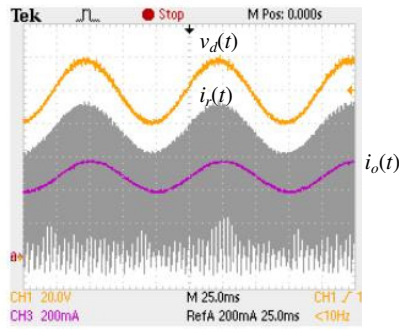
(b₁)



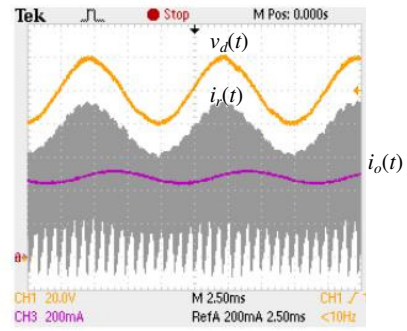
(a₂)



(b₂)

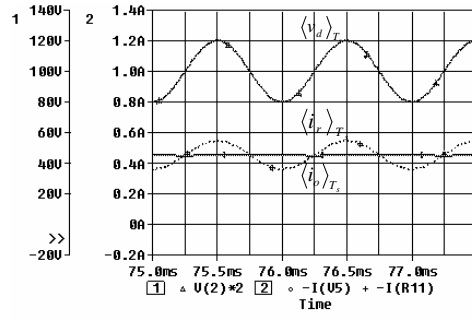


(a₃)

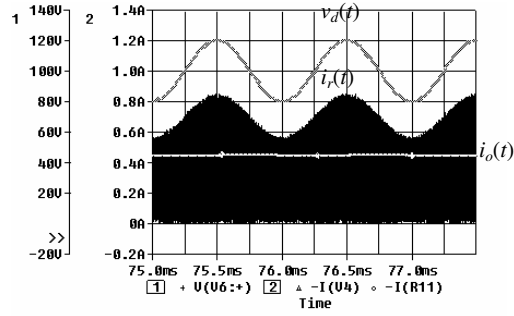


(b₃)

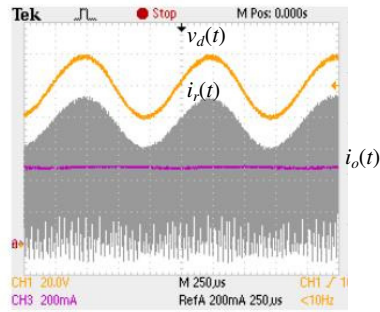
Fig. 5.9: Response of Topology T_3 to sinusoidal perturbations in dc voltage. (cont.)



(a)



(b)



(c)

Fig. 5.9: Response of Topology T_3 to sinusoidal perturbations in dc voltage. (a₁)-(a₃): 10 Hz, (b₁)-(b₃): 100 Hz and (c₁)-(c₃): 1000 Hz.. Parts (a₁), (b₁) and (c₁) show the predicted average response from the equivalent circuit model [Top trace: $\langle v_d \rangle_{T_s}$, dotted trace: $\langle i_r \rangle_{T_s}$ and continuous trace: $\langle i_o \rangle_{T_s}$]. Parts (a₂), (b₂) and (c₂) show the results of cycle-by-cycle simulation. Parts (a₃), (b₃) and (c₃) show the experimental results. In (b₂)-(b₃) and (c₂)-(c₃), the waveform at the top shows $v_d(t)$, the envelope shows $i_r(t)$ and the trace at the bottom shows $i_o(t)$.

(or, $\langle i_o \rangle_{T_s}$) is governed by the output filter.

3. In Fig. 5.8, $i_r(t)$ (or, $\langle i_r \rangle_{T_s}$) is almost constant under the transient condition following the step change in R_L . The waveform of $i_o(t)$ (or, $\langle i_o \rangle_{T_s}$) shows transient undershoot and overshoot due to additional current absorbed or delivered by C_f to maintain the charge balance with varying $v_o(t)$ (or, $\langle v_o \rangle_{T_s}$) due to changing R_L .
4. The proposed equivalent circuit model simplifies and speeds up the large signal transient analysis of the converter. Simulation of the model takes a few seconds in contrast to 10s of minutes required for cycle-by-cycle simulation.

The results of Fig. 5.9 (pages 136 and 137) which show that perturbations in $i_r(t)$ (or, $\langle i_r \rangle_{T_s}$) are in phase with the sinusoidal perturbations in $v_d(t)$ (or, $\langle v_d \rangle_{T_s}$) over a wide range of frequency (1 Hz to 1000 Hz). However, perturbations in $i_o(t)$ (or, $\langle i_o \rangle_{T_s}$) are significantly attenuated and shifted in phase at higher frequencies due to output filter capacitor. Figure 5.10 shows these waveforms obtained using cycle-by-cycle simulation at 10 kHz and 50 kHz modulation frequency. $i_r(t)$ follows $v_d(t)$ at 10 kHz. However, the effect of Type-II RIN at 50 kHz as predicted in Fig. 5 is also seen in Fig. 5.10(b), wherein $i_r(t)$ significantly lags $v_d(t)$. While the results of Fig. 5.9 establish the concurrence among the predicted, simulated and experimental results, the simulation results of Fig. 5.10 could not be validated experimentally due to non-availability of a high frequency power source.

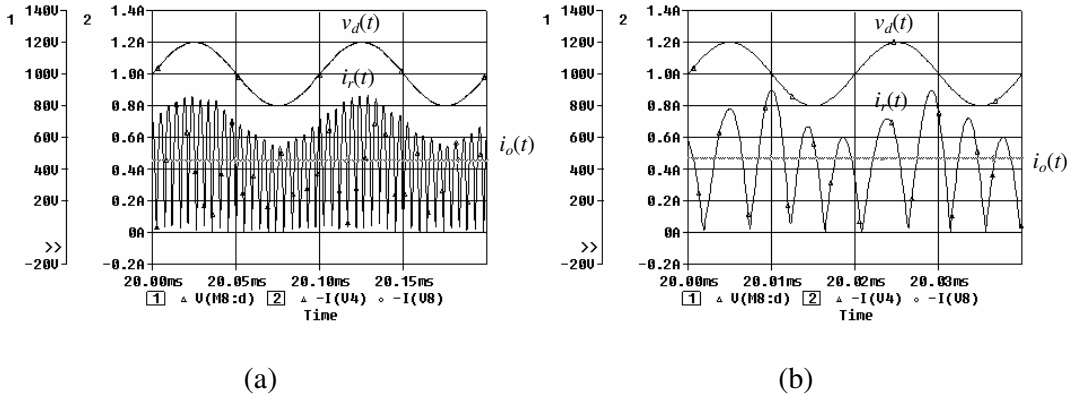


Fig. 5.10: Simulated response of Topology T₃ to sinusoidal perturbations in dc voltage at (a) 10 kHz and (b) 50 kHz. Waveform from top to bottom: $v_d(t)$, $i_r(t)$ and $i_o(t)$.

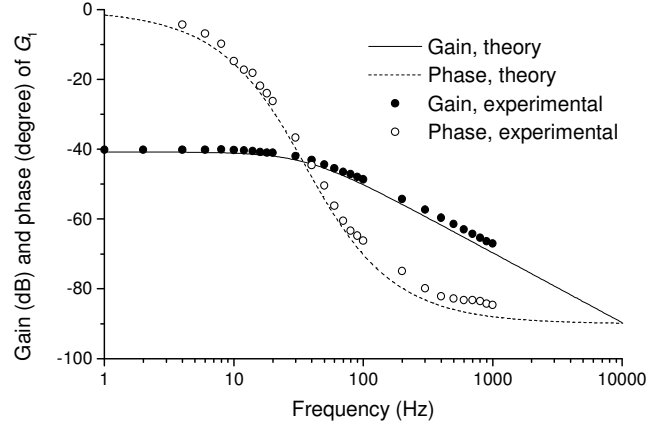


Fig. 5.11: Theoretical and experimental line-to-output small-signal transfer function of Topology T_3 .

Finally, converter's line-to-output small-signal transfer function given by (5.11) with $C_f = 47 \mu\text{F}$, $R_L = 94 \Omega$ and $\rho = 109.66$, is found to be in excellent agreement with experimental observations as shown in Fig. 5.11.

5.4 Conclusion

Equivalent circuit model of Type-II RICs is proposed. Subsequently, a small-signal model is derived for derivation of small-signal transfer function and visualization of frequency response. These models greatly simplifies and speeds-up the analysis either via simple analytical treatment or by using the model in circuit simulation tools. The models are validated by comparison with the cycle-by-cycle simulation and experimental results.

It is observed that the low-frequency open-loop transient and small-signal ac behaviour of Type-II RIC is governed by only the filter and the converter along with RIN does not contribute to the low-frequency dynamics.

Chapter 6

Application Examples

The property of Type-II RICs that it converts a voltage source into a current source is very useful in variety of applications wherein a CC source is either inherently required or can be advantageously applied. These application areas include:

1. Capacitor charging power supplies,
2. Battery chargers,
3. Laser diode drivers,
4. Power supplies for electromagnets,
5. Power supplies for electro-chemical processes,
6. HV DC power supplies,
7. CC and CCCV power supplies for electric arc welding,
8. Illumination systems, etc.

Applicability of Type-II RIC topologies in some of these application areas is discussed in this chapter.

6.1 HV DC Power Supply

Design of a HV power supply is complex because of high L_{lk} and significant C_w associated with the transformer. Since these parasitic components can easily be

integrated as a part of RN, RCs are popularly applied for these applications. The SRC, PRC and LCC RC [206]-[209] have been extensively explored in the past.

Type-II RICs can be an attractive alternative for HV power supplies due to the following merits:

1. Partial discharge and arcing can occur frequently in HV loads. Since Type-II RICs behave as an inherent CC source, semiconductor devices are inherently protected against these faults.
2. HV power supplies required for sensitive and expensive loads like klystrons need to have minimum energy storage in the output filter as stored energy is dissipated in the load in case of arcing. Fast closing switches (sparkgap, thyatron, ignitron, light activated thyristors) operating in parallel to the klystron path (known as crowbars) are used for protection. To avoid false firing and reliability issues of crowbars, a crowbar-less power supply is preferred wherein stored energy in the power supply is kept less than the maximum energy handling capability of klystron. Multiphase Type-II RIC is a potential alternative for such applications since phase-staggered operation can reduce (or even eliminate) filter capacitor and the stored energy.
3. Some of Type-II RICs absorb L_{lk} and C_w in the RIN.

6.1.1 Suitable Type-II RIC Topologies

LCL-T RC is the simplest Type-II RIC topology with three reactive elements. While L_{lk} is absorbed into the RIN, C_w is not gainfully utilized and the latter can significantly affect the converter characteristics.

Some of Type-II RIC topologies, namely, T_2 - T_4 , T_7 , T_9 , P_1 , P_2 , P_4 - P_6 , LA_1 - LA_6 are suitable for application in HV power supply since L_{lk} and C_w is absorbed as a part of RIN.

A simplified analysis is first presented to quantify the effect of C_w in LCL-T RC. Subsequently issues in the design of topology LA_2 or LC-LC RC in the most practical case, experimental results on a prototype converter and performance comparison of LC-LC RC with LCL-T RC are described.

6.1.2 Effect of C_w on LCL-T RC

The circuit diagram of half-bridge LCL-T RC is shown in Fig. 6.1, in which L_{lk} , and C_w are shown explicitly in the transformer lumped-element equivalent model inside the shaded area. $C_w' = C_w/n^2$ is the winding capacitance referred to the secondary side.

LCL-T RC behaves as a constant current source if inductances $L_t (=L_2 + L_{lk})$ and L_1 are equal and if circuit is operated at the resonant frequency $\omega_o = 1/\sqrt{L_1 C_1}$. Under these conditions current i_{L_t} in inductors L_2 and L_{lk} is constant and independent of load resistance. Since the power transfer to output is primarily via the fundamental component of square-wave input v_{in} , current i_{L_t} is nearly sinusoidal and can be expressed as,

$$i_{L_t} = I_{L_t, pk} \sin \omega t \quad (6.1)$$

wherein, $I_{L_t, pk}$ is the amplitude of i_{L_t} and is derived from (3.18) as,

$$I_{L_t, pk} = \frac{4 V_d}{\pi Z_n} \quad (6.2)$$

In order to approximately quantify the effect of C_w on output current regulation, it is assumed that C_w does not significantly change the operation of preceding LCL-T RIN. Input half-bridge converter and RIN of LCL-T RC are thereby replaced by the sinusoidal current source i_{L_t} in an equivalent circuit shown in Fig. 6.2(a). Output filter capacitor C_f is assumed to be large so that the output voltage is ripple free. Figure 6.2(b) shows the key waveforms in the equivalent circuit.

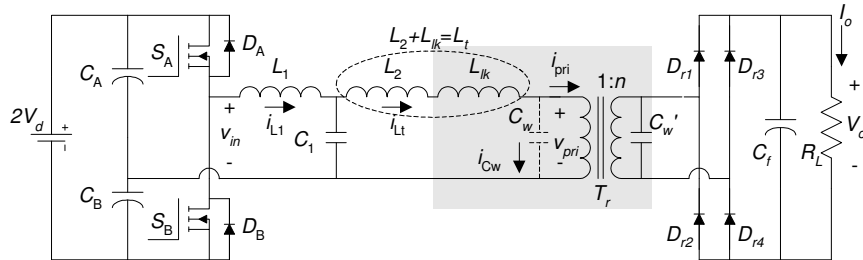
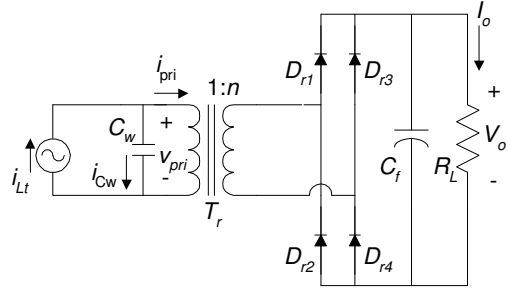
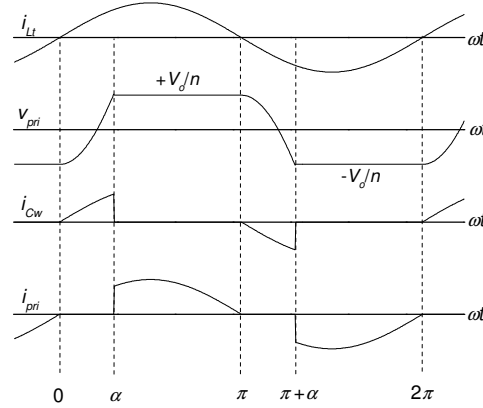


Fig. 6.1: Circuit diagram of half-bridge LCL-T RC. Transformer L_{lk} and C_w are shown explicitly inside the shaded area.



(a)



(b)

Fig. 6.2: (a) Equivalent circuit diagram of the output stage of LCL-T RC and (b) its waveforms for analysis of the effect of C_w .

In the absence of C_w , transformer primary voltage, v_{pri} , is square-wave of amplitude $\pm V_o/n$ and in phase with i_{Lt} . Presence of C_w slows down the transition of v_{pri} from $+V_o/n$ to $-V_o/n$ and vice versa.

For $\omega t < 0$, i_{Lt} is negative. On the secondary side of T_r , diodes D_{r2} and D_{r3} conduct clamping v_{pri} to $-V_o/n$. At $\omega t = 0$, i_{Lt} reverses its direction, thereby turning D_{r2} and D_{r3} off. However, D_{r1} and D_{r4} are not forward biased until capacitor C_w is discharged from $-V_o/n$ and charged to $+V_o/n$. Therefore immediately after $\omega t > 0$, i_{Lt} flows through C_w and v_{pri} can be derived as,

$$v_{pri} = -\frac{V_o}{n} + \frac{I_{Lt, pk}}{\omega C_w} (1 - \cos \omega t) \quad (6.3)$$

This mode of operation ends at $\omega t = \alpha$, when v_{pri} reaches $+V_o/n$, thereby causing D_{r1} and D_{r4} to conduct. From (6.3),

$$\alpha = \cos^{-1} \left(1 - \frac{2V_o \omega C_w}{n \hat{I}_{Lr}} \right) \quad (6.4)$$

which can be simplified as,

$$\alpha = \cos^{-1} \left(\frac{1 - \frac{2\psi}{\pi Q}}{1 + \frac{2\psi}{\pi Q}} \right) \quad (6.5)$$

where $Q = \frac{n^2 Z_n}{R_L}$, and $\psi = \frac{C_w}{C_1}$.

For the interval $\alpha < \omega t < \pi$, D_{r1} and D_{r4} conduct clamping v_{pri} to $-V_o/n$. The operation for the next half-cycle is similar to the above. The average value of rectified output current can be derived as,

$$I_o = \frac{V_d}{Z_n} \frac{4}{n\pi^2} (1 + \cos \alpha) \quad (6.6)$$

From (6.5) and (6.6), the current gain, H , of the converter can be expressed as,

$$H = \frac{nI_o}{V_d/Z_n} = \frac{8}{\pi^2} \left(\frac{1}{1 + \frac{2\psi}{\pi Q}} \right) \quad (6.7)$$

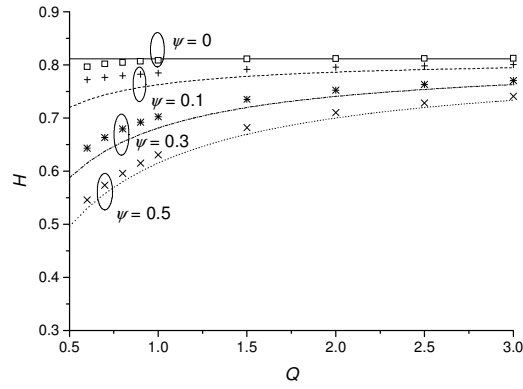
At $Q = Q_{opt}$, we get,

$$H|_{Q=Q_{opt}} = \frac{8}{\pi^2} \left(\frac{1}{1 + \frac{\pi}{4}\psi} \right) \quad (6.8)$$

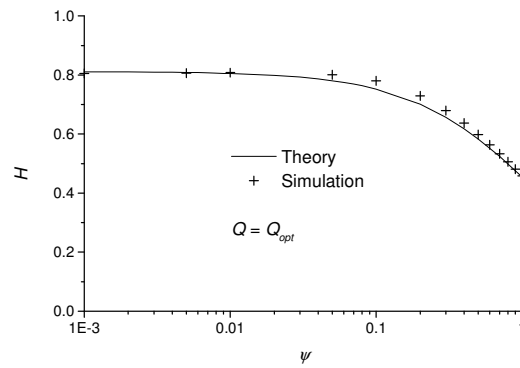
Using (6.7), variation of H as a function of load (that is, Q) for different values of ψ is plotted in Fig. 6.3(a). The curves are compared with the results obtained from simulation which are shown by markers. The circuit parameters used for simulation are given in Table 6.1. The simulation results, normalized according to the definition of H given in (3.5) and plotted in Fig. 6.3, are seen to match adequately with the prediction of simplified analysis. The average output current of LCL-T RC decreases as C_w increases.

Table 6.1: Specifications and design parameters of the converter used for simulation studies to compare the analytical and simulation results as shown in Fig. 6.3.

Parameter	Value
<u>Specifications</u>	
I_o (A)	1
V_o (V), maximum	500
$2 V_d$ (V)	200
F_s (kHz)	100
<u>Designed component values</u>	
L_1 (μ H)	25.8
L_t (μ H)	25.8
C_1 (μ F)	0.098
N_1/N_2	0.2



(a)



(b)

Fig. 6.3: Effect of C_w on the current gain of LCL-T RC. (a) Variation of H as a function of Q . (b) Variation of H as a function of ψ at $Q=Q_{opt}$. Markers show the data points obtained from simulation.

Further, the output current drops from its no-load value progressively with increase in load (that is, with reduction in Q). Thus the converter loses its current-source behaviour under the influence of C_w . Similarly, plots of (6.8) along with simulation results are shown in Fig. 6.3(b). The plot indicates that the drop in output current is more significant if $\psi > 0.2$. Therefore, it is important to limit C_w within 20% of C_1 .

To compensate for the drop in output current due to C_w , n needs to be increased to achieve maximum output voltage $V_{o,\max}$ at full-load $Q=Q_{FL}$ and minimum input dc voltage $V_{d,\min}$. An expression for n can be derived using (6) and (7) as,

$$n = \frac{\pi^2}{8} Q_{FL} \left(1 + \frac{2}{\pi} \frac{\psi}{Q_{FL}} \right) \left(\frac{V_{o,\max}}{V_{d,\min}} \right) \quad (6.9)$$

At $Q=Q_{opt}$, (6.9) reduces to,

$$n|_{Q=Q_{opt}} = \left(1 + \frac{\pi}{4} \psi \right) \left(\frac{V_{o,\max}}{V_{d,\min}} \right) \quad (6.10)$$

6.1.3 Design of Topology LA₂ as a HV Power Supply

The presence of C_w , in fact, changes the third-order LCL-T resonant tank into a fourth-order LC-LC circuit (Topology LA₂), which is also a Type-II RIC. Thus both the L_{lk} and C_w are gainfully absorbed in the RN. Steady-state characteristics of LC-LC RC is described in section 3.2. Although an optimization method described in section 3.2 uniquely identifies ψ_{opt} and Q_{opt} , it would be practically difficult to ensure $\psi = \psi_{opt}$ by design. This is because the prediction of C_w is intricate and its actual value is prone to significant variation due to tolerances in winding and spacing. Therefore in the most practical case, the following steps can be followed to design the converter:

1. Design the converter as LCL-T RC neglecting C_w as described in section 3.1 with $Q_{FL} = Q_{opt} = 8/\pi^2$ and obtain the values of L_1 , $L_t = L_2 + L_{lk}$, C_1 and n .
2. Make the transformer and measure L_{lk} and C_w . Determine $\psi = C_w/C_1$.
3. The values of resonant inductors to be placed in the circuit can then be found out as: $L_2 = L_t - L_{lk}$, and, $L_1 = \gamma L_t = (1 - \psi)L_t$.

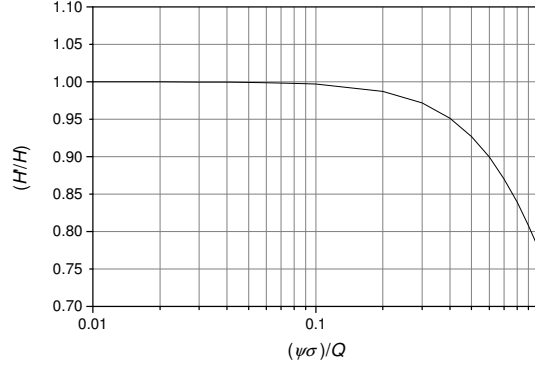


Fig. 6.4: Plot of ratio (H'/H) as a function of $(\psi\sigma/Q)$ showing the effect of manufacturing tolerances in C_w on the current gain of LC-LC RC at $\omega_n = 1$.

The actual value of C_w is affected by manufacturing tolerances and its value can vary from piece-to-piece. To quantify the effect, let $\pm\Delta C_w$ be the variation in C_w due to manufacturing tolerances. Ratio ψ modifies to ψ' , given as,

$$\psi' = \frac{C_w \pm \Delta C_w}{C_1} = \psi(1 \pm \sigma) \quad (6.10)$$

where, $\sigma = (\Delta C_w / C_w)$. Due to this, the condition (3.29) is not followed strictly and the modified current gain, H' , becomes a weak function of Q at $\omega_n = 1$. The ratio (H'/H) can be derived as,

$$\left. \frac{H'}{H} \right|_{\omega_n=1} = \frac{1}{\sqrt{1 + \left(\frac{8}{\pi^2} \frac{\psi\sigma}{Q} \right)^2}} \quad (6.11)$$

Figure 6.4 shows the variation of (H'/H) as a function of a dimensionless parameter $(\psi\sigma/Q)$. To limit degradation of current gain due to manufacturing tolerances in C_w to say 5%, $(\psi\sigma/Q)$ must be limited to 0.4. For instance, this means if $Q_{FL} = \frac{8}{\pi^2}$, $\psi\sigma \leq 0.324$. So, if $\psi = 0.5$, $\sigma \leq 0.648$, which is easily achievable. Note that if ψ is lower, the constraint on σ is further relaxed.

6.1.4 Experimental Results

A 100 mA, 2 kV laboratory prototype has been designed, built and tested to experimentally validate the effect of C_w on output characteristic of LCL-T RC and improvement with its design as LC-LC RC. The specifications are: input dc voltage ($2V_d$) = 200 V, output current = 100 mA, maximum load resistance (full load) = 20 k Ω , switching frequency = 100 kHz. Designing the converter for $Q_{FL} = 8/\pi^2$ leads to $n=20$ and the values of reactive components are calculated as: $L_1=L_r=64.49$ μ H and $C_1=0.039$ μ F. The closest off-the-shelf available value of C_1 is 0.047 μ F. Accordingly the value of L_r is scaled to 77.7 μ H to retain same Z_n . The resonant and switching frequency is therefore modified to 83.66 kHz. The transformer has been made in EE42.21.20 ferrite core with 10 primary turns and 200 secondary turns. L_{lk} is measured to be 1.1 μ H. Therefore L_2 is chosen to be 76.6 μ H to get $L_r = 77.7$ μ H. C_w is measured to be 0.02 μ F. IRF 840 MOSFETs are used as the switches S_A and S_B in half-bridge converter and four MUR 4100 diodes connected in series are used as diodes D_{r1} through D_{r4} for rectifier on secondary side. A 0.22 μ F, 5000 V capacitor forms output filter in the prototype. This experimental prototype is operating in open loop without any feedback control. Fig. 6.5 shows the photograph of the experimental prototype.

In order to experimentally quantify the effect of C_w , converter is first configured as LCL-T RC with $L_1=L_r=77.7$ μ H and $C_1=0.047$ μ F. R_L is varied in steps

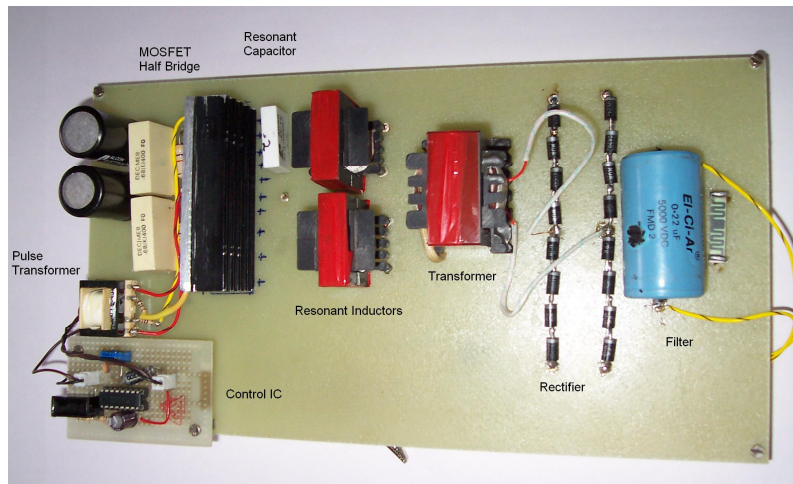


Fig. 6.5: Photograph of the experimental prototype HV power supply.

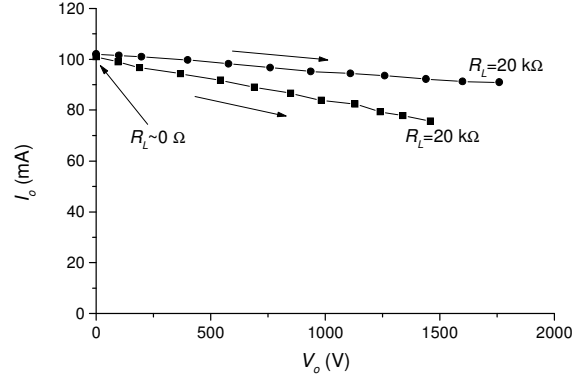


Fig. 6.6: Output characteristic of open-loop LCL-T RC (—■—) and LC-LC RC (—●—) with C_w .

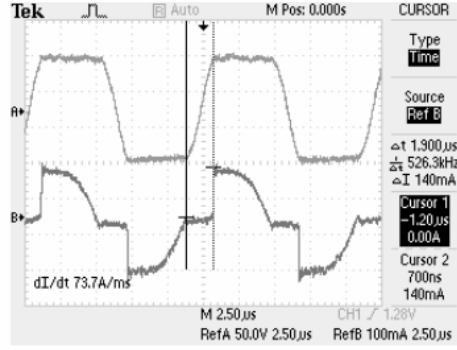


Fig. 6.7: Waveforms of transformer primary voltage (Ref A, 50V/div) and secondary current (Ref B, 100 mA/div) in LCL-T RC at $R_L=20\text{ k}\Omega$. X-scale: $2.5\text{ }\mu\text{s/div}$.

from near-zero to $20\text{ k}\Omega$ and values of output current and voltage are noted in each step. Figure 6.6 shows the output characteristic of LCL-T RC (solid squares) with the effect of C_w . The full-load output current at $R_L=20\text{ k}\Omega$ drops significantly from its design value of 100 mA . The waveforms of transformer primary voltage and secondary current at $R_L=20\text{ k}\Omega$ are shown in Fig. 6.7. As analyzed in section II, presence of C_w slows down the transition of v_{pri} from $+V_o/n$ to $-V_o/n$ and vice versa. This reduces the conduction angle of secondary diodes and therefore the average output current is low. From the cursor positions in Fig. 6.7, the value of α can be calculated as 1.008 radian, which when substituted in (6.5) gives $\psi = 0.383$. Since $C_1=0.047\text{ }\mu\text{F}$, we get $C_w=0.018\text{ }\mu\text{F}$ which matches reasonably with the measured

value. Another set of the same waveforms at $R_L=5\text{ k}\Omega$ is shown in Fig. 6.8 to demonstrate varying conduction angle with loading condition.

Next, the converter is designed as LC-LC RC satisfying the additional design constraint of (3.32) simply by changing the value of L_1 to $44\text{ }\mu\text{H}$. Output characteristic of LC-LC RC is obtained by varying R_L in steps from near-zero to $20\text{ k}\Omega$ and is also shown (solid circles) in Fig. 6.6. As compared to LCL-T RC, output current regulation of LC-LC RC is significantly improved. Although output current is theoretically constant irrespective of variation in the load resistance, practically it droops slightly with load due to increase in conduction losses in the bridge and the RIN. The bridge output voltage and current waveforms are shown in Fig. 6.9 (a) and (b) for $R_L=20\text{ k}\Omega$ and $1\text{ k}\Omega$, respectively, wherein it can be observed that current is slightly lagging the voltage thereby creating favourable ZVS condition for switches S_A and S_B . The current is also seen to reduce with load as predicted in the analysis.

The plots of experimental efficiency of LCL-T RC (solid squares) and LC-LC RC (solid circles) are shown in Fig. 6.10 measured by varying R_L from $1\text{ k}\Omega$ to $20\text{ k}\Omega$ at 200 V input dc voltage. Efficiency of both the converters is observed to be nearly the same.

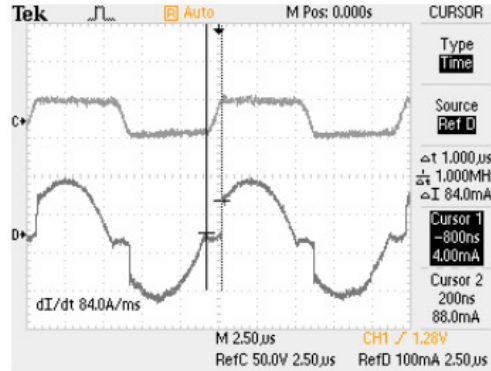


Fig. 6.8: Waveforms of transformer primary voltage (Ref A, 50V/div) and secondary current (Ref B, 100 mA/div) in LCL-T RC at $R_L=5\text{ k}\Omega$. X-scale: $2.5\text{ }\mu\text{s/div}$.

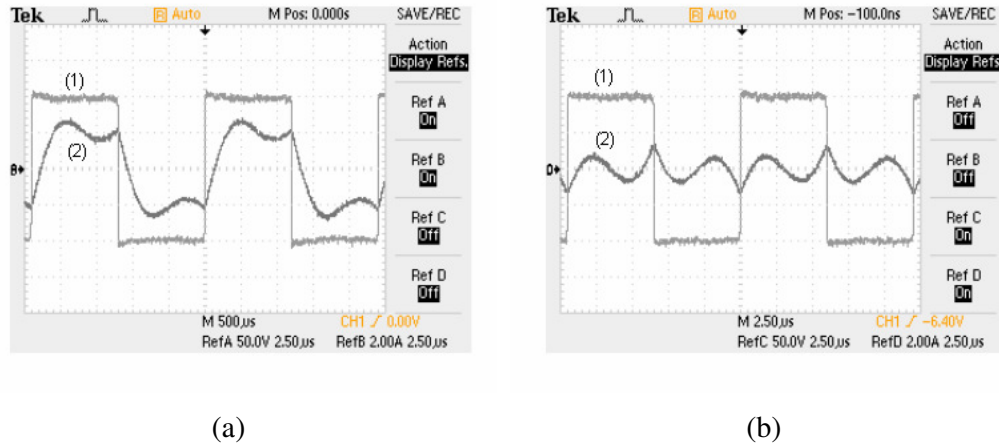


Fig. 6.9: Waveforms of bridge output voltage [trace (1), 50 V/div] and current [trace (2), 2 A/div] in LC-LC RC with (a) $R_L=20\text{ k}\Omega$, and, (b) $R_L=1\text{ k}\Omega$. X-scale: $2.5\text{ }\mu\text{s/div}$.

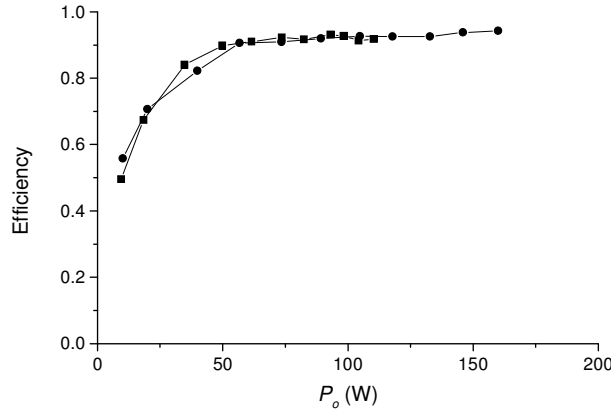


Fig. 6.10: Experimental efficiency of LCL-T RC (—■—) and LC-LC RC (—●—).

6.2 Capacitor Charging Power Supply

Various industrial applications require pulsed energy transfer. The required energy is provided to the pulsed loads by rapidly discharging a pre-charged capacitor. A special type of power supply required for charging of the capacitor is commonly termed as capacitor charging power supply (CCPS). The applications of a CCPS include flash-lamps for food sterilization and lasers, radio frequency modulators, high voltage pulse generators, plasma source implantation, non-thermal pollution gas treatment, pulsed magnets in particle accelerators, etc.

The charge cycle of a CCPS, shown in Fig. 6.11, consists of charging mode during which the capacitor charges to its pre-set value and the refresh mode during

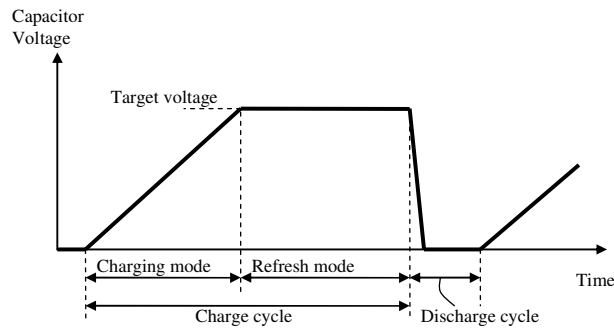


Fig. 6.11: Typical charge – discharge cycle of a CCPS

which the voltage across capacitor is maintained stable within specified tolerance. The CCPS enters the charging mode with capacitor initially un-charged. During charging, it is important to limit the output (charging) current for safe operation and CCPS operates in constant-current (CC) mode. In refresh mode the capacitor voltage is maintained constant and CCPS is required to operate in constant-voltage (CV) mode. While the capacitor is being discharged in the load (discharge cycle), CCPS is disabled. A CCPS therefore requires an elaborate and intricate feedback control and timing circuit.

A topological extension of Type-II RIC with built-in CC-CV characteristics (discussed in section 3.5.1) is ideally suited for this application without any need for complex control to regulate output current in charging mode, and output voltage in the refresh mode. As opposed to SRC [188]-[191], which has been extensively examined for its application as a CCPS, Type-II RICs with clamp diodes offer following benefits:

1. Being an inherent CC source, it is not necessary to sense and regulate the current in Type-II RICs
2. Bridge output voltage and currents are in phase under all loading conditions, thereby minimizing the conduction loss.
3. Since the bridge output current is very low (ideally zero) under output-short-circuit condition the safe operation of the converter is inherently guaranteed eliminating the need of timing circuit to disable its operation when the energy storage capacitor is being discharged into the load.

4. Switching frequency is constant which simplifies the design of magnetic and filter components.
5. The converter operation automatically and smoothly changes from CC to CV mode after the load capacitor is charged to rated voltage. Note that this transition takes place passively due to conduction of clamp diodes and the sensing of output voltage or current and their regulation using feedback control circuits is not required.

Application of Type-II RICs with clamp diodes for CCPS application is exemplified in the following paragraphs with LCL-T RC shown in Fig. 6.12.

6.2.1 Design of LCL-T RC with Clamp Diodes as a CCPS

The following parameters are assumed to be the inputs for the design:

1. Value of energy storage capacitor, C_o
2. Maximum charging voltage, $V_{o,max}$
3. Charging time, T_c
4. Input dc supply voltage, $2V_d$
5. Switching frequency, f_s

Output capacitor charging current required is given by,

$$I_o = \frac{C_o V_{o,max}}{T_c} \quad (6.12)$$

Substituting (6.12) in (3.8) for LCL-T RC and simplifying we get,

$$Z_n = \frac{8}{\pi^2} \left(\frac{V_d}{V_{o,max}} \right)^2 \frac{T_c}{C_o} \quad (6.13)$$

Since switching frequency of LCL-T resonant converter is equal to the resonant frequency for CC operation,

$$f_s = \frac{1}{2\pi\sqrt{L_1 C_1}} \quad (6.14)$$

Using equations (6.13) and (6.14) and the condition $\gamma=1$, the required values of L_1 , L_2 and C_1 can be computed. The expression for transformer turns ratio can be derived as,

$$n = \frac{V_{o,max}}{V_d} \quad (6.15)$$

6.2.2 Experimental Results

A laboratory prototype (see Fig. 6.12) of half-bridge LCL-T converter with clamp diodes has been designed, built and tested to experimentally verify the operation as CCPS [68]. The prototype was designed to charge a 2 μF capacitor from 0 to 500 V in 1 ms time. The input dc supply available is 200 V and switching frequency is 100 kHz. The designed values of resonant circuit element are as follows: $L_1 = L_2 = 25.8 \mu\text{H}$ and $C_1 = 0.098 \mu\text{F}$. The nearest capacitor value available was 0.1 μF and therefore the values of L_1 and L_2 are scaled to 26.2 μH . IRF 840 MOSFETs are used as the switches in the half-bridge converter. Fast-recovery diodes MUR 8100 are used as the clamp diodes as well as for the output bridge rectifier. The turns ratio of transformer (designed as well as actual) is: $n = 5$. In the prototype, EE42 core is used for transformer and EE36 core is used for inductors L_1 and L_2 . An insulated gate bipolar transistor (IGBT) switch in series with 10 Ω resistor connected across the output energy storage capacitor simulates the pulse discharge in the prototype.

Figure 6.13 shows the principal circuit waveforms during charging and refresh mode of the charging cycle. Before $t=t_1$, the IGBT switch is on and the capacitor voltage is nearly zero. However, the load current is constant indicated by the waveform of transformer primary current. Consistent with the prediction of equation (3.17), i_{L1} is smaller than its value when the capacitor is being subsequently charged. Since V_{pri} is less than V_d , the clamp diodes are off and the clamp diode current is zero. At $t=t_1$, the IGBT switch is turned off and the charging mode commences. The voltage across energy storage capacitor builds linearly, once again confirming CC operation of the converter. At $t=t_2$, capacitor charges to 500 V. Observe that there is no overshoot. The charging time is nearly 1 ms (indicated in Fig. 6.13 by the difference

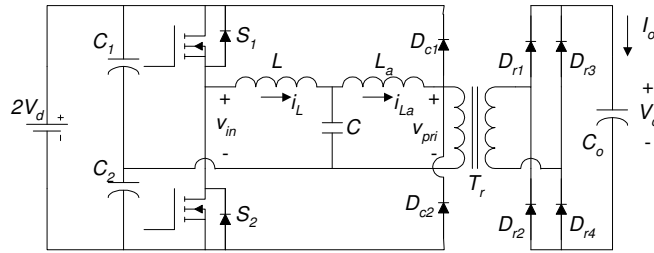


Fig. 6.12: Circuit diagram of LCL-T half-bridge RC with clamp diodes as a CCPS.

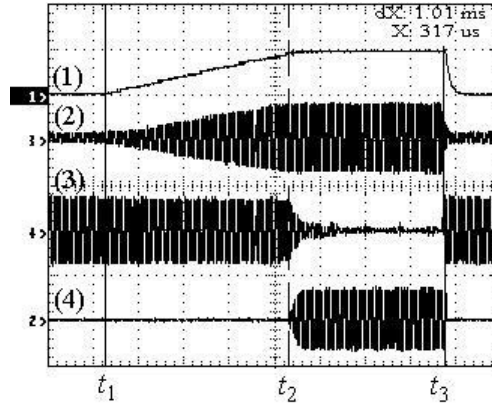


Fig. 6.13: Circuit waveforms of experimental prototype CCPS during charging and refresh mode of the charging cycle. Legends: (1) Output voltage, V_o , 500 V/div. (2) Current in resonant inductor L , i_{L1} , 10 A/div. (3) Transformer primary current, 10 A/div. (4) Clamp diode current, $i_{Dc1}-i_{Dc2}$, 10 A/div. X-scale: 250 μ s/div.

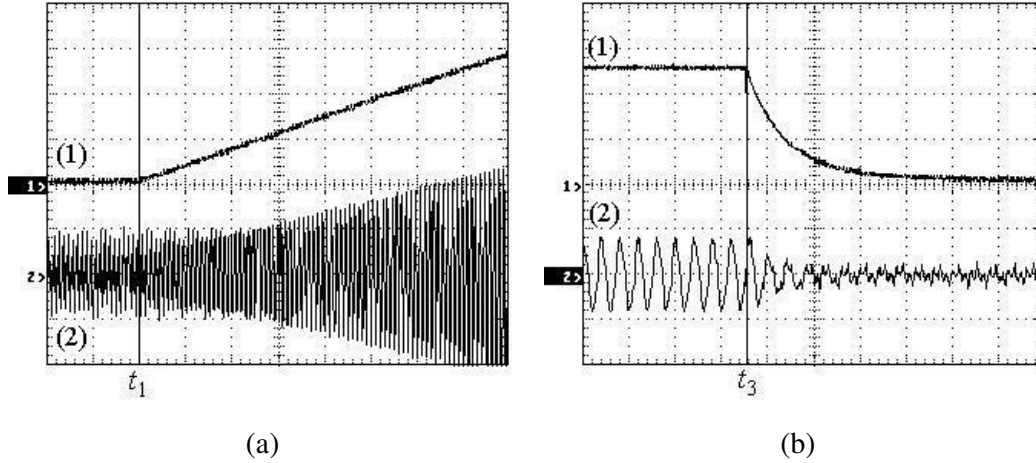


Fig. 6.14: Magnified waveforms of V_o and i_{L1} at the commencement of (a) charging mode (details around $t=t_1$ of Fig. 6.11) and (b) discharge cycle (details around $t=t_3$ of Fig. 6.11). Legends: (1) V_o , 100 V/div. (2) i_{L1} , 2 A/div.

X-scale: 100 μ s/div

dX in two vertical cursors placed at the start and end of charging mode) confirming the charging current of 1 A during this mode of operation. i_{L1} builds smoothly as the instantaneous output power of the converter rises during charging cycle. The transformer primary current is constant indicating CC operation. Clamp diodes are off

during the charging mode. At $t=t_2$, capacitor is charged to 500 V and converter operation changes from CC to CV mode. Transformer primary current is no longer constant and decays quickly to zero. The clamp diodes conduct and maintain the output voltage constant at 500 V. At $t=t_3$, IGBT switch is turned on again discharging the capacitor. The converter changes its operation from CV mode to CC mode inherently and almost instantaneously, as the clamp diodes stop conducting and transformer primary current builds to its CC value as shown in Fig. 6.13.

Unlike some of the conventional CCPS, the prototype converter operates continuously without any timing circuit to periodically enable and disable its operation. Neither the output voltage nor the current was sensed and regulated in the prototype.

The magnified waveforms of V_o and i_{L1} at the commencement of charging mode (details around $t=t_1$) are shown in Fig. 6.14(a). Observe that i_{L1} builds slowly and safely. Similarly, the magnified view of these waveforms at the commencement of discharge cycle (details around $t=t_3$) are shown in Fig. 6.14(b). As V_o drops, observe that i_{L1} also drops quickly ensuring the safe operation of half-bridge converter.

6.3 Ultracapacitor Charger

Electrical energy storage is required in many applications. The devices for electrical energy storage are specified in terms of stored energy, maximum power as well as size, weight, initial cost and life.

The most common electrical energy storage device is the battery because it can store large amounts of energy in relatively small volume and weight, and, provide suitable levels of power for many applications. However, batteries have limited shelf life and cycle life. In the recent times, the power requirements in a number of applications have increased markedly and have exceeded the capability of batteries of standard design. This has led to the design of special high power, pulse batteries often with the sacrifice of energy density and cycle life.

As power requirements for many applications become more demanding, it was felt prudent to consider separating energy and power requirements by providing for

the peak power by using a pulse power device (capacitor) that is charged periodically from a primary energy storage unit (battery). For these applications, ultracapacitor is the most suitable choice [240]. Ultracapacitors have shelf and cycle life at least an order higher than the batteries and can be charged more quickly than batteries.

The complementary characteristics of batteries and ultracapacitors have triggered their use in conjunction, for instance in electric vehicles, wherein batteries provide necessary energy and ultracapacitors deliver peak power demand. With this arrangement, battery is relieved of peak power demands, causing reduction in required installed battery capacity and improving its life.

Ultracapacitors can suitably be charged with a CC current, therefore making Type-II RICs (with or without clamp diodes) as an intuitive choice. However, considerations in the design of these circuits as a charger for ultracapacitors are different than those described in section 6.2 for the following reasons:

1. Ultracapacitors feature very large capacitance value (in Farads) but at very low voltage (typically, 2.5 V). Individual ultracapacitor cells are connected in series-parallel configuration to get desired value at working voltage level.
2. Ultracapacitors are capable of being charged with high charging current.
3. Ultracapacitors are very sensitive against the overvoltage. Still, they must be charged near to the maximum rated value in order to utilize their full capability.
4. Ultracapacitors have relatively higher series resistance and inductance.

6.3.1 Accounting Diode Drops in Design

In contrast with the previously described high-output-voltage and low-output-current applications, the charger for ultracapacitors is designed for low-output-voltage and high-output-current. Therefore, secondary-side drops, which are dominated by the drops across conducting rectifier diodes, need to be accounted for ultracapacitor charger application to avoid errors in the prediction of final charged voltage. Figure 6.15 shows the circuit arrangement of Type-II RIC with clamp diodes used as a CCCV charger for ultracapacitor. Center-tap transformer is chosen for reduced drops and losses as compared to the full-bridge rectifier. When ultracapacitor is charged to a voltage V_o , the amplitude of square-wave primary voltage waveform, V_{pri} , will be,

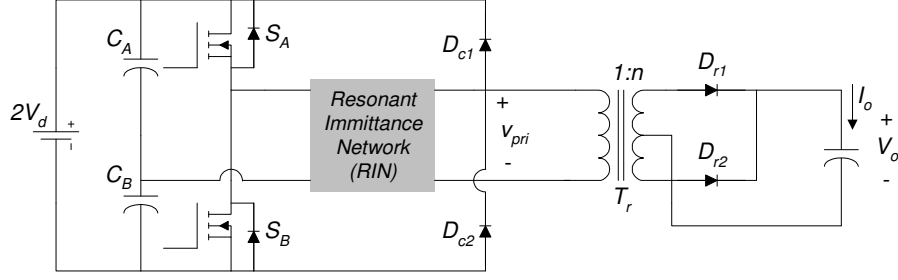


Fig. 6.15: Circuit diagram of Type-II RIC with clamp diodes used as a CC charger for ultracapacitor.

$$V_{pri} = \frac{(V_o + V_{dr})}{n} \quad (6.16)$$

wherein V_{dr} is voltage drop across diodes D_{r1} and D_{r2} in the on state. Considering fundamental component of v_{pri} , an expression for equivalent ac resistance can be derived as:

$$R_{ac} = \frac{8}{\pi^2} \frac{V_o + V_{dr}}{I_o n^2} = \frac{8}{\pi^2} \frac{(R_L + R_{dr})}{n^2} = \frac{8}{\pi^2} \frac{R_{eff}}{n^2} \quad (6.17)$$

wherein $R_L \equiv (V_o / I_o)$, $R_{dr} \equiv (V_{dr} / I_o)$ and $R_{eff} \equiv R_L + R_{dr}$

Therefore, circuit Q is defined as:

$$Q = \frac{\omega_o n^2 L_1}{R_{eff}} = \frac{n^2 Z_n}{R_{eff}} \quad (6.18)$$

Since,

$$I_o = \frac{8}{\pi^2} \frac{V_d}{n Z_n} \quad (6.19)$$

from (6.18) and (6.19) we get,

$$\frac{1}{n} = \frac{8}{\pi^2} \frac{V_d}{I_o R_{eff} Q} = \frac{8}{\pi^2} \frac{V_d}{(V_o + V_{dr}) Q} \quad (6.20)$$

Figure 6.15 also shows clamp diodes D_{c1} and D_{c2} connected at the primary side of the transformer in order to clamp the primary voltage to supply voltage and limit the maximum voltage to which ultracapacitor can be charged. Owing to low output voltage levels and sensitivity of ultracapacitors to overvoltage, the drops across

clamp diodes must also be considered. In clamped-mode operation, the following equality is satisfied:

$$\frac{(V_o + V_{dr})}{n} = (V_d + V_{dc}) \quad (6.21)$$

wherein V_{dc} is voltage drop across diodes D_{c1} and D_{c2} in the on state. From (6.20) and (6.21), we get,

$$Q = \frac{8}{\pi^2} \frac{V_d}{(V_d + V_{dc})} \quad (6.22)$$

and

$$\frac{1}{n} = \frac{V_d + V_{dc}}{V_o + V_{dr}} \quad (6.23)$$

6.3.2 Effect of L_{lk}

Figure 6.16 shows the same circuit of Fig. 6.15, wherein L_{lk} is explicitly shown. While L_{lk} is gainfully utilized as a part of the resonant inductor, it changes the circuit operation in the circuit with clamp diodes. The drop across inductor L_{lk} changes the waveform at the point of connection of clamp diodes. The terminal primary voltage, v_{pri} , waveform is now the phasor sum of square-wave voltage of amplitude $\pm(V_o + V_{dr})/n$ and voltage drop across L_{lk} . Figure 6.17 shows the simulated waveforms in a typical case when L_{lk} is taken to be 0.3 times the value of resonant inductor inside the RIN. The simulated waveforms clearly show that the waveform of v_{pri} changes significantly in the presence of L_{lk} with the peak of v_{pri} being significantly larger than the ideal value $\pm(V_o + V_{dr})/n$.

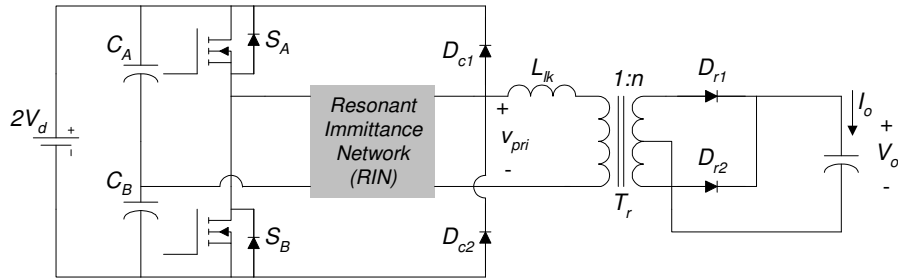


Fig. 6.16: Circuit diagram of CC charger for ultracapacitor showing L_{lk} explicitly.

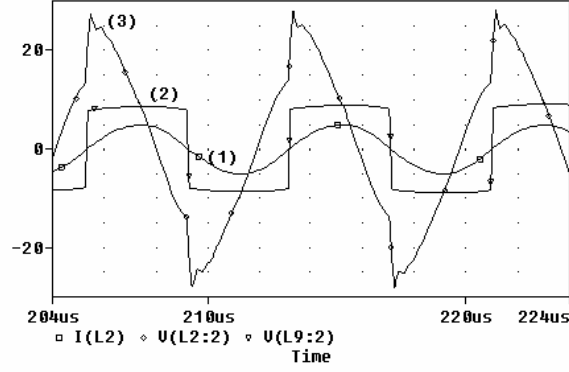


Fig. 6.17: Simulated waveforms: (1) primary current, (2) v_{pri} when L_{lk} is insignificant and (3) v_{pri} when L_{lk} is 0.3 times the value of resonant inductor.

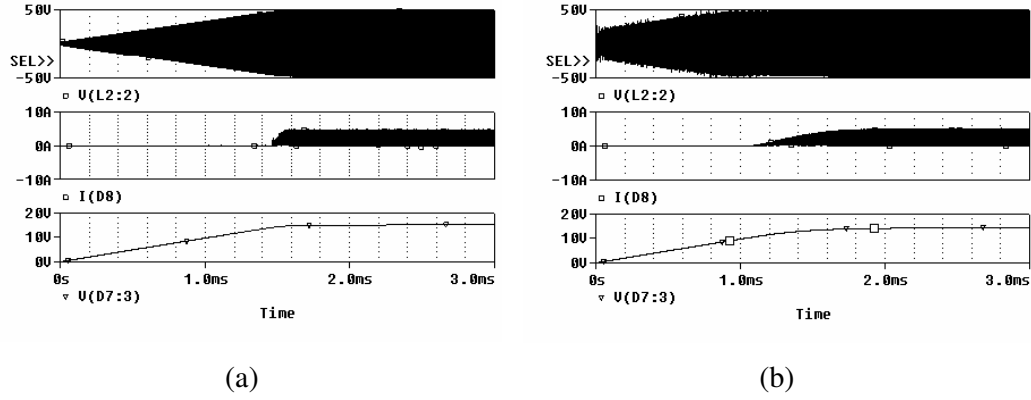


Fig. 6.18: Simulated waveforms of v_{pri} (upper plot), the current in D_{C1} (middle plot) and the voltage across output capacitor (lower plot) when (a) L_{lk} is insignificant and (b) L_{lk} is 0.3 times the value of resonant inductor.

The higher peak value of v_{pri} causes the clamp diodes to come into conduction much earlier in the charge cycle than intended. This phenomenon is termed as the premature clamping and is illustrated by the simulated waveforms of Fig. 6.18 during a typical charge cycle. The upper plot shows v_{pri} , the middle plot shows the current in D_{C1} and the lower waveform shows the charging of output capacitor. Figure 6.18(a) shows the waveforms when L_{lk} is insignificant. The charging of ultracapacitor is linear and takes 1.4 ms to complete when the clamp diodes start conduction. Figure 6.18(b) shows the waveforms when L_{lk} is 0.3 times the value of resonant inductor. Pre-mature conduction of the clamp diodes or the pre-mature clamping, starting after 1.1 ms, reduces the charging current and therefore the rate of charging. Therefore, capacitor

charging is non-linear and takes 2 ms to completely charge the capacitor. Besides premature clamping also results in additional conduction loss in clamp diodes.

6.3.3 Experimental Results

A charger has been developed to charge a 58 F, 15 V ultracapacitor with 10 A dc current based on half-bridge LCL-T RC with clamp diodes. The following are the details of the prototype converter:

- Input dc voltage: 96 V (regulated on un-regulated)
- Output current: 10 A
- Output voltage: 15 V
- Resonant inductors (L_1 and L_2): 15.5 μ H
- Resonant capacitor (C_1): 0.1 μ F
- Transformer turns ratio: 4:1:1 (center-tap transformer)
- Transformer leakage inductance: 3.5 μ H

Photographs of Fig. 6.19 show the developed charger for ultracapacitor. It is made on single 4U card of length 220 mm, including the control as well as power circuit. The converter is operating in free-running mode without any feedback. Input voltage can be regulated or un-regulated. In the former case the clamp diodes would be enough to prevent the capacitor from over-charging. However, to increase safety

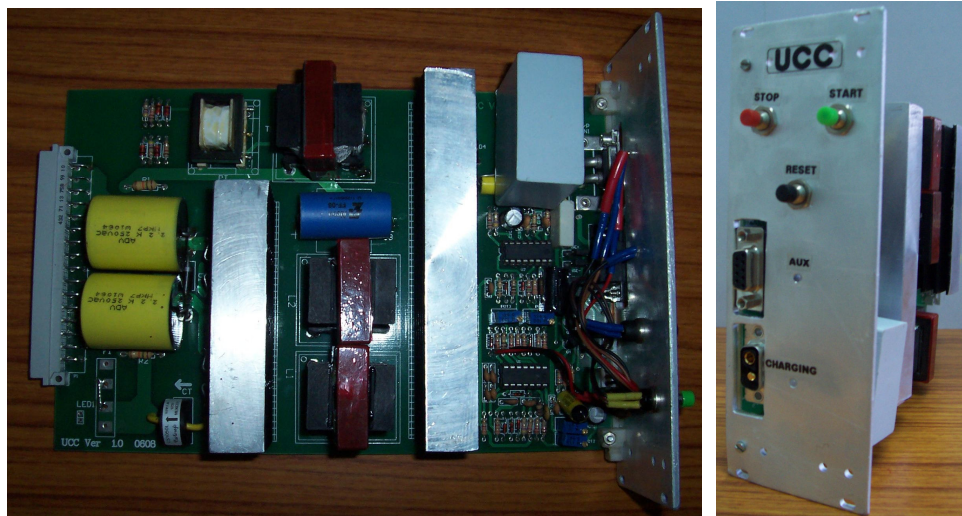


Fig. 6.19: Photographs showing the charger for ultracapacitor.

against possible overcharging and to allow the converter's operation with unregulated input dc voltage, an end-of-charge detection circuit based on a simple voltage comparator is used to stop the operation of the charger as soon as pre-set voltage is reached. Therefore, the fascia plate of the converter only has three push-button controls START (to start the charging), STOP (to terminate charging), RESET (to reset the converter and make it ready for the next charging cycle after end-of-charge detection).

The waveforms of Fig. 6.20(a) show the charging cycle of an 58 F ultracapacitor. The upper waveform shows the capacitor voltage and the lower waveform shows the charging current. The effect of transformer leakage inductance causing pre-mature clamping, thereby reducing the charging current and increasing the charging time, can be clearly seen. If the clamp diodes are disconnected, this effect is absent as demonstrated by the waveforms of Fig. 6.20(b), wherein fairly constant charging current till the end of cycle and linear charging is evident. Note that all experimental results are obtained with un-regulated dc input, which itself drops with instantaneous increase in the output power during the charging cycle. Therefore, the droop in output current is more pronounced.

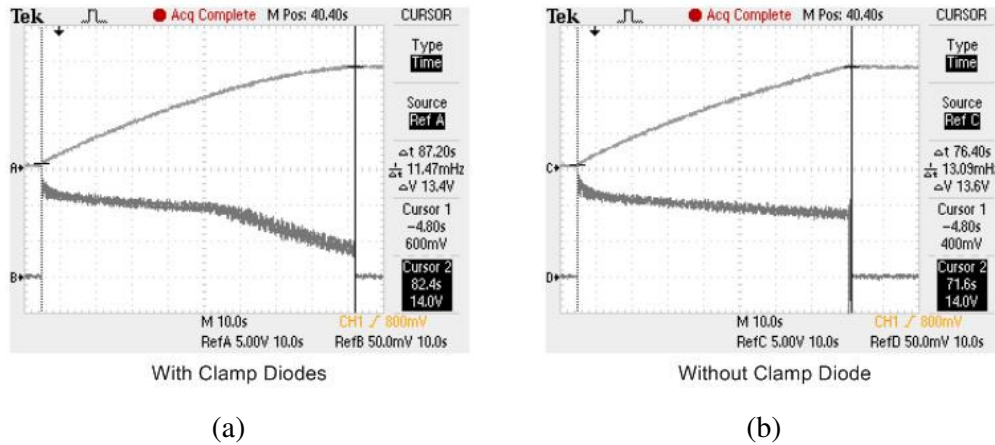


Fig. 6.20: Experimental waveforms of capacitor voltage (upper trace, 5 V/div) and charging current (lower trace, 5 A/div) with (a) clamp diodes and (b) without clamp diodes showing the effect of pre-mature clamping. X-scale: 10 sec/div.

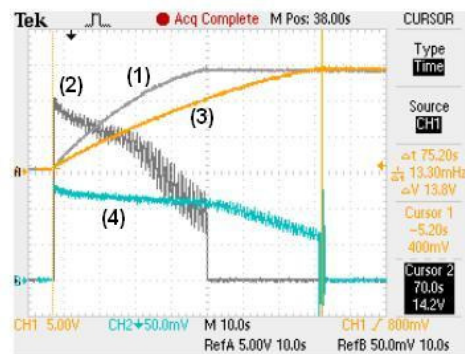


Fig. 6.21: Charging cycle of ultracapacitor showing capacitor voltage [(1), 5 V/div] and charging current [(2), 5 A/div] when two chargers are operating in parallel. (3) and (4) respectively show these waveforms with one charger. X-scale: 10 sec/div.

Since the converter is an inherent current source, it can directly be paralleled. Figure 6.21 shows the charging cycles of the ultracapacitor when two such chargers are connected in parallel. The figure also shows the charging cycle with one converter for direct comparison.

6.4 Pulsed Current Sources

Pulsed current sources are required in many applications including arc welding, battery charging, pulse electroplating, semiconductor diode lasers etc.

In arc welding, pulsed current power supplies have been in use for SMAW, GTAW, gas metal arc welding (GMAW), FCAW and SAW. The most common are those for GTAW and GMAW. Pulsed power supplies are used with GMAW to reduce arc power and wire deposition rate while retaining desirable spray transfer [211], [212]. For welding current below certain level, called as a critical current or transition current, the metal transfers from wire electrode at a small rate (typically 10 drops per second). This is called as the globular mode. For welding current above critical current, the transfer rate is few 100s of drops per second. This is called as the spray arc mode. By pulsing the current above and below critical current it is possible to achieve desirable quality of spray transfer while reducing average arc current and deposition rate. In practice the lower current is kept small enough to prevent metal transfer but large enough to sustain ionization of arc. This is called as background

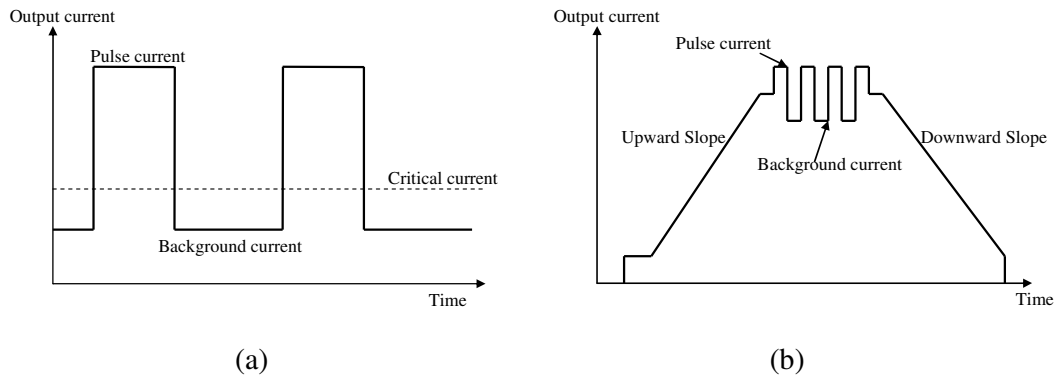


Fig. 6.22: Profile of pulse current required for (a) GMAW, and, (b) GTAW

current or keep-alive current. Typical profile of pulsed current output is shown in Fig. 6.22(a). In precision machine and automatic applications where exceptional directional properties and arc stability is required, high frequency pulsed arc welding sources are advantageous. In such sources, the arc current switches between the background and peak level at frequencies up to 20 kHz. The concept of pulsing has also been used with GTAW effectively. However, the pulse frequency is lower. Additionally, it should be possible to control the profile of weld current with controlled current slopes. Figure 6.22(b) shows a typical pulsed GTAW current programming.

Several methods are practiced for charging of batteries, such as, CV charging, CC charging, taper current charging, trickle current charging, automatic charging, high- rate or boost charging and diagnostic charging. As the demand for battery power grows, the size of the battery pack gets bigger and charging techniques become more complicated. As a significant damage done to a battery is usually while it's being charged, intelligent control is necessary to properly charge a battery. There are two ways to accomplish this task: pulse charging and burp charging [222]-[224]. Pulse charging method involves sending charge back into the battery; however, it is not done at constant current. Instead, constant current pulses are forced into the battery with a small resting period between the pulses, as seen in Fig. 6.23. The idea behind this technique is to allow time for the chemical reaction to settle, so the battery is charged more uniformly. In the burp charging technique, a discharge pulse of small duration is included in the charge pulsing cycle. The idea behind the discharge pulse

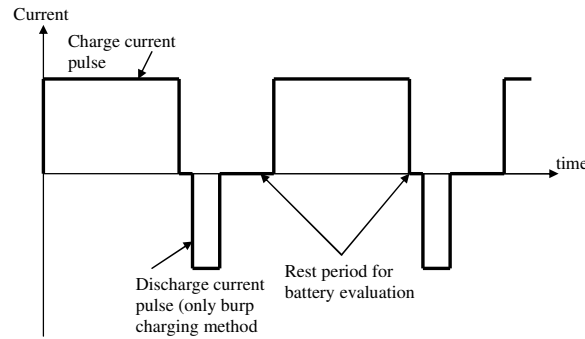


Fig. 6.23: Advanced pulse charging cycle for batteries. The discharge pulse is present only in burp-charging method.

is to redirect the migration of oxide gas away from the reacting plates, preventing oxidization, allowing the battery to prolong its life and capacity.

Electro-chemical processes, such as electrolysis, electrophoresis, electroplating, electro-deposition, anodizing and printed circuit board (PCB) fabrication use CC power supplies. They are of both types: continuous or pulsed. While the former is the most common and used in variety of electro-chemical processes the latter is particularly used in the pulse-electroplating. The pulse plating [225] improves the deposit properties (porosity, ductility, hardness, electrical conductivity, roughness etc.). It is used for deposition of alloys, the composites and structures of which are not obtainable with DC plating. By periodic inversion of polarity of current pulse, plating thickness distribution can be improved.

6.4.1 Configurations of Type-II RICs as Pulsed Current Sources

Output current of Type-II RICs is constant and independent of load resistance under steady-state condition. However, under transient conditions, the output current deviates significantly from its steady-state value. The extent of deviation and its duration depends on the value of output filter capacitor. This behaviour is already demonstrated with simulation and experimental results using equivalent circuit model presented in Chapter 5.

It is possible to reduce peak-peak ripple in the output current and increase the ripple frequency using multi-phase RICs described in Section 3.5 of Chapter 3.

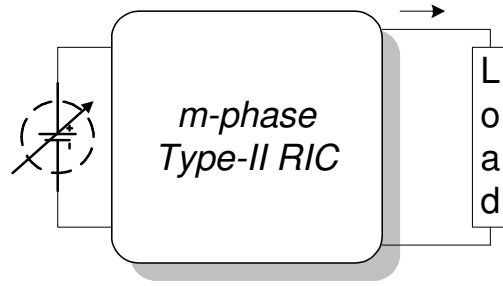


Fig. 6.24: Realization of pulsed current source by modulating the source voltage.

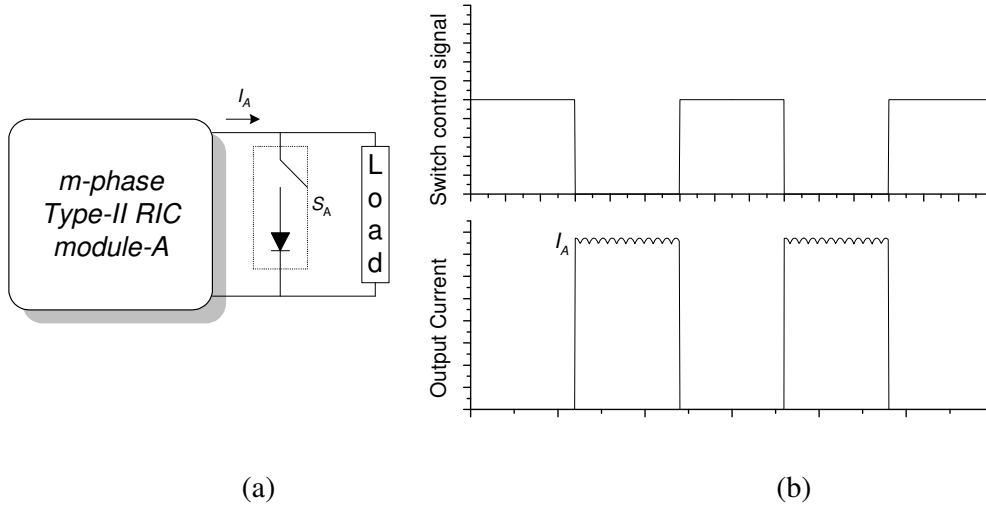


Fig. 6.25: (a) Configuration of pulsed current source using *m-phase RIC* and switch.
(b) Timing waveforms

Therefore, the value of output filter capacitor can be significantly reduced. If inherent ripple of multi-phase RICs is tolerable in an application or alternatively using sufficient number of modules in multi-phase RICs, output filter capacitor can be altogether eliminated. With this arrangement, it is possible to have constant load current even under the transient conditions, making it suitable for application as pulsed current sources.

Since output current is proportional to the supply dc voltage, one possible way of realizing a pulsed current source is to modulate the dc source itself, as illustrated in Fig. 6.24, in a profile similar to the required output current. Due to limited bandwidth of input dc source, this approach would have applicability limited to lower pulse repetition frequency and slower transitions.

A more versatile configuration of pulsed current source can be realized using a dc current source with multiphase Type-II RIC and switch(es).

A simplest configuration is shown in Fig. 6.25(a), which is suitable for application wherein the output current is required to be pulsed between zero and the set value. The switch with series diode signifies a unilateral switch, in which the current can flow only in one direction. Figure 6.25(b) shows the switch control signal and load current waveform. When the switch is closed the load current is zero, and vice versa. Duty-cycle of the output current pulse can be controlled easily by controlling the switch duty-cycle. The attainable transition times and pulse repetition frequency is only a function of switch parameters and modern-day semiconductor switches are faster.

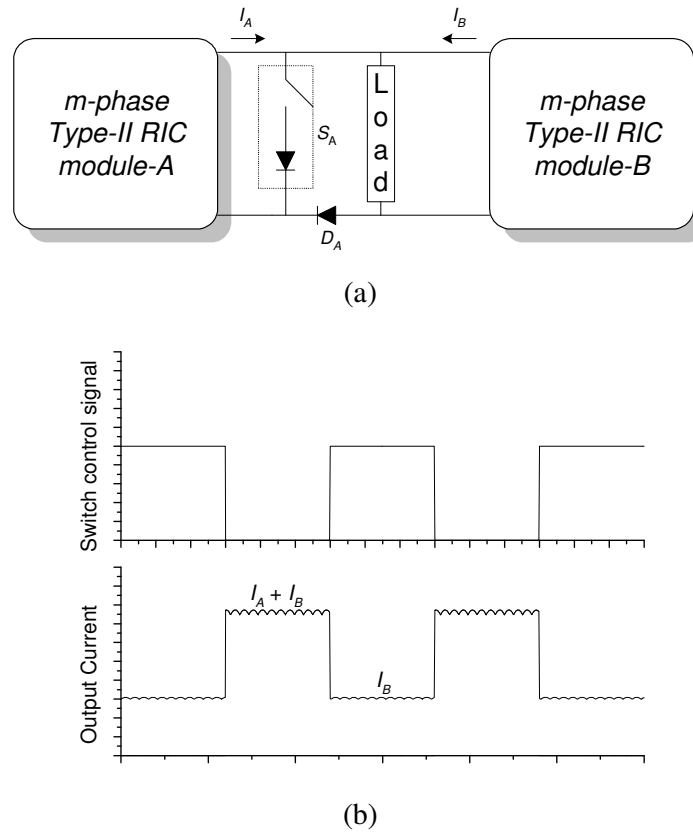
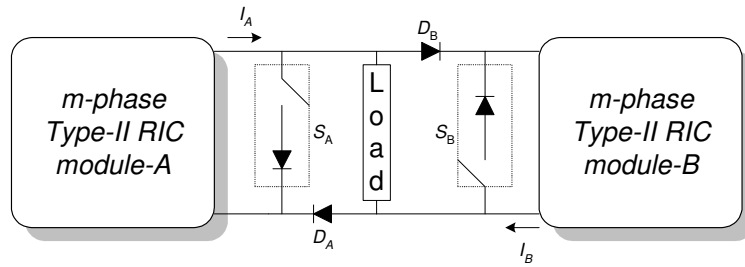
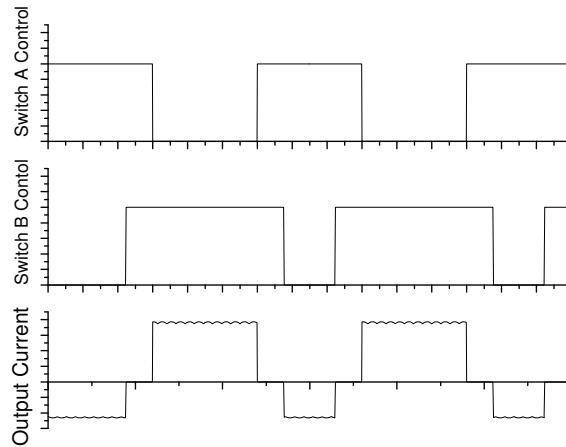


Fig. 6.26: (a) Configuration of pulsed current source using two *m*-phase RICs and a switch to generate current pulse with offset. (b) Timing waveforms

If an application demands that the output current should pulsate from a non-zero value (for instance, background current in welding applications) to some peak value, the configuration shown in Fig. 6.26(a) can be used. Two multiphase RIC modules are required. Module-A is used to set the peak current and module-B is used to set the background current. Diode D_A isolates module-B from the switch, which is used to program the duty-cycle and repetition rate of the output current pulse. Timing waveforms are shown in Fig. 6.26(b). When the switch is on, the output current of module-A is bypassed from the load and the load current is equal to the output current of module-B, which is set as the background current. When the switch is open, load current is equal to the sum of output currents of modules A and B, which is set equal to the amplitude of required pulse current.



(a)



(b)

Fig. 6.27: (a) Configuration of pulsed current source using two *m*-phase RICs and two switches to generate bipolar current pulse. (b) Timing waveforms

The configuration of Fig. 6.26(a) can be further modified by reversing the polarity of module-B and adding an extra unilateral switch and isolating diode, as shown in Fig. 6.27(a). It is possible to generate positive and negative current pulses required for battery charging-discharging applications, as illustrated with the waveforms of Fig. 6.27(b).

6.5 Conclusion

Type-II RICs are very useful in variety of applications wherein a CC source is either inherently required or can be advantageously applied. The adverse effect of transformer winding capacitance on the output characteristics is seen to have been overcome in LC-LC RC. Application of Type-II RIC for capacitor charging is exemplified using LCL-T RC. Particularly in charging application for ultracapacitors, due consideration is required to take into account the effects of diode drops and transformer leakage inductance to calculate the final charged voltage and the time required to charge the ultracapacitor to the required voltage. Various configurations are suggested for application of Type-II multi-phase RICs for applications demanding pulsed current sources.

Chapter 7

Conclusions

RCs has been an active area of research in power electronics field due to variety of topologies, diverse, peculiar and useful characteristics and wide applicability. A large number of RC topologies have been explored and analyzed using a variety of techniques. Integration of reactive and magnetic components has helped to reduce the number of discrete components and to achieve high power density. RCs have been a potential candidate in many power electronics applications such as voltage regulator modules, ballasts for fluorescent lamps, power factor correction, capacitor charging, induction heating, welding, inductive power transfer, HV power supply, due to soft switching, high frequency operation, high efficiency, and small size.

A CC power supply is either inherently required or can be advantageously applied in a many applications including electric arc welding, laser diode drivers, magnet power supplies, capacitor charging, illumination systems, battery charging, electrochemical processes etc. Conventional techniques for realizing a CC power supply are limited, less efficient and bulky.

While the majority of the previous work on RCs has been directed towards developing methods of analysis and control techniques for other applications, very little has been done to explore the suitability of RCs for application as a CC power supply. Discontinuous-mode SRC is unattractive for higher conduction loss and

bigger output filter. Poor part-load efficiency of PRC, LCC RC and hybrid RC due to high circulating current has been a serious limitation.

ICs, due to immittance conversion characteristics, are suitable for transforming a CV source to CC source and is deemed to be a promising alternative for developing topologies suitable for CC power supplies. Since distributed constant line type ICs are not suitable for power electronics applications, a few lumped-element IC topologies, based on transmission line approximation emulated using discrete inductors and capacitor, were studied and reported earlier. However, the efforts to identify, study, characterize and apply the lumped-element IC topologies have been largely discrete in nature and systematic investigation to identify and explore a family of IC topologies has not been carried out so far. Moreover, the published work mainly emphasizes on the peculiarities in the applications of a couple of IC topologies. The published IC topologies also have certain limitations. All of the published IC topologies are not suitable for power electronics applications, wherein the exciting voltage is commonly square-wave, which is conveniently obtained by operating power semiconductor switches at high frequency.

Motivated from these facts, this dissertation has been dedicated to present an orderly search procedure for identification of a family of lumped-element IC topologies suitable for power converter circuits, termed here as the RIC topologies, perform detailed analysis, design optimization, investigate control issues and experimentally demonstrate the suitability of a new family of RIC topologies for application as a CC power supply.

7.1 Accomplishments

A term, RIN, has been defined in Chapter 2 to identify a family electrical network that exhibits immittance conversion characteristics and are resonant. These networks are not necessarily the lumped-element approximation of a distributed constant line. When a RIN is used in place of ordinary RN in a RC, the resulting power converter topology has been termed as the RIC. A family of lumped-element RIC topologies is identified by investigating transmission parameters of various

topological structures of electrical networks. In all 24 RINs have been identified with three and four reactive elements.

Nine RINs are useful for applications demanding current-to-voltage conversion. RCs using these RINs are termed Type-I RICs. Fifteen RINs are suitable for application as a CC power supply. RCs using these RINs are termed Type-II RICs.

RICs exhibit immittance conversion characteristics only if various reactances obey certain conditions, which are satisfied only at a particular frequency of operation and when the values of reactive elements are suitably chosen. The circuits have different characteristics at other frequencies. These operating points and design conditions have been derived and discussed.

Suitability of various RIC topologies in terms of absorbing parasitic components and providing inherent dc blocking to the transformer has been examined. It is concluded that L_{lk} can be advantageously used as the part of all RINs. Further, topologies T_4 , T_5 , T_9 , P_5 , P_7 , LA_4 , LA_7 and LA_8 absorb L_m and L_{lk} associated with loosely coupled transformers in inductive power transmission systems. The L_{lk} and C_w of transformers in HV power supplies are absorbed into T_2 - T_4 , T_7 , T_9 , P_1 , P_2 , P_4 - P_6 , LA_1 - LA_6 .

Analysis and design procedure of Type-II RICs as a CC power supply has been exemplified in Chapter 3 with selected topologies, namely Topology T_1 , Topology T_3 and Topology LA_2 . Newly explored fourth-order Topology T_3 and Topology LA_2 respectively overcome two limitations of the third-order Topology T_1 , namely, the lack of inherent dc blocking and absorption of C_w in the RIN. Fundamental frequency ac analysis is performed to gain insight into the steady-state characteristics, derive closed-form expressions for converter gain and the ratings of various components. A way to design the converter by minimizing the kVA/kW rating of RIN has been presented. Closed form expressions for the optimum value of Q , and the values of reactive elements of RIN are derived in each case.

Experimental results on prototype converters have been presented to demonstrate the converter performance and CC behaviour. Experimental results have been found in close agreement with the analytical values and nearly true CC behaviour is demonstrated with good efficiency under full-load and part-load conditions.

RIC topologies with maximum of four reactive elements have been explored in Chapter 2 by suitably constraining the number of reactive elements in various branches of various topological structures that exhibit immittance conversion characteristics. The constraint on the number of reactive elements in a branch can be relaxed to further explore the RIC topologies with higher reactive elements. As an illustration, a fifth-order RIC topology derived from topological structure N_5 is analyzed further and validated with experimental results in Chapter 3 since it overcomes a limitation of Topology T_1 by inherent providing dc blocking for the transformer. Moreover, resonant inductors and transformer can be integrated in a single magnetic component, thereby reducing number of discrete magnetic components and overall size and weight of the converter.

Two topological extensions of Type-II RIC circuits, namely Type-II RICs with CCCV characteristics and multi-phase RICs, are described in Chapter 3. While CCCV characteristic is useful in many practical applications and to protect the converter under over-load and open-load condition, multi-phase RICs result in reduced input and output side current ripple and filtering requirement, thereby reducing the converter size and improving converter dynamics.

For practical application of Type-II RIC as a current-source power supply, it should be possible to regulate the output current, particularly against the input voltage variations. The output current can be regulated and varied over a wide range by either varying the input dc voltage using another converter at the front-end or using fixed-frequency control methods. Feasibility of APWM control to RICs is exemplified in Chapter 4 with LCL-T RC. Four distinct operating modes have been identified. The mode-boundaries have been obtained and plotted on the D - Q plane. A region on the D - Q plane has been identified for the converter design wherein all the switches operate with ZVS. It is observed that APWM control allows ZVS operation over a wider range than CM control. Experimental results on a prototype half-bridge converter demonstrated the existence of various operating modes and the performance of APWM controlled LCL-T RC.

An approximate equivalent circuit model Type-II RICs has been derived in Chapter 5 that predicts the averaged response of the terminal voltages and currents under the large-signal variation in the operating conditions. A small-signal model has

been subsequently derived by applying perturbation and linearization to the average model. These models greatly simplify and speed-up the analysis either via simple analytical treatment or by using the model in circuit simulation tools. These models have been validated by comparing their transient and small-signal results with those obtained from cycle-by-cycle simulation and experiment. It has been shown that the low-frequency transient and small-signal ac behaviour of Type-II RIC is governed only by the filter and the converter along with RIN does not contribute to the low-frequency response.

Applicability of Type-II RIC topologies in some of the application areas such as high-voltage dc power supply, CCPS and a CC charger for ultracapacitor have been demonstrated with application-specific design issues and prototype implementation in Chapter 6.

Type-II RICs are advantageous for HV DC power supplies due to inherent protection against partial discharge and arcing, reduction in output filter and associated stored energy and gainful utilization of circuit parasitic components, which otherwise could have detrimental effect of circuit performance. Effect of C_w on the output characteristics of LCL-T RC has been quantified with simplified analysis and design of LC-LC RC for the most practical case to accommodate C_w has been presented.

As compared to SRC used conventionally for CCPS operation, Type-II RICs offers many advantages such as elimination of current sensing and its regulation, higher efficiency, no need for timing circuit to disable CCPS operation in discharge cycle, constant frequency operation and inherent CC-CV characteristics.

Type-II RICs are very useful to quickly charge ultra-capacitors with constant charging current. A way to accommodate diode drops in the design, which are significant in low-output-voltage applications, is presented. It is shown L_{lk} gives rise to a phenomenon called pre-mature clamping in Type-II RICs with clamp diodes used as the ultra-capacitor charger.

Application areas of multi-phase RICs with source-switch configurations for applications as pulsed current sources laser diode drivers, welding, battery charging and electrochemical processes are also suggested and discussed.

7.2 Suggestions for Future Research

The identification of RIC topologies has been restricted in this dissertation to those with maximum of four reactive elements since more reactive elements increase size, weight, cost of the converter and complicates the circuit analysis and design. The constraint on the number of reactive elements in a branch can be relaxed to further explore the RIC topologies with higher reactive elements, as illustrated in this dissertation with a fifth-order RIC topology.

Only a few selected type-II RIC topologies have been studied for detailed steady-state analysis in this dissertation. Similar analysis can also be carried out for other Type-II RIC topologies to assess their merits and limitations.

This dissertation has been dedicated towards the identification of topologies for CC power supplies and their analysis, modeling, control and applications. In the process, a family of RIC topologies suitable for current-to-voltage conversion (Type-I RICs) has also been identified. Possible application areas of current-to-voltage conversion and suitability of Type-I RICs can be examined.

An approximate small-signal model for Type-II RICs has been proposed in this dissertation. This model is valid for low-frequency region, assuming that the overall converter response is governed by the dominant pole of output filter. The work can be extended further to include the effect of RIN, thereby enabling a more accurate prediction of small-signal behaviour also in the high-frequency region. Subsequently, closed loop controllers for various topologies can be designed and implemented in the hardware.

Appendix I

Illustrative Derivation of Current Gain, H

Steady-state analysis of selected Type-II RIC topologies has been performed in this thesis. Closed-form expressions have been obtained for the quantification of current gain and voltage/current ratings of various components as a function of normalized switching function and other circuit parameters. To illustrate the procedure, derivation of the current gain, H , of LA₂ RIC or the LC-LC RC given by (3.28) is reported in this appendix.

The circuit diagram of LC-LC RC is shown in Fig. 3.7. Under the fundamental frequency approximation, the square-wave voltage source at the input of RIN is replaced by a sinusoidal voltage source of rms value $V_{in,rms}$ and the transformer, rectifier, filter and load is replaced by equivalent ac resistance R_{ac} , given by (3.1). An equivalent circuit for fundamental frequency ac analysis can therefore be drawn as shown in Fig. A1.1. An expression for rms current in R_{ac} (I_{Rac}) can then be derived as:

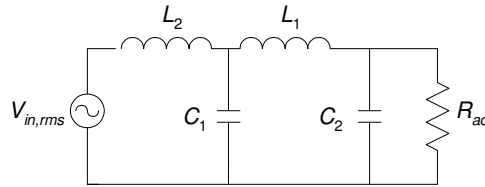


Fig. A1.1: Equivalent circuit diagram of LC-LC RC for ac analysis.

$$I_{R_{ac}} = \frac{V_{in,rms}}{\left[(L_1 C_1 L_2 C_2 R_{ac}) s^4 + (L_2 C_1 L_1) s^3 + (L_2 C_1 R_{ac} + L_2 C_2 R_{ac} + L_1 C_2 R_{ac}) s^2 + (L_1 + L_2) s + R_{ac} \right]} \quad (A1.1)$$

Substituting

$$V_{in,rms} = \frac{2\sqrt{2}}{\pi} V_d, \quad \gamma = \frac{L_2}{L_1} \quad \text{and} \quad \psi = \frac{C_2}{C_1}$$

we get,

$$I_{R_{ac}} = \frac{2\sqrt{2}}{\pi} \frac{V_d}{\left[(\gamma \psi L_1^2 C_1^2 R_{ac}) \omega^4 + j(\gamma L_1^2 C_1) \omega^3 - (\gamma L_1 C_1 R_{ac} + \gamma \psi L_1 C_1 R_{ac} + \psi L_1 C_1 R_{ac}) \omega^2 + j(L_1 + \gamma L_1) \omega + R_{ac} \right]} \quad (A1.2)$$

Substituting

$$\omega_o = \frac{1}{\sqrt{L_1 C_1}}$$

we get,

$$I_{R_{ac}} = \frac{2\sqrt{2}}{\pi} \frac{V_d}{\left[(\gamma \psi R_{ac}) \left(\frac{\omega}{\omega_o} \right)^4 + j(\gamma \omega_o L_1) \left(\frac{\omega}{\omega_o} \right)^3 - (\gamma R_{ac} + \gamma \psi R_{ac} + \psi R_{ac}) \left(\frac{\omega}{\omega_o} \right)^2 + j\omega_o (L_1 + \gamma L_1) \left(\frac{\omega}{\omega_o} \right) + R_{ac} \right]} \quad (A1.3)$$

Substituting

$$\omega_n = \frac{\omega}{\omega_o}$$

we get,

$$I_{R_{ac}} = \frac{2\sqrt{2}}{\pi} \frac{V_d}{R_{ac} \left[1 + \gamma \psi \omega_n^4 - (\gamma + \gamma \psi + \psi) \omega_n^2 \right] + j \frac{\omega_o L_1}{R_{ac}} \left[(1 + \gamma) \omega_n - \gamma \omega_n^3 \right]} \quad (A1.4)$$

Substituting

$$R_{ac} = \frac{8}{\pi^2} \frac{R_L}{n^2}$$

and re-arranging, we get,

$$I_{R_{ac}} = \frac{2\sqrt{2}}{\pi} \frac{\frac{V_d}{Z_n} Z_n}{\left\{ \frac{8}{\pi^2} \frac{R_L}{n^2} \left[1 + \gamma \psi \omega_n^4 - (\gamma + \gamma \psi + \psi) \omega_n^2 \right] + j \left(\frac{\omega_o L_1}{\left(\frac{8}{\pi^2} \frac{R_L}{n^2} \right)} \right) \left[(1 + \gamma) \omega_n - \gamma \omega_n^3 \right] \right\}} \quad (A1.5)$$

Substituting

$$Q = \frac{n^2 \omega_o L_1}{R_L} = \frac{n^2 Z_n}{R_L}$$

we get,

$$I_{R_{ac}} = \frac{\pi}{2\sqrt{2}} \frac{Q}{\left[1 + \gamma \psi \omega_n^4 - (\gamma + \gamma \psi + \psi) \omega_n^2 \right] + j \frac{\pi^2}{8} Q \left[(1 + \gamma) \omega_n - \gamma \omega_n^3 \right]} \left(\frac{V_d}{Z_n} \right) \quad (A1.6)$$

Now, due to rectifier action,

$$I_o = \frac{2\sqrt{2}}{\pi} \left(\frac{I_{R_{ac}}}{n} \right) \quad (A1.7)$$

From (A1.6) and (A1.7),

$$I_o = \frac{1}{n} \frac{Q}{\left[1 + \gamma \psi \omega_n^4 - (\gamma + \gamma \psi + \psi) \omega_n^2 \right] + j \frac{\pi^2}{8} Q \left[(1 + \gamma) \omega_n - \gamma \omega_n^3 \right]} \left(\frac{V_d}{Z_n} \right) \quad (A1.8)$$

Therefore, after re-arrangement, we get the final expression of current gain as,

$$H = \frac{n I_o}{V_d / Z_n} = \frac{1}{\frac{1}{Q} \left[1 + \gamma \psi \omega_n^4 - (\gamma + \gamma \psi + \psi) \omega_n^2 \right] + j \frac{\pi^2}{8} \left[(1 + \gamma) \omega_n - \gamma \omega_n^3 \right]} \quad (A1.9)$$

References

- [1] W. McMurray, "Selection of snubbers and clamps to optimize the design of transistor switching converters," *IEEE Trans. Ind. Appl.*, vol. IA-16, no. 4, pp. 513-523, July/Aug 1980.
- [2] K. Smith Jr. and K. Smedley, "Engineering design of passive lossless soft-switching methods for PWM converters," *IEEE Trans. Power Electron.*, vol. 16, no. 3, pp. 890-899, July 2001.
- [3] K. Liu, R. Oruganti and F.C. Lee, "Quasi-resonant converters – topologies and characteristics," *IEEE Trans. Power Electron.*, vol. PE-2, no. 1, pp. 62-71, January 1987.
- [4] G. Hua, E. Yang, Y. Jiang and F. C. Lee, "Novel zero-current-transition PWM converters," *IEEE Trans. Power Electron.*, vol. 9, no. 6, pp. 601-606, November 1994.
- [5] P. K. Jain, W. Kang, H. Soin and Y. Xi, "Analysis and design considerations of a load and line independent zero voltage switching full bridge DC/DC converter topology," *IEEE Trans. Power Electron.*, vol. 17, no. 5, pp. 649-657, Sept. 2002.
- [6] J. G. Cho, J. A. Sabate, G. Hua and F. C. Lee, "Zero-voltage and zero-current-switching full bridge PWM converter for high power applications," *IEEE Trans. Power Electron.*, vol. 11, no. 4, pp. 622-627, July 1996.
- [7] M. Jovanovic, "Merits and limitations of resonant and soft-switched converters," *IEEE International Telecommunication Conference Proc.*, 1992, pp. 51-58.

- [8] M. Jovanovic, "Resonant, quasi-resonant, multi-resonant and soft-switching techniques - merits and limitations," *International Journal of Electronics*, vol. 77, no. 5, pp. 537-554, 1994.
- [9] R. Severns, "Topologies for three-element resonant converters," *IEEE Trans. Power Electron.*, vol. 7, no. 1, pp. 89-98, January 1992.
- [10] I. Batarseh, "Resonant converter topologies with three and four energy storage elements," *IEEE Trans. Power Electron.*, vol. 9, no. 1, pp. 64-73, January 1994.
- [11] F. Schrarz, "An improved method of resonant current pulse modulation for power converter," *IEEE Trans. Ind. Electron.*, vol. IECI-23, no. 2, pp. 133-141, May 1976.
- [12] F. Schrarz and J. Klaassens, "A controllable secondary multi-kilowatt dc current source with constant maximum power factor," *IEEE Trans. Ind. Electron.*, vol. IECI-23, no. 2, pp. 142-150, May 1976.
- [13] F. Schrarz and J. Klaassens, "A controllable 45 kW current source for dc machines," *IEEE Trans. Ind. Appl.*, vol. IA-15, no. 4, pp. 437-444, July/August 1979.
- [14] N. Tilgenkamp, S. De Hann and H. Huisman, "A novel series resonant converter topology," *IEEE Trans. Ind. Electron.*, vol. IE-34, no. 2, pp. 240-246, May 1987.
- [15] J. Klaasens, W. Moise De Chateleux and M. Van Wesenbeeck, "Phase staggering control of a series resonant dc-dc converter with paralld power modules," *IEEE Trans. Power Electron.*, vol. 3, no. 2, pp. 164-173, April 1988.
- [16] R. King and T. Stuart, "A normalized model for the half-bridge series resonant converter," *IEEE Transactions on Aerospace and Electronic Systems*, vol. 17, no. 2, pp. 190-198, March 1981.
- [17] R. King and T. Stuart, "Modeling the full bridge series resonant power converter," *IEEE Transactions on Aerospace and Electronic Systems*, vol. AES-18, no. 4, pp. 449-459, July 1982.

- [18] D. Devan, "Design considerations for very high frequency resonant mode DC/DC converters," IEEE Trans. Power Electron., vol. PE-2, no. 1, pp. 45-54, 1987.
- [19] J. Klaassens, "Steady state analysis of a series-resonant dc-dc converter with bipolar power flow," IEEE Trans. Ind. Electron., vol. 36, no. 1, pp. 48-55, February 1989.
- [20] I. Pitel, "Phase modulated resonant power conversion techniques for high frequency link converters," IEEE Trans. Ind. Appl., vol. IA-22, no. 6, pp. 1044-1051, November/December 1986.
- [21] P. Jain and S. Dewan, "A performance comparison of full and half-bridge series resonant inverters in high frequency high power applications," IEEE Trans. Ind. Appl., vol. 26, no. 2, pp. 317-323, March/April 1990.
- [22] T. Sloane, "Design of high efficiency series resonant converters above resonance," IEEE Transactions on Aerospace and Electronic Systems, vol. AES-26, no. , pp. 393-402, March 1990.
- [23] A. Witulski and R. Erickson, "Steady-state analysis of series resonant converter," IEEE Transactions on Aerospace and Electronic Systems, vol. AES-21, no. 6, pp. 791-799, November 1985.
- [24] A. Witulski and R. Erickson, "Design of series resonant converter for minimum stress," IEEE Transactions on Aerospace and Electronic Systems, vol. AES-22, no. 4, pp. 356-363, July 1986.
- [25] R. King and T. Stuart, "Inherent overload protection for the series resonant converter," IEEE Transactions on Aerospace and Electronic Systems, vol. AES-19, no. 6, pp. 820-830, November 1983.
- [26] J. Vieira and I. Barbi, "Constant frequency PWM capacitor voltage-clamped series resonant power supply," IEEE Trans. Power Electron., vol. 8, no. 2, pp. 120-126, April 1993.
- [27] V. Ranganathan, P. Ziogas and V. Stetanovic, "A regulated dc-dc voltage source converter using high frequency link," IEEE Trans. Ind. Appl., vol. IA-18, no. 3, pp. 279-287, May/June 1982.

- [28] Y. King and A. Upadhyay, "Analysis and design of a half-bridge parallel resonant converter," *IEEE Trans. Power Electron.*, vol. 3, no. 3, pp. 254-265, July 1988.
- [29] S. Deb, A. Joshi and S. Doradla, "A novel frequency domain model for a parallel resonant converter," *IEEE Trans. Power Electron.*, vol. 3, no. 2, pp. 208-215, April 1988.
- [30] M. Rico, J. Sebastian, J. Uceda, M. Perez and F. Aldana, "Dynamic modeling of the parallel resonant converter," *IEEE Power Electronics Specialist Conference Proc*, 1989, pp. 728-735.
- [31] S. Johnson and R. Erickson, "Steady-state analysis and design of parallel resonant converter," *IEEE Trans. Power Electron.*, vol. 3, no. 1, pp. 93-104, January 1988.
- [32] A. Bhat and M. Swamy, "Analysis and design of high frequency parallel resonant converter operating above resonance," *IEEE Transactions on Aerospace and Electronic Systems*, vol. AES-25, no. , pp. 449-458, July 1989.
- [33] A. Bhat and M. Swamy, "Analysis and design of a parallel resonant converter including the effect of a high-frequency transformer," *IEEE Trans. Ind. Electron.*, vol. 37, no. 4, pp. 297-306, October 1990.
- [34] M. M. Swamy and A.K.S. Bhat, "Analysis of a parallel resonant converter with secondary side resonance," *IEEE Transactions on Aerospace and Electronic Systems*, vol. 28, no. 4, pp. 1042-1055, October 1992.
- [35] A. Bhat, "Analysis and design of a parallel resonant converter with the resonating capacitor on a tertiary winding," *IEEE Trans. Ind. Appl.*, vol. 29, no. 6, pp. 1069-1075, November/December 1993.
- [36] M. Swamy and A. K. S. Bhat, "A comparison of parallel resonant converters in lagging power factor mode," *IEEE Trans. Power Electron.*, vol. 9, no. 2, pp. 181-195, March 1994.
- [37] M. Borage, S. Tiwari and S. Kotaiah, "A parallel resonant constant-current power supply," *Journal of Indian Institute of Science*, vol. 83, no. , pp. 117-125, Sept.-Dec. 2003.

- [38] V. Caliskan, J. Gegner and C. Lee, "Current-driven zero-voltage switched resonant converter with capacitive output filter," IEEE Applied Power Electronics Conference Proc., 1992, pp. 211-218.
- [39] M. Matsuo, T. Suetsugu, S. Mori and I. Sasase, "Class DE current-source parallel resonant inverter," IEEE Trans. Ind. Electron., vol. 46, no. 2, pp. 242-249, April 1999.
- [40] A. Shenkman, B. Axelrod and V. Chudnovsky, "A new simplified model of dynamics of the current-fed parallel resonant inverter," IEEE Trans. Ind. Electron., vol. 47, no. 2, pp. 282-286, April 2000.
- [41] M. Elbuluk and M. Chavez, "A complete normalized analysis of the current fed series resonant dc/dc converter," IEEE Industrial Electronics Conference, 1989, pp. 27-32.
- [42] S. Sooksatra and C. Lee, "Current driven series resonant converter," IEEE Applied Power Electronics Conference Proc., 1990, pp. 128-136.
- [43] M. Gulko and S. Ben-Yaakov, "Current-sourcing push-pull parallel resonance inverter (CS-PPRI): Theory and application as discharge lamp driver," IEEE Trans. Ind. Electron., vol. 41, no. 3, pp. 285-291, June 1994.
- [44] E. J. Dede, J. Jordan, J. Linares, J. Gonzalez, V. Esteve, D. Ramirez and E. Maset, "On the design of medium and high power current fed inverters for induction heating," IEEE Industry Applications Society Annual Meeting, 1991, pp. 1047-1053 .
- [45] J. Alonso, J. Cardesin, J. Martin-Ramos, J. Garcia and M. Rico-Secades, "Using current-fed parallel-resonant inverters for electrodischarge applications: a case of study," IEEE Applied Power Electronics Conference Proc., 2004, pp. 109- 115.
- [46] H. Benqassmi, J. Crebier and J. Ferrieux, "Comparison between current-driven resonant converters used for single-stage isolated power factor correction," IEEE Trans. Ind. Electron., vol. 47, no. 3, pp. 518-524, June 2000.
- [47] M. Kazimierczuk and A. Abdulkarim, "Current-source parallel-resonant dc/dc converter," IEEE Trans. Ind. Electron., vol. 42, no. 2, pp. 199-208, April 1995.

- [48] A. P. Hu, G. A. Covic and J. T. Boys, "Direct ZVS start-up of a current-fed resonant inverter," *IEEE Trans. Power Electron.*, vol. 21, no. 3, pp. 809- 812, May 2006.
- [49] R. Liu and C. Q. Lee, "Series resonant converter with third order commutation network," *IEEE Trans. Power Electron.*, vol. 7, no. 3, pp. 462-468, July 1992.
- [50] I. Batarseh and K. Siri, "LLC-type series resonant converter with PWM control," *IEE Proc. Circuits Devices Syst.*, vol. 141, no. 2, pp. 73-81, April 1994.
- [51] A. K. S. Bhat, "Analysis and design of modified series resonant converter," *IEEE Trans. Power Electron.*, vol. 8, no. 4, pp. 423-430, October 1993.
- [52] A. K. S. Bhat, "Analysis and design of LCL-type series resonant converter," *IEEE Trans. Ind. Electron.*, vol. 41, no. 1, pp. 118-124, February 1994.
- [53] A. K. S. Bhat, "Analysis and design of a fixed-frequency LCL type series resonant converter with capacitive output filter," *IEE Proc. Circuits Devices Syst.*, vol. 144, no. 2, pp. 97-103, 1997.
- [54] A. K. S. Bhat, "A fixed frequency modified series resonant converter: analysis, design and experimental results," *IEEE Trans. Power Electron.*, vol. 10, no. 6, pp. 766-775, November 1995.
- [55] M. Youssef and P. Jain, "Design and performance of a Resonant LLC 48V voltage regulator module with a self-sustained oscillation controller," *IEEE Applied Power Electronics Conference Proc.*, 2007, pp. 141-147.
- [56] Y. Fang, D. Xu, Y. Zhang, G. Yanjun, Z. Fengchuan and L. Zhu, "Design of high power density LLC resonant converter with extra wide input range," *IEEE Applied Power Electronics Conference Proc.*, 2007, pp. 976-981.
- [57] C. Lai and K. Shyu, "A single-stage AC/DC converter based on zero voltage switching LLC resonant topology," *IET Proc. Electr. Power. Appl.*, vol. 1, no. 5, pp. 743-752, September 2007.
- [58] W. Liu and J. D. van Wyk, "Design of integrated LLCT module for LLC resonant converter," *IEEE Applied Power Electronics Conference Proc.*, 2005, pp. 362- 368 .

- [59] Y. Zhang, D. Xu, K. Mino and K. Sasagawa, "1MHz-1kW LLC resonant converter with integrated magnetics," IEEE Applied Power Electronics Conference Proc., 2007, pp. 955-961.
- [60] X. Xie, J. Zhang, C. Zhao, Z. Zhao and Z. Qian, "Analysis and optimization of LLC resonant converter with a novel over-current protection circuit," IEEE Trans. Power Electron., vol. 22, no. 2, pp. 435-443, March 2007.
- [61] C. Chakraborty, M. Ishida and T. Hori, "Performance and design of an LCL converter for voltage regulator type applications," Transactions of IEE of Japan, vol. 119-D, no. 6, pp. 848-856, June 1999.
- [62] S. Dieckerhoff, M. Ryan and R. Doncker, "Design of an IGBT-based LCL-resonant inverter for high frequency induction heating," IEEE Industry Applications Society Annual Meeting, 1999, pp. 2039-2045.
- [63] C. Wang, G. A. Covic and O. H. Stielau, "Investigating an LCL load resonant inverter for inductive power transfer applications," IEEE Trans. Power Electron., vol. 19, no. 4, pp. 995-1002, July 2004.
- [64] H. Pollock, "Simple constant frequency constant current load-resonant power supply under variable load conditions," IEE Electronics Letters, vol. 33, no. 18, pp. , August 1997.
- [65] M. Borage, S. Tiwari and S. Kotaiah, "Analysis and design of LCL-T resonant converter as a constant-current power supply," IEEE Trans. Ind. Electron., vol. 52, no. 6, pp. 1547-1554, December 2005.
- [66] H. Seidel, "A high power factor tuned class D converter," IEEE Power Electronics Specialist Conference Proc, 1988, pp. 1038-1042.
- [67] M. Borage, S. Tiwari and S. Kotaiah, "LCL-T resonant converter with clamp diodes: A novel constant-current power supply with inherent constant-voltage limit," IEEE Trans. Ind. Electron., vol. 54, no. 2, pp. 741 - 746, April 2007.
- [68] M. Borage, S. Tiwari and S. Kotaiah, "A constant-current, constant-voltage half-bridge resonant power supply for capacitor charging," IEE Proc. Electr. Power. Appl., vol. 153, no. 3, pp. 343-347, May 2006.
- [69] C. Chakraborty and M. Ishida, "Performance, design and control of a series-parallel (CL2-type) resonant dc-dc converter," IEE Proc. Electr. Power. Appl., vol. 149, no. 2, pp. 360-368, September 2002.

- [70] M. Castilla, L. Garcia de Vicuna, J. M. Guerrero, J. Miret and J. Matas, "Half-bridge CLL resonant rectifier with quantum mode control," IEE Proc. Electr. Power. Appl., vol. 152, no. 3, pp. 543- 550, May 2005.
- [71] C. Chakraborty and M. Ishida, "Low-harmonic resonant CLL-type AC/DC converter," IEE Proc. Electr. Power. Appl., vol. 148, no. 2, pp. 187-192, March 2001.
- [72] C. Q. Lee, R. Liu and I. Bataresh, "Analysis and design of parallel resonant converter with LLC type commutation," IEEE Transactions on Aerospace and Electronic Systems, vol. AES-25, no. 6, pp. 844-847, November 1989.
- [73] D. C. Hamill, "On the LLC type parallel resonant converter," IEEE Transactions on Aerospace and Electronic Systems, vol. 27, no. 3, pp. 564-566, May 1991.
- [74] A.K.S. Bhat and S. B. Dewan, "Analysis and design of a high frequency resonant converter using LCC-type commutation," IEEE Trans. Power Electron., vol. PE-2, no. 4, pp. 291-301, 1987.
- [75] A. Bhat, "Analysis of series parallel resonant power supply," IEEE Transactions on Aerospace and Electronic Systems, vol. 28, no. 1, pp. 249-258, January 1992.
- [76] A.K.S. Bhat, "Analysis and design of a series-parallel resonant converter," IEEE Trans. Power Electron., vol. 8, no. 1, pp. 1-11 , January 1993.
- [77] M. Kazimierzuk and N. Thirunarayan, "Analysis of a series parallel resonant converter," IEEE Transactions on Aerospace and Electronic Systems, vol. 29, no. 1, pp. 88-98, 1993.
- [78] V. Agarwal and A. K. S. Bhat, "Large signal analysis of LCC-type parallel resonant converter using discrete time domain modeling," IEEE Trans. Power Electron., vol. 10, no. 2, pp. 222-238, March 1995.
- [79] S. Ben-Yaakov and G. Rahav, "Average modeling and simulation of series-parallel resonant converters by SPICE compatible behavioral models," IEEE Applied Power Electronics Conference Proc., 1996, pp. 116-120.
- [80] H. Sewell, M. Foster, C. Bingham, D. Stone, D. Hante and D. Howe, "Analysis of voltage output LCC resonant converters, including boost mode

- operation," IEE Proc. Electr. Power. Appl., vol. 150, no. 6, pp. 673-679, November 2003.
- [81] M. Foster, H. Sewell, C. Bingham, D. Stone and D. Howe, "Methodologies for the design of LCC voltage-output resonant converters," IEE Proc. Electr. Power. Appl., vol. 153, no. 4, pp. 559- 567, September 2006.
 - [82] A. Bhat, "Analysis and design of a series parallel resonant converter with capacitive output filter," IEEE Trans. Ind. Appl., vol. 27, no. 3, pp. 523-530, May/June 1991.
 - [83] J. A. Martín-Ramos, J. Díaz, A. M. Pernía, F. Nuño and J. Sebastián, "Large-signal modeling of the PRC-LCC resonant topology with a capacitor as output filter," IEEE Applied Power Electronics Conference Proc., 2002, pp. 1120-1126.
 - [84] J. Cardesin, J. M. Alonso, E. Lopez-Corominas, A. J. Calleja, J. Ribas, M. Rico-Secades and J. Garcia, "Design optimization of the LCC parallel-series inverter with resonant current mode control for 250-W HPS lamp ballast," IEEE Trans. Power Electron., vol. 20, no. 5, pp. 1197- 1204, September 2005.
 - [85] V. Belaguli and A. K. S. Bhat, "Operation of the LCC-type parallel resonant converter as a low-harmonic rectifier," IEEE Trans. Ind. Electron., vol. 46, no. 2, pp. 288-299, April 1999.
 - [86] H. Pollock and J. O. Flower, "Series-parallel load-resonant converter for controlled-current arc welding power supply," IEE Proc.Electr. Power Appl., vol. 143, no. 3, pp. 211-218, May 1996.
 - [87] B. Pollard and R. Nelms, "Using the series-parallel resonant converter in capacitor charging applications," IEEE Applied Power Electronics Conference Proc., 1992, pp. 245-252.
 - [88] J. Sabate, M. Jovanovic, F. C. Lee and R. Gean, "Analysis and design optimization of LCC resonant inverter for high frequency AC distributed power system," IEEE Trans. Ind. Electron., vol. 42, no. 1, pp. 63-71, February 1995.
 - [89] R. Casanueva, L. Chiquito, F. Azcondo and S. Bracho, "Current source LCC resonant converter for EDM power supply," IEEE Industrial Electronics Conference, 2001, pp. 1027-1032.

- [90] A. Bhat and R. Zheng, "A three phase series parallel resonant converter - analysis, design, simulation, and experimental results," IEEE Trans. Ind. Appl., vol. 32, no. 4, pp. 951-960, July/August 1996.
- [91] S. Akre, M. Egan and M. Willers, "Practical design methodology for a new three phase dc-dc fully resonant converter employing LCC type tank," International Conf. on Power Electronics and Variable Speed Drives, 2000, pp. 340-345.
- [92] A. Bhat, "Fixed frequency PWM series parallel resonant converter," IEEE Trans. Ind. Appl., vol. 28, no. 5, pp. 1002-1009, Sept./Oct. 1992.
- [93] D. Czarkowski and M. Kazimierczuk, "Phase-controlled series-parallel resonant converter," IEEE Trans. Power Electron., vol. 8, no. 3, pp. 309-319, July 1993.
- [94] S. Morrison, "Analysis of a hybrid series parallel resonant bridge converter," IEEE Trans. Power Electron., vol. 7, no. 1, pp. 119-127, January 1992.
- [95] R. Casanueva, F. J. Azcondo and C. Branas, "Output current sensitivity analysis of the LCpCs resonant inverter: current-source design criteria," IEEE Trans. Ind. Electron., vol. 54, no. 3, pp. 1560-1568, June 2007.
- [96] H. Fujita and H. Akagi, "Control and performance of a pulse density modulated series resonant inverter for corona discharge process," IEEE Trans. Ind. Appl., vol. 35, no. 3, pp. 621-626, May/June 1999.
- [97] M. Schutten, R. L. Steigerwald and M. Kheraluwala, "Characteristics of load resonant converter operated in high-power factor mode," IEEE Trans. Power Electron., vol. 7, no. 2, pp. 304-314, April 1992.
- [98] V. Belaguli and A. Bhat, "Characteristics of fixed frequency hybrid resonant converter operating on the utility line," IEEE Trans. Ind. Appl., vol. 35, no. 6, pp. 1413-1423, November/December 1999.
- [99] P. Jain and H. Soin, "A constant frequency parallel tuned resonant dc/dc converter for high voltage applications," IEEE Power Electronics Specialist Conference Proc, 1992, pp. 71-77.
- [100] I. Batarseh and C. Lee, "Steady state analysis of parallel resonant converter with LLCC-type commutation network," IEEE Trans. Power Electron., vol. 6, no. 3, pp. 525-538, July 1991.

- [101] I. Batarseh and C. Lee, "High-frequency link parallel resonant converter with fourth order commutation network," IEE Proc. G, vol. 138, no. 1, pp. 34-37, February 1991.
- [102] P. Jain, "Parallel tuned resonant DC/DC converter topologies," IEEE International Telecommunication Conference Proc., 1992, pp. 74-80.
- [103] O. Ojo and I. Bhat, "Steady state and dynamic analysis of high-order parallel resonant converters," IEE Proc. B, vol. 140, no. 3, pp. 209-215, May 1993.
- [104] Y. Ang, C. Bingham, M. Foster, D. Stone and D. Howe, "Design oriented analysis of fourth-order LCLC converters with capacitive output filter," IEE Proc. Electr. Power. Appl., vol. 152, no. 2, pp. 310- 322, March 2005.
- [105] C. Liu, F. teng, C. Hu and Z. Zhang, "LCLC resonant converter for multiple lamp operation ballast," IEEE Applied Power Electronics Conference Proc., 2003, pp. 1209-1213.
- [106] E. Kim, H. Lee, Y. Kong and Y. Kim, "Operating characteristics in LCLC resonant converter with a low coupling transformer," IEEE Applied Power Electronics Conference Proc., 2007, pp. 1651-1656.
- [107] A.K.S. Bhat, A. Biswas and B.S.R. Iyengar, "Analysis and design of a (LC)(LC) type series parallel resonant converter," IEEE Transactions on Aerospace and Electronic Systems, vol. 31, no. 3, pp. 1186-1193, 1995.
- [108] A. Ghahary and B. Cho, "Design of a transcutaneous energy transmission system using a series resonant converter," IEEE Trans. Power Electron., vol. 7, no. 2, pp. 261-269, April 1992.
- [109] C. Chakraborty, M. Ishida and T. Hori, "Novel half bridge resonant converter topology realized by adjusting transformer parameters," IEEE Trans. Ind. Electron., vol. 49, no. 1, pp. 197-205, February 2002.
- [110] K. Singh, G. Bachmann, S. Doradla, P. Mutschler and R. Ghosh, "An LCLC resonant dc-dc converter with PWM control - analysis, simulation and implementation," IEEE Applied Power Electronics Conference Proc., 2002, pp. 1113-1119.
- [111] H. Suryavanshi, K. Thakre, S. Tarnekar, D. Kothari and A Kothari, "Power factor improvement and closed loop control of an AC-to-DC resonant

- converter," IEE Proc. Electr. Power. Appl., vol. 149, no. 2, pp. 101-109, March 2002.
- [112] M. A. Chaudhari and H. M. Suryawanshi, "High-power-factor operation of three-phase ac-to-dc resonant converter," IEE Proc. Electr. Power. Appl., vol. 153, no. 6, pp. , November 2006.
 - [113] G. Joung and G. Cho, "An energy transmission system for an artificial heart using leakage inductance compensation of trancutaneous transformer," IEEE Trans. Power Electron., vol. 13, no. 6, pp. 1013-1022, November 1998.
 - [114] H. Pollock, C. Fu and C. Pollock, "Load-resonant converter with zero current switching and variable output power," IEE Electronics Letters, vol. 33, no. 25, pp. , December 1997.
 - [115] H. Pollock and J. O. Flower, "New method of power control for series-parallel load resonant converters maintaining zero current switching and unity power factor operation," IEEE Trans. Power Electron., vol. 12, no. 1, pp. 103-115, January 1997.
 - [116] R. Steigerwald, "High frequency transistor DC-DC converters," IEEE Trans. Ind. Electron., vol. IE-31, no. 2, pp. 181-191, May 1984.
 - [117] R. Steigerwald, "A comparison of half-bridge resonant converter topologies," IEEE Trans. Power Electron., vol. 3, no. 2, pp. 174-182, April 1988.
 - [118] R. Steigerwald, "Practical design methodologies for load resonant converters operating above resonance," IEEE International Telecommunication Conference Proc., 1992.
 - [119] P. Jain, "Performance comparison of pulse width modulated resonant mode DC/DC converters for space applications," IEEE Industry Applications Society Annual Meeting, 1989, pp. 1106-1114.
 - [120] M. Kazimierczuk, "Synthesis of phase modulated resonant dc/ac inverter and dc/dc converters," IEE Proc. B, vol. 139, no. 4, pp. 387-393, July 1992.
 - [121] M. Kazimierczuk, D. Czarkowski and N. Thrunarayan, "A new phase-controlled parallel resonant converter," IEEE Trans. Ind. Electron., vol. 40, no. 6, pp. 542-552, December 1993.

- [122] D. Czarkowski and M. Kazimierczuk, "Phase-controlled CLL resonant converter," IEEE Applied Power Electronics Conference Proc., 1993, pp. 432-438.
- [123] M. Kazimierczuk and M. Jutty, "Fixed-frequency phase controlled full bridge resonant converter with a series load," IEEE Trans. Power Electron., vol. 10, no. 1, pp. 9-18, January 1995.
- [124] F. Tsai, Y. J. Sabate and F. Lee, "Constant frequency clamped mode resonant converters," IEEE Trans. Power Electron., vol. 3, no. 4, pp. 460-473, October 1988.
- [125] F. Tsai and F. C. Lee, "A complete DC characterization of a constant frequency clamped-mode, series resonant converter," IEEE Power Electronics Specialist Conference Proc, 1988, pp. 987-996.
- [126] M. Kim and J. Kim, "Modeling and optimal trajectory control of the series resonant converter pulse-width modulated or current-controlled for low switching loss," IEEE Applied Power Electronics Conference Proc., 1993, pp. 752-758.
- [127] H. Kifune, Y. Hatanaka and M. Nakaoka, "Cost effective phase shifted pulse modulation soft switching high frequency inverter for induction heating applications," IEE Proc. Electr. Power. Appl., vol. 151, no. 1, pp. 19- 25, January 2004.
- [128] F. Tsai, Y. Chin and F. Lee, "State plane analysis of a constant frequency clamped mode parallel resonant converter," IEEE Trans. Power Electron., vol. 3, no. 3, pp. 364-377, July 1988.
- [129] F. Tsai, J. Sabate and F.C. Lee, "Constant frequency, zero voltage switched, clamped mode parallel resonant converter," IEEE International Telecommunication Conference Proc., 1989, pp. 16-4.
- [130] C. S. Wang, G. A. Covic and O. H. Stielau, "Power transfer capability and bifurcation phenomena of loosely coupled inductive power transfer systems," IEEE Trans. Ind. Electron., vol. 51, no. 1, pp. 148-157, February 2004.
- [131] H. Sheng, D. Fu, X. Yang, F. Wang and F. Lee, "Comparison of ZVS operation modes with and without phase shift for three-level resonant converters," IEEE Applied Power Electronics Conference Proc., 2006.

- [132] P. Jain, H. Soin and M. Cardella, "Constant frequency resonant dc-dc converters with zero switching loss," IEEE Transactions on Aerospace and Electronic Systems, vol. 30, no. 2, pp. 534-543, April 1994.
- [133] S. Gonzalez, M Valla and C. Muravchik, "Analysis and design of clamped mode resonant converters with variable load," IEEE Trans. Ind. Electron., vol. 48, no. 2, pp. 812-819, August 2001.
- [134] H. W. Koertzen, J. D. Van Wyk and J. A. Ferreira, "Comparison of swept frequency and phase shift control for forced commutated series resonant induction heating converters," IEEE Industry Applications Society Annual Meeting, 1995, pp. 1964-1969 .
- [135] J. Hayes and M. Egan, "A comparative study of phase-shift, frequency and hybrid control of series resonant converter supplying the electric vehicle inductive charging interface," IEEE Applied Power Electronics Conference Proc., 1999, pp. 450-457.
- [136] P. Jain, A. Martin and G. Edwards, "Asymmetrical pulse-width-modulated resonant DC-DC converter topologies," IEEE Trans. Power Electron., vol. 11, no. 3, pp. 413-422, May 1996.
- [137] S. Mangat, M. Qui and P. Jain, "Modified asymmetrical pulse width modulated resonant dc-dc converter topology ," IEEE Trans. Power Electron., vol. 19, no. 1, pp. 104-111, January 2004.
- [138] M. Qiu, P. K. Jain and H. Zhang, "An APWM resonant inverter topology for high frequency AC power distribution systems," IEEE Trans. Power Electron., vol. 19, no. 1, pp. 121-129, January 2004.
- [139] D. Tschirhart and P. Jain, "A CLL resonant asymmetrical pulsewidth-modulated converter with improved efficiency", IEEE Trans. Power Electron., vol. 55, no. 1, pp. 114-122, January 2008.
- [140] J. M. Burdío, L. A. Barragán, F. Monterde, D. Navarro and J. Acero, "Asymmetrical voltage-cancellation control for full-bridge series resonant inverters," IEEE Trans. Power Electron., vol. 19, no. 2, pp. 461-469, March 2004.
- [141] L. A. Barragan, J. M. Burdio, J. I. Artigas, D. Navarro, J. Acero and D. Puyal, "Efficiency optimization in ZVS series resonant inverters with

- asymmetrical voltage-cancellation control," *IEEE Trans. Power Electron.*, vol. 20, no. 5, pp. 1036- 1044, September 2005.
- [142] G. Joung, C. Rim and G. Cho, "Integral cycle mode control of series resonant converter," *IEEE Trans. Power Electron.*, vol. 4, no. 1, pp. 83-91, January 1989.
- [143] J. Ko, S. Hong, T. Ann and M. Youn, "Dynamic modeling and current control technique for quantum series resonant converter with nonperiodic integral cycle mode," *International Journal of Electronics*, vol. 71, no. 5, pp. 885-897, 1991.
- [144] W. Kwon and G. Cho, "Modified quantum and phase control of series resonant converter," *IEEE Power Electronics Specialist Conference Proc*, 1991, pp. 498-503.
- [145] J. Ko, S. Hong, M. Kim and M. Youn, "Modeling and improved current control of series resonant converter with non-periodic integral cycle mode," *IEEE Trans. Power Electron.*, vol. 7, no. 2, pp. 280-288, April 1992.
- [146] W. K. Kwon and G. Cho, "Optimum quantum sequence control of quantum series resonant converter for minimum output voltage ripple," *IEEE Trans. Power Electron.*, vol. 9, no. 1, pp. 74-89, January 1994.
- [147] Y. Liu and X. He, "PDM and PFM hybrid control of a series-resonant inverter for corona surface treatment," *IEE Proc. Electr. Power. Appl.*, vol. 152, no. 6, pp. 1445- 1450, November 2005.
- [148] H. Pinheiro, P. Jain and G. Joos, "Self-sustained oscillating resonant converters operating above the resonant frequency," *IEEE Trans. Power Electron.*, vol. 14, no. 5, pp. 803-815, September 1999.
- [149] M. Z. Youssef and P. K. Jain, "Series-parallel resonant converter in self-sustained oscillation mode with the high-frequency transformer-leakage-inductance effect: analysis, modeling, and design," *IEEE Trans. Ind. Electron.*, vol. 54, no. 3, pp. 1329-1341, June 2007.
- [150] Z. Ye, P. Jain and P. Sen , "A Half-Bridge Hybrid Resonant Inverter with Novel Pulse Phase Modulation Control," *IEEE Power Electronics Specialist Conference Proc*, 2006, pp. 2686-2692.

- [151] S. Wong and A. Brown, "Macro-modeling series resonant converter circuits," IEE Proc. Circuits Devices Syst., vol. 142, no. 1, pp. 83-89, February 1995.
- [152] R. Oruganti and F. Lee, "Resonant power processors, parts I and II," IEEE Trans. Ind. Appl., vol. IA-21, no. , pp. 1453-1971, November/December 1985.
- [153] C. Lee and K. Siri, "Analysis and design of series resonant converter by state plane diagram," IEEE Transactions on Aerospace and Electronic Systems, vol. AES-22, no. 6, pp. 757-763, November 1986.
- [154] I. Batarseh, "State-plane approach for analysis of half-bridge parallel resonant converters," IEE Proc. Circuits Devices Syst., vol. 142, no. 3, pp. 200-204, June 1995.
- [155] S. K. Kim, H. S.Han, Y. J. Woo and G. H. Cho, "Detection and regulation of CCFL current and open-lamp voltage while keeping floating condition of the lamp," IEEE Trans. Ind. Electron., vol. 53, no. 2, pp. 707- 713, April 2006.
- [156] A. Bhat, "A unified approach for the steady-state analysis of resonant converters," IEEE Trans. Ind. Electron., vol. 38, no. 4, pp. 251-259, August 1991.
- [157] M. Kazimierczuk, "Class D voltage switching MOSFET power amplifiers," IEE Proc. B, vol. 138, no. 6, pp. 285-296, November 1991.
- [158] M. Kazimierczuk, W. Szaraniec and S. Wang, "Analysis and design of parallel resonant converter at high QL," IEEE Transactions on Aerospace and Electronic Systems, vol. 28, no. 1, pp. 35-49, January 1992.
- [159] W. Sulistiyona and P. Enjeti, "A series resonant AC-to-DC rectifier with high frequency isolation," IEEE Trans. Power Electron., vol. 10, no. 6, pp. 784-790, November 1995.
- [160] R. Casanueva, F. J. Azcondo, C. Brañas and S. Bracho, "Analysis, design and experimental results of a high-frequency power supply for spark erosion," IEEE Trans. Power Electron., vol. 20, no. 2, pp. 361-369, March 2005.
- [161] P. Jain, "A novel frequency domain modelling of a series resonant DC/DC converter," IEEE International Telecommunication Conference Proc., 1990, pp. 343-349.

- [162] M. Kazimierczuk and S. Wang, "Frequency domain analysis of series resonant converter for continuous conduction mode," *IEEE Trans. Power Electron.*, vol. 7, no. 2, pp. 270-279, April 1992.
- [163] A. K. S. Bhat, "A generalized steady state analysis of resonant converters using two-port model and fourier series approach," *IEEE Trans. Power Electron.*, vol. 13, no. 1, pp. 142-151, January 1998.
- [164] M. Kim and M. Youn, "A discrete time domain modeling and analysis of controlled series resonant converter," *IEEE Trans. Ind. Electron.*, vol. 38, no. 1, pp. 32-40, February 1991.
- [165] R. King and T. Stuart, "Small signal modeling of series resonant converter," *IEEE Transactions on Aerospace and Electronic Systems*, vol. AES-21, no. 3, pp. 301-319, May 1985.
- [166] V. Agarwal and A. Bhat, "Small signal analysis of the LCC-type parallel resonant converter using discrete time domain modeling," *IEEE Trans. Ind. Electron.*, vol. 42, no. 6, pp. 604-614, December 1995.
- [167] V. Vorperian and S. Cuk, "Small signal analysis of resonant converters," *IEEE Power Electronics Specialist Conference Proc*, 1983, pp. 265-278.
- [168] V. Vorperian, "Approximate small signal analysis of series and parallel resonant converters," *IEEE Trans. Power Electron.*, vol. 4, no. 1, pp. 15-24, January 1989.
- [169] A. Witulski, A. Hernandez, R. Erickson, "Small signal equivalent circuit modeling of resonant converters," *IEEE Trans. Power Electron.*, vol. 6, no. 1, pp. 11-27, January 1991.
- [170] I. Batarseh and K. Siri, "Generalized approach to the small signal modeling of DC-DC resonant converters," *IEEE Transactions on Aerospace and Electronic Systems*, vol. 29, no. 3, pp. 894-908, July 1993.
- [171] M. Eshani, O. Stielau, J. D. van Wyk and I. Pitel, "Integrated reactive components in power electronic circuits," *IEEE Trans. Power Electron.*, vol. 8, no. 2, pp. 208-215, April 1993.
- [172] K. Laouamri, J. Ferrieux, S. Catellani and J. Barbaroux, "Modeling and analysis of wound integrated LCT structure for single stage resonant PFC

- rectifier," IEEE Trans. Power Electron., vol. 18, no. 1, pp. 256-269, January 2003.
- [173] P. A. Janse van Rensburg, J. D. van Wyk and J. A. Ferreira, "Design and construction of a generic multi-kVA planar integrated LCT for a family of series resonant converters," IEEE Industry Applications Society Annual Meeting, 1996, pp. 1361-1368.
- [174] I. Hofsjager, J. Ferreira and J. D. van Wyk, "Design and analysis of planar integrated L-C-T components for converters," IEEE Trans. Power Electron., vol. 15, no. 6, pp. 1221-1227, November 2000.
- [175] M. Meinhardt, M. Duffy, T. O'Donnell, S. Reilly, J. Flannery and C. O'Mathuna, "New method for integration of resonant inductor and transformer - design, realization, measurements," IEEE Applied Power Electronics Conference Proc., 1999, pp. 1168-1174.
- [176] J.T. Strydom and J.D. van Wyk, "Improved Loss Determination for Planar Integrated Power Passive Modules," IEEE Applied Power Electronics Conference Proc., 2002, pp. 332-338.
- [177] J. Strydom and J. D. van Wyk, "Volumetric limits of planar integrated resonant transformer: A 1 MHz case study," IEEE Trans. Power Electron., vol. 18, no. 1, pp. 236-247, January 2003.
- [178] R. Chen, F. Canales, B. Yang and J. D. van Wyk, "Volumetric optimal design of passive integrated power electronic module (IPEM) for distributed power system (DPS) front-end dc/dc converter," IEEE Trans. Ind. Appl., vol. 41, no. 1, pp. 9-17, Jan/Feb 2005.
- [179] L. Zhao, J.T. Strydom and J.D. van Wyk, "Optimization and design of an integrated L-C resonant module for medium and high power application," IEEE Power Electronics Specialist Conference Proc, 2001, pp. 594-599.
- [180] E. Nho, K. Jee and G. Cho, "New soft-switching for high efficiency electronic ballasts with simple structure," International Journal of Electronics, vol. 71, no. 3, pp. 529-542, 1991.
- [181] M. Cosby and R. Nelms, "Designing a parallel-loaded resonant inverter for an electronic ballast using the fundamental approximation," IEEE Applied Power Electronics Conference Proc., 1993, pp. 418-423.

- [182] J. Alnoso, C. Blanco, E. Lopez, A. Calleja and M. Rico, "Analysis design and optimization of LCC resonant inverter as a high intensity discharge lamp ballast," *IEEE Trans. Power Electron.*, vol. 3, no. , pp. 573-585, May 1988.
- [183] R. M. Nelms, T. D. Jones and M. C. Cosby Jr., "A comparison of resonant inverter topologies for HPS lamp ballasts," *IEEE Industry Applications Society Annual Meeting*, 1993, pp. 2317-2322 .
- [184] A. Bhat, "Analysis, selection, and, design of resonant inverters for electronic ballasts," *IEEE Power Electronics Specialist Conference Proc*, 1994, pp. 796-804.
- [185] Y. Ho, T. Lee, H. Chung and S. Hui, "A comparative study on dimming control methods for electronic ballasts," *IEEE Trans. Power Electron.*, vol. 16, no. 6, pp. 828-836, November 2001.
- [186] J. Hong, D. Maksimovic, R. Erickson and I. Khan, "Half-cycle control of parallel resonant converter operated as a high power factor rectifier," *IEEE Trans. Power Electron.*, vol. 10, no. 1, pp. 1-8, January 1995.
- [187] W. Sulistyono and P. Enjeti, "A series resonant ac-dc rectifier with high frequency isolation," *IEEE Applied Power Electronics Conference Proc.*, 1994, pp. 397-403.
- [188] A. C. Lippincott and R. M. Nelms, "A capacitor-charging power supply using a series-resonant topology, constant on-time/variable frequency control," *IEEE Trans. Ind. Electron.*, vol. 38, no. 6, pp. 438-447, December 1991.
- [189] M. Souda, F. Endo, C. Yamazaki, K. Okamura and K. Fukushima, "Development of high power capacitor charging power supply for pulsed power applications ," *12th IEEE International Pulsed Power Conference*, 1999, pp. 1414-1416.
- [190] B. Cathell, S. Pronko, S. Eckhouse and N. Nelms, "8 kJ/s high frequency capacitor charging power supply using parallel inverters ," *12th IEEE International Pulsed Power Conference*, 1999, pp. 245-248.
- [191] G. H. Rim, I. W. Jeong, Y. W. Choi, H. J. Ryoo, J. S. Kim, K. H. Kim, S. P. Lee and H. K. Chang, "A constant current high voltage capacitor charging power supply for pulsed power applications ," *IEEE Conference Record Pulsed Power Plasma Science*, 2001, pp. 342.

- [192] H. Sheng, Y. Pei, X. Yang, F. Wang and C. Tipton, "Frequency Tracking Control for a Capacitor-Charging Parallel Resonant Converter with Phase-Locked Loop," IEEE Applied Power Electronics Conference Proc., 2007, pp. 1287-1292.
- [193] H. Pollock, "High efficiency, high frequency for capacitor and battery charging," IEE Colloquium on Power Electronics for Demanding Applications, 1999, pp. 9/1-9/10.
- [194] L. Hobson and D. Tebb, "Transistorized power supplies for induction heating," International Journal of Electronics, vol. 59, no. 5, pp. 543-552, 1985.
- [195] H. Ahn, B. Jo and M. Youn, "Improved performance current regulated delta modulator in series resonant inverter for induction heating application," IEEE Industrial Electronics Conference, 1993, pp. 857-862.
- [196] H. Koertzen, J. D. van Wyk and J. A. Ferreira, "Design of the half-bridge series resonant converter for induction cooking," IEEE Power Electronics Specialist Conference Proc, 1995, pp. 729-735.
- [197] F. Forest, E. Laboure and J. Yves, "Principle of a multi-load/single converter system for low power induction heating," IEEE Trans. Power Electron., vol. 15, no. 2, pp. 223-230, March 2000.
- [198] E. Dede, V. Esteve, J. Garcia, A. Navarro, E. Maset and E. Sanchis, "Analysis of losses and thermal design of high power high frequency resonant current fed inverters for induction heating," IEEE Industrial Electronics Conference, 1993, pp. 1046-1051.
- [199] R. Bonard and J. Lavers, "Simple starting scheme for a parallel resonance converter for induction heating," IEEE Trans. Power Electron., vol. 9, no. 3, pp. 281-287, May 1994.
- [200] F. Dawson and P. Jain, "A comparison of load commutated inverter system for induction heating and melting applications," IEEE Trans. Power Electron., vol. 6, no. 3, pp. 430-441, July 1991.
- [201] J. Ferreira and J. Roux, "A series resonant converter for arc-striking applications," IEEE Trans. Ind. Electron., vol. 45, no. 4, pp. 585-592, August 1998.

- [202] L. Malesani, P. Mattavelli, L. Rossetto, P. Tenti and W. Marin, A. Pollmann, "Electronic welder with high frequency resonant inverter," IEEE Trans. Ind. Appl., vol. 31, no. 2, pp. 273-279, March/April 1995.
- [203] N. Kutkut, "A full bridge LCL resonant battery charger for an EV conductive coupler," IEEE Industry Applications Society Annual Meeting, 1998, pp. 2069-2075.
- [204] F. Zhuo, M. Cui, T. Liu, T. Han and Z. Wang, "Efficiency and Frequency Bifurcating Phenomenon Research of Series Resonance Converter Applied in a Contact-less Power Transmission System," IEEE Power Electronics Specialist Conference Proc, 2006, pp. 1007-1012.
- [205] W. Zhou and H. Ma, "Design Considerations of Compensation Topologies in ICPT System," IEEE Applied Power Electronics Conference Proc., 2007, pp. 985-990.
- [206] S. D. Johnson, A. F. Witulski and R. W. Erickson, "Comparison of resonant topologies in high voltage dc applications," IEEE Transactions on Aerospace and Electronic Systems, vol. 24, no. 3, pp. 263-274, May 1988.
- [207] H. Takano, J. Takahashi and M. Nakaoka, "Feasible characteristic evaluation of resonant tank PWM inverter-linked dc-dc high-power converters for medical-use high-voltage application," IEEE Applied Power Electronics Conference Proc., 1995, pp. 913-919.
- [208] J. Sun, X. Ding, M. Nakaoka and H. Takano, "Series resonant ZCS-PFM DC-DC converter with multistage rectified voltage multiplier and dual mode PFM control scheme for medical use high voltage x-ray power generator," IEE Proc. Electr. Power. Appl., vol. 147, no. 6, pp. 527-534, November 2000.
- [209] Sanbao Zheng and Darisuz Czarkowski, "High-voltage High-power Resonant Converter for Electrostatic Precipitator," IEEE Applied Power Electronics Conference Proc., 2003, pp. 1100-1104.
- [210] H. Fujita and H. Akagi, "A 2 MHz 2 kW voltage source inverter for low temperature plasma generators: Implementation of fast switching with a third order resonant circuit," IEEE Trans. Ind. Appl., vol. 35, no. 1, pp. 21-27, Jan/Feb 1999.

- [211] Welding handbook, volume 2 – welding processes, 8th edition, American welding society, Miami FL, R. L. O'Brien – Editor, February 1992.
- [212] Welding and brazing of carbon steels, Book-1, Arc Welding, American Society of Metals, Metals Park, Editor – Charles A. Davis, 1976.
- [213] Metals Handbook, Vol-6., Welding Brazing and Soldering, 9th edition, American Society of Metals, Metals Park, 1983.
- [214] D. Novotny, D. Breckinridge and K. Hartke, “Power supplies adapted for diode pumped laser systems”, Laser Focus World, April 2002, pp. 97-99.
- [215] M. K. Koli, S. R. Tiwari and M. B. Borage, “QCW laser diode driver – pulsed current source”, Proc. of DAE-BRNS National Laser Symposium (NLS) 2002, pp 175-176.
- [216] C. Coleman and R. Sherwood, “Inductive storage yields efficient power alternative”, Laser Focus World, April 2003, pp. 94-97.
- [217] P. Bryant, “Performance requirements for accelerators” in Proc. CERN Accelerator School on Power Converters for Particle Accelerator, CERN 90-07, pp. 1-14.
- [218] F. Bordry and A. Dupaquier, “High current low voltage power converters for LHC: Present development directions,” Proc. of European Particle Accelerator Conference, EPAC'96, Sitges, 1996.
- [219] “Constant current regulator type THO”, Augier S.A., France, <http://www.augier.com>
- [220] “Constant Current Regulators CCR-10 and CCR-25”, Honeywell airfield lighting product catalog, Honeywell International Inc.
- [221] M. Day, “LED driver considerations”, Electronics design news – Asia, Jan. 2004, pp. 62-65.
- [222] C. Simpson, “Battery charging”, National Semiconductors.
- [223] “Switch mode, linear and pulse charging techniques for Li+ batteries in mobile phones and PDAs”, Application note, Maxim Semiconductors, AN 913, Dec. 2001.
- [224] “Portable devices need high performance battery chargers”, Application note, Maxim Semiconductors, AN 721, Dec. 2000.

- [225] J. Puippe and F. Leaman, "Theory and practice of pulse plating", American electroplaters and surface finishers society, Orlando, FL, 1986.
- [226] P. Pollak, "DC power supplies", publication no. 103, Dynapower Corporation.
- [227] H.Irie and H.Yamana, "Immittance converter suitable for power electronics", *Trans. of I.E.E. Japan*, vol. 117D, no. 8, pp.962-969, 1997.
- [228] H. Ohguchi, M. H. Ohsato, T. Shimizu, G. Kimura and H. Takagi, "A high-frequency electronic ballast for HID lamp based on a $\lambda/4$ -long distributed constant line," *IEEE Trans. Power Electron.*, vol. 13, no. 6, pp. 1023-1029, November 1998.
- [229] T. Shimizu and M. Shioya, "Characteristics of electric power transmission on high-frequency inverter having distributed constant line," *IEEE Trans. Ind. Electron.*, vol. 38, no. 2, pp. 115-120, April 1991.
- [230] H. Ohguchi, M. Tamate, R. Shimotaya, H. Takagi and M. Ito, "13.56 MHz current source generator based on third harmonic power transmission using immittance conversion topology and investigation on novel immittance conversion element," *Proc. IEEE ISIE*, 2000, pp. 477-481.
- [231] T. Shimizu, H. Kinjyo and K. Wada, "A novel high-frequency current output inverter based on an immittance conversion element and a hybrid MOSFET-SIC diode switch," *Proc. IEEE PESC*, 2003, pp. 2003-2008.
- [232] Y. Sakamoto, K. Wada and T. Shimizu, "A 13.565 MHz current-output-type inverter utilizing an immittance conversion element," *Proc of Int. Power Electronics and Motion Control Conference (EPE- PEMC)*, 2008, pp. 288-294.
- [233] M. A. Razzak, S. Takamura, Y. Uesugi and N. Ohno, "Efficient radio frequency inductive discharge in near atmospheric pressure using immittance conversion topology," *Journal of Plasma and Fusion Research*, vol. 81, no. 3, pp. 204-211, March 2005.
- [234] E. Zhang, "Inverter design shiens in photovoltaic systems," *Power Electronics Technology*, pp. 20-25, July 2008.
- [235] H. Irie, N. Minami, H. Minami and H. Kitayoshi, "Non-contact energy transfer system using immittance converter," *Electrical Engineering in Japan*, vol. 136, no. 4, pp. 58-64, July 2001.

- [236] N. Kimura, K. Tanaka, T. Morizane and K. Taniguchi, "Analysis of HVDC converter with immittance conversion link," Proc. EPE, 1999, pp. P.1-P.9.
- [237] M. Tamate, H. Ohguchi, M. Hayashi, H. Takagi and M. Ito, "A novel approach of power converter topology based on immittance conversion theory," Proc. IEEE ISIE, 2000, pp. 482-487.
- [238] Y. Yin, R. Zane, J. Glaser and R. W. Erickson, " Small-signal analysis of frequency-controlled electronic ballasts," IEEE Trans. Circuits and Systems – I, Fundamental Theory and App., vol. 50, no. 8, pp. 1103-1110, August 2003.
- [239] S. Lineykin, S. Ben-Yaakov, "Unified SPICE-compatible model for large and small-signal envelop simulation of linear circuits excited by modulated signals," IEEE Trans. Ind. Electron., vol. 53, no. 3, pp. 745-751, June 2006.
- [240] A. Burke, "Ultracapacitors: why, how and where is the technology," Journal of Power Sources, vol. 91, pp. 37-50, 2000.